



PLACE IN RETURN BOX to remove this checkout from your record.  
TO AVOID FINES return on or before date due.  
MAY BE RECALLED with earlier due date if requested.

DATE DUE	DATE DUE	DATE DUE
05042952005	<del>118608</del>	
DEC 01 2008		
NOV 25 2008		
15170.215		

**Microwave Plasma Assisted Chemical Vapor Deposition of  
Ultra-nanocrystalline Diamond Films**

**VOLUME I**

**By**

**Wen-Shin Huang**

**A DISSERTATION**

**Submitted to  
Michigan State University  
in partial fulfillment of the requirements  
for the degree of**

**DOCTOR OF PHILOSOPHY**

**Department of Electrical and Computer Engineering**

**2004**



## ABSTRACT

# Microwave Plasma Assisted Chemical Vapor Deposition of Ultra-nanocrystalline Diamond Films

By

Wen-Shin Huang

Microwave plasma assisted ultra-nanocrystalline diamond film deposition was investigated using hydrogen deficient, carbon containing argon plasma chemistries with MSU-developed microwave plasma reactors. Ultra-nanocrystalline diamond film deposition on mechanically scratched silicon wafers was experimentally explored over the following input variables: (1) pressure: 60-240Torr, (2) total gas flow rate: 101-642 sccm, (3) input microwave power 732-1518W, (4) substrate temperature: 500°C-770°C, (5) deposition time: 2-48 hours, and (6) N<sub>2</sub> impurities 5-2500 ppm. H<sub>2</sub> concentrations were less than 9%, while CH<sub>4</sub> concentration was 0.17-1.85%. It was desired to grow films uniformly over 3" diameter substrates and to minimize the grain size.

Large, uniform, intense, and greenish-white discharges were sustained in contact with three inch silicon substrates over a 60-240 Torr pressure regime. At a given operating pressure, film uniformity was controlled by adjusting substrate holder geometry, substrate position, input microwave power, gas chemistries, and total gas flow rates. Film ultra-nanocrystallinity and smoothness required high purity deposition conditions. Uniform

ultra-nanocrystalline films were synthesized in low leak-rate system with crystal sizes ranging from 3-30 nm. Films with 11-50 nm RMS roughness and respective thickness values of 1-23  $\mu\text{m}$  were synthesized over 3" wafers under a wide range of different deposition conditions. Film RMS roughness 7 nm was synthesized with thickness of 430 nm. Film uniformities of almost 100% were achieved over three inch silicon wafers. UV-Raman and XRD characterization results indicated the presence of diamond in the synthesized films. Optical Emission Spectroscopy measurements showed that the discharge gas temperature was in excess of 2000 K.

The synthesized films are uniformly smooth and the as grown ultra-nanocrystalline diamond can be used for a high frequency SAW device substrate material. IR measurements indicated that the films have a wide-band, low-loss transmission window.

Copyright by  
Wen-Shin Huang  
2004

**To my mother and my husband**

## ACKNOWLEDGEMENTS

The author wishes to express her sincere appreciation to Professor Jes Asmussen, Jr. for his encouragement and support for this thesis research. Thanks are also due to the other members of the author's guidance committee: Professor Donnie Reinhard, Professor Timothy Grotjohn, Professor Brage Golding, and Professor Martin A. Crimp. The author is grateful to Dr. Dieter Gruen and the late Dr. Alan Krauss for the introduction to ultra-nanocrystalline diamond. A special note of thanks is extended to Dr. Baokang Bi for training on AFM and FESEM, for his collaborative efforts in the research of SAW devices based on UNCD and for valuable discussions. In addition, the author owes a debt of gratitude to Dr. Rui Huang and Dr. Liang Zeng for training and sharing their knowledge on XRD and TEM, respectively. The author also thanks Dr. Suilong Jiao for assistance with TEM photos and Dr. Anirudha Sumant for assistance with Raman spectra. The author thanks Brian Wright for his technical support and for assistance with SiC seal substrate holder design.

The author acknowledges use of the Keck Microfabrication Facility and the National Science Foundation for support under MRSEC program grant DMR-9809688 for the financial assistance which made this thesis research possible.

## TABLE OF CONTENT

<b>LIST OF TABLES . . . . .</b>	<b>xiii</b>
---------------------------------	-------------

<b>LIST OF FIGURES . . . . .</b>	<b>xv</b>
----------------------------------	-----------

<b>1</b>	<b>Introduction . . . . .</b>	<b>1</b>
1.1	Motivation . . . . .	3
1.2	Research Objectives . . . . .	4
1.3	Dissertation Outline . . . . .	4
<b>1</b>	<b>Background . . . . .</b>	<b>6</b>
2.1	General Introduction . . . . .	6
2.2	Diamond Synthesis. . . . .	8
2.2.1	Polycrystalline Diamond Synthesis . . . . .	13
2.2.1.1	Methyl Radical and Acetylene Growth Processes . . . . .	13
2.2.1.2	Polycrystalline Diamond Competitive Growth Model . . . . .	16
2.2.2	Ultra-nanocrystalline Diamond Synthesis . . . . .	18
2.2.2.1	Carbon Dimer Growth Processes For The Synthesis of Ultra-nanocrystalline Diamond Films . . . . .	18
2.2.2.2	Ultra-nanocrystalline Diamond Re-nucleation Growth Model	21
2.3	Nanocrystalline Diamond Film Deposition Techniques and Conditions. . . . .	22
2.4	Nanocrystalline Diamond Applications . . . . .	35
2.4.1	IR Optical Transmission Window . . . . .	35
2.4.2	Tribological Application-Seal Coatings . . . . .	45

2.4.3	SAW Devices Based on Nanocrystalline Diamond. . . . .	54
<b>3</b>	<b>Description of Experimental Systems and Procedures . . . . .</b>	<b>58</b>
3.1	Introduction . . . . .	58
3.2	Experimental systems . . . . .	58
3.2.1	Microwave Power Supply and Waveguide/Transmission System . . .	60
3.2.2	Vacuum Pump and Gas Flow Control System. . . . .	62
3.2.2.1	MSU-MPACVD System I . . . . .	62
3.2.2.2	MSU-MPACVD System II . . . . .	64
3.2.3	Computer Control System. . . . .	68
3.2.3.1	MSU-MPACVD System I . . . . .	68
3.2.3.2	MSU-MPACVD System II . . . . .	70
3.2.4	Reactor Geometry. . . . .	72
3.2.4.1	Microwave Cavity Plasma Reactor. . . . .	72
3.2.4.2	Substrate Heating Stage . . . . .	79
3.2.5	Microwave Cavity Plasma Reactor General Operating Field Map in Ultra-nanocrystalline Diamond Synthesis . . . . .	82
3.3	Experimental Procedures . . . . .	86
3.3.1	Seeding Procedures. . . . .	86
3.3.1.1	Photoresist Seeding . . . . .	86
3.3.1.2	Scratch Seeding . . . . .	89
3.3.1.3	Comparison of Photoresist Seeding and Scratch Seeding . . .	91
3.3.2	Start-up and Shut-down Procedures . . . . .	97
3.3.2.1	System I . . . . .	97
3.3.2.2	System II . . . . .	99
3.4	Experimental Parameter Space . . . . .	101
3.5	Measurement Methodologies . . . . .	106
3.5.1	Reactor Performance . . . . .	106
3.5.1.1	Total Growth Rate. . . . .	106
3.5.1.2	Average Growth Rate. . . . .	106
3.5.1.3	Specific Yield . . . . .	106





3.5.1.4	Carbon Conversion Efficiency . . . . .	106
3.5.2	Film Characteristics . . . . .	107
3.5.2.1	Film Texture . . . . .	107
3.5.2.2	Film Roughness and Morphology . . . . .	108
3.5.2.3	Film Quality . . . . .	108
3.5.2.4	Crystal Size . . . . .	110
3.5.2.5	Optical Property . . . . .	112
<b>4</b>	<b>MSU-MPACVD Reactor Experimental Output Variables -</b>	
	<b>Reactor Performance (<math>Y_1</math>) . . . . .</b>	<b>113</b>
4.1	Introduction . . . . .	113
4.2	System I . . . . .	119
4.2.1	Introduction . . . . .	119
4.2.2	Total Growth Rate= $g(\text{Ar}/\text{H}_2/\text{CH}_4, t, f_t, p, P_{\text{abs}})$ . . . . .	120
4.2.3	Specific Yield= $g(\text{Ar}/\text{H}_2/\text{CH}_4, t, f_t, p, P_{\text{abs}})$ . . . . .	127
4.2.4	Carbon Conversion Efficiency= $g(\text{Ar}/\text{H}_2/\text{CH}_4, t, f_t, p, P_{\text{abs}})$ . . . . .	134
4.3	System II. . . . .	141
4.3.1	Introduction . . . . .	141
4.3.2	Total Growth Rate = $g(\text{Ar}/\text{H}_2/\text{CH}_4, t, f_t, p, P_{\text{abs}}, T_s)$ . . . . .	141
4.3.3	Specific Yield = $g(\text{Ar}/\text{H}_2/\text{CH}_4, t, f_t, p, P_{\text{abs}})$ . . . . .	152
4.3.4	Carbon Conversion Efficiency = $g(\text{Ar}/\text{H}_2/\text{CH}_4, t, f_t, p, P_{\text{abs}})$ . . . . .	158
4.4	Controlled Nitrogen Impurity Study By System II. . . . .	164
4.5	Summary. . . . .	169
<b>5</b>	<b>MSU-MPACVD Reactor Experimental Output Variables -</b>	
	<b>Reactor Performance (<math>Y_1</math>) . . . . .</b>	<b>174</b>
5.1	Introduction . . . . .	174
5.2	System I . . . . .	177
5.2.1	Film Texture= $g(\text{Ar}/\text{H}_2/\text{CH}_4, t, f_t, p)$ . . . . .	177
5.2.2	Film Roughness= $g(\text{Ar}/\text{H}_2/\text{CH}_4, t, f_t, p)$ . . . . .	183

5.2.3	Film Quality= $g(t, p)$ . . . . .	186
5.2.4	Morphology and Crystal Size= $g(\text{Ar}/\text{H}_2/\text{CH}_4, t, f_t, p)$ . . . . .	188
5.3	System II . . . . .	202
5.3.1	Film Texture= $g(\text{Ar}/\text{H}_2/\text{CH}_4, f_t, p)$ . . . . .	202
5.3.2	Film Roughness= $g(\text{Ar}/\text{H}_2/\text{CH}_4, t, f_t, p)$ . . . . .	206
5.3.3	Film Quality= $g(\text{Ar}/\text{H}_2/\text{CH}_4, t, p)$ . . . . .	211
5.3.4	Morphology= $g(\text{Ar}/\text{H}_2/\text{CH}_4, t, f_t, p)$ . . . . .	215
5.3.5	Growth Mechanism & Crystal Size= $g(\text{Ar}/\text{H}_2/\text{CH}_4)$ . . . . .	238
5.4	Controlled Nitrogen Impurity Study By System II. . . . .	251
5.5	Summary . . . . .	259
5.5.1	System I. . . . .	259
5.5.2	System II . . . . .	260
<b>6</b>	<b>Plasma Diagnostics . . . . .</b>	<b>266</b>
6.1	Introduction . . . . .	266
6.2	Background Fundamental of $\text{C}_2$ Emission Spectroscopy . . . . .	267
6.3	Gas Kinetic Temperature Measurement Theory . . . . .	270
6.4	Experimental Method and Measurement. . . . .	272
6.5	Experimental Results . . . . .	275
6.5.1	$\text{C}_2$ Emission Intensity . . . . .	275
6.5.2	Gas Temperature . . . . .	284
6.5.3	CN Emissions versus Controlled Nitrogen Impurities . . . . .	294
6.6	Summary . . . . .	295
<b>7</b>	<b>Ultra-nanocrystalline Diamond Film Application . . . . .</b>	<b>297</b>
7.1	Introduction. . . . .	297
7.2	IR Optical Transmission Window . . . . .	298
7.2.1	Introduction . . . . .	298
7.2.2	Experimental Method . . . . .	300
7.2.3	Theoretical Calculation and Transmission Measurement . . . . .	303

7.2.3.1	Theoretical Calculations . . . . .	303
7.2.3.2	IR Transmission Measurements . . . . .	306
7.2.4	Experimental Results . . . . .	307
7.2.4.1	Introduction . . . . .	307
7.2.4.2	Single Layer One Side With Ultra-nanocrystalline Diamond Optical Coatings . . . . .	307
7.2.4.3	Single Layer Both Side With Ultra-nanocrystalline Diamond Optical Coatings . . . . .	315
7.2.4.4	Two Layer One Side Diamond/SiO <sub>2</sub> /Si/SiO <sub>2</sub> Optical Coatings . . . . .	318
7.2.4.5	Two Layer Both Side Diamond/SiO <sub>2</sub> /Si/SiO <sub>2</sub> /Diamond Optical Coatings . . . . .	320
7.2.5	Summary . . . . .	322
7.3	Tribological Application-Seal Coatings . . . . .	323
7.3.1	Introduction . . . . .	323
7.3.2	Experimental Deposition Method . . . . .	325
7.3.3	Experimental Measurements and Results. . . . .	327
7.3.4	Summary . . . . .	333
7.4	SAW Devices Based on Ultra-nanocrystalline Diamond . . . . .	334
7.4.1	Introduction . . . . .	334
7.4.2	Experimental Method . . . . .	335
7.4.3	Theoretical Calculations and Measurements. . . . .	338
7.4.4	Experimental Results. . . . .	338
7.4.5	Summary . . . . .	339
<b>8</b>	<b>Summary . . . . .</b>	<b>340</b>
8.1	Introduction . . . . .	340
8.2	The Performance Comparison Between Systems I and II . . . . .	342
8.3	Summary of Experimental Performance . . . . .	344
8.4	Plasma Diagnostics Using System II . . . . .	348
8.5	Controlled Nitrogen Impurity Study by System II . . . . .	349

8.6	Ultra-nanocrystalline Diamond Film Application . . . . .	350
8.7	Recommendations for Future Research . . . . .	351
<b>9</b>	<b>Appendix . . . . .</b>	<b>354</b>
9.1	System I . . . . .	354
9.2	System II. . . . .	357
9.3	OES . . . . .	361
9.4	Gas Temperature Measurements . . . . .	364
9.5	X-ray Diffraction Crystallography . . . . .	366
9.6	Atomic Force Microscopy . . . . .	367
<b>10</b>	<b>References . . . . .</b>	<b>369</b>

## LIST OF TABLES

TABLE 2.1:	Some Properties of Natural, CVD Diamond And The Applications .....	6
TABLE 2.2:	Nanocrystalline Diamond Film Deposition Methodology and Film Characteristics .....	30
TABLE 2.3:	Polycrystalline Diamond Film Deposition Methodology and The Transmittance.....	37
TABLE 2.4:	Nanocrystalline Diamond Film Deposition Methodology and The Transmittance.....	43
TABLE 2.5:	Diamond Film Deposition Methodology and The Friction Coefficient....	47
TABLE 2.6:	SAW Velocities .....	55
TABLE 2.7:	Calculated SAW Velocities [Naka 1995] .....	56
TABLE 3.1:	Parameter Space For Experiments Performed at System I .....	104
TABLE 3.2:	Parameter Space For Experiments Performed at System II.....	105
TABLE 4.1:	Parameter Space for Experiments Performed on System I.....	117
TABLE 4.2:	Parameter Space for Experiments Performed on System II.....	118
TABLE 4.3:	Reproducible Experiment Data for System I .....	170
TABLE 4.4:	Reproducible Experiment Data for System II.....	171
TABLE 4.5:	Quantitative Comparison of The Reactor Performance of Systems I and II .....	172

TABLE 5.1:	Parameter Space For Experiments Performed on System I .....	175
TABLE 5.2:	Parameter Space for Experiments Performed on System II.....	176
TABLE 5.3:	Film Uniformity Study.....	265
TABLE 6.1:	Experimental Parameters [Goy1 1998], [Goy2 1998] .....	268
TABLE 8.1:	Experimental Performance of Systems I & II.....	343
TABLE 8.2:	Crystal Size Comparison of Ultra-nanocrystalline Diamond Films .....	347
TABLE 9.1:	Experiment Data for System I.....	354
TABLE 9.2:	Experiment Data for System II .....	357
TABLE 9.3:	Controlled N <sub>2</sub> Impurity Study by System II .....	360
TABLE 9.4:	OES Data .....	361
TABLE 9.5:	CN Study.....	363

## LIST OF FIGURES

FIGURE 2.1:Diamond Cubic Crystal Structure .....	9
FIGURE 2.2:Graphite Crystal Structure .....	10
FIGURE 2.3:Phase Diagram by Bachmann et al. [Bach 1991] .....	12
FIGURE 2.4:Polycrystalline Diamond Film .....	17
FIGURE 2.5: Diamond(110) Surface Growth Mechanism with C <sub>2</sub> As A Growth Species.....	20
FIGURE 2.6:Ultra-nanocrystalline Diamond Film .....	22
FIGURE 3.1:MSU-MPACVD System .....	59
FIGURE 3.2:Microwave Power Supply and Waveguide/Transmission System for MSU-MPACVD Reactor .....	61
FIGURE 3.3:Vacuum Pump and The Gas Flow Controller System for MSU-MPACVD Reactor I .....	63
FIGURE 3.4:Vacuum Pump and the Gas Flow Controller system for MSU-MPACVD Reactor II .....	67
FIGURE 3.5:Computer Control System for MSU-MPACVD Reactor I .....	69
FIGURE 3.6:Computer Control System for MSU-MPACVD Reactor II .....	71
FIGURE 3.7:The Cross Sectional View of the MCPR .....	76
FIGURE 3.8:Substrate Temperature Measurement Method .....	77

FIGURE 3.9:Thermally Floating Substrate Holder Set Up	78
FIGURE 3.10:Substrate Heating Stage Set Up .....	79
FIGURE 3.11:The Substrate Heating Stage	81
FIGURE 3.12:The MPACVD Operating Field Map Under Thermally Floating Substrate Holder Set Up .....	83
FIGURE 3.13:P-P <sub>abs</sub> -T <sub>s</sub> Relationship under Thermally Floating Substrate Holder Set Up .....	85
FIGURE 3.14:Photoresist Seeding	88
FIGURE 3.15:Scratch Seeding	90
FIGURE 3.16:Photoresist Seeding Film Morphology and Roughness Inspected by AFM.....	92
FIGURE 3.17:Scratch Seeding Film Morphology and Roughness Inspected by AFM .....	95
FIGURE 3.18:Relationship Between Input, Internal, and Output Parameters In A MPCVD-System.	102
FIGURE 4.1:MCPR Block Diagram for The Experiments	116
FIGURE 4.2:Total Growth Rate vs. Hydrogen Concentration	121
FIGURE 4.3:Total Growth Rate vs. Deposition Time	122
FIGURE 4.4:Total Growth Rate vs. Total Gas Flow Rate	123
FIGURE 4.5:Total Growth Rate vs. Deposition Pressure	125
FIGURE 4.6:Total Growth Rate vs. Absorbed Power	126
FIGURE 4.7:Specific Yield vs. Hydrogen Concentration	128
FIGURE 4.8:Specific Yield vs. Deposition Time	129



FIGURE 4.9:Specific Yield vs. Total Gas Flow Rate	130
FIGURE 4.10:Specific Yield vs. Deposition Pressure	132
FIGURE 4.11:Specific Yield vs. Microwave Power	133
FIGURE 4.12:Carbon Conversion Efficiency vs. Hydrogen Concentration	135
FIGURE 4.13:Carbon Conversion Efficiency vs. Deposition Time	136
FIGURE 4.14:Carbon Conversion Efficiency vs. Total Gas Flow Rate	137
FIGURE 4.15:Carbon Conversion Efficiency vs. Deposition Pressure	139
FIGURE 4.16:Carbon Conversion Efficiency vs. Microwave Power	140
FIGURE 4.17:Total Growth Rate vs. H <sub>2</sub> Flow Rate	142
FIGURE 4.18:The Influence of H <sub>2</sub> flow rate on T <sub>s</sub> and P <sub>abs</sub>	144
FIGURE 4.19:Total Growth Rate vs. Deposition Time	145
FIGURE 4.20:Total Growth Rate vs. Total Gas Flow Rate	146
FIGURE 4.21:The Influence of Total Gas Flow Rate on T <sub>s</sub> and P <sub>abs</sub>	148
FIGURE 4.22:Total Growth Rate vs. Pressure	150
FIGURE 4.23:Total Growth Rate vs. Microwave Power	151
FIGURE 4.24:Specific Yield vs. H <sub>2</sub> Flow Rate	152
FIGURE 4.25:Specific Yield vs. Deposition Time	153
FIGURE 4.26:Specific Yield vs. Total Gas Flow Rate	154
FIGURE 4.27:Specific Yield vs. Pressure	156
FIGURE 4.28:Specific Yield vs. Microwave power	157
FIGURE 4.29:Carbon Conversion Efficiency vs. H <sub>2</sub> Flow Rate	158
FIGURE 4.30:Carbon Conversion Efficiency vs. Deposition Time	159
FIGURE 4.31:Carbon Conversion Efficiency vs. Total Gas Flow Rate	160

FIGURE 4.32:Carbon Conversion Efficiency vs. Pressure	162
FIGURE 4.33:Carbon Conversion Efficiency vs. Microwave Power	163
FIGURE 4.34:Total Growth rate vs. N <sub>2</sub> Impurities	164
FIGURE 4.35:The Influence of N <sub>2</sub> Impurities on T <sub>s</sub> and P <sub>abs</sub>	166
FIGURE 4.36:Specific Yield vs. N <sub>2</sub> Impurities	167
FIGURE 4.37:Carbon Conversion Efficiency vs. N <sub>2</sub> Impurities	168
FIGURE 5.1:I(220)/I(111) vs. Hydrogen Concentration	178
FIGURE 5.2:I(220)/I(111) vs. Deposition Time	179
FIGURE 5.3:I(220)/I(111) vs. Total Gas Flow Rate	180
FIGURE 5.4:I(220)/I(111) vs. Deposition Pressure	182
FIGURE 5.5:RMS Roughness vs. Hydrogen Concentration	183
FIGURE 5.6:RMS Roughness vs. Deposition Time	184
FIGURE 5.7:RMS Roughness vs. Deposition Pressure	185
FIGURE 5.8:Raman Spectra	186
FIGURE 5.9:Raman spectra	187
FIGURE 5.10:Film Morphology vs. Gas Chemistry	190
FIGURE 5.11:Film Morphology vs. Gas Chemistry	193
FIGURE 5.12:Film Morphology vs. Deposition Time	96
FIGURE 5.13:Film Morphology vs. Deposition Pressure	200
FIGURE 5.14:I(220)/I(111) vs. H <sub>2</sub> Flow Rate	202
FIGURE 5.15:I(220)/I(111) vs. Total Gas Flow Rate	203
FIGURE 5.16:I(220)/I(111) vs. Deposition Pressure	205
FIGURE 5.17:RMS Roughness vs. H <sub>2</sub> Flow Rate	206

FIGURE 5.18:RMS Roughness vs. Deposition Time	207
FIGURE 5.19:RMS Roughness vs. Total Gas Flow Rate	208
FIGURE 5.20:RMS Roughness vs. Deposition Pressure	210
FIGURE 5.21:Raman Spectra	212
FIGURE 5.22:Raman Spectra	213
FIGURE 5.23:Raman spectra	214
FIGURE 5.24:Film Morphology vs. H <sub>2</sub> Flow Rate	216
FIGURE 5.25:Film Morphology vs. Deposition Time	221
FIGURE 5.26:Film Morphology vs. Total Gas Flow Rate	224
FIGURE 5.27:Film Morphology vs. Deposition Pressure	228
FIGURE 5.28:Film Morphology vs. Deposition Pressure	234
FIGURE 5.29:Bright Field TEM Image	239
FIGURE 5.30:Bright Field(a) & Dark Field(b) TEM Images	241
FIGURE 5.31:Dark Field TEM Image	242
FIGURE 5.32:Dark Field TEM Image by ANL [Huan 2000]	244
FIGURE 5.33:High Resolution TEM image by ANL [Huan 2000]	245
FIGURE 5.34:A Histogram of Figure 5.32 by ANL [Huan 2000]	246
FIGURE 5.35:Dark Field TEM Image	248
FIGURE 5.36:Bright Field TEM Image	250
FIGURE 5.37:I(220)/I(111) vs. Nitrogen Impurities	251
FIGURE 5.38:RMS Roughness vs. Nitrogen Impurities	252
FIGURE 5.39:Film Morphology vs. Nitrogen Impurities	254
FIGURE 6.1:Carbon Dimer d <sup>3</sup> Π -a <sup>3</sup> Π Swan Band Emission	269

FIGURE 6.2:Experimental Set-up for OES Measurements	274
FIGURE 6.3:C <sub>2</sub> Emission Intensity vs. H <sub>2</sub> Flow Rate	276
FIGURE 6.4:C <sub>2</sub> Emission Intensity vs. Total Gas Flow Rate	277
FIGURE 6.5:C <sub>2</sub> Emission Intensity vs. Pressure	280
FIGURE 6.6:C <sub>2</sub> Emission Intensity vs. Microwave Power	281
FIGURE 6.7:Growth Rate vs. C <sub>2</sub> Emission Intensity	283
FIGURE 6.8:Gas Temperature vs. H <sub>2</sub> Flow Rate	284
FIGURE 6.9:Growth Rate vs. Gas Temperature	285
FIGURE 6.10:Gas Temperature vs. Total Gas Flow Rate	286
FIGURE 6.11:Gas Temperature vs. Pressure	288
FIGURE 6.12:Gas Temperature vs. Microwave Power	289
FIGURE 6.13:Growth Rate vs. Gas Temperature	291
FIGURE 6.14:Growth Rate vs. Substrate Temperature	293
FIGURE 6.15:CN Emission Intensity vs. Nitrogen Impurities	294
FIGURE 7.1:A Sketch of Cross-Section View of UNCD Coated Si Substrates	302
FIGURE 7.2:Optical Transmission of Single Layer One Side	308
FIGURE 7.3:Optical Transmission of Single Layer One Side	310
FIGURE 7.4:Optical Transmission of Single Layer One Side	311
FIGURE 7.5:Optical Transmission of Single Layer One Side	313
FIGURE 7.6:Optical Transmission of Single Layer One Side	314
FIGURE 7.7:Optical Transmission of Single Layer	316
FIGURE 7.8:Optical Transmission of Single Layer Both Sides	317
FIGURE 7.9:Optical Transmission of Two Layers One Side	319

<b>FIGURE 7.10:Optical Transmission of Two Layers</b>	<b>321</b>
<b>FIGURE 7.11:Seal Coating Substrate Holder Setup</b>	<b>326</b>
<b>FIGURE 7.12:An Ultra-nanocrystalline Diamond Coated SiC Seal</b>	<b>328</b>
<b>FIGURE 7.13:Surface Profile Inspected by Interferometric Imaging [Huan 2001]</b>	<b>329</b>
<b>FIGURE 7.14:Surface Profile Inspected by Optical Microscopy</b>	<b>332</b>
<b>FIGURE 7.15:SEM Images of UNCD on a Si Substrate [Bi 2002]</b>	<b>337</b>

# 1 Introduction

Many attempts to control polycrystalline diamond's microstructure have been made but success has been limited to the control of crystal morphology through influencing the crystal's preferred orientation (film texture). Recently it was discovered that the microstructure of diamond can be manipulated so the crystal size decreases from microns to nanometers [Kond 1990]. One of the most common diamond thin film deposition processes is microwave plasma assisted chemical vapor deposition (MPACVD). In contrast to other diamond synthesis processes, i.e. hot filament CVD, plasma torch, combustion synthesis, etc., MPACVD has a number of advantages. MPACVD is excellent for investigating the fundamental science of the synthesis of nanocrystalline diamond films because (1) it is easy to operate, (2) it is a simple technology, (3) it can be operated in a wide range of pressure and power, (4) it produces high quality films with reproducibility, and (5) it is reliable and safe for long-time experiments.

The research described in this thesis is concerned with developing a microwave plasma assisted chemical vapor deposition process and methodology that enables ultra-nanocrystalline diamond films to be uniformly deposited over large areas. The MSU-invented and -developed reactors are the outcome of a long-term research effort [Zhan 1993], [Zhan 1994], [Kuo 1997], [Khat 1997] and are utilized in this dissertation. Building upon the experimental results of Gruen et al. [Grue 1998], microwave plasma assisted ultra-nanocrystalline diamond film deposition is investigated using hydrogen poor, carbon containing argon plasma chemistries. In order to better understand the argon-hydrogen-methane plasma discharges, the plasma species concentrations and the

gas temperature of the deposition conditions were studied by optical emission spectroscopy.

This exploratory investigation is concerned with depositing smooth, nanometer sized diamond films using a MSU-MPACVD reactor. Experimental operations was carried out between 60-240 Torr. This research has extended the reactor operation pressure from 20-150 Torr [Zhan 1994], [Kuo 1997] to the higher pressures of 240 Torr. The work of this thesis develops experimental methods that allow (1) the creation of large, uniform, mostly argon discharges over a 60-240 Torr pressure regime and (2) the synthesis of uniform, smooth ultra-nanocrystalline diamond films on 3" diameter substrates. When first reported during 1999-2000, these experiments were the first in the world to produce uniform ultra-nanocrystalline diamond over 3" diameter substrate areas. Some of the results have been presented at international conferences [Huan 1999], [Huan 2000] and two patent disclosures have been submitted to MSU. As part of this thesis [Asmu 2002], [Bi 2002], the use of ultra-nanocrystalline diamond for a few important applications was investigated. For example, applications such as IR optical transmission windows, tribological coatings (SiC chemical process pump seal), and SAW (surface acoustic wave) devices were briefly investigated. The successful fabrication and operation of ultra-nanocrystalline diamond films as SAW device substrates, in collaboration with the Physics Department at MSU, has been published [Bi 2002].

## 1.1 Motivation

Microwave plasma assisted chemical vapor deposition of diamond thin films has been extensively investigated by many research groups throughout the world. These experimental investigations have shown that diamond films can be synthesized from dissociated  $\text{CH}_4/\text{H}_2$  gas mixtures. As synthesized, these films typically consist of 1-100 micron-sized grains and hence they have a surface roughness that is of the same order as the grain size. The rough surface usually requires costly and time-consuming post processing such as polishing and thus this additional step and associated cost often prevents these films from being used in many applications. Thus, it is desirable to develop new methods to synthesize diamond films with very small grains and a smooth surface.

The nucleation and growth of ultra-nanocrystalline diamond films from a “hydrogen poor” argon-hydrogen-methane microwave discharges has been demonstrated by Gruen et. al [Zhou] on substrate areas of less than  $25 \text{ cm}^2$ . A practical importance is that ultra-nanocrystalline diamond grown from  $\text{Ar}/\text{H}_2/\text{CH}_4$  gases has advantages in many applications as compared to the more common  $\text{H}_2/\text{CH}_4$  grown polycrystalline diamond films. Ultra-nanocrystalline diamond films have smaller RMS (root mean square) roughness i.e., 20~40 nm vs. 1-100 micron for conventional CVD polycrystalline diamond, and a lower film wear coefficient, and counterface wear coefficient [Erde 1999], which reduces frictional energy losses over polycrystalline diamond films. Thus the ultra-nanocrystalline films may be the preferred diamond films for many applications where smooth diamond coatings are desired. One potential application is in wear coatings such as pump seal coat-





ings. The smaller crystal size has the benefit of smaller gaps, which result in smaller seal leakage. As a consequence, it reduces hazardous emissions.

## **1.2 Research Objectives**

The objectives of the research covered in this dissertation were to (1) develop microwave plasma assisted process methodologies that synthesize smooth ultra-nanocrystalline diamond films uniformly over large areas using MSU-MPACVD (Michigan State University-Microwave Plasma Assisted Chemical Vapor Deposition) reactors, (2) evaluate the performance of the MSU-MPACVD reactor for ultra-nanocrystalline diamond synthesis by investigating the reactor conditions and geometry over a wide range of experimental parameters, (3) characterize the ultra-nanocrystalline diamond film quality and properties versus various deposition conditions, (4) develop a better understanding of the plasma, species concentrations, and gas temperature during the deposition process by performing OES (Optical Emission Spectrum) measurements, and (5) explore the use of ultra-nanocrystalline diamond in a few important applications, i.e. IR optical transmission window, tribological coatings (SiC chemical process pump seal), and SAW (surface acoustic wave) device.

## **1.3 Dissertation Outline**

Chapter 2 presents background and reviews the related literature. Chapter 3 describes the experimental systems and the experimental procedures; identifies the important input, internal and output variables; reports the parameter space used in this research; and describes the measurement methodology for reactor performance and film character-

ization. Chapters 4 through 6 summarize the experimental results of this investigation. In particular, Chapter 4 experimentally determines the relationships of input, internal and output variables and relates the film deposition results with the reactor performance over the range of the experimental parameters, and reports the influence of adding  $N_2$  impurities on ultra-nanocrystalline diamond synthesis. Chapter 5 presents the deposited film quality and properties versus the experimental variables. Chapter 6 presents the OES investigation of the microwave plasma during film deposition process and particularly relates the  $C_2$  concentrations with the deposition conditions, and also determines gas temperature versus deposition conditions. In Chapter 7, the application to an IR optical transmission window, tribological coatings (SiC chemical process pump seal), and a SAW device are explored. Chapter 8 summarizes the conclusions of the research in this thesis and presents some speculations on future research/development of the ultra-nanocrystalline diamond film deposition using microwave technology.

: B

10

7

10

10

10

10

10

10

10

10

10

10

10

10

10

10

10

10

10

10

10

## 2 Background

### 2.1 General Introduction

Throughout the world, researchers have long been attracted to diamond's unique properties. They include extreme hardness, high thermal conductivity, a wide spectral optical transmission range, and chemical resistance. In addition, diamond has semiconductor characteristics such as high breakdown electrical fields, a large band gap, and high electron and hole mobility. Table 1.1 lists some of diamond's properties and some applications related to them [Angu 1989], [Grae 1992], [Grot 1994], [Kani 1993], [Liu 1995], [Mori 1993], [Orr 1988], [Pan 1993], [Pier 1993], [Qadr 1993], [Shio 1990], [Spit 1981], [Tamh 1992], and [Vavi 1992].

TABLE 2.1: SOME PROPERTIES OF NATURAL, CVD DIAMOND AND THE APPLICATIONS

Property	Type IIa	CVD	Comparison	Application
Hardness (Gpa)	57-104	50-100	2.1(Cu) 31.5(SiC)	Abrasive Coatings for cutting tools
Thermal Conductivity (W/cm/K) at 298K	20-23	10-21	3.99(Cu)	Heat sink for electronic & microwave power devices
Electrical Resistivity (ohm-cm)	$10^{16}$	$10^{12}$ - $10^{16}$		Heat sink for electrical device
Thermal Expansion Coeffi- cient ( $\times 10^{-6}/K$ ) between 298-473K	0.8-1.2	$\sim 2.0$	17(Cu) 5.5( $SiO_2$ )	Microelectronic circuit boards, Semiconductor sub- strates
Band Gap (eV)	5.45	$\sim 5.5$	1.124(Si) (GaAs)	Semiconductor & micro- wave power devices
Optical Transparency	UV( $\sim 230nm$ ) to microwave (mm)	Visible to mid-IR		Optical coating, electro-optical device

TABLE 2.1 (cont'd)

Property	Type IIa	CVD	Comparison	Application
Rel. Dielectric Constant at 45 MHz to 20 GHz	5.7	5.6	11.7(Si) (GaAs)	RF electronic device
Lattice Electron Mobility (V/cm <sup>2</sup> )	1900-2200	1350-1500	1350(Si)	High speed electronic device
Lattice Hole Mobility (V/cm <sup>2</sup> )	1600	10-1000	480(Si)	High speed electronic device
Breakdown Field (V/m)	10 <sup>7</sup>		3x10 <sup>5</sup> (Si) 3.5x10 <sup>5</sup> (GaAs)	Semiconductor device
Electron Saturation Velocity (cm/sec)	2.7x10 <sup>7</sup>	2.7x10 <sup>7</sup>	1x10 <sup>7</sup> (Si)	Semiconductor device

Ever since Tennant discovered that diamond is a crystalline form of carbon in 1797, researchers have attempted to synthesize it [Tenn 1797]. Since the early 1980's, applications and deposition processes for thin polycrystalline diamond films have been pursued. At Michigan State University (MSU), East Lansing, Michigan, past reactor research by Asmussen et al. [Zhan 1994] has led to some MSU-owned and -patented microwave plasma technologies. One outcome of this activity is the MSU-MPCVD (Microwave Plasma Chemical Vapor Deposition) reactor, which is used for diamond synthesis experiments. The experimental and theoretical knowledge developed in earlier investigations with this reactor has been applied to diamond film deposition. Extensive experimental studies using H<sub>2</sub>/CH<sub>4</sub> gas mixtures to deposit diamond films are available for this reactor configuration including uniformity of coating, optimization of growth rate, and control of morphology [Zhan 1993], [Kuo 1997], and [Khat 1997].

As potential applications of CVD diamond are continuously developed, it is expected that this emerging diamond technology will have an important impact on space, defense, science, engineering, and commercial technologies. For example, nowadays, tooling engineers and tool fabricators are incorporating CVD diamond products into their product lines. As a result, an end user can buy more reliable and more readily available thick-film diamond inserts for the consistent production of highly accurate parts. CVD diamond offers significantly longer tool life and increased machining productivity because of its pureness, hardness, and rigidity, which gives it a low coefficient of friction, great abrasion resistance, high thermal conductivity, and good chemical and thermal stability.

However, the conventional  $H_2/CH_4$  CVD polycrystalline diamond synthesis methodologies exhibit columnar growth. The grain size increases rapidly with the thickness of the film, and usually the larger the grains the rougher the surface of the films. The surface roughness requires additional post processing to smooth the films and thereby increases the cost of the films being used in many wear and cutting tool applications. Thus, it is desirable to develop new methods to synthesize small crystalline and smooth diamond films.

## **2.2 Diamond Synthesis**

This section briefly describes the atomic and crystalline structure of diamond, as well as the competing forms of carbon, such as graphite or amorphous phases, which might be produced during the synthesis process.

Two basic crystal structures, cubic symmetry and hexagonal symmetry, are found in diamond. The dominant crystal structure in both natural and synthetic diamond is cubic structure because of the slightly lower energy (0.1-0.2 eV/carbon atom) [Pier 1993]. The diamond cubic crystal structure (Fig.2.1) consists of two interpenetrating face-centered cubic (FCC) lattices, displaced from each other by one quarter of a body diagonal. Each carbon atom is tetrahedrally coordinated (using  $sp^3$  atomic orbitals), creating strong, directed sigma bonds with its four neighboring carbon atoms. The bond length and lattice constant are 1.54 and 3.56 angstroms, respectively.

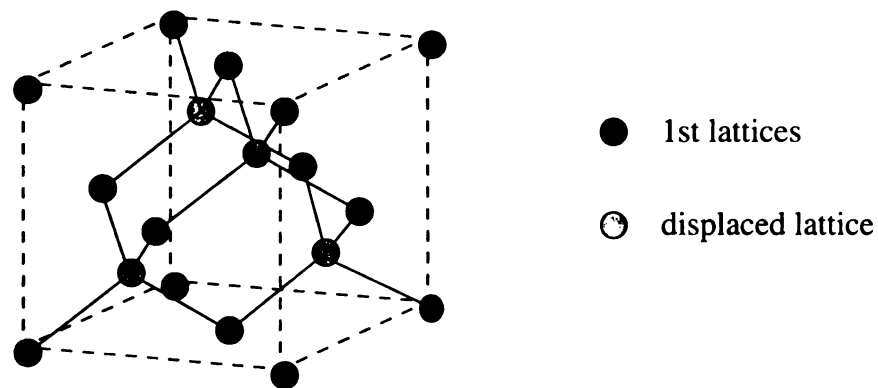


**FIGURE 2.1 : DIAMOND CUBIC CRYSTAL STRUCTURE**  
 Diamond symmetry covalent structure:  
 each carbon atom combines with four other tetrahedra

Graphite is the most common form of carbon. Each in-plane carbon atom combines with its three neighbors using hybrid  $sp^2$  atomic orbits, with a covalent  $\sigma$  bond length of 1.42 angstroms. The repeating layers are van der Waals bonded, perpendicular to the planes with a 3.35 angstrom lattice constant (Fig. 2.2).



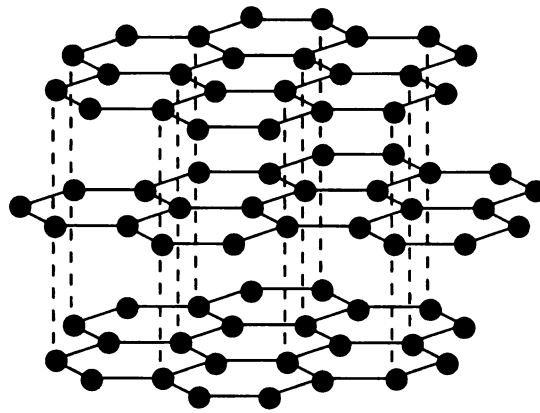


FIGURE 2.2 : GRAPHITE CRYSTAL STRUCTURE

Graphite stacking-sheet structure:  
in-layer carbon atoms form a two dimensional network of regular hexagons

Diamond is stable once formed, but the formation of diamond is less likely than graphite or other possible phases of carbon. During the formation, diamond is thermodynamically stable relative to graphite only at high pressure. Graphite to diamond conversion faces a considerable kinetic barrier, although the free energy difference between them is only 0.02 eV [Liu 1995]. In 1953, direct conversion from graphite to diamond, under high pressure (6Gpa) and high temperature ( $\sim 1300^{\circ}\text{C}$ ), using a liquid solvent catalyst, was developed by H. Liander in Sweden [Liu 1995]. In 1949, the first successful attempts to form CVD (chemical vapor deposition) diamond at low pressure were achieved by W.G. Eversole [Ever 1958], who discovered that diamond could be deposited on a substrate from a  $\text{CO}/\text{CO}_2$  mixture or a hydrocarbon gas. In 1968, more research was reported by Derjaguin et al. [Derj 1968] and Angus et al. [Angu 1968], but the low growth rate of this method (less than 0.1 micrometer per hour) was discouraging and prevented it from achieving industrial success. The breakthrough in synthesizing diamond at low pressure

came when Spitsyn et al. [Spit 1981] and Matsumoto et al. [Mats 1982] succeeded at producing diamond film growth at higher rates (up to 5 micrometers per hour) at high temperature from hydrocarbon-hydrogen gas mixtures.

P.K. Bachmann et. al. [Bach 1991] described the diamond growth region with the C-H-O gas phase diagram, shown in Figure 2.3. It is apparent that diamond can be grown from a wide range of gases mixed with hydrogen, including methane ( $\text{CH}_4$ ), ethane ( $\text{C}_2\text{H}_6$ ), ethylene ( $\text{C}_2\text{H}_4$ ), acetylene ( $\text{C}_2\text{H}_2$ ), and carbon dioxide ( $\text{CO}_2$ ). The diagram is independent of deposition technique but not independent of temperature. Bachmann concluded that diamond synthesis depends on the overall content of C, O, and H in the input gases and the specific carbon containing input gases are not important. He also described “above temperature of 1300 °C, only graphitic carbon can be deposited and below temperature of 400 °C, amorphous carbon tends to grow”.

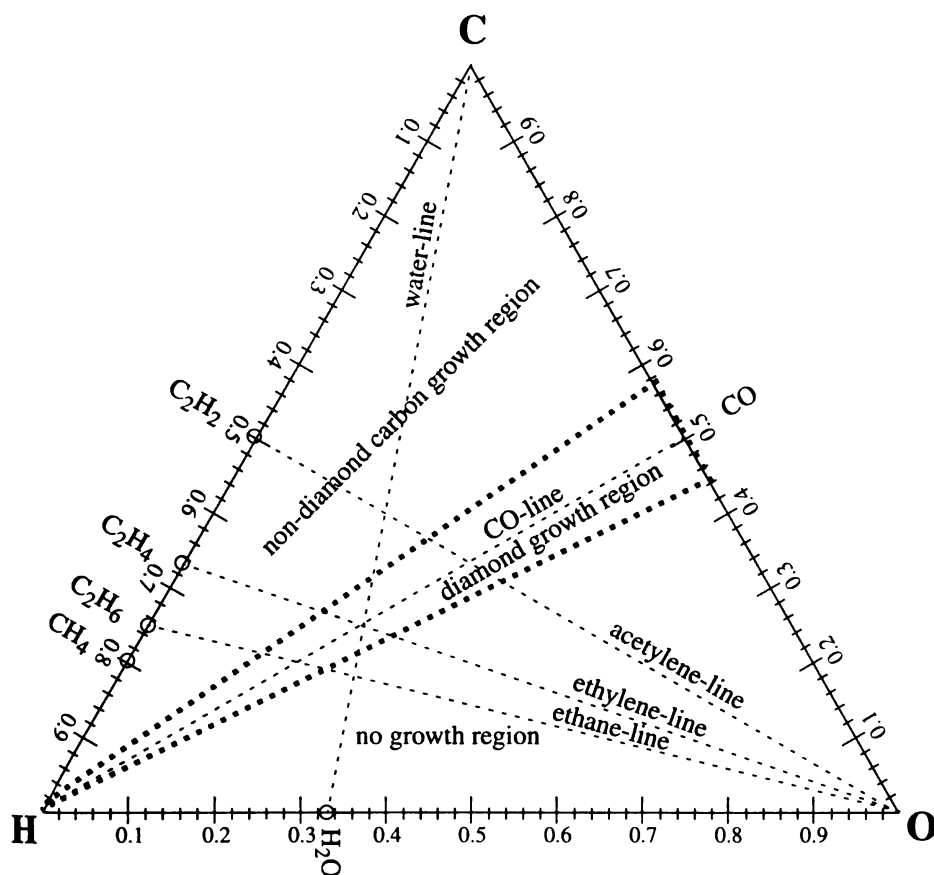


FIGURE 2.3 : PHASE DIAGRAM BY BACHMANN ET AL. [BACH 1991]  
 Identification of the possible gas combinations in reported successful  
 polycrystalline-diamond-growth experiments. [Bach 1991]

## **2.2.1 Polycrystalline Diamond Synthesis**

### **2.2.1.1 Methyl Radical and Acetylene Growth Processes**

The current knowledge of diamond growth is described in this section. In 1995, Huimin Liu and David S. Dandy divided the typical growth process associated with the CVD assisted deposition of polycrystalline diamond films into several steps [Liu 1995]: (i) incubation period, (ii) three dimensional nucleation of an individual crystal on a substrate surface, (iii) termination of surface nucleation and three dimensional growth of an individual crystal, (iv) coalescence of an individual crystal and the formation of a continuous film, and (v) the growth of a continuous film.

Experimental observations found that diamond did not nucleate directly on a non-diamond substrate surface. The nucleation takes places on an intermediate layer which is formed between diamond and the non-diamond substrate during the incubation period. This layer is formed by chemical interactions of activated gas species with the substrate surface. Such an intermediate layer provides nucleation sites for diamond crystalline growth.

The surface nucleation process may include the following events [Liu 1995]:

- a) Atoms from the gas species impinge upon the deposition substrate and are adsorbed onto the substrate surface.
- b) The adsorbed atoms may desorb and diffuse over the substrate surface and may bond to other surface atoms.
- c) As time progresses, the concentrations of adsorbed atoms increase and clusters are formed.
- d) These clusters grow or decay according to statistical fluctuation of the adsorbed atom concentrations.
- e) There exists a critical cluster size above which the cluster is more likely to survive and grow than to decay.

Those clusters whose size exceeds the critical size during the concentration fluctuation are called the stable clusters, which provide suitable sites for growth either from the direct impingement of atoms from the gas species or from the continued migration of the adsorbed atoms.

Nuclei are formed and crystals grow independently of each other during the nucleation step. Nucleation will stop when crystals have occupied all the available nucleation sites. Three dimensional growth of individual crystals continues until crystals coalesce and then a continuous film forms.

The chemical mechanism of CVD diamond growth is not completely understood. But it is well established that  $H_2$  and hydrocarbon gases such as  $CH_4$ ,  $CH_3$ ,  $C_2H_2$ , etc. play an important role in the quite complex CVD growth environment. C.C. Battail, D.J. Srolovitz, and J.E. Butler proposed a possible growth theory by studying the morphologies of diamond films from three dimensional atomic-scale simulations of chemical vapor dep-

osition in atmosphere containing H, H<sub>2</sub>, CH<sub>3</sub> and various partial pressures of C<sub>2</sub>H<sub>2</sub> [Batt 1997]. The diamond growth species are believed to be C<sub>2</sub>H<sub>2</sub> and CH<sub>3</sub>. Some important facts about the diamond growth on diamond surfaces are summarized in (a) through (g) below:

- a) Diamond grows by the chemisorption of hydrocarbons on the substrate surface. The chemical environment (which affects the rate at which chemisorption occurs at each surface site) and the surface crystal structure (which determines how chemisorbed hydrocarbon must be coordinated to form diamond) play interdependent roles in governing growth behavior.
- b) Among {111}, {110}, and {100} faces, the growth of the {111} face is the most sensitive to C<sub>2</sub>H<sub>2</sub> partial pressure and the {100} face is the least sensitive.
- c) A single C<sub>2</sub>H<sub>2</sub> molecule contributes two neighboring C atoms (CH<sub>3</sub> contributes only one) when it chemisorbs. Therefore, the presence of C<sub>2</sub>H<sub>2</sub> effectively reduces the requisite number of chemisorbed hydrocarbons for the deposition into neighboring sites to nucleate diamond on a flat surface.
- d) At low C<sub>2</sub>H<sub>2</sub> partial pressures, {110} films grow slowly, and {111} films grow very slowly, because the nucleation of a monolayer on flat {110} and {111} faces requires the bonding of two and three neighboring chemisorbed C atoms, respectively.
- e) Once a monolayer has been initiated, for the {111} surface subsequent growth of the monolayer requires bonding of at most two (at some sites only one) neighboring chemisorbed C atoms, and for the {110} requires only one C atom. So, the growth of the {111} and {110} layers is faster than their initial nucleation.
- f) Low C<sub>2</sub>H<sub>2</sub> concentration yields low growth rates on both {111} and {110} faces, because at low C<sub>2</sub>H<sub>2</sub> partial pressures, the growth of {111} and {110} facets is controlled by the limited nucleation of monolayers on atomically smooth facets. Thus, growth in C<sub>2</sub>H<sub>2</sub>-poor environments occurs primarily from CH<sub>3</sub>.
- g) CH<sub>3</sub> might be responsible for the major growth events, while C<sub>2</sub>H<sub>2</sub> controls the growth rate by controlling the nucleation of growth layers.

Gas mixtures of high hydrogen concentrations are commonly used to provide an in-situ graphite etching. At less than or equal to one atmosphere, in which CVD systems operate, graphite codeposition results from the higher probability of graphite formation than diamond or other possible phases of carbon. In the CVD process, hydrogen atoms play a crucial deposition role [May 1995]. For example:

- a) H-atoms remove the 'dangling' carbon bonds on the growing diamond surface and stop them from cross-linking and constructing graphite-like surfaces.
- b) Atomic hydrogen etches both diamond and graphite, but unlike other forms of carbon, diamond's growth rate exceeds its etching rate. This is believed to be the reason that diamond growth predominates over growth of other forms of carbon under this condition.
- c) H abstraction reactions with stable hydrocarbon molecules produce highly reactive carbon-containing radical species, such as methyl ( $\text{CH}_3$ ), which diffuses to the substrate surface and reacts with it, thereby forming the C-C bonds necessary to propagate the diamond lattice.

Atomic H helps stabilize the diamond phase by preferentially etching  $\text{sp}^2$ -bonded carbon and passivating radical sites on the growing surface [Butl 1993], [Good 1996].

#### **2.2.1.2 Polycrystalline Diamond Competitive Growth Model**

Diamond films produced by regular  $\text{H}_2/\text{CH}_4$  CVD methodologies results in 1-100 micro-sized polycrystals. In CVD-polycrystalline-diamond films, the texture is usually perpendicular to the substrate. The Van der Drift [Van] competitive growth model has two assumptions: (1) the absence of secondary nucleation, and (2) crystalline morphology is independent of crystalline orientation. Polycrystalline diamond films grown from randomly oriented nuclei exhibit columnar growth, which is evidence of "evolutionary selection" by this model. Competitive growth between differently oriented grains deter-

mines the subsequent film growth. With increasing film thickness, only those crystals with the fastest vertical growth rate will survive and determine the final texture and surface morphology of the film.

The surface morphology is often very important in industrial applications. A typical SEM plan-view image of a  $\text{H}_2/\text{CH}_4$  CVD diamond film, shown in Figure 2.4, displays the often rough surface of polycrystalline diamond film.

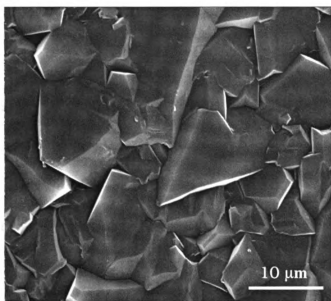


FIGURE 2.4 : POLYCRYSTALLINE DIAMOND FILM

The evolutionary selection of the crystal growth and the determination of the surface morphology by the survived crystals with the fastest vertical growth rate.

Deposition condition: Pressure=120 Torr,  $\text{H}_2:\text{CH}_4=90:10$ ,  $f_t=223$  sccm and deposition time =8 hours by system I.



## 2.2.2 Ultra-nanocrystalline Diamond Synthesis

### 2.2.2.1 Carbon Dimer Growth Processes For The Synthesis of Ultra-nanocrystalline Diamond Films

Ultra-nanocrystalline diamond films have crystal sizes on the order of nanometers. These crystal sizes are usually much smaller than polycrystalline diamond films synthesized by  $\text{H}_2$ - $\text{CH}_4$  chemistries, such as shown in Figure 2.4. Nanocrystalline diamond is often grown in a lower hydrogen concentration environment. Noble gases, such as Ar, are sometimes used in place of  $\text{H}_2$ . When a noble gas such as Ar is added to a  $\text{H}_2/\text{CH}_4$  discharge, the plasma chemistry changes. That is, ionization, dissociation, and species concentrations are greatly modified and thereby changes the emission intensity of various species of plasma. As  $\text{H}_2$  input is reduced and replaced by Ar,  $\text{C}_2$  emission is greatly increased. This increase in  $\text{C}_2$  emission is interpreted as being due to the increased  $\text{C}_2$  ground state population in the plasma since excitation and quenching (competing de-excitation mechanism) rates can be expected to change only marginally under these conditions [Grue 1995]. This rise in  $\text{C}_2$  population is correlated with the observed increase in growth rate, and thus supports that  $\text{C}_2$  is a growth species for UNCD synthesis. Thus, dicarbon ( $\text{C}_2$ ) is believed to be the key growth species [Grue 1995] for ultra-nanocrystalline diamond growth instead of methyl ( $\text{CH}_3$ ) and acetylene ( $\text{C}_2\text{H}_2$ ), which are believed to be the important species in traditional  $\text{CH}_4/\text{H}_2$  polycrystalline diamond growth.

A two-step  $\text{C}_2$  addition mechanism for growth from a  $\text{CH}_4$  precursor in Ar plasmas for a (110)-(1x1):H unreconstructed surface was proposed by Gruen et al. [McCa 1998],

as shown in Figure 2.5. The ultra-nanocrystalline diamond growth process is summarized as follows:

- a) One  $C_2$  adds to the unreconstructed monohydride surface by inserting itself into first one C-H surface bond without abstraction of the terminating hydrogen bond (step1) (at the Hartree-Fock level of theory,  $C_2$  can insert into a C-H bond of methane with no activation barrier, forming a stable  $H_3C-CH=C$  molecule).
- b) The  $C_2$  molecule then rotates about the newly formed bond to insert its other carbon into the C-H bond across from it, thus forming a (100)-oriented surface dimer row (step 2), producing an adsorbed ethylene-like structure (III).
- c) A subsequent  $C_2$  molecule then inserts itself into the adjacent surface C-H bond, parallel to the newly inserted surface  $C_2$  dimer (III) to produce a surface with two adjacent ethylene-like groups (V), (steps 3 and 4).
- d) The original state of the (110) surface is finally recovered by the formation of a C-C single bond between adjacent ethylene-like groups and produces a new layer on the diamond surface via step 5 (formation of a singlet diradical, structure VI, directly from structure V) This direct insertion growth mechanism for  $C_2$  is unique in that it is not dependent on the abstraction of hydrogen atoms from the surface. Specially, the path for the formation of a C-C single bond between adsorbed, two-carbon moieties via step 5 does not involve any gas-phase atomic hydrogen.

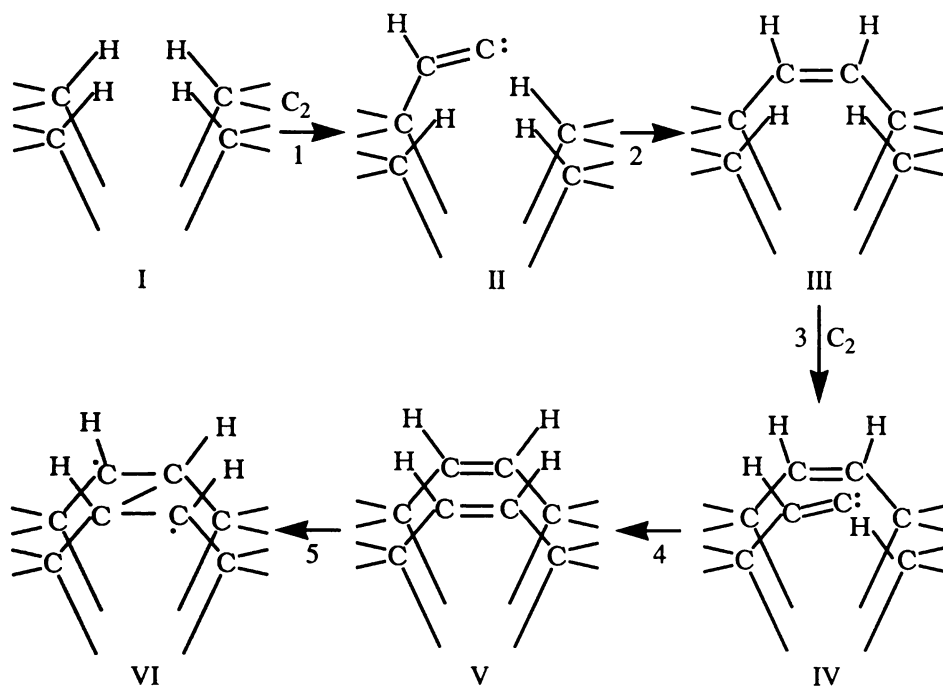


**FIGURE 2.5 : DIAMOND (110) SURFACE GROWTH MECHANISM  
WITH  $C_2$  AS A GROWTH SPECIES**

A schematic representation of the proposed mechanism for direct two-step  $C_2$  addition to the (110)-(1x1):H diamond surface [McCa 1998].

In 1999, D.M. Gruen reported: (1) the reaction of a singlet  $C_2$  with the C=C double bond of the  $C_9H_{12}$  cluster gives carbene structures, which lead to the formation of new diamond critical nuclei during growth. (2) On the other hand, the reaction of singlet  $C_2$  with the HC-CH single bond or C-H bonds of the  $C_9H_{14}$  cluster results in a cyclobutene-like geometry, which leads to growth on the (100) surface in a series of steps. (3) The nucleation rates increase dramatically under conditions where small fractions of the reconstructed (100) surface are unhydrided and  $C_2$  concentrations in the plasma reach



levels of  $10^{12} \text{ cm}^{-3}$ , and (4) low hydrogen content plasma favor these conditions [Grue 1999].

#### **2.2.2.2 Ultra-nanocrystalline Diamond Re-nucleation Growth Model**

In contrast to CVD polycrystalline diamond films (grown by the traditional method involving  $\text{CH}_4/\text{H}_2$  mixtures), which frequently have a crystal-facet morphology with rough surfaces (Van der Drift's "survival of the largest"), ultra-nanocrystalline diamond films (grown from carbon containing Ar plasma) have a "featureless" morphology with RMS surface roughness on the order of a few to 10's of nanometers. Unlike polycrystalline diamond films, ultra-nanocrystalline films are grown by continuous re-nucleation. An ultra-nanocrystalline growth model explains the structural evolution of the film based on a substrate seeded with diamond nuclei that grow isotropically. Very high heterogeneous renucleation rates ( $10^{10} \text{ cm}^{-2} \text{ sec}^{-1}$ ) ensure that growth occurs and results in the formation of smooth, phase-pure ultra-nanocrystalline diamond films. This high secondary nucleation rate make the transition from microcrystalline to nanocrystalline diamond films. A typical SEM plan-view image, shown in Figure 2.6, illustrates the surface morphology of a UNCD film.

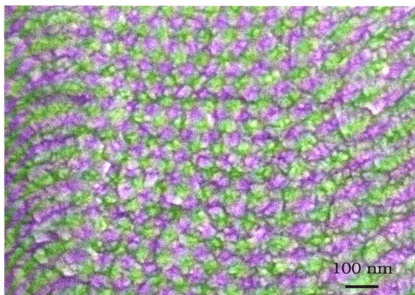


**FIGURE 2.6 : ULTRA-NANOCRYSTALLINE DIAMOND FILM**

The renucleation growth and the determination of the surface morphology by the small crystallinity.

Deposition condition: Pressure=120 Torr, Ar:H<sub>2</sub>:CH<sub>4</sub>=100:4:1,  $f_t$ =105 sccm, and deposition time=8 hours by system II.

## **2.3 Nanocrystalline Diamond Film Deposition Techniques and Conditions**

This section describes the past experimental work associated with nanocrystalline diamond film synthesis. In general, most investigations do not use hydrogen poor, carbon containing argon discharges and most of the synthesized films have crystal sizes greater than 50 nm. Thus this thesis will refer to those films as nanocrystalline films. On the other hand, when a high concentration of Ar discharge is combined with a 0.5-2% CH<sub>4</sub> and zero to a few percentage of H<sub>2</sub>, the resulting crystal sizes are usually smaller than 50 nm and often are as small as 10 or less nm. Due to the different input gas mixtures, plasma chem-

istries, and the very small resulting crystal sizes, this thesis will refer to the deposited films as ultra-nanocrystalline diamond (UNCD) films.

Ever since nanocrystalline diamond was recognized as an important structural class in the diamond family, a number of different deposition techniques and conditions have been employed to synthesize nanocrystalline diamond films. Among these are hot filament CVD [Lin 2000], [Wang 2004], TMHFCVD (time modulated hot filament chemical vapor deposition) [Ali 2003], RF plasma CVD reactor [Nied 2001], biased hot flame [Holl 1998], remote tubular microwave CVD [Erz 1993], DC arc plasma [Kono 1995], [Nist 1997], dual ECR (electron cyclotron resonance)-rf plasma [Zarr 1997], condensing carbon ions [Dava 1996], and microwave plasma CVD reactors [Zuik 1995], [Yosh 2001], [Hong 2002], [Xu 2001], [Bhus 1998], [Grue 1998], [Chen 2000], [Shar 2001], [Shar 2003], [Yang 2002], [Li 2002]. A summary of the deposition techniques, conditions, and results of the synthesis of nanocrystalline diamond films is listed in Table 2.2. Some of these investigations are briefly described below.

Lin et al. [Lin 2000] studied the influence of argon concentration in the transition of the morphology of diamond crystal from microcrystalline to nanocrystalline using an argon-methane-hydrogen mixture in a conventional hot filament chemical vapor deposition system. A transitional boundary between polycrystalline and nanocrystalline occurred when 95.5% argon concentration was used.

The nanocrystalline diamond films were deposited on 2" Si (100) wafers by decreasing the deposition pressure and increasing the acetone in hydrogen ratio with a hot

filament technique [Wang 2003]. Averages grain sizes of approximately 4-8 nm were achieved. However, HRTEM (high resolution transmission electron microscopy) images of the nanocrystalline diamond films show grains are surrounded with amorphous graphite.

Ali et al. fabricated the nanocrystalline diamond films on cemented tungsten carbide (WC-Co) substrates using a new growth technique, identified as TMHFCVD (time modulated hot filament chemical vapor deposition) [Ali 2003]. The modulated methane flow promoted the secondary nucleation of nanometer crystalline diamond.

With a RFPACVD (radio frequency plasma assisted CVD) reactor, an appropriate thickness of nanocrystalline diamond layer as an anti-abrasive coating on cemented carbide substrates without post mechanical polishing can improve the friction coefficient in sliding against wood [Nied 2001]. The results of this study are helpful in the selection of the optimum thickness of the nanocrystalline diamond films to be coated on the cemented carbide tools to improve cutting of the mills used in the wood industry.

Nanocrystalline diamond coated spherical cemented carbide substrates have been tested in air, lubricant (water and oil) sliding against ball-bearing steel, cemented carbide, stainless steel, titanium, and aluminum [Holl 1998]. The smooth nanocrystalline diamond coatings show exceptionally low friction and wear when slid against ball-bearing steel, cemented carbide, stainless steel in air and lubricant (water or oil). But when sliding against titanium and aluminum, the nanocrystalline diamond coatings need to be polished slightly to have the similar behavior.



Erz et al. fabricated nanocrystalline diamond optical transparent films on silicon and quartz substrates using a methane-oxygen-hydrogen mixture by a remote tubular microwave CVD [Erz 1993]. In this investigation, they used different diamond powder with grain sizes ranging from 0.01-3  $\mu\text{m}$  to enhance diamond nucleation on the substrates. The results showed that a nucleation density up to  $3 \times 10^{10}$  nuclei  $\text{cm}^{-2}$  was achieved by scratching the substrates with 10 nm diamond powder. The high nucleation density led to a flat diamond film with a smooth surface. However, by increasing the film thickness from 1  $\mu\text{m}$  to 10  $\mu\text{m}$ , the surface roughness increases more than 6 times ( $30 \pm 10$  nm to 200 nm).

Konov et al. [Kono 1995] and Nistor et al. [Nist 1996] grew fine-grain diamond films on silicon substrates using a methane-hydrogen argon gas mixture with fixed argon flow (50 sccm) and varied the methane flow from 5-50 sccm and the hydrogen flow from 45-0 sccm in a D.C. arc discharge plasma. After the ultrasonic seeding process (ultrasonic seeding with 5 nm sized diamond powder suspension in ethanol), pulsed excimer laser irradiation generated by an excimer KrF laser (pulse duration 15 nanosecond) was used to remove the undesirable non-uniformities in the surface distribution of the seeded crystals, while leaving the uncoalesced particles for subsequent growth undisturbed. The two-step seeding procedure led to highly smooth films owing to the irradiation on the pretreated substrates by laser assisted disintegration of the coalesced seeds and removal of large residue diamond particles [Kono 1995]. The improvement of the growth of nanocrystalline diamond films was obtained by the combination of the uniformly seeded substrates and a high methane concentration (50% of argon-methane-hydrogen mixture) [Nist 1996].

HRTEM and EELS (electron energy loss spectroscopy) characterization results of the films synthesized with a dual ECR-rf plasma by Zarrabian et al. showed the 4-30 nm diamond crystallinities were embedded in, amorphous matrix, DLC (diamond like carbon) [Zarr 1997]. Hexagonal diamond crystals that were changed to cubic diamond crystals were observed when the bias voltage was increased.

Nanophase diamond films were deposited on stainless steel substrates using condensing carbon ions carrying kinetic energy of the order of kiloelectronvolts, generated from the laser ablation of graphite at target intensity near  $10^{11} \text{ W cm}^{-2}$  by Davanloo et al. [Dava 1996]. Deep penetration of carbon atoms into the steel substrates was shown within the interfacial layers examined by TEM images. The measured mechanical properties (low friction coefficient [Coll 1994] and a hardness, in excess of 78 GPa [Coll 1993], [Coll 1994]) confirmed that the nanophase diamond films were suited to a wide range of industrial applications.

Zuiker et al. [Zuik 1995] and Gruen et al. [Grue 1998] grew nanocrystalline and ultra-nanocrystalline diamond films with an argon-carbon ( $\text{C}_{60}$  in argon) microwave plasma and controlled the diamond crystal microstructure by argon additions to methane-hydrogen microwave plasma discharges in a microwave plasma CVD reactor (ASTeX PDS-17). It was found that nanometer sized diamond could be synthesized with either a  $\text{C}_{60}$  or a  $\text{CH}_4$  carbon precursor [Zuik 1995]. Cross-section and plan-view SEM images showed that the morphology, grain size, and growth mechanism are affected by the ratio of argon to hydrogen in the gas mixture. The transition from microcrystalline to nanocrystalline, which depended on the ratio of argon to hydrogen, was confirmed by X-ray

diffraction and Raman spectroscopy. The nanocrystalline diamond was synthesized at an Ar/H<sub>2</sub> volume ratio of 9 and CH<sub>4</sub> volume percentage of 1%. The ultra-nanocrystalline diamond was synthesized at 0-2% of H<sub>2</sub> and 1% of CH<sub>4</sub> (vol%). An OES (Optical Emission Spectroscopy) study reveal that the C<sub>2</sub> dimer concentration is promoted significantly by increasing the argon concentration [Grue 1998].

A nanocrystalline diamond film was synthesized on a 4" Si(100) wafer with hydrogen flow rate of 100 sccm and methane flow rate of 10 sccm using a microwave plasma CVD system. The silicon substrate was scratched twice by dry diamond powders with the sizes of 250 nm and 5 nm respectively [Yosh 2001]. The high nucleation density, approximately  $1 \times 10^{11} \text{ cm}^{-2}$ , led to a smooth (RMS=8.4 nm by atomic force microscopy) and fine-grain (about 10 nm observed by field emission scanning electron microscopy) diamond film with 3.5  $\mu\text{m}$  in thickness. The FTIR (fourier transform infrared spectrometer) spectra showed C-H bands: sp<sup>3</sup>-CH<sub>2</sub> symmetric stretch at 2850 cm<sup>-1</sup> and sp<sup>3</sup>-CH<sub>2</sub> asymmetric stretch at 2925 cm<sup>-1</sup>, in the film. Hong et al. used the same technique and similar conditions to deposit nanocrystalline diamond films also on a 4" Si(100) wafer, but modified the two-step scratch seeding procedure with dry diamond powders of the sizes of 1  $\mu\text{m}$  and 5 nm for tribological characteristics study [Hong 2002]. A slightly thinner film (2.2  $\mu\text{m}$  thick) with approximately same size crystals (10-15 nm) showed a very close surface roughness value (10 nm).

Bhusari et al. [Bhus 1998] and Chen et al. [Chen 2001] deposited diamond films with grain sizes ranging from 4 nm to a few hundreds of nanometers in methane, hydrogen, and oxygen gas mixture by an AsTex 5 kW microwave reactor. The growth results of

the quartz substrates pretreated, with two different diamond-powder sizes, 4 nm and 0.1  $\mu\text{m}$ , were compared. The ultrasmooth and highly transparent nanocrystalline diamond films were coated on the quartz substrates (1) scratched by 4 nm sized diamond powder and with low ( $\leq 20\%$ ) methane concentration, and (2) scratched by 0.1  $\mu\text{m}$  sized diamond powder and with high ( $\geq 20\%$ ) methane concentration. According to the in situ OES (optical emission spectroscopy) study, the  $\text{C}_2$  dimer continued to increase as methane concentration increased, while other hydrocarbon ( $\text{CH}^+$ ,  $\text{C}_3$ ,  $\text{CH}$ ) species that decreased significantly as methane concentration increased. Thus, it was speculated that  $\text{C}_2$  may be the predominant growth species at higher methane fractions [Chen 2001].

Sharda et al. compared the optical properties of microcrystalline and nanocrystalline diamond films fabricated on silicon substrates by microwave plasma chemical vapor deposition with a mixture of 5% methane in hydrogen. The substrate was pretreated with bias enhanced nucleation. The nanocrystalline diamond film grown at 700  $^{\circ}\text{C}$  had a very high optical absorption coefficient, i.e.  $>10^4 \text{ cm}^{-1}$  (higher than that of the microcrystalline diamond film), even though it was smoother than microcrystalline diamond film. Nevertheless, the nanocrystalline diamond film grown at 600  $^{\circ}\text{C}$ , was smoother, had 78% transmittance in the infrared region, and thus had demonstrated a potential for application as optical windows [Shar 2001]. A homogeneous refractive index within the nanocrystalline diamond films and negligible changes at the interface between the film and the substrate were observed [Shar 2003].

Transparent nanocrystalline diamond protective coatings on quartz glasses were grown with a MPECVD technique in methane-hydrogen-oxygen plasma discharges [Yang

2002]. The substrates were ultrasonically polished with 0.5  $\mu\text{m}$  diamond powder prior to deposition. The nucleation density was generally higher than  $10^{11} \text{ cm}^{-2}$  as revealed by TEM examination. By 3% of methane fraction, with coatings of 1  $\mu\text{m}$  in thickness, and about 12 nm surface roughness, an optimal transmittance of 65% in the visible light region was achieved.

Nanocrystalline diamond thin films deposited on both sides of silicon wafers with a flow rate ratio of methane to hydrogen fixed at 1:100 in a MPECVD reactor had shown that the diamond coatings greatly enhanced the infrared transmission of silicon wafers [Li 2002]. A maximum transmittance of 85% at the wavenumber of  $2200 \text{ cm}^{-1}$  (at 4.55  $\mu\text{m}$ ) was achieved with 0.5  $\mu\text{m}$  and 0.3  $\mu\text{m}$  film thickness on each side of the silicon wafer and approximately 27 nm surface roughness.

**TABLE 2.2: NANOCRYSTALLINE DIAMOND FILM DEPOSITION METHODOLOGY AND FILM CHARACTERISTICS**

Reactor	Substrate	Pretreatment (diamond powder)	Gas Chemistry	Flow Rate (sccm)	P (Torr)	Power (W)	T <sub>s</sub> (°C)	t <sub>Film</sub> (μm)	Crystal Size (nm)	S.R. (nm)
HFCVD [Lin 2000]	Si(100)	ultrasonic scratching	Ar:H <sub>2</sub> :CH <sub>4</sub> =430:19:1.3	450.3	60	filament bias is not avail- able	870	2.6	< 50	NA
HFCVD [Wang 2003]	2" Si(100)	0.5 μm diamond paste scratched	CH <sub>3</sub> COCH <sub>3</sub> :H <sub>2</sub> =(3-4):100	NA	5-10	filament temp. 1900-2300 °C	850-9 50	11.5	4-8 *NCD	30-50
TMHFCVD [Ali 2003]	WC-Co	ultrasonic polishing	CH <sub>4</sub> :H <sub>2</sub> =(2-4):(96-98)	NA	30	filament power 300W	NA	>1	≤ 100	100
RFPACVD [Nied 2001]	CC	NA	CH <sub>4</sub>	50-100	0.375	input power 3000	900	NA	NA	1215 to 1575
Biased Hot Flame [Holl 1998]	CC	1 μm polished	O <sub>2</sub> :C <sub>2</sub> H <sub>2</sub> =930:1030	1960	760	flame power is not available	850 ± 30	NA	NA	30
RTMCVD [Erz 1993]	quartz	0.01-3 μm diluted in aque- ous media scratched	CH <sub>4</sub> :H <sub>2</sub> :O <sub>2</sub> =2:97:1	100	37.5	550	800	1	20	30 ± 10
DC arc discharges [Kono 1995]	Si	5 nm suspension in alcohol	Ar:H <sub>2</sub> :CH <sub>4</sub> =50:(45-0): (5-50)	NA	100	NA	600-8 00	0.1-2	30-50	< 30



Table 2.2 Continue

Reactor	Substrate	Pretreatment (diamond powder)	Gas Chemistry	Flow Rate (sccm)	P (Torr)	Power (W)	T <sub>s</sub> (°C)	t <sub>Film</sub> (μm)	Crystal Size (nm)	S.R. (nm)
DC arc discharges [Nist 1996]	Si	5 nm suspension in ethanol	Ar:H <sub>2</sub> :CH <sub>4</sub> =50:(45-0): (5-50)	100	100	NA	700	1-1.5	10-50	>13 < 30
Condensing Carbon Ions [Dava 1996]	Stainless Steel	(a or b or c or d or e) and f	condensing car- bon ions	NA	NA	NA	≤ 35	1-3	10-50	NA
MPAVD [Yosh 2001]	4" Si(100)	250 nm & 5 nm scratched	CH <sub>4</sub> :H <sub>2</sub> =10:100	110	34	NA	670-7 50	3.5	10	8.4
MWPCVD [Hong 2002]	Si	1 μm & 5 nm scratched	CH <sub>4</sub> :H <sub>2</sub> =10:100	NA	24	1800-2200	640-6 80	2.2	10-15	10
MPAVD [Zuik 1995]	Si	0.1 μm polished	Ar:H <sub>2</sub> =100:2 C <sub>60</sub> : 600 °C	102	100	1500	850	1.7	10-300 ave. =14.9	30
MPAVD [Zuik 1995]	Si	0.1 μm polished	Ar:H <sub>2</sub> =90:10 C <sub>60</sub> : 630 °C	100	100	1500	850	2	10-300 ave. =14.9	105
MPAVD [Zuik 1995]	Si	0.1 μm polished	Ar:H <sub>2</sub> =98:2 C <sub>60</sub> : 630 °C	100	100	1500	850	2	10-300 ave. =14.9	41





Table 2.2 Continue

Reactor	Substrate	Pretreatment (diamond powder)	Gas Chemistry	Flow Rate (sccm)	P (Torr)	Power (W)	T <sub>s</sub> (°C)	t <sub>Film</sub> (μm)	Crystal Size (nm)	S.R. (nm)
MPAVD [Zuik 1995]	Si	0.1 μm polished	Ar:H <sub>2</sub> :CH <sub>4</sub> =90:10:0.8 C <sub>60</sub> : 20 °C	100.8	100	1500	850	2	NA	125
MPAVD [Zuik 1995]	Si	0.1 μm polished	Ar:H <sub>2</sub> :CH <sub>4</sub> =98:1.5:0.8 C <sub>60</sub> : 20 °C	100.3	100	1500	850	2.3	NA	53
MPAVD [Zuik 1995]	Si	0.1 μm polished	Ar:H <sub>2</sub> :CH <sub>4</sub> =100:2:1 C <sub>60</sub> : 20 °C	103	100	800	850	10	NA	45
MPAVD [Grue 1998]	Si(100)	0.1 μm polished	Ar:H <sub>2</sub> :CH <sub>4</sub> =90:9:1	100	100	1200	800	5	30-50	54.19
MPAVD [Grue 1998]	Si	0.1 μm polished	Ar:H <sub>2</sub> :CH <sub>4</sub> =97:2:1	100	100	1200	800	5	10-30	18.84
MPAVD [Grue 1998]	Si	0.1 μm polished	Ar:H <sub>2</sub> :CH <sub>4</sub> =99:0:1	100	100	1200	800	5	3-20	NA
MPECVD [Xu 2001]	Si	0.5 μm diamond paste scratched	C <sub>2</sub> H <sub>2</sub> :H <sub>2</sub> =16:84	NA	60	2000	750	0.8	70-400	28
MPCVD [Bhus 1998] [Chen 2000]	quartz	4 nm ultrasonic polishing	CH <sub>4</sub> :H <sub>2</sub> :O <sub>2</sub> =(4-20): (95.9-79.9):0.1	200	22	1000	590-600	0.5-0.6	4-a few 100	6- 200

Table 2.2 Continue

Reactor	Substrate	Pretreatment (diamond powder)	Gas Chemistry	Flow Rate (sccm)	P (Torr)	Power (W)	T <sub>s</sub> (°C)	t <sub>film</sub> (μm)	Crystal Size (nm)	S.R. (nm)
MPCVD [Bhus 1998] [Chen 2000]	quartz	0.1 μm ultrasonic polishing	CH <sub>4</sub> :H <sub>2</sub> :O <sub>2</sub> =(20-42): (79.9-57.9):0.1	200	22	1000	590-600	0.5-0.6	4-a few 100	6- 200
MPCVD [Shar 2001] [Shar 2003]	Si(100)	Biased Enhanced. -260 V	CH <sub>4</sub> :H <sub>2</sub> =5:100	NA	30	1000	600	1.1	a few- a few 10	17
MPCVD [Shar 2001] [Shar 2003]	Si(100)	Biased Enhanced. -260 V	CH <sub>4</sub> :H <sub>2</sub> =5:100	NA	30	1000	700	1.3	a few- a few 100	34
MWCVD [Yang 2002]	quartz	0.5 μm ultrasonic polishing	CH <sub>4</sub> :H <sub>2</sub> :O <sub>2</sub> =3:96.8:0.2	~200	30	1500	500	~1.0	65	12
MPECVD [Li 2002]	n-Si	ultrasonic polishing	CH <sub>4</sub> :H <sub>2</sub> =1:100	NA	30	2500	650	0.5	NA	NA
MPECVD [Li 2002]	n-Si	ultrasonic polishing	CH <sub>4</sub> :H <sub>2</sub> =1:100	NA	30	2500	650	0.5 & 0.3	NA	27
MPECVD [Li 2002]	n-Si	ultrasonic polishing	CH <sub>4</sub> :H <sub>2</sub> =1:100	NA	30	2500	650	1.3	NA	NA
MPECVD [Li 2002]	n-Si	ultrasonic polishing	CH <sub>4</sub> :H <sub>2</sub> =1:100	NA	30	2500	650	1.3 & 0.9	NA	NA

T<sub>s</sub>: substrate temperature

S.R.: surface roughness

t<sub>film</sub>: film thickness

\*NCD: nanocrystalline diamond crystals were surrounded by amorphous structure

WC-Co: cemented tungsten carbide

CC: cemented carbide

CH<sub>4</sub>:H<sub>2</sub>:O<sub>2</sub> : O<sub>2</sub> was added after 2 hours of experiments

a: electrolytically polishing with solution of 10% HClOH and 90% ethylglycolmonobutylether

b: lapping and polishing with 9 μm calcined aluminum oxide powder

c: lapping and polishing with 3 μm calcined aluminum oxide powder

d: lapping and polishing with 1 μm calcined aluminum oxide powder

e: tumbler polishing with 1000 grit size SiC particles

f: general cleaning, sonicating in ultra-pure 1:1 trichlorotrifluoroethane and methane solution for 60 min, followed by Ar plasma cleaning for 30 min

## **2.4 Nanocrystalline Diamond Applications**

### **2.4.1 IR Optical Transmission Window**

Proper coating protection has become a necessity because many optical components are operated in a hostile environment, such as infrared windows for aerodynamic applications. By combining the good optical transparency of diamond and its exceptional physical, mechanical, and chemical properties, like high strength and chemical inertness, diamond films make excellent protective coatings for optical elements. Thus, during the past 15 years, researchers have given much effort to investigating the deposition of diamond films for optical coatings. Table 2.3 summarizes the past experiments concerned with the deposition of polycrystalline diamond for optical application. The different deposition methodologies that were employed for polycrystalline diamond deposition are summarized along with the transmission performance of the resulting structures. The results of a number of these investigations are briefly described below.

A low temperature ( $\sim 400^\circ\text{C}$ ) plasma enhanced chemical vapor deposition process (by varying the time duration of the plasma pulse and the number of the pulses to control the substrate temperature) was developed to coat diamond on fused quartz slides. It used a methane, hydrogen, and oxygen gas mixture as deposition gases [Ong 1989]. The films' transmission is over 60% in the range of 0.6-2  $\mu\text{m}$  wavelength. In 1990, Wang et al. noticed that by etching away the substrate and polishing the rough surfaces of polycrystalline diamond, the transmittance of the free-standing diamond film was increased from the range of 14-45% to the range of 64-75% ( $4000\text{ cm}^{-1}$  to  $600\text{ cm}^{-1}$ ) [Wang 1990]. Sun et al. [Sun 1992] produced another free-standing diamond film by etching away the silicon sub-



strate. Without polishing the diamond surface, the mean transmission was 71% around a wavelength of 20  $\mu\text{m}$  and 57% around a wavelength of 2.5  $\mu\text{m}$ . Another investigation which makes use of the traditional  $\text{CH}_4/\text{H}_2$  polycrystalline diamond growth achieved as-deposited, non-polished CVD polycrystalline thin diamond films with near idea optical transmission throughout the visible and near- to mid- infrared [Ulcz 1998] and [Rein 2000]. Tang et al. reported that the transmittance of the polished diamond films (by another thick polycrystalline diamond film) could be increased more than one order in magnitude when the surface roughness were decreased from 3.2  $\mu\text{m}$  to 0.55  $\mu\text{m}$  and the other from 5.2  $\mu\text{m}$  to 1.35  $\mu\text{m}$  [Tang 2003].

**TABLE 2.3: POLYCRYSTALLINE DIAMOND FILM DEPOSITION METHODOLOGY AND THE TRANSMITTANCE**

Reactor	Substrate	Pretreatment (diamond powder)	Gas Chemistry	Flow Rate (sccm)	P (Torr)	Power (W)	T <sub>s</sub> (°C)	t <sub>film</sub> (µm)	Transmittance	S.R. (nm)	Crystal Size (nm)
MWPCVD [Ong 1989]	fused quartz	0.5-1 µm scratched	CH <sub>4</sub> :H <sub>2</sub> :O <sub>2</sub> = 0.3:99.5:0.2	100	30	400	~400	0.92	over 60% (0.6-2 µm)	20	≤ 300
MWPCVD [Ong 1989]	fused quartz	0.5-1 µm scratched	CH <sub>4</sub> :H <sub>2</sub> :O <sub>2</sub> = 0.3:99.5:0.2	100	30	400	~400	1.25	over 60% (1.2-1.38 µm) &(1.6-1.9 µm)	200	≤ 300
MPCVD [Wang 1990]	Si	scratched	CH <sub>4</sub> :H <sub>2</sub> = 0.5:99.5	100	90	790	1000	21	<sup>a</sup> 14-45% (2.5-16.7 µm)	NA	micron
MPCVD [Wang 1990]	Si	scratched	CH <sub>4</sub> :H <sub>2</sub> = 0.5:99.5	100	90	790	1000	20	<sup>b</sup> 64-75% (2.5-16.7 µm)	NA	NA
MPCVD [Wang 1990]	Si	scratched	CH <sub>4</sub> :H <sub>2</sub> = 4:96	100	90	670	980	15.6	<sup>b</sup> 61-69% (2.5-16.7 µm)	NA	NA
HFCVD [Sun 1992]	Si(100)	0.5 µm paste scratched	CH <sub>4</sub> :H <sub>2</sub> = 0.75:99.25	100	7.5	Filament 2100 °C	900	4.1	<sup>a</sup> 71% at 20 µm <sup>a</sup> 57% at 2.5µm	NA	ave.= 2000
HFCVD [Sun 1992]	Si(100)	0.5 µm paste scratched	CH <sub>4</sub> :H <sub>2</sub> = 1.25:98.75	100	7.5	Filament 2100 °C	900	4	<sup>a</sup> 59% at 20 µm <sup>a</sup> 54% at 2.5µm	NA	ave.= 1000
MPACVD [Tang 2003]	Si	NA	CH <sub>4</sub> :H <sub>2</sub> = 4:100	NA	100-1 10	3200-400 0	800-9 50	170	0.25-0.63% (2.5-10 µm)	3320	ave.= 30000
MPACVD [Tang 2003]	Si	NA	CH <sub>4</sub> :H <sub>2</sub> = 4:100	NA	100-1 10	3200-400 0	800-9 50	150	<sup>c</sup> 19.79-21.43 %	550	NA





Table 2.3 Continue

Reactor	Substrate	Pretreatment (diamond powder)	Gas Chemistry	Flow Rate (sccm)	P (Torr)	Power (W)	T <sub>s</sub> (°C)	t <sub>film</sub> (μm)	Transmittance	S.R. (nm)	Crystal Size (nm)
MPACVD [Tang 2003]	Si	NA	CH <sub>4</sub> :H <sub>2</sub> = 4:100	NA	100-1 10	3200-400 0	800-9 50	335	0.04-0.1%	5200	ave.= 30000
MPACVD [Tang 2003]	Si	NA	CH <sub>4</sub> :H <sub>2</sub> = 4:100	NA	100-1 10	3200-400 0	800-9 50	310	~8-17%	1350	NA
MPACVD [Rein 2000]	Si	scratched	*CH <sub>4</sub> :H <sub>2</sub>	NA	NA	NA	450-5 00	0.4	63-66% (3-5 μm)	10-2 0	ave. ≤ 200
MPACVD [Rein 2000]	Si	scratched	*CH <sub>4</sub> :H <sub>2</sub>	NA	NA	NA	450-5 00	0.4	80-89% (3-5 μm) & ave.=86% (3-5 μm)	10-2 0	ave. ≤ 200
MPACVD [Rein 2000]	SiO <sub>2</sub> /Si	scratched	*CH <sub>4</sub> :H <sub>2</sub>	NA	NA	NA	450-5 00	0.15	67-74% (3-5 μm)	10-2 0	ave. ≤ 200
MPACVD [Rein 20003]	SiO <sub>2</sub> /Si	scratched	*CH <sub>4</sub> :H <sub>2</sub>	NA	NA	NA	450-5 00	0.15	85-98% (3-5 μm) & ave.=90% (3-5 μm)	10-2 0	ave. ≤ 200
MPCVD [Shar 2001] [Shar 2003]	Si(100)	Biased Enhanced. -200 V	CH <sub>4</sub> :H <sub>2</sub> = (2:100)-> (1:100)	NA	30-> 50	1000-> 1300	700-> 600	1.5	~0-80% (0.2-2 μm)	60	ave.= 1000

$T_s$ : substrate temperature  
S.R.: surface roughness  
 $t_{\text{film}}$ : film thickness  
a: free-standing film, transmittance measured after the substrate is etched away  
b: free-standing film, transmittance measured after the substrate is etched away and the sample is polished  
c: transmittance measured after the diamond's surface is polished  
\*CH<sub>4</sub>:H<sub>2</sub>: in some cases, CO<sub>2</sub> was added  
SiO<sub>2</sub>: 250 nm-thick SiO<sub>2</sub> layer was thermally grown in a furnace with high purity dry oxygen at 1100 °C



Due to the significant impact of the surface roughness on optical transmission of diamond coated samples, i.e. the reflected and transmitted light from the rough surfaces are scattered in various directions, which leads to poor transparency. Consequently, in recent years, the effort of depositing diamond optical coatings has been directed toward nanocrystalline diamond. The smooth surfaces of nanocrystalline diamond films have enhanced the optical transmittance of as-grown diamond films for optical coating applications. Table 2.4 summarizes the past experiments concerned with the deposition of nanocrystalline diamond for optical application. The different deposition methodologies that were employed for nanocrystalline diamond deposition are summarized along with the transmission performance of the resulting structures. The results of a number of these investigations are briefly described below.

In 1998, the optical transparency of nanocrystalline diamond films grown using methane, hydrogen, and oxygen gas mixture in a microwave reactor with different sizes of diamond powder for substrate (quartz) pretreatment was investigated [Bhus 1998]. A few discoveries was made by Bhusari et al. and Chen et al. [Bhus 1998], [Chen 2000] and summarized below.

- (1) The optical transmittance and surface roughness data exhibited some crossover behavior.
- (2) The films reached the saturation of optical transmittance of the films around 80-84% even though the surface roughness continued to decrease from 13 nm to 6 nm.

- (3) as long as the  $sp^2$  bonded carbon in the film was minimum, the surface roughness was the dominant factor that controls the optical transmission of the films,
- (4) the grain size of the nanocrystalline diamond films did not have as much influence as the surface roughness on the optical transparency, and
- (5) smooth and highly transparent nanocrystalline diamond films could be synthesized with (i) low methane concentration (between 4-20%) on finer-diamond-powder (4 nm)-scratched quartz substrates, and (ii) high methane concentration (between 20-42%) on coarser-diamond-powder (0.1  $\mu\text{m}$ )-scratched quartz substrates. The optical transmittance was around 80% at a wavelength 700 nm and was achieved on the quartz substrate.

The comparison of the optical properties of free-standing diamond and nano-diamond was performed by Sharda et al. [Shar 2001]. Although the nano-diamond grown at 600 °C had a somewhat higher absorption coefficient, its lower surface roughness (17 nm of nano-diamond versus 60 nm of polycrystalline diamond) gave it the potential for applications as optical windows in the near IR region (transmittance close to 78%).

A 0.1  $\mu\text{m}$ -thick nanocrystalline diamond protective coating on quartz glass, synthesized by microwave chemical vapor deposition system with methane and hydrogen gas mixtures, achieved 65% of optical transmittance in the visible light range when the surface roughness was controlled under 12 nm [Yang 2002].

Jing et al. used a microwave plasma enhanced chemical vapor deposition technique to grow nanocrystalline diamond on both sides of a silicon wafer with thickness of 0.3  $\mu\text{m}$  and 0.5  $\mu\text{m}$ , and reported a maximum transmittance of 85% at the wavenumber of 2200  $\text{cm}^{-1}$  ( $\sim 4.5 \mu\text{m}$ ) [Jing 2002].

**TABLE 2.4: NANOCRYSTALLINE DIAMOND FILM DEPOSITION METHODOLOGY AND THE TRANSMITTANCE**

Reactor	Substrate	Pretreatment (diamond powder)	Gas Chemistry	Flow Rate (sccm)	P (Torr)	Power (W)	T <sub>s</sub> (°C)	t <sub>Film</sub> (μm)	Transmittance	S.R. (nm)	Crystal Size (nm)
MPCVD [Bhus 1998] [Chen 2000]	quartz	4nm&0.1μm ultrasonic polishing	CH <sub>4</sub> :H <sub>2</sub> :O <sub>2</sub> =(4-42): (95.9-57.9): 0.1	200	22	1000	590-600	0.5-0.6	30-84% at 0.7 μm	6-200	4-a few 100
MPCVD [Bhus 1998] [Chen 2000]	quartz	4nm ultrasonic polishing	CH <sub>4</sub> :H <sub>2</sub> :O <sub>2</sub> =(4-20): (95.9-79.9): 0.1	200	22	1000	590-600	0.5-0.6	80-84% at 0.7 μm	6-200	4-a few 100
MPCVD [Bhus 1998] [Chen 2000]	quartz	0.1μm ultrasonic polishing	CH <sub>4</sub> :H <sub>2</sub> :O <sub>2</sub> =(20-42): (79.9-57.9): 0.1	200	22	1000	590-600	0.5-0.6	80-84% at 0.7 μm	6-200	4-a few 100
MPCVD [Shar 2001] [Shar 2003]	Si(100)	Biased Enhanced. -260 V	CH <sub>4</sub> :H <sub>2</sub> =5:100	NA	30	1000	600	1.1	~0-78% (0.2-2 μm)	17	a few- a few 10
MPCVD [Shar 2001] [Shar 2003]	Si(100)	Biased Enhanced. -260 V	CH <sub>4</sub> :H <sub>2</sub> =5:100	NA	30	1000	700	1.3	~0-36% (0.2-2 μm)	34	a few- a few 100
MWCVD [Yang 2002]	quartz	0.5 μm ultrasonic polishing	CH <sub>4</sub> :H <sub>2</sub> :O <sub>2</sub> =3.96.8:0.2	~200	30	1500	500	~1.0	60-91% (0.67-2.5 μm) ave.=65% (0.67-0.79μm)	12	65



Table 2.4 Continue

Reactor	Substrate	Pretreatment (diamond powder)	Gas Chemistry	Flow Rate (sccm)	P (Torr)	Power (W)	T <sub>s</sub> (°C)	t <sub>film</sub> (μm)	Transmittance	S.R. (nm)	Crystal Size (nm)
MPECVD [Li 2002]	n-Si	ultrasonic polishing	CH <sub>4</sub> :H <sub>2</sub> =1:100	NA	30	2500	650	0.5	54-66% (2.78-8.33μm) ave.=66% (4.44-6.67μm)	NA	NA
MPECVD [Li 2002]	n-Si	ultrasonic polishing	CH <sub>4</sub> :H <sub>2</sub> =1:100	NA	30	2500	650	0.5 & 0.3	66-85% (2.78-8.33μm) ave.=80% (3.33-6.67μm)	27	NA
MPECVD [Li 2002]	n-Si	ultrasonic polishing	CH <sub>4</sub> :H <sub>2</sub> =1:100	NA	30	2500	650	1.3	48-53% (4.76-14.3μm)	NA	NA
MPECVD [Li 2002]	n-Si	ultrasonic polishing	CH <sub>4</sub> :H <sub>2</sub> =1:100	NA	30	2500	650	1.3 & 0.9	58-80% (4.76-14.3μm) ave.=75% (6.67-12.5μm)	NA	NA
RTMCVD [Erz 1993]	quartz	0.01 μm diamond powder diluted in aqueous media, scratched	CH <sub>4</sub> :O <sub>2</sub> :H <sub>2</sub> =2:1:97	100	37.5	550	800	1	5-66% (0.185-0.88 μm)	20-40	20

RTMCVD: remote tubular microwave chemical vapor deposition

CH<sub>4</sub>:H<sub>2</sub>:O<sub>2</sub>\*: O<sub>2</sub> was added after 2 hours of experiments

a: free-standing film, transmittance measured after the substrate is etched away

## 2.4.2 Tribological Application-Seal Coatings

Since the first success of chemical vapor deposition diamond synthesis, there has been great interest in producing high-quality, smooth diamond films on various substrates (for example, steel, WC-Co, SiC, etc.) for use in a wide range of engineering applications. This is because diamond, the hardest among all materials, has high thermal conductivity and is impervious to most chemicals. However, microcrystalline diamond films are usually rough due to the large faceted crystallinity, which makes post processing, like polishing, a necessity to improve its friction and wear characteristics. Thick polycrystalline diamond films grown by the hot filament CVD method was coated on cemented carbide. However, it only reduced the wear of cutting edge if the cutting path was short [Mori 1998], [Endl 1999]. When the polycrystalline diamond films were used in sliding wear applications and machining, their rough surfaces cause severe wear damage on the mating surfaces and high frictional loss [Hayw 1992].

The importance of smooth diamond surface in tribological contacts has been theoretically studied and experimentally explored [Case 1973], [Miyo 1993], [Holl 1994], [Kohz 1994]. Miyoshi et al. tested diamond coated pins sliding against diamond coatings in both dry nitrogen and humid air and found that the initial friction coefficients were 0.14 and 0.6 with the film surface roughness of 15 nm and 160 nm, respectively [Miyo 1993]. When the roughness of diamond films was reduced from 530 nm to 75 nm, a 50-75% decrease in friction for sliding against aluminum and about 50% for carbon steel were observed by Hollman et al. [Holl 1994]. As a result, the development of smooth, as-deposited nanocrystalline diamond coatings is desirable. Table 2.5 shows the results of a number

of different investigations concerned with diamond film for tribological application. Both the growth methods and testing techniques are described.

**TABLE 2.5: DIAMOND FILM DEPOSITION METHODOLOGY AND THE FRICTION COEFFICIENT**

Reactor	Deposition Method	Sample	Characterization Technique	$t_{\text{Film}}$ ( $\mu\text{m}$ )	S.R. (nm)	Friction	Wear ( $\text{mm}^3/\text{N.m}$ )	S.D. (m)
MPCVD [Silv 2003]	1 $\mu\text{m}$ diamond powder ultrasonic polishing	PCD/Ni/Cu/Ti/Steel	sphere-on-flat geometry, micro-abrasion apparatus by a rotating ball with diamond slurry (10-20 $\mu\text{m}$ -sized diamond particles in water). AISI 52100 steel ball, dia.=25 mm, rotation speed=80 rpm (8.38 rad/sec), 0.25 N normal load	PCD: 13.5 Ni: 3-4 Cu: 32-36 Ti: 0.5-2.5	16280	NA	$2.5 \times 10^{-3} \text{ mm}^3$	55
NA [Silv 2003]	Ni&Cu by electro-plating method, Ti by PVD method	Ni/Cu/Ti/Steel	Same as above	Ni: 3-4 Cu: 32-36 Ti: 0.5-2.5	NA	NA	$26.25 \times 10^{-3} \text{ mm}^3$	55
NA [Silv 2003]	NA	AISI M2 Steel	Same as above	NA	NA	NA	$34.2 \times 10^{-3} \text{ mm}^3$	55
RFPACVD [Nied 2001]	$\text{CH}_4$ , 50-100 sccm, 50Pa, 3 kW, 300 min, $T_s=900^\circ\text{C}$	NCD/CC	pin-on-disk, wood pin, 60N, sliding speed=1 m/sec	NA	1215	poplar:0.84 Oak:0.88	NA	990
RFPACVD [Nied 2001]	$\text{CH}_4$ , 50-100 sccm, 50Pa, 3 kW, 30 min, $T_s=900^\circ\text{C}$	NCD/CC	Same as above	NA	1575	poplar:0.88 Oak:0.86	NA	990
NA [Nied 2001]	NA	CC	Same as above	NA	930	poplar:1.1 Oak:0.83	NA	990

Table 2.5 Continue

Reactor	Deposition Method	Sample	Characterization Technique	t <sub>Film</sub> (μm)	S.R. (nm)	Friction	Wear (mm <sup>3</sup> /N.m)	S.D. (m)
MWPCVD [Hong 2002]	10% CH <sub>4</sub> -H <sub>2</sub> , 24Torr, T <sub>s</sub> =640-680°C, 1.8-2.2 kW, 1μm&5nm diamond powder scratched	NCD/Si	pin-on-disk tribometer, SiC ball, dia.=6.36 mm, dry air, 0.5 N, speed=5 cm/sec	2.2	10	0.05-0.07	NCD: ~0 SiC: 1.6x10 <sup>-7</sup>	720
MWPCVD [Hong 2002]	10% CH <sub>4</sub> -H <sub>2</sub> , 24Torr, T <sub>s</sub> =640-680°C, 1.8-2.2 kW, 1μm&5nm diamond powder scratched	NCD/Si	pin-on-disk tribometer, SiC ball, dia.=6.36 mm, dry air, 1 N, speed=10 cm/sec	2.2	10	0.11	NA	720
Biased Hot Flame [Holl 1998]	O <sub>2</sub> :C <sub>2</sub> H <sub>2</sub> =0.9:1, 1960 sccm, T <sub>s</sub> =850 ± 30°C, 1μm diamond powder scratched	NCD/CC	ball-on-disk, BBS ball, 2N, speed=0.1 m/sec, air (30-50% RH, 20°C), ^water, ^oil (polyalfaolefin oil)	NA	30	a: 0.1, w: 0.08, o: 0.07, (initial: 0.3, for 5-10 m in air)	NA	120
NA [Holl 1998]	NA	BBS	ball-on-disk, BBS ball, 2N, speed=0.1 m/sec, air (30-50% RH, 20°C), water, oil (polyalfaolefin oil)	NA	NA	a: 0.8, w: 0.4, o: 0.13	NA	120
NA [Holl 1998]	NA	BBS	ball-on-disk, BBS ball, 2N, speed=0.1 m/sec, oil (polyalfaolefin oil)	NA	NA	NA	2.1x10 <sup>-8</sup>	8640



Table 2.5 Continue

Reactor	Deposition Method	Sample	Characterization Technique	t <sub>Film</sub> (μm)	S.R. (nm)	Friction	Wear (mm <sup>3</sup> /N.m)	S.D. (m)
Biased Hot Flame [Holl 1998]	O <sub>2</sub> :C <sub>2</sub> H <sub>2</sub> =0.9:1, 1960 sccm, T <sub>s</sub> =850 ± 30°C, 1μm diamond powder scratched	NCD/CC	ball-on-disk, CC ball, 2N, speed=0.1 m/sec, air (30-50% RH, 20°C), ^water, ^oil (polyalfaolefin oil)	NA	30	a: 0.08, w: 0.07, o: 0.08, (initial: 0.3, for 5-10 m in air)	NA	120
NA [Holl 1998]	NA	BBS	ball-on-disk, CC ball, 2N, speed=0.1 m/sec, air (30-50% RH, 20°C), water, oil (polyalfaolefin oil)	NA	NA	a: 0.75, w: 0.2, o: 0.1	NA	120
Biased Hot Flame [Holl 1998]	O <sub>2</sub> :C <sub>2</sub> H <sub>2</sub> =0.9:1, 1960 sccm, T <sub>s</sub> =850 ± 30°C, 1μm diamond powder scratched	NCD/CC	ball-on-disk, SS ball, 2N, speed=0.1 m/sec, air (30-50% RH, 20°C), ^water, ^oil (polyalfaolefin oil)	NA	30	a: 0.07, w: 0.06, o: 0.08, (initial: 0.3, for 5-10 m in air)	NA	120
Biased Hot Flame [Holl 1998]	Same as above	NCD/CC	ball-on-disk, SS ball, 2N, speed=0.1 m/sec, air (30-50% RH, 20°C),	NA	30	NA	1.9x10 <sup>-10</sup>	8640
NA [Holl 1998]	NA	BBS	ball-on-disk, SS ball, 2N, speed=0.1 m/sec, air (30-50% RH, 20°C), water, oil (polyalfaolefin oil)	NA	NA	a: 0.6, w: 0.3, o: 0.11	NA	120





*Table 2.5 Continue*

Reactor	Deposition Method	Sample	Characterization Technique	$t_{\text{Film}}$ ( $\mu\text{m}$ )	S.R. (nm)	Friction	Wear ( $\text{mm}^3/\text{N.m}$ )	S.D. (m)
Biased Hot Flame [Holl 1998]	$\text{O}_2:\text{C}_2\text{H}_2=0.9:1$ , 1960 sccm, $T_s=850 \pm 30^\circ\text{C}$ , 1 $\mu\text{m}$ diamond powder scratched	NCD/CC	ball-on-disk, Ti ball, 2N, speed=0.1 m/sec, air (30-50% RH, $20^\circ\text{C}$ ), water, oil (polyalfaolefin oil)	NA	30	a: 0.5, w: 0.35, o: 0.32	NA	120
Biased Hot Flame [Holl 1998]	Same as above	*NCD/CC	Same as above	NA	2.5	a: 0.1, w: 0.06, o: 0.04,	NA	120
NA [Holl 1998]	NA	BBS	Same as above	NA	NA	a: 0.45, w: 0.41, o: 0.4	NA	120
Biased Hot Flame [Holl 1998]	$\text{O}_2:\text{C}_2\text{H}_2=0.9:1$ , 1960 sccm, $T_s=850 \pm 30^\circ\text{C}$ , 1 $\mu\text{m}$ diamond powder scratched	NCD/CC	ball-on-disk, Al ball, 2N, speed=0.1 m/sec, air (30-50% RH, $20^\circ\text{C}$ ), water, oil (polyalfaolefin oil)	NA	30	a: 0.53, w: 0.51, o: 0.11	NA	120
Biased Hot Flame [Holl 1998]	Same as above	*NCD/CC	Same as above	NA	2.5	a: 0.1, w: 0.03, o: 0.04	NA	120
NA [Holl 1998]	NA	BBS	Same as above	NA	NA	a: 0.55, w: 0.52, o: 0.15	NA	120



Table 2.5 Continue

Reactor	Deposition Method	Sample	Characterization Technique	$t_{\text{film}}$ ( $\mu\text{m}$ )	S.R. (nm)	Friction	Wear ( $\text{mm}^3/\text{N.m}$ )	S.D. (m)
MPCVD [Erde 1996]	BEN at -150V for 30-60 min, 60 Torr, $T_s=800-850^\circ\text{C}$ , $\text{H}_2/\text{CH}_4=98/2$ sccm, 1500 W	PCD(111) on Si or $^*\text{SiC}$ or $^*\text{Si}_3\text{N}_4$	pin-on-disk tribometer, speed=0.05-0.2 m/sec $\text{Si}_3\text{N}_4$ ball, 2N, dai.=9.5mm, air (20% RH)	NA	315	0.25, initial: 0.56	$6.5 \times 10^{-6}$ , $5.7 \times 10^{-4}$	6000 rev.
MPCVD [Erde 1996]	Same as above	PCD(100) on Si or $^*\text{SiC}$ or $^*\text{Si}_3\text{N}_4$	pin-on-disk tribometer, speed=0.05-0.2 m/sec $\text{Si}_3\text{N}_4$ ball, 2N, dai.=9.5mm, air (20% RH)	NA	208	0.1, initial: 0.23	Same as above	6000 rev.
MPCVD [Erde 1996]	Same as above	PCD on Si or $^*\text{SiC}$ or $^*\text{Si}_3\text{N}_4$	pin-on-disk tribometer, speed=0.05-0.2 m/sec $\text{Si}_3\text{N}_4$ ball, 2N, dai.=9.5mm, dry $\text{N}_2$ , air (30-50% RH)	NA	125	0.2-0.7	Same as above	4000 rev.
MPCVD [Erde 1996]	BEN at -150V for 30-60 min, 100 Torr, $T_s=800-850^\circ\text{C}$ , $\text{Ar}/\text{H}_2/\text{CH}_4=98/2/1$ sccm, 800 W	NCD on Si or $^*\text{SiC}$ or $^*\text{Si}_3\text{N}_4$	pin-on-disk tribometer, speed=0.05-0.2 m/sec $\text{Si}_3\text{N}_4$ ball, 2N, dai.=9.5mm, dry $\text{N}_2$ , air (40% RH)	NA	NA	$\text{N}_2$ : 0.09 air: 0.15	$1.8 \times 10^{-7}$ , $5 \times 10^{-7}$	5000 rev.
MPCVD [Erde 1996]	BEN at -150V for 30-60 min, 100 Torr, $T_s=800-850^\circ\text{C}$ , $\text{Ar}/\text{H}_2/\text{C}_{60}=97/2/1$ sccm, 800 W	NCD on Si or $^*\text{SiC}$ or $^*\text{Si}_3\text{N}_4$	pin-on-disk tribometer, speed=0.05-0.2 m/sec $\text{SiC}$ pin, 5N, r=12.7 cm, dry $\text{N}_2$ , air (50% RH)	NA	40	$\text{N}_2$ : 0.08 air: 0.19	Same as above	8000 rev.

Table 2.5 Continue

Reactor	Deposition Method	Sample	Characterization Technique	$t_{\text{film}}$ ( $\mu\text{m}$ )	S.R. (nm)	Friction	Wear ( $\text{mm}^3/\text{N.m}$ )	S.D. (m)
MPCVD [Erde 1996]	BEN at -150V for 30-60 min, 100 Torr, $T_s=800-850^\circ\text{C}$ , $\text{Ar}/\text{H}_2/\text{C}_{60}=97/2/1$ sccm, 800 W	NCD on Si or $^*\text{SiC}$ or $^*\text{Si}_3\text{N}_4$	pin-on-disk tribometer, speed=0.04 m/sec $\text{Si}_3\text{N}_4$ ball, 5N, dai.=9.5mm, dry $\text{N}_2$ ,	NA	20-45	0.04, (initial: 0.4) jump=0.4	$1.8 \times 10^{-7}$ to $10^{-7}$	1000 rev.
MPCVD [Erde 1996]	BEN at -150V for 30-60 min, 100 Torr, $T_s=800-850^\circ\text{C}$ , $\text{Ar}/\text{H}_2/\text{CH}_4=98/2/1$ sccm, 800 W	NCD on Si or $^*\text{SiC}$ or $^*\text{Si}_3\text{N}_4$	Same as above	NA	NA	0.04, (initial: 0.4) jump=0.4	Same as above	1000 rev.
MPCVD [Erde 1996]	BEN at -150V for 30-60 min, 100 Torr, $T_s=800-850^\circ\text{C}$ , 800 W $\text{Ar}/\text{H}_2/\text{CH}_4=98/2/1$ sccm, or $\text{Ar}/\text{H}_2/\text{C}_{60}=97/2/1$ sccm	NCD on Si or $^*\text{SiC}$ or $^*\text{Si}_3\text{N}_4$	pin-on-disk tribometer, speed=0.05-0.2 m/sec $\text{Si}_3\text{N}_4$ ball, 2N, dai.=9.5mm, air (30-50% RH)	NA	NA	0.13-0.15, initial: 0.35	Same as above	a few 1000 rev.
MPECVD [Xu 2001]	$\text{C}_2\text{H}_2:\text{H}_2=16:84$ , 0.5 $\mu\text{m}$ diamond paste scratched, 750 $^\circ\text{C}$ , 60 Torr, 2kW	NCD/Si	ball-on-disk, $\text{Al}_2\text{O}_3$ ball, dia=3 mm, 3N, speed=2.5 mm/sec, 40-50% RH	0.8	28	initial: 0.7 final: 0.45	wear scar dia=0.32	250 cycles
MPECVD [Xu 2001]	Same as above	$^a\text{NCD/Si}$	Same as above	~0.8	NA	initial: 0.28 final: 0.23	wear scar dia=0.4	1000 cycles

Table 2.5 Continue

Reactor	Deposition Method	Sample	Characterization Technique	t <sub>Film</sub> (μm)	S.R. (nm)	Friction	Wear (mm <sup>3</sup> /N.m)	S.D. (m)
MPECVD [Xu 2001]	Same as above	<sup>b</sup> NCD/Si	Same as above	~0.8	NA	initial: 0.15 final: 0.08	wear scar dia=0.05	1000 cycles

T<sub>s</sub>: substrate temperature

S.R.: surface roughness

t<sub>Film</sub>: film thickness

S.D.: sliding distance

RH: relative humidity

BEN: biased enhanced nucleation

PCD: polycrystalline diamond

NCD: nanocrystalline diamond

\*NCD: lightly polished nanocrystalline diamond

<sup>a</sup>NCD/Si: N<sub>2</sub> implementation at 1x10<sup>16</sup> ions/cm<sup>2</sup> at 80 °C

<sup>b</sup>NCD/Si: N<sub>2</sub> implementation at 1x10<sup>17</sup> ions/cm<sup>2</sup> at 80 °C

<sup>^</sup>water: Water was introduced after 5-10 m of dry sliding when the friction had reached a steady-state value.

<sup>^</sup>oil: Oil was introduced after 5-10 m of dry sliding when the friction had reached a steady-state value.

\*SiC: polished, 0.1±0.02 μm CLA (centerline average)

\*Si<sub>3</sub>N<sub>4</sub>: polished, 0.1±0.02 μm CLA (centerline average)

rev.: revolution

CC: cemented carbide

BBS: ball-bearing steel

SS: stainless steel

Cu: copper, Ti: titanium, Al: aluminum

### 2.4.3 SAW Devices Based on Nanocrystalline Diamond

Surface acoustic wave (SAW) devices are largely used as frequency filters or resonators in the range of 100 MHz - 1 GHz and are applied to such applications as digital communications, mobile phones and video systems. SAW devices have the advantage in that their size is smaller than the equivalent electromagnetic device. Due to the rapid development of the high speed communication systems, the demand for large volume data transmission and mobile communication is increasing and requires devices to operate at high frequency with high power durability and low loss. Multi-layered diamond substrates are of interest because of their high SAW velocities which satisfy the need for increasing the operational frequency range without reducing the electrode spacing into sub-micron region. Diamond is not piezoelectric. Thus, it is necessary to incorporate piezoelectric materials, like ZnO, into the composite layered structure. Higaki et al. [Higa 1997] compared the performance of ZnO/Diamond/Si SAW devices with the conventional SAW devices composed of LiTaO<sub>3</sub> (X-112°Y) and found that at 2.9 GHz, up to 36 dBm of the input power, the input-output relationship was maintained for ZnO/Diamond/Si SAW filters, whereas the LiTaO<sub>3</sub> SAW filters that operated at 822 MHz, degraded significantly with only 27.7 dBm of input power, and the input-output relationship became nonlinear starting from the input power of only 23 dBm. Clearly, compared to LiTaO<sub>3</sub> SAW filters, ZnO/Diamond/Si SAW filters were durable for 8 dB higher input power even at 3.5 times higher frequency.

Table 2.6 lists the typical SAW velocities of layered structure with a diamond layer and those of conventional SAW materials [Higa 1997], [Naka 2003], [Chen 2003], [Jian

1991], [Begh 2002], [Ferr 1999]. The surfaces of the diamond films, which were used as SAW device substrates were mechanically polished until a less than 3 nm surface roughness was obtained.

**TABLE 2.6: SAW VELOCITIES**

Sample	Velocity (m/sec)
SiO <sub>2</sub> /ZnO/IDT/Diamond/Si [Naka 2003]	9000
SiO <sub>2</sub> /IDT/ZnO/Diamond/Si [Naka 2003]	10000
ZnO/IDT/Diamond/Si [Naka 2003]	10500
IDT/ZnO/Diamond/Si [Higa 1997], [Naka 2003]	11600
IDT/LiNbO <sub>3</sub> /Diamond/Si [Naka 2003]	11900
IDT/LiTaO <sub>3</sub> /Diamond/Si [Naka 2003]	10600
IDT/ZnO/R-sapphire [Chen 2004]	10500
ZnO/sapphire [Naka 2003]	5500
LiNbO <sub>3</sub> (128Y cut X prop.) [Naka 2003]	3980
LiNbO <sub>3</sub> (64Y cut X prop.) [Naka 2003]	4742
LiTaO <sub>3</sub> (X cut 112Y prop.) [Higa 1997], [Naka 2003]	3290
LiTaO <sub>3</sub> (36Y cut X prop.) [Naka 2003]	4160
ST-cut quartz [Naka 2003]	3160
36°Y-cut quartz [Naka 2003]	5100
a-H:C [Jian 1991]	4583
ta-C (8 nm thick) [Begh 2002]	5138
ta-C (76 nm thick) [Ferr 1999]	6250
DLC/Quartz (1 µm thick diamond-like carbon) [Zhan 2001]	3243
ta-C/Quartz (120 nm thick ta-C) [Zhan 2001]	3278

A comprehensive theoretical study was carried out by Nakahata et al. [naka 1995] and they concluded that when diamond was combined with a piezoelectric thin film, the SAW velocities up to 12000 m/sec could be reached as propagating in ZnO/Diamond/Si, LiNbO<sub>3</sub>/Diamond/Si, and LiTaO<sub>3</sub>/Diamond/Si structures. Table 2.7 shows the calculated SAW velocities of layered structure with a diamond layer and those of conventional SAW materials [Naka 1995].

**TABLE 2.7: CALCULATED SAW VELOCITIES [Naka 1995]**

Sample	Velocity (m/sec)
SiO <sub>2</sub> /ZnO/Diamond/Si ( $kH_{ZnO}=0.3$ , $kH_{SiO_2}=0.45$ )	10710
SiO <sub>2</sub> /ZnO/Diamond/Si ( $kH_{ZnO}=0.5$ , $kH_{SiO_2}=0.72$ )	8050
ZnO/Diamond/Si ( $kH_{ZnO}=0.5$ )	10520
ZnO/Diamond/Si ( $kH_{ZnO}=1.0$ )	7180
LiNbO <sub>3</sub> /Diamond/Si	11890
LiTaO <sub>3</sub> /Diamond/Si	10610
ZnO/glass	2600
LiNbO <sub>3</sub> (128Y cut X prop.)	3980
LiNbO <sub>3</sub> (64Y cut X prop.)	4742
LiTaO <sub>3</sub> (X cut 112Y prop.)	3290
LiTaO <sub>3</sub> (36Y cut X prop.)	4160
ST-cut quartz	3158

Smooth diamond surface is an important fabrication requirement for utilizing diamond films as SAW materials. Smooth diamond films: (1) reduce the propagation loss which affects the insertion loss of SAW devices and (2) ensure the correct generation and propagation of surface acoustic wave. Polishing the surface of the diamond films is a diffi-



cult task especially for large wafers. Thick nanocrystalline diamond films, with good insulating properties can offer considerable advantages over traditionally grown polycrystalline diamond in SAW applications. Therefore, the application of nanocrystalline diamond films to SAW substrate are of interest for the fabrication of high frequency SAW devices.

## **3 Description of Experimental Systems and Procedures**

### **3.1 Introduction**

This chapter, in Section 3.2, first describes the two experimental systems, reactor geometry, and reactor conditions that were utilized in this thesis research, including microwave power supply, waveguide/transmission system, vacuum pump and the gas flow control system, computer control system, and reactor operating field map. The experimental procedure, including seeding procedures, start-up and shut-down procedures are described in Section 3.3. The experimental parameter space that was employed in the experiments for this thesis is described in Section 3.4. and the measurement methodologies for reactor performance and film characterization are described in Section 3.5.

### **3.2 Experimental systems**

As shown in Figure 3.1, two MSU-MPACVD systems that were used in this thesis research consisted of (1) a microwave cavity plasma reactor, (2) a microwave power supply and waveguide/transmission system, (3) a vacuum pump and the gas flow control system, and (4) a computer control system. These systems are described in detail in the subsections below.

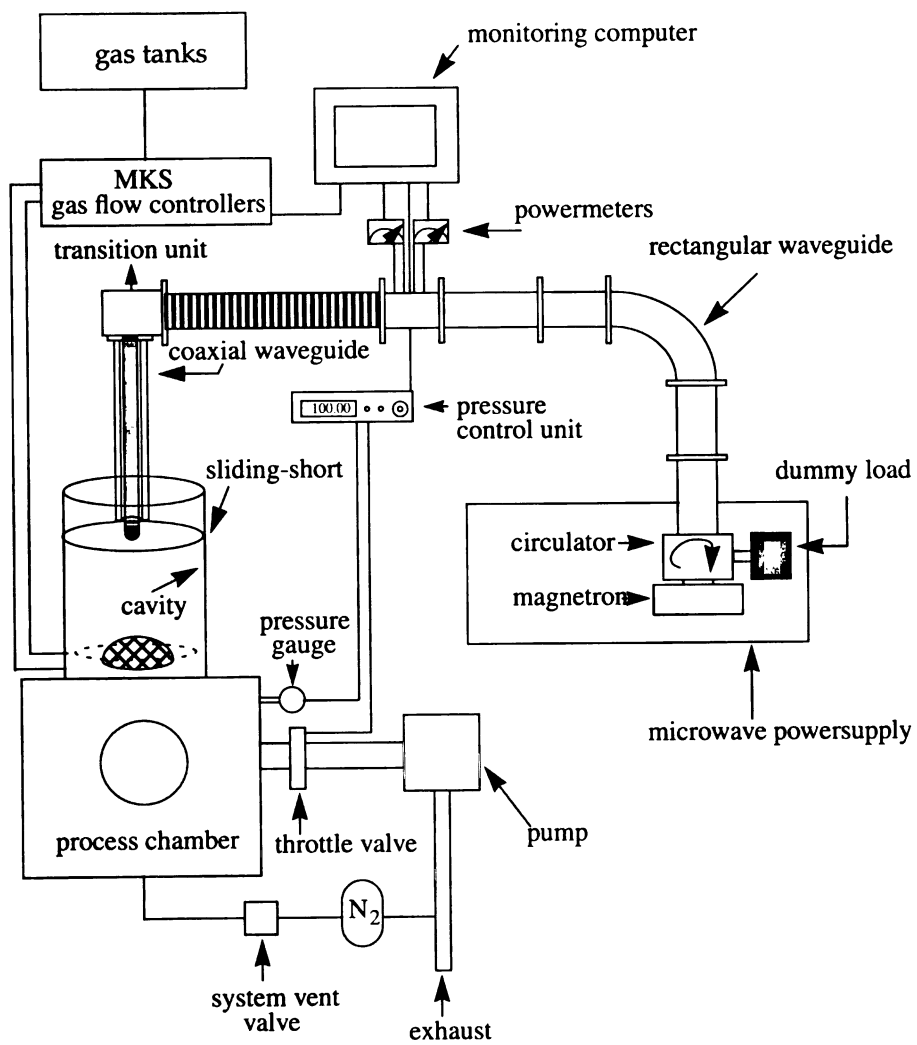


FIGURE 3.1 : MSU-MPACVD SYSTEM

### 3.2.1 Microwave Power Supply and Waveguide/Transmission System

Figure 3.2 shows a schematic drawing of the microwave power and waveguide/transmission system. The microwave power supply (1) consists of a magnetron (2), a circulator (3) and a dummy load (4). The waveguide/transmission system consists of the rectangular waveguides (5), a dual-directional coupler (6), incident and reflected power meters (7) and (8), a flexible waveguide (9), and a waveguide to coaxial transition unit (10).

The microwave power supplied by the magnetron (2) is transmitted to a coaxial waveguide (11) by the transition unit (10) after it propagates through waveguides (5) and (9). Microwave power is coupled into the cavity applicator (14) through a mechanically tunable coaxial excitation probe (12). The excitation probe (12) is located at the center of the sliding short (13). Both the excitation probe depth,  $L_p$ , and the sliding short position,  $L_s$ , can be manually adjusted. That is,  $L_s$  and  $L_p$  can be moved up and down along the reactor axis and can be adjusted independently from each other. Whenever there is a tuning mismatch between the impedance of the cavity applicator and the waveguides, some of the incident power is reflected back from the cavity applicator and propagates in the opposite direction of the incident power. This reflected power passes through the dual-directional coupler (6), and is directed by the circulator (3) into a matched dummy load (4), where it is absorbed and dissipated as thermal energy. The circulator and the matched dummy load protect the power source from being damaged by preventing the propagation of the reflected power back into the power supply. The microwave power source is a Cober (Model No. S6F/4503), 2.45 GHz, 6 kW power source. The dual-direc-

tional power coupler attenuation factors for incident and reflected power are 55.6 dB and 55.7 dB for system I, and for system II are 55.88 dB and 55.96 dB respectively.  $P_{abs}$  (absorbed power) =  $P_{in}$  (input power) -  $P_{ref}$  (reflected power).

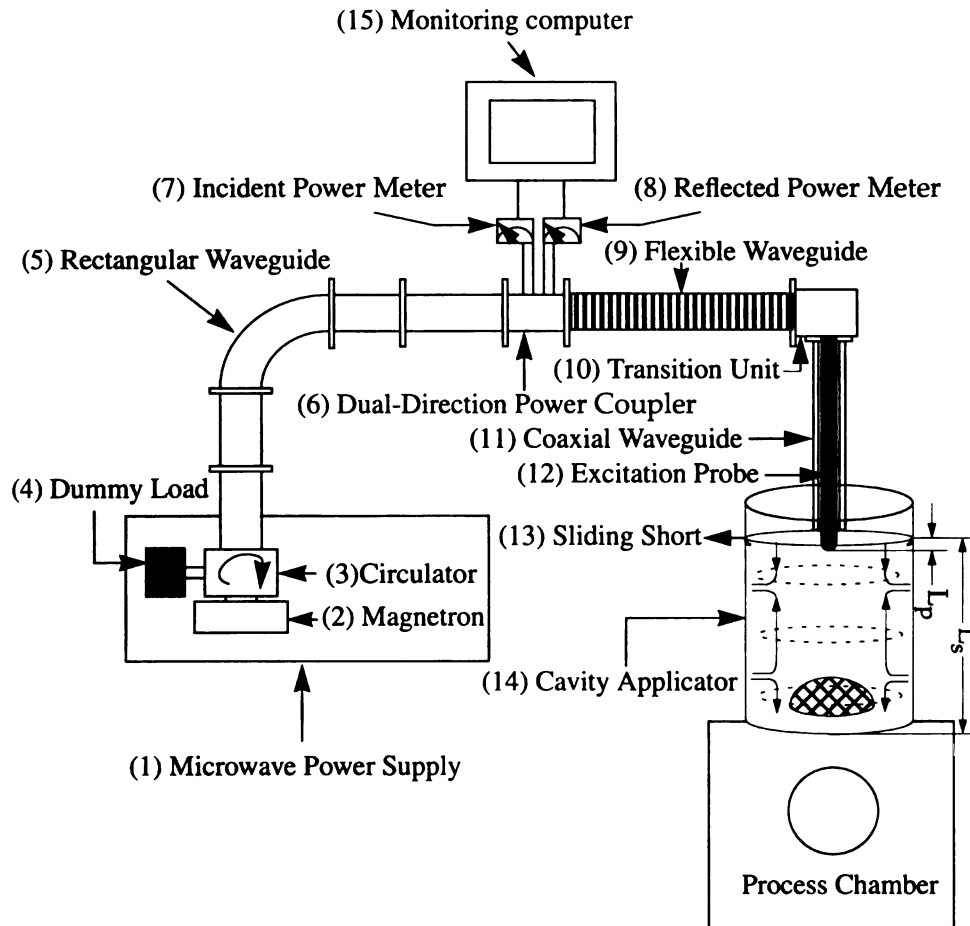


FIGURE 3.2 : MICROWAVE POWER SUPPLY AND WAVEGUIDE/TRANSMISSION SYSTEM FOR MSU-MPACVD REACTOR

### 3.2.2 Vacuum Pump and Gas Flow Control System

#### 3.2.2.1 MSU-MPACVD System I

Figure 3.3 displays a schematic drawing of the vacuum pump and gas flow control systems for the MSU-MPACVD reactor I. The source gases consist of Ar (1), H<sub>2</sub> (2), H<sub>2</sub> (3), and CH<sub>4</sub> (4) with a respective purity of 99.999%, 99.999%, 99.999%, and 99.99%. The gas flow control is monitored by four MKS type 1159 mass flow controllers (5) along with a 4-channel MKS type 247C flow controller (6). The system operator sets the flow rates of the source gases and the values are displayed on the 4-channel MKS flow controller (6). The source gases with desired flow rates are mixed before they enter the baseplate (7). An ALCATEL 2033 type mechanical roughing pump (16) is used to pump down the chamber pressure to ~ 0.01 Torr, which is measured by a MKS type 286 TC-1 (Thermal Conductivity) vacuum gauge (11). The system operator sets the pressure on the MKS type 651C pressure controller (14) and its value is displayed on the Baratron 1000 Torr gauge (13). An automatic throttle valve (10) controls the pressure of the process chamber (8) with the value set in the pressure controller. A manual valve (9), normally open, is installed and can be used to manually control the pressure of the chamber if the automatic throttle valve malfunctions. During the experiment, the manual valve is open and the chamber pressure is controlled by the throttle valve. A pirani gauge (12) is installed for routine leakage check. Nitrogen gas (17) is released through the system vent valve (15) to bring the chamber pressure up to atmospheric pressure. It is also used to dilute the exhaust gases (19) through an exhaust valve (18) with the N<sub>2</sub> flow rate equal to or greater than twenty times of the total flow rate. The mixing of nitrogen into the exhaust gases ensures that the exhaust gases are not in a flammable condition.

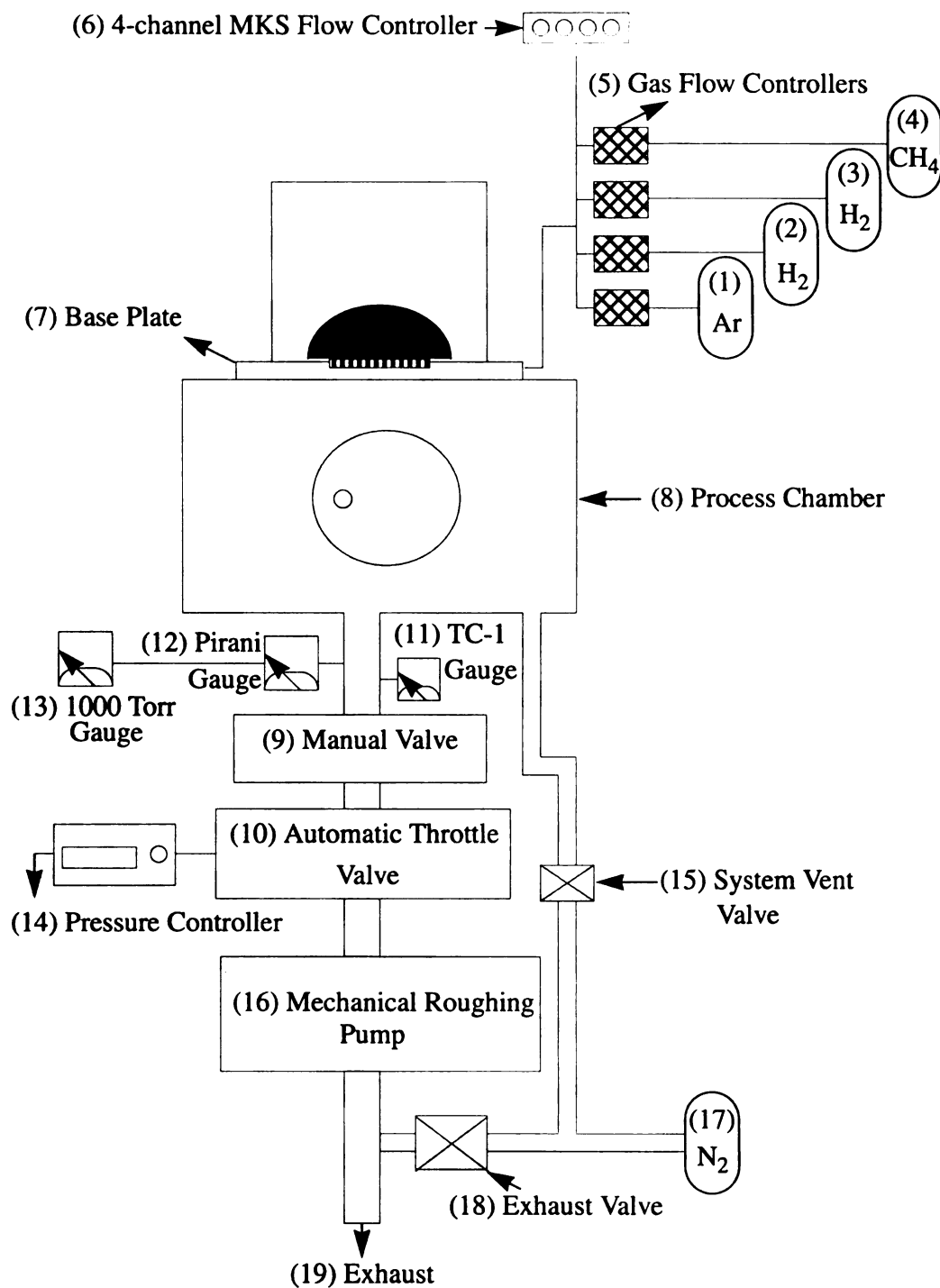


FIGURE 3.3 : VACUUM PUMP AND THE GAS FLOW CONTROLLER SYSTEM  
FOR MSU-MPACVD REACTOR I

### 3.2.2.2 MSU-MPACVD System II

Figure 3.4 displays a schematic drawing of the vacuum pump and gas flow control systems for MSU-MPACVD reactor II. The source gases consist of N<sub>2</sub> impurity pre-mixed tanks, N<sub>2</sub>-H<sub>2</sub> 1% (1), N<sub>2</sub>-H<sub>2</sub> 2% (2), N<sub>2</sub>-Ar 5% (3), Ar (4), H<sub>2</sub> (5), CH<sub>4</sub> (6), and He (7) with a respective purity of 99.995%, 99.995%, 99.995%, 99.999%, 99.9995%, 99.99%, and 99.995%. The gas flow control is monitored by six MKS type 1179 mass flow controllers (8) along with a 8-channel MKS type 247C flow controller (9). The system operator sets the flow rates of source gases and the values are displayed on this 8-channel MKS flow controller. A process gas flow valve (labeled as gas on the panel) (10) is installed to have manual control on when the input gases are following into the reactor and isolates the gas lines from the main chamber. The source gases with desired flow rates are mixed before they enter the baseplate (11). A mechanical roughing pump (24) is used to pump down the chamber pressure to the low pressure required for the ALCATEL PTM 5150 turbo molecular pump (15) to work efficiently, and to remove gases from the outlet of the turbo pump. A turbo isolation valve (23) is connected between the turbo pump and the mechanic roughing pump to protect the turbo pump. It's only open when the system pressure is below 10<sup>-3</sup> Torr. A SensaVac 919 hot cathode ion gauge (13) is used to measure the pressure of this high vacuum system. A PPT Quadrupole RGA (Residual Gas Analyzer) (14) is available to determine the gas composition of the remaining gases at low pressure, i.e. 10<sup>-7</sup> ~ 10<sup>-6</sup>Torr, before starting an experiment. An automatic throttle valve (20) adjusts the pressure of the process chamber (12) to the value set by the system operator in the MKS 651C pressure controller (21). A roughing valve (labeled as process on the panel) (22) is installed between the automatic throttle valve and the mechanic roughing pump.



70-  
71-  
72-  
73-  
74-  
75-  
76-  
77-  
78-  
79-  
80-  
81-  
82-  
83-  
84-  
85-  
86-  
87-  
88-  
89-  
90-  
91-  
92-  
93-  
94-  
95-  
96-  
97-  
98-  
99-  
100-

Three temperature controlled Baratron gauges with capacitance manometer technology: 10 Torr gauge (17), 100 Torr gauge (18), and 1000 Torr gauge (19) are installed to function at different pressure regimes. There are two isolation valves (16). One is connected between process chamber and the 10-Torr head and it closes when the pressure is greater than 9.5 Torr to protect the 10-Torr head. The other one is located between process chamber and the 100-Torr head and it closes when the pressure is greater than 99.5 Torr to protect the 100-Torr head. Either nitrogen (26) or Ar with 99.999% purity (27) is released through the system vent valve (25) when raising the chamber pressure to the atmospheric pressure. Nitrogen gas (29) is used to dilute the exhaust gases (30) through a 5000 sccm gas flow controller (28) with a  $N_2$  flow rate equal to 2000 sccm. The mixing of nitrogen into the exhaust gases ensures that the exhaust gases are not in a flammable condition.

Compared to MSU-MPACVD system I, the vacuum pump and gas flow control systems of MSU-MPACVD system II are greatly improved, providing a better high purity controlled environment for deposition experiments. (System I has a leak rate of 12.6 mTorr/hr, which yields a purity of 99.987%. System II has a leak rate of 4 mTorr/hr, which yields a purity of 99.995%.) The low-pressure-pump-down capability of system II ensures that there is a low leak rate before each experiment. In addition, it removes the impurities that come off the chamber walls at very low pressures. The use of argon as a vent gas in system II also reduces  $N_2$  impurities in the system and the low leak rate of system II ensures negligible introduction of impurities from the atmosphere. In system II, the source gases have higher purity to minimize the introduction of impurities, such as nitrogen, oxygen, etc., into the system. The high vacuum capability of system II lowers the combined

N<sub>2</sub> impurities from the input gases to 5-8 ppm level, as compared to system I where N<sub>2</sub> impurities are 30-50 ppm (Nitrogen-impurity determination was measured by optical emission spectroscopy technique and was performed by Dr. Mossbrucker.) The influence of nitrogen on the growth, morphology, and crystalline quality of MPACVD diamond films has been studied by Asmussen et al. [Asmu 1998]. It was found nitrogen impurities as low as 20 ppm could affect the morphology and quality of the films. With limited impurities in the system II and the precise gas flow controllers, the operator can (if desired) carefully control the nitrogen impurities and then can investigate the influence of nitrogen impurities on film deposition quality and properties.

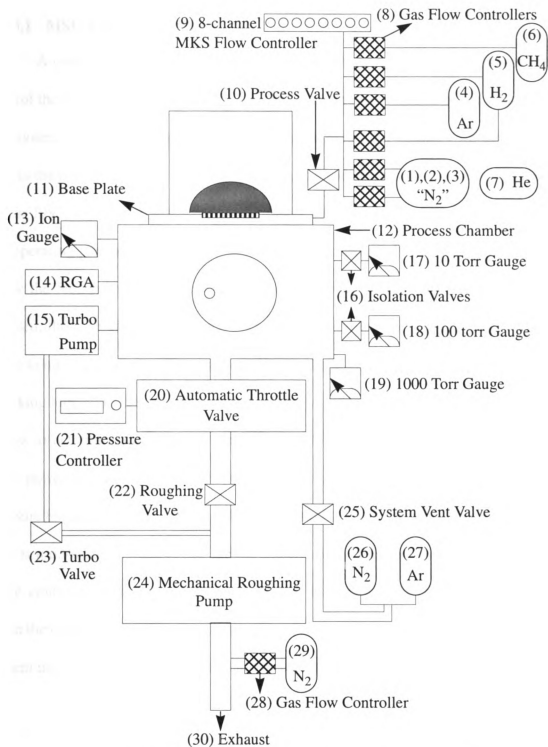


FIGURE 3.4 : VACUUM PUMP AND THE GAS FLOW CONTROLLER SYSTEM FOR MSU-MPCVD REACTOR II

### **3.2.3 Computer Control System**

#### **3.2.3.1 MSU-MPACVD System I**

A computer is used to monitor and regulate system I operating conditions and to control the experimental running time and shut down procedures. The preset running time and system operating pressure along with the reflected power readings are the input signals to the computer. Figure 3.5 shows the flow chart of the computer monitoring program [Zhan 1993]. As shown, the experimental running time, reflected power upper limit, and the operating pressure threshold are first set. The experimental system is then enabled to allow the feed gases to flow and the microwave power to turn on. After the system is enabled, the automatic throttle valve operates in a remote mode controlled by the computer control system to adjust the pressure of the chamber. During the experiment, a checking loop compares the pressure, reflected microwave power, and time with the preset values to determine the state of the experiment. An emergency shut down of the microwave power and feed gas is performed if the reflected microwave power, and/or operating pressure exceed the preset values, and/or power supply is shut down, and/or cooling water flow is too low at any time during the experiment. In an emergency, the automatic throttle valve controls the pressure of the system with the preset value. At normal conditions, when the experiment is complete (i.e., the timer expires), the computer program directs the system into a normal shut-down sequence (see Section 3.3.2.1) when the timer expires.

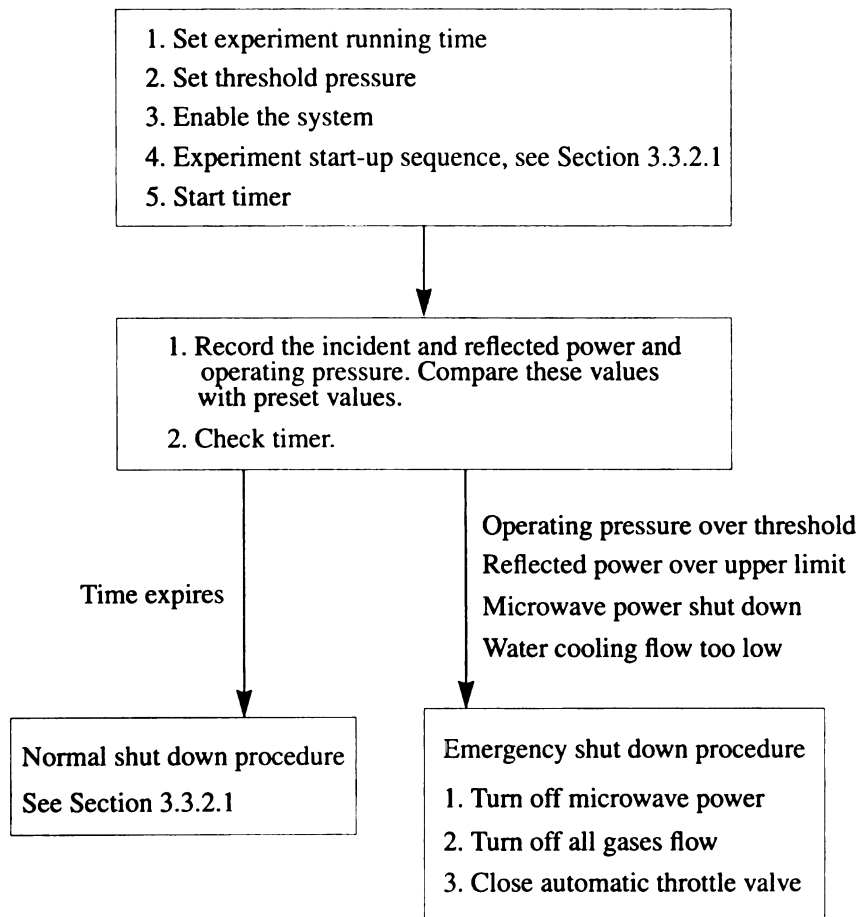


FIGURE 3.5 : COMPUTER CONTROL SYSTEM FOR MSU-MPACVD REACTOR I

### 3.2.3.2 MSU-MPACVD System II

System II is also equipped with a computer to monitor and regulate the system operating conditions and to control the experimental running time and shut down procedure of the experiments. The preset system operating pressure and input microwave power along with running time are the input signals to the computer. Figure 3.5 shows the flow chart of the computer monitoring program written by Michael J. Ulczynski. As shown, the operating pressure, input microwave power, and the experimental running time are first set in the computer monitoring program. The experimental system is then enabled to allow the feed gases to flow and the microwave power to turn on. After the system is enabled, the automatic throttle valve operates in a remote mode controlled by the program to adjust the pressure of the chamber. During the experiment, a checking loop compares the pressure, incident microwave power, and time with the preset values to determine the state of the experiment. An emergency shut down of the microwave power and feed gas is performed if the reflected microwave power is more than 25% of incident microwave power value, and/or operating pressure exceeds  $\pm 5$  Torr of the preset values at any time during the experiment. In an emergency, the automatic throttle valve controls the pressure of the system with the preset value. It closes if the chamber pressure drops below 10 Torr of preset value. It opens if there is a leak in the system and the gases are pushed into the system from atmosphere. At normal conditions, when the experiment is complete (i.e., the timer expires), the computer program directs the system into a normal shut-down sequence (see Section 3.3.2.2) when the timer expires.

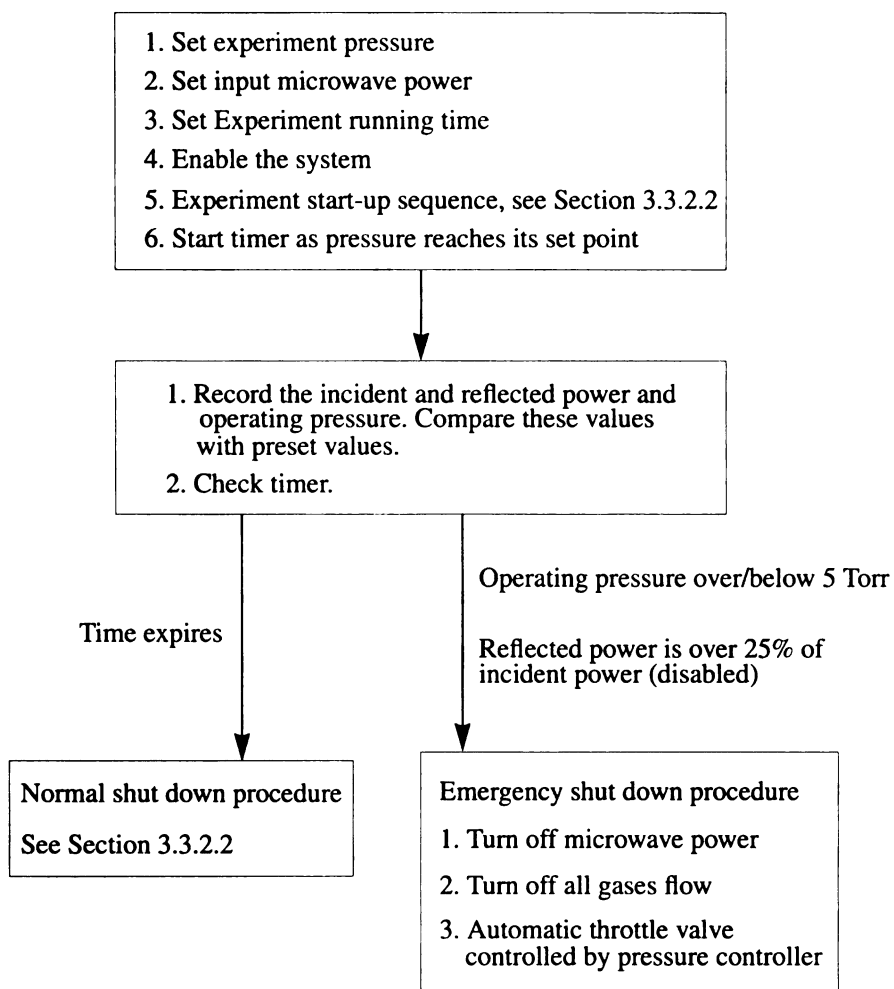


FIGURE 3.6 : COMPUTER CONTROL SYSTEM FOR MSU-MPACVD REACTOR II



### 3.2.4 Reactor Geometry

#### 3.2.4.1 Microwave Cavity Plasma Reactor

Figure 3.7 shows a cross sectional drawing of the microwave cavity plasma reactor configuration. As shown, the cavity applicator side wall (1) is made of a 17.78 cm inside diameter cylindrical brass tube. This brass tube which forms the conducting shell of the cavity applicator is electrically shorted to a water-cooled baseplate assembly (2 - 4) and a water cooled (21) sliding short (8) via a finger stock (9). Thus the cylindrical volume bounded by the sliding short, the cavity applicator side wall and the baseplate forms the cylindrical cavity applicator electromagnetic excitation region. With a fixed excitation frequency and cavity radius, a cavity length was determined by J. Zhang et. al. [Zhan 1994] to have  $TM_{013}$  mode for exciting a ellipsoid-like discharge (12) in good contact with the substrate (7). The  $TM_{013}$  mode was used so that the probe was located far enough away from the discharges to eliminate the near field effect caused by coaxial excitation probe (11). 2.45 GHz (CW) microwave power is coupled into the cylindrical cavity applicator through a mechanically tunable coaxial excitation probe which is inside a coaxial waveguide (10) and is located in the center of the sliding short. The sliding short controls the applicator height,  $L_s$  and the excitation probe controls the depth of the coaxial excitation probe,  $L_p$ . Both  $L_s$  and  $L_p$  can be moved up and down along the longitudinal axis of the applicator cavity wall and can be adjusted independently to excite the desired electromagnetic mode and optimally match the resonance. The applicator height  $L_s$  is adjusted approximately to 21.7 cm and the probe depth,  $L_p$  is about 3.2 cm [Zhan 1993]. The baseplate assembly consists of a water-cooled (22) and air-cooled (19) baseplate (2), an annular input gas feed plate (3), and a gas distribution plate (4). A 12.5cm inside diameter

quartz dome (5) is sealed by O-ring (20) in contact with baseplate assembly. The thermally floating substrate holder setup assembly includes a flow pattern regulator (15), a metal tube (16), a quartz tube with I.D.=95 mm, O.D.=100 mm, and height=50 mm, (17), and a holder-baseplate (6). The premixed input gases are fed into the gas inlet (23) in the baseplate assembly. The substrate (7) is placed on top of a molybdenum substrate holder (15), also called a flow pattern regulator, which is supported by a quartz tube (17). Quartz tubes of different heights may be used to change the position of the substrate with respect to the plasma to optimize the film deposition. A metal tube (16) which serves as an electromagnetic field resonance breaker is placed inside the quartz tube. The metal tube prevents the plasma discharge from forming underneath the substrate by reducing the electric field underneath the substrate. The metal tube (16) and quartz tube (17) are placed on a substrate holder-baseplate (6) which has 3 cm diameter hole at its center to pass the hot gases from within the quartz dome (5) to the exhaust roughing pump. The baseplate, the annular input gas feed plate, and the gas distribution plate introduce an uniform ring of input gases into the quartz dome where the electromagnetic fields produce a microwave discharge. The plasma consists of a mixture of neutral gases, electrons, and ions, i.e. dissociated species. A screened view window (13) is cut into the cavity wall for viewing the discharge. By focusing an optical pyrometer onto the substrate through the view window, the substrate temperature can be determined. A air blower with 60 CFM (cubic foot per minute) blows the cooling air stream into the air blower.inlet (14), onto the quartz dome (5) and cavity side wall (1), and then finally flows out of the cavity through the screened window (13) and optical access ports(19) in the baseplate (2). The air blower existing inside the Cober microwave power supply adds another air cooling stream into the microwave cavity

100

101

102

103

104

105

106

107

108

109

110

111

112

113

114

115

116

117

118

119

120

121

122

123

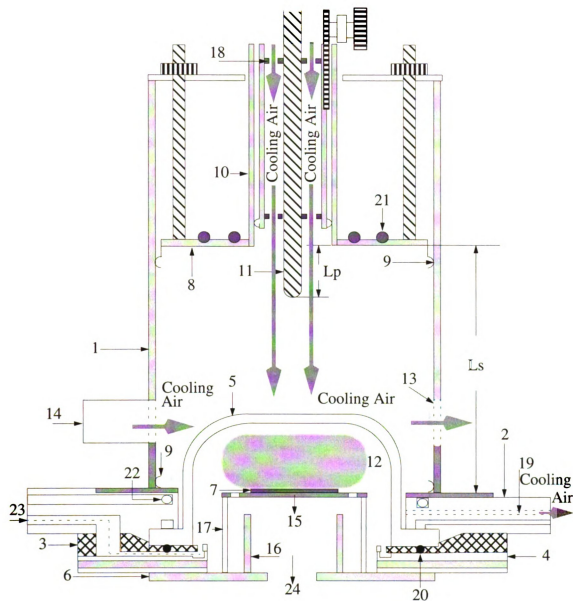
124

plasma reactor. Two Teflon pieces (18) were drilled with four of 1/8" diameter holes. This allows the cooling air from the air blower in the microwave power supply to flow through the coaxial waveguide, onto quartz dome and cavity side walls, and then flows out of the air blower outlet and the optical access ports. On the system I, one fan is used to cool the cavity applicator side wall. On system II, two fans are used to cool the cavity applicator side wall and the air cooling provided by the fans also extends the lifetime of the quartz dome. The microwave cavity plasma reactor is mounted on a process chamber with the chamber outlet leading to vacuum pumps. On system II, water cooling: (21) and (22) is replaced by a chiller which controls the temperature of the input coolant liquid. The coolant temperature can be set by the system operator.

The thermally floating substrate holder setup utilizes a flow pattern regulator for the molybdenum substrate holder (I.D.=3.03125" and O.D.=4.03125") as shown in Fig. 3.9. The flow pattern regulator is a plate with a series of holes arranged in a circle right inside the big circumference. The gas flow coming out the gas inlet, into the quartz dome, is directed by the flow pattern regulator as it flows through the plasma. The configuration is designed to increase the uniformity of the film deposition by changing the flow pattern in the plasma discharge and influencing the shape of the plasma discharge [Zhan 1993].

The top-side substrate temperature measurement was carried out by focusing the pyrometer onto the substrate through the screen view window for system I. Strong argon emissions interfere with top-side substrate temperature measurements using the pyrometer positioned to look through the plasma discharge. A silicon wafer back-side substrate temperature measurement was made in system II by aiming the pyrometer at the back side of

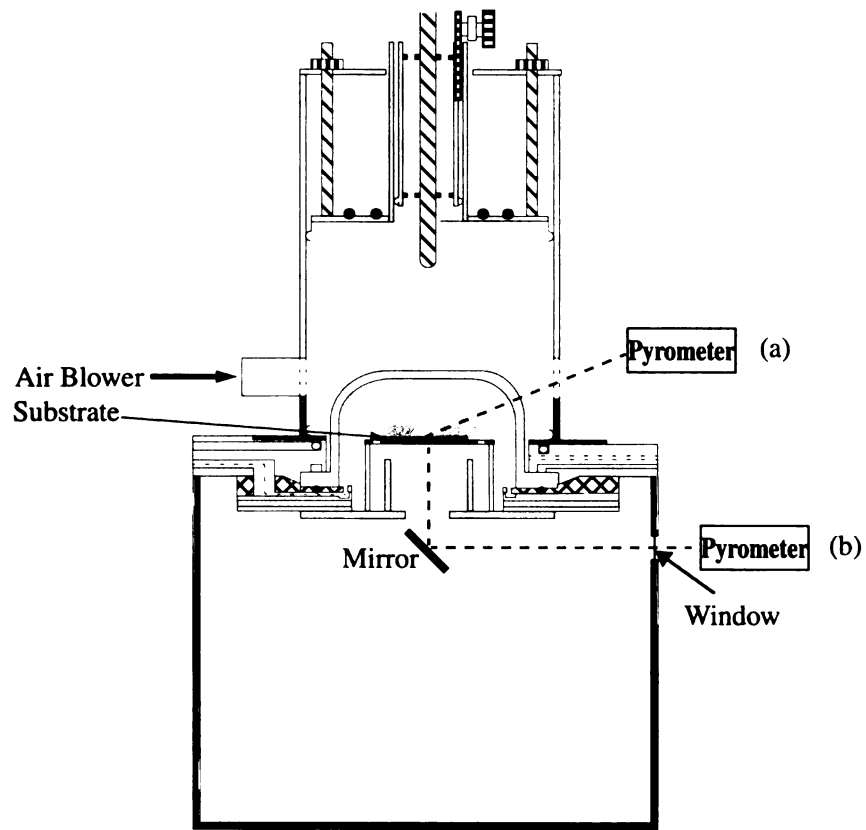
the wafer image that was reflected off the mirror for system II. In system II, the holder-baseplate has a 1" diameter hole cut in the center to allow the optical access to the backside of the wafer. The pyrometer detects 1  $\mu\text{m}$  (near IR) wavelength light. Since the mirror is not a perfect reflector, the bottom temperature measurement may be somewhat low. Also, there is a slight reflection loss at the window. However, these effects probably not significant because blackbody radiation is proportional to  $T^4$ . Figure 3.8 displays how the substrate temperature was measured for systems I and II.



#### Legend

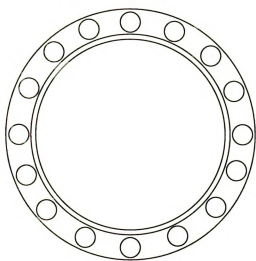
- |                             |                            |                          |
|-----------------------------|----------------------------|--------------------------|
| (1) Cavity Side Wall        | (2) Baseplate              | (3) Annular Plate        |
| (4) Distribution Plate      | (5) Quartz Dome            | (6) Holder-baseplate     |
| (7) Substrate               | (8) Sliding Short          | (9) Finger Stock         |
| (10) Coaxial Waveguide      | (11) Excitation Probe      | (12) Plasma discharge    |
| (13) View Window (grid)     | (13) Air Blower Outlet     | (14) Air Blower Inlet    |
| (15) Flow Pattern Regulator | (15) Substrate Holder      | (16) Metal Tube          |
| (17) Quartz Tube            | (18) Teflon Pieces         | (19) Optical Access Port |
| (20) Seal O-ring            | (21) Cooling Sliding Short | (22) Cooling Baseplate   |
| (23) Gas Inlet              | (24) Gas Outlet            |                          |

FIGURE 3.7 : THE CROSS SECTIONAL VIEW OF THE MCPR



**FIGURE 3.8 : SUBSTRATE TEMPERATURE MEASUREMENT METHOD**

- (a) Top side substrate temperature measurement through view window for system I.
- (b) Back side substrate temperature measurement by the mirror reflection for system II.



Top view of the substrate holder (flow pattern regulator) [Zhan 1993].

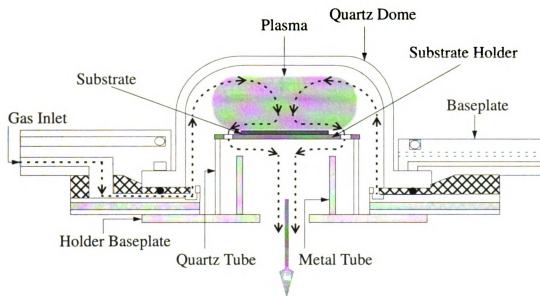
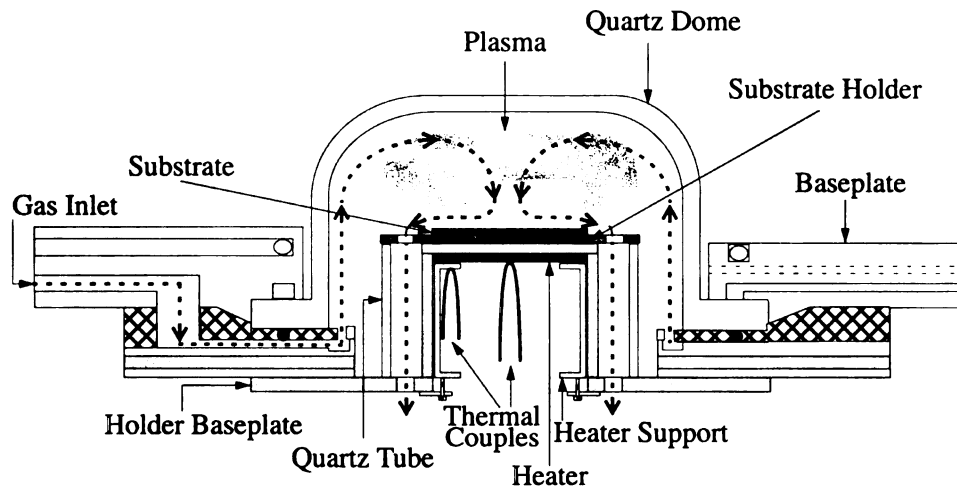


FIGURE 3.9 : THERMALLY FLOATING SUBSTRATE HOLDER SET UP  
Optimized substrate holder design that achieves deposition uniformity.



### 3.2.4.2 Substrate Heating Stage

Unlike conventional  $\text{H}_2/\text{CH}_4$  CVD diamond growth, ultra-nanocrystalline diamond is not grown in a hydrogen rich environment. A noble gas, Ar is the dominant input gas. Argon changes the plasma chemistry, including the gas temperature and thus has an impact on substrate temperature. Gas temperatures and the power densities are lower in the “hydrogen poor” carbon containing argon plasmas than in the more conventional  $\text{H}_2/\text{CH}_4$  discharge. In order to increase the deposition rate and provide independent control of the substrate temperatures, a substrate heating stage may be desirable. Figure 3.10 shows the cross sectional view of the substrate heating stage that was developed for ultra-nanocrystalline diamond film deposition.



**FIGURE 3.10 : SUBSTRATE HEATING STAGE SET UP**  
Substrate heater stage design for independent temperature control.

Revised

part of

part of

part of

part of

part of

part of

part of

part of

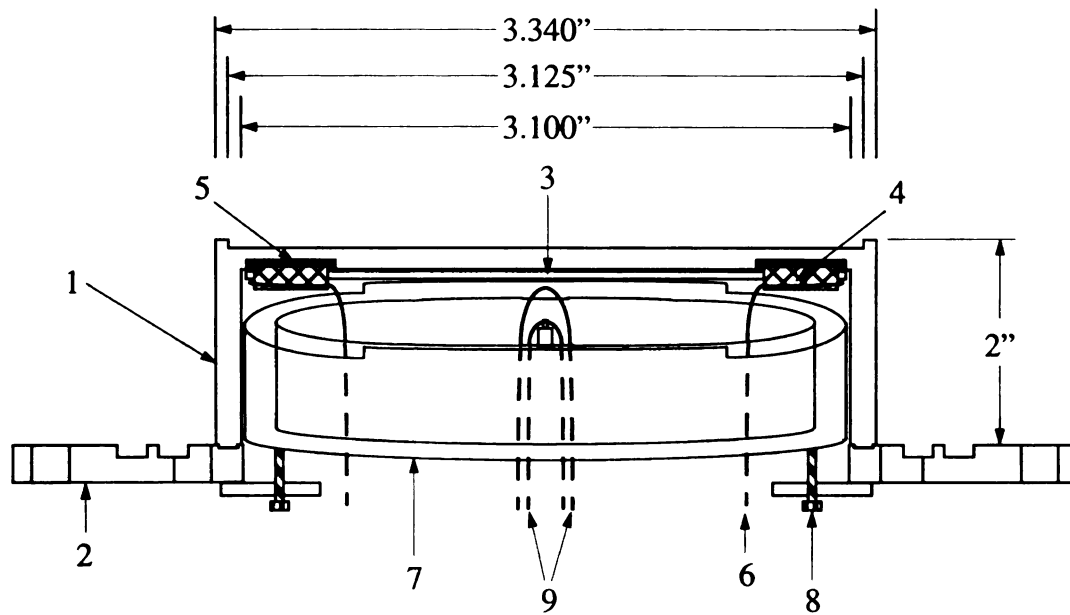
part of

part of

part of

part of

Figure 3.11 illuminates the construction of the prototype substrate heating stage. The substrate heating stage consists of a can body (1), which is machined out of a solid piece of stainless steel, and a bottom plate (2). These two parts were welded together to prevent the plasma discharge from forming beneath the substrate. A Boralectric PBN/PG (Pyrolytic Boron Nitride/Pyrolytic Graphite) type HT-63, diagonal pattern heater (3) is placed inside the top part of the can body as shown in Fig. 3.11. A pair of ceramic hats served as insulators (5) to prevent the electrical connectors (4) from being electrically shorted by the can body. The electrical connector consists of a molybdenum threaded rod, tantalum nuts, tantalum washers, and a graphite washer for good electrical contact in the hazardous environment. A pair of molybdenum wires are used as the heater wire (6). These wires are connected via vacuum feedthrough to a DC power supply located outside the vacuum chamber. A heater support (7) and 4 height adjusters (8) are designed to adjust the heater longitudinal position. Two K-type thermal couples (9), insulated by ceramic beads, are used to measure the temperature. One is located at the center of the heater. The other one is located at the edge.



#### Legend

- |                          |                     |                     |
|--------------------------|---------------------|---------------------|
| (1) Can Body             | (2) Bottom Plate    | (3) Heater          |
| (4) Electrical Connector | (5) Insulator       | (6) Heater Wire     |
| (7) Heater Support       | (8) Height Adjuster | (9) Thermal Couples |

FIGURE 3.11 : THE SUBSTRATE HEATING STAGE

### 3.2.5 Microwave Cavity Plasma Reactor General Operating Field Map for Ultra-nanocrystalline Diamond Synthesis

The experimental measurements of the general operating field map for ultra-nanocrystalline diamond synthesis was carried out with the microwave cavity plasma reactor operating under the thermally floating substrate holder set up that was utilized throughout this thesis. Under the thermally floating substrate holder set up, the deposition pressure,  $p$ , the microwave power,  $P_{\text{abs}}$ , and the substrate temperature,  $T_s$ , are interrelated and interdependent. Figure 3.12 displays the repeatable experimental non-linear relationships between these variables. As shown, with fixed Ar/H<sub>2</sub>/CH<sub>4</sub> gas chemistry, the substrate temperature,  $T_s$ , and the discharge volume,  $V_d$ , are affected both by the deposition pressure,  $p$ , and the microwave power,  $P_{\text{abs}}$ . The substrate temperature,  $T_s$ , increases with either increases in the deposition pressure,  $p$ , and/or the microwave power,  $P_{\text{abs}}$ . For a fixed deposition pressure,  $p$ , the discharge volume,  $V_d$ , increases with increases in the microwave power,  $P_{\text{abs}}$ . For a fixed microwave power,  $P_{\text{abs}}$ , the discharge volume,  $V_d$ , decreases with increases in the deposition pressure,  $p$ . By the observation through the view window in the cavity wall, the lower absorbed microwave power limit is determined by the minimum power required to maintained a discharge volume  $(V_d)_{\text{min}}$  that covers a 3" diameter substrate. Below  $(V_d)_{\text{min}}$ , the discharge volume is too small to fully cover the 3" substrate surface, and also in higher deposition pressure region, an orange color starts to appear in the outer edge of the plasma, which is usually undesirable. Specially, with too small a plasma and above 220 Torr, the discharge becomes flashing. The upper limit of the microwave power is determined by the maximum power that can be used to generate a discharge volume  $(V_d)_{\text{max}}$  that is not too big to touch the quartz dome walls. The upper limit of the microwave power is the maximum microwave power that can be used to operate the

reactor safely for ultra-nanocrystalline diamond deposition without over heating the quartz dome. It is very critical for the higher pressure region. The measurements were performed using system II.

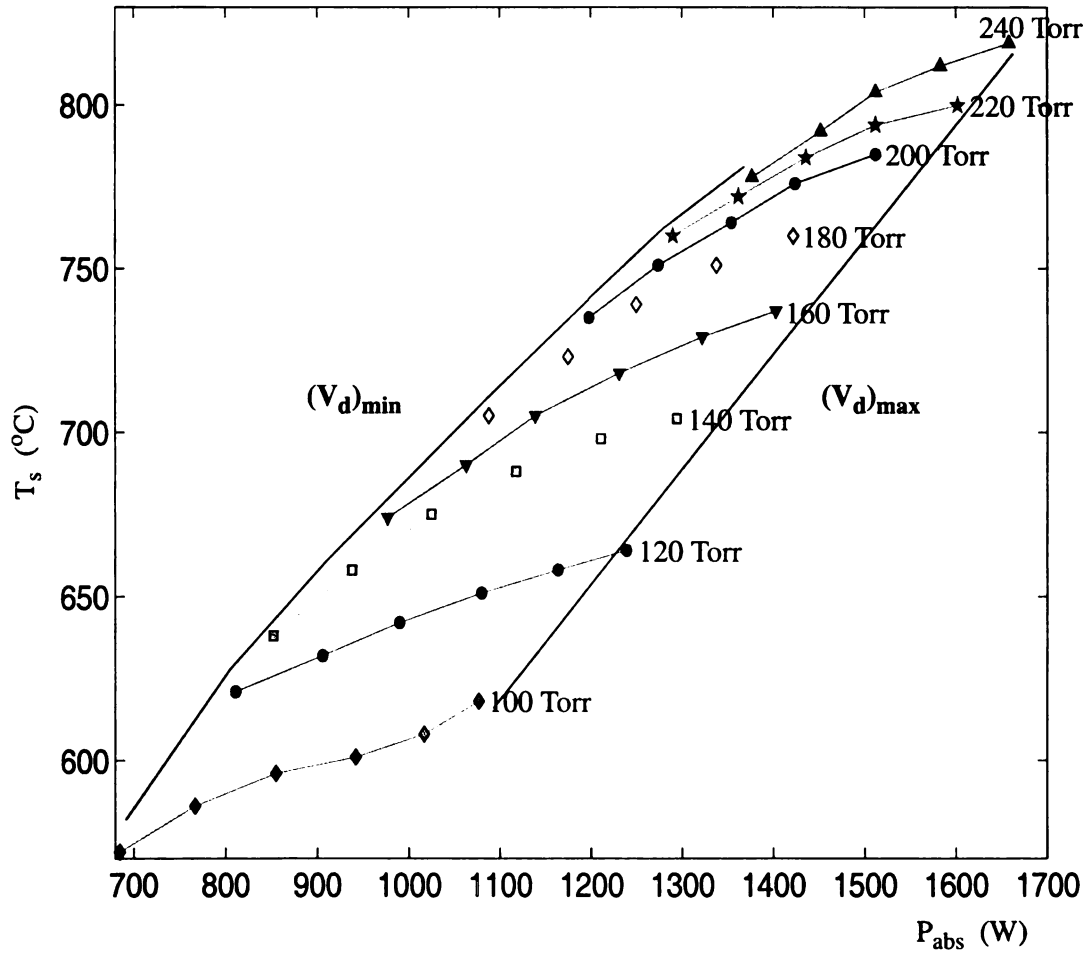


FIGURE 3.12 : THE MPACVD OPERATING FIELD MAP UNDER THERMALLY FLOATING SUBSTRATE HOLDER SET UP For 5" quartz dome and 3" substrate reactor geometry configuration. The gas chemistry is Ar/H<sub>2</sub>/CH<sub>4</sub>=100/4/1 sccm.

The influence of the total gas flow rate has also been studied. The results indicate that the total gas flow rates have no significant influence in  $P$ - $P_{\text{abs}}$ - $T_s$  relationship, as shown in Figure 3.13(a) and (b). In Figure 3.13(a), the substrate temperature,  $T_s$  increases as the pressure increases. The corresponding microwave power,  $P_{\text{abs}}$  is shown in Figure 3.13(b). The experimental results displayed in Figure 3.13 shows that the field map curves of Figure 3.12 vary as the gas chemistry changes. Thus, one needs a separate operating field map for each gas chemistry ratio.

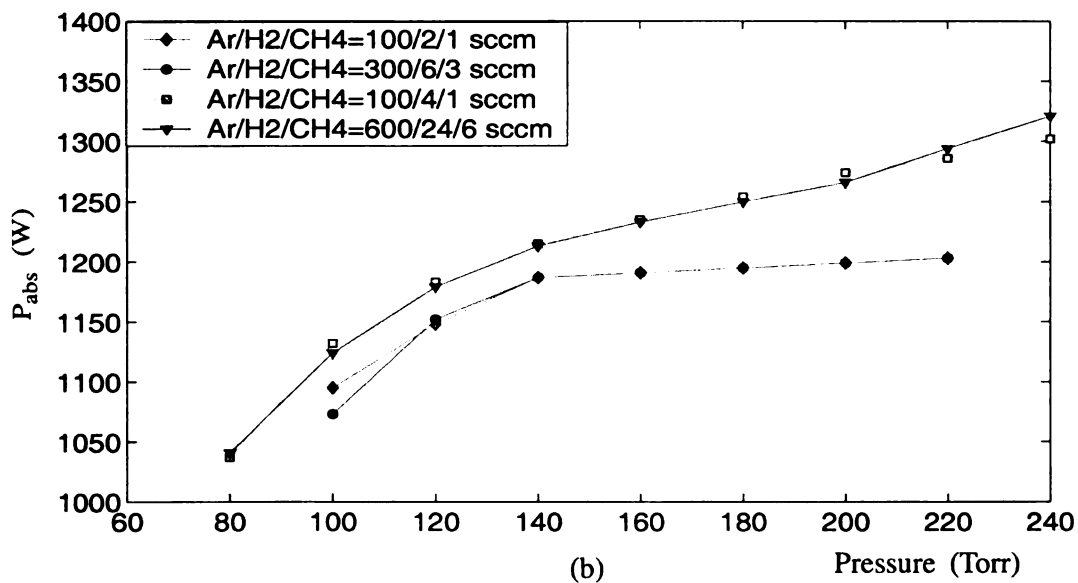
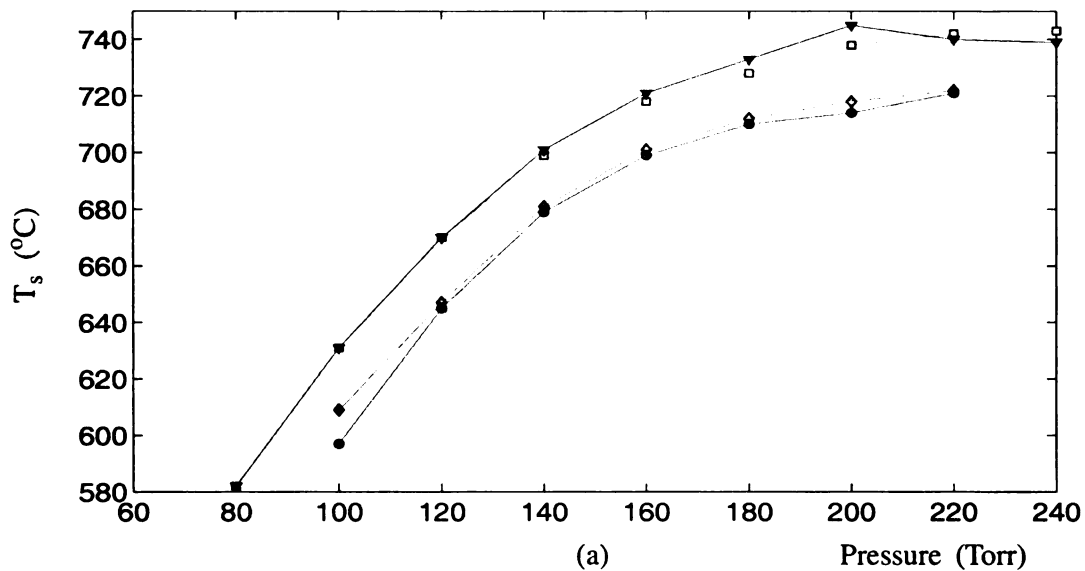


FIGURE 3.13 :  $P$ - $P_{abs}$ - $T_s$  RELATIONSHIP UNDER THERMALLY FLOATING SUBSTRATE HOLDER SET UP

For 5" quartz dome and 3" substrate reactor geometry configuration.

The gas chemistry ratios are Ar:H<sub>2</sub>:CH<sub>4</sub>=100:4:1 and 100:2:1.



## **3.3 Experimental Procedures**

### **3.3.1 Seeding Procedures**

Without wafer pre-treatment, CVD ultra-nanocrystalline diamond films could not be synthesized during 8-hour experimental runs. Therefore, a nucleation enhancement step was required for the deposition of CVD ultra-nanocrystalline diamond from gas phase onto non-diamond substrates, like mirror-polished silicon wafers. Two substrate seeding methods were investigated in this thesis. The comparison of photoresist seeding and scratch seeding is presented in Section 3.3.1.3.

#### **3.3.1.1 Photoresist Seeding**

The process for the photoresist seeding is as followed.

- 1) Put 310mg of Amplex 0.1 $\mu$ m sized natural diamond powder into a clean brown bottle.
- 2) Dehydrate diamond powder on a hot plate at 150°C for 2 hours with bottle open partly covered with aluminum foil to let the moisture vapor out.
- 3) Add 12 ml of type P Shipley photoresist thinner into the bottle.
- 4) Put a magnetic stirrer in the bottle.
- 5) Place the bottle on a stirring plate with setting at 4.5 for 15minutes.
- 6) Place the bottle in an ultrasonic bath for one hour.
- 7) Add 30 ml of Shipley 1813 photoresist into the bottle.
- 8) Stir the solution on a stirring plate with the setting at 4.5 for one hour.
- 9) Place the bottle in an ultrasonic bath for two hours.
- 10) Drop the diamond powder/photoresist solution on the substrate surface with full coverage. Spin the substrate at 2500 rpm for 30 seconds.
- 11) Bake the seeded substrate in an oven at 150°C for 15 minutes.
- 12) Check the substrate seeding result under the optical microscopy. If there are big diamond chunks, repeat step 8 and step 9 to break the big diamond chunks in the solution. Then continue to perform step 10 through 12.

Figure 3.14 shows the result of a photoresist seeding followed by the above steps. The picture was taken by a digital camera under an optical microscope. In the image, no chunks of diamond are found.

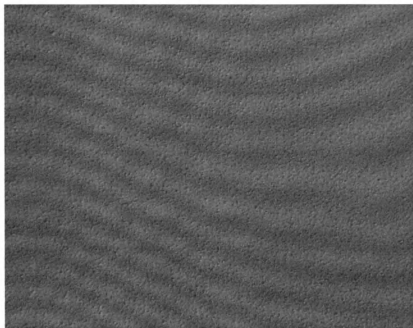


FIGURE 3.14 : PHOTORESIST SEEDING  
Image size: 13  $\mu\text{m}$  x 10  $\mu\text{m}$ .

### **3.3.1.2 Scratch Seeding**

The procedure for mechanical scratch seeding is as followed.

- 1) Place the substrate on the seeding stage.
- 2) Connect the seeding stage to a pump and turn on the power. The vacuum sucks the substrate and keeps the substrate from moving.
- 3) Sprinkle some quantity of Amplex 0.1  $\mu\text{m}$  sized natural diamond powder onto the surface of the substrate. If the humidity in the room is high, bake the diamond powder at 150°C for 2 hours before usage.
- 4) Use a finger wrapped in a Kim Wipe<sup>TM</sup> to polish the substrate with the combination of several different angles of straight line motion and several different diameters of circular motion. Make sure the substrate surface is scratched everywhere with a median force.
- 5) Put a piece of curved glass inside a container. Pick up the substrate from the seeding stage and put it in the container, on top of the curved glass, with the scratched surface facing down.
- 6) Fill the container with methanol to the liquid line above the substrate about 1 cm.
- 7) Put the container in an ultrasonic bath for 30 minutes for cleaning and agitation purpose.
- 8) Take the substrate out and put it in another container with the scratched surface facing up. Fill the container with enough acetone to cover the substrate.
- 9) Use Q-tip gently wipe the substrate surface to remove any dirt or diamond powder.
- 10) Put the substrate on a wafer holder.
- 11) Rinse the substrate with acetone and methanol for 2 minutes each step.
- 12) Rinse the substrate with de-ionized water for 15 minutes.
- 13) Blow dry with a clean room nitrogen gun.
- 14) Check the substrate surface cleanness under optical microscopy. If there is dirt or diamond powder left on the substrate surface, repeat step 8 to step 14.

Figure 3.15 shows the result of a mechanical scratch seeding followed by the above steps. The picture was taken by a digital camera under an optical microscope. In the image, there is no dirt or diamond powder residue but the different width and depth lines left on the scratched silicon wafer are clearly shown. The different width and depth of scratching lines were caused by different sized diamond particles and the applied scratching forces.

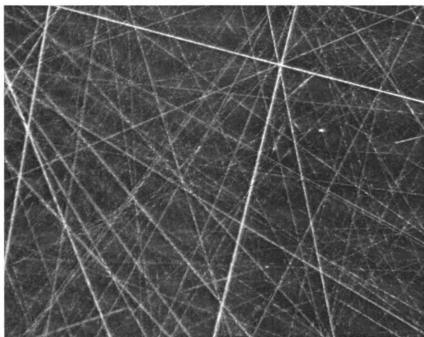


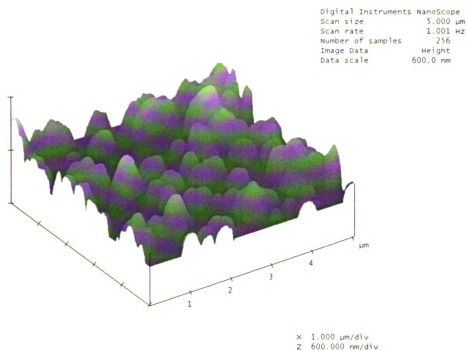
FIGURE 3.15 : SCRATCH SEEDING  
Image size: 13  $\mu\text{m}$  x 10  $\mu\text{m}$ .

### **3.3.1.3 Comparison of Photoresist Seeding and Scratch Seeding**

Two set of experiments were performed to compare the growth results of photoresist seeding and mechanical scratch seeding in this thesis research. The experiments were all done at 120 Torr with argon gas flow of 100 sccm, hydrogen gas flow of 4 sccm, and methane gas flow of 1 sccm, but the deposition times were varied.

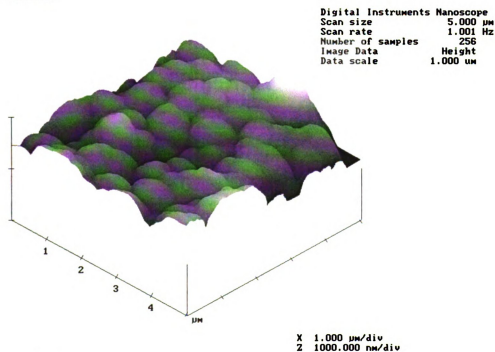
Figures 3.16 (a), (b), and (c) show the deposition results for photoresist seeding after 10 minutes, 1-hour, and 8-hour runs respectively. Under these conditions, the photoresist seeding usually (1) produced a non continuous film, (2) larger crystals were nucleated, (3) seeding results were more uniform and repeatable.

(a)



arn077.001

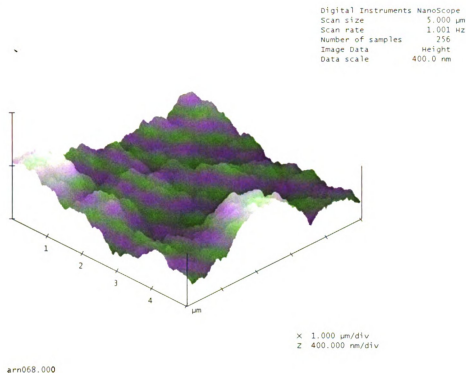
(b)



arn139.000

FIGURE 3.16 : PHOTORESIST SEEDING FILM MORPHOLOGY AND ROUGHNESS INSPECTED BY AFM

(c)



(a)

t=10 minutes

$T_s^{\text{top}}=700^\circ\text{C}$

$T_s^{\text{back}}=659^\circ\text{C}$

$P_{\text{abs}}=977\text{W}$

Ave. Growth Rate

$=0 \mu\text{m/hr}$

Img. RMS=112.78 nm

(b)

t=1 hrs

$T_s^{\text{top}}=700^\circ\text{C}$

$T_s^{\text{back}}=638^\circ\text{C}$

$P_{\text{abs}}=880\text{W}$

Ave. Growth Rate

$=0.239 \mu\text{m/hr}$

Img. RMS=134.86 nm

(c)

t=8 hrs

$T_s^{\text{top}}=660^\circ\text{C}$

$T_s^{\text{back}}=692^\circ\text{C}$

$P_{\text{abs}}=977\text{W}$

Ave. Growth Rate

$=0.488 \mu\text{m/hr}$

Img. RMS=81.748 nm

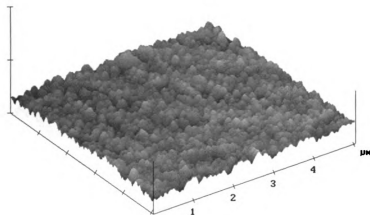
FIGURE 3.16 (cont'd)



Figure 3.17 (a), (b), and (c) show the deposition results for scratching seeding after 10 minutes, 1-hour, and 8-hour runs respectively. The scratch seeding method (1) produced a continuous film, (2) smaller crystals were nucleated, (3) higher nucleation density occurred due to higher seeding density, (4) some big crystals developed at deep scratches, (5) lower RMS surface roughness was achieved.

(a)

Digital Instruments Nanoscope  
Scan size 5.000  $\mu\text{m}$   
Scan rate 1.001 Hz  
Number of samples 256  
Image Data Height  
Data scale 400.0 nm

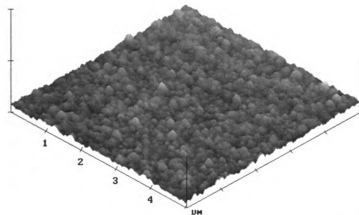


X 1.000  $\mu\text{m}/\text{div}$   
Z 400.000 nm/div

arn092.000

(b)

Digital Instruments Nanoscope  
Scan size 5.000  $\mu\text{m}$   
Scan rate 1.001 Hz  
Number of samples 256  
Image Data Height  
Data scale 500.0 nm



X 1.000  $\mu\text{m}/\text{div}$   
Z 500.000 nm/div

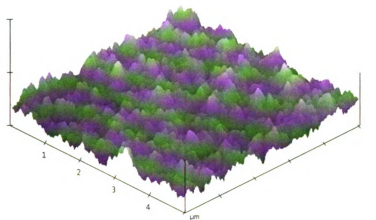
arn143.000

FIGURE 3.17 : SCRATCH SEEDING FILM MORPHOLOGY AND ROUGHNESS  
INSPECTED BY AFM



(c)

Digital Instruments NanoScope  
Scan size 5.000  $\mu\text{m}$   
Scan rate 1.001 Hz  
Number of samples 256  
Image Data Height  
Data scale 300.0 nm



X 1.000  $\mu\text{m}/\text{div}$   
Z 300.000 nm/div

arn076.000

(a)

$t=10$  minutes

$T_s^{\text{top}}=720^\circ\text{C}$

$T_s^{\text{back}}=664^\circ\text{C}$

$P_{\text{abs}}=898\text{W}$

Ave. Growth Rate

$=0 \mu\text{m/hr}$

Img. RMS=17.827 nm

(b)

$t=1$  hrs

$T_s^{\text{top}}=715^\circ\text{C}$

$T_s^{\text{back}}=630^\circ\text{C}$

$P_{\text{abs}}=886\text{W}$

Ave. Growth Rate

$=0.295 \mu\text{m/hr}$

Img. RMS=13.086 nm

(c)

$t=8$  hrs

$T_s^{\text{top}}=695^\circ\text{C}$

$T_s^{\text{back}}=666^\circ\text{C}$

$P_{\text{abs}}=981\text{W}$

Ave. Growth Rate

$=0.347 \mu\text{m/hr}$

Img. RMS=23.860 nm

FIGURE 3.17 (cont'd)

When there is a higher nucleation density, competition between neighboring grains prevents individual grains from growing at the speed of film growth rate. So, at the same thickness, a higher nucleation rate results in smoother films [Wild 1991]. Therefore, for thin films, the influence of seeding is very important. It may not be as important for thicker films. From Fig. 3.16 and Fig. 3.17, the results clearly show the seeding procedure plays an important role on thin film growth and its influence on thick films is less observable.

Because the mechanical scratch seeding (R.M.S. surface roughness ranges from 13 to 24 nm) produces better film quality than photoresist seeding (R.M.S. surface roughness ranges from 82 to 135 nm), the scratch seeding method was chosen to be utilized throughout this thesis.

### **3.3.2 Start-up and Shut-down Procedures**

#### **3.3.2.1 System I**

After loading the sample, the system is pumped down to approximately 10mTorr. Now, one can start the experiment.

- Turn on the water to microwave power supply.
- Turn on the microwave power supply. The power level control knob should be zero.
- Turn on the nitrogen purge to the pump.
- Turn on the water for MPCR water cooling system.

- Set the experimental running time and threshold pressure in the plasma software. Set the gas flow rates on the MKS type 247C flow controller.
- Set the experimental pressure on the pressure controller of the throttle valve.
- Adjust the cavity length to 21.7 cm by moving the sliding short position and set the probe depth at  $L_p=3.2$  cm.
- Set the throttle valve at auto position and enable the system to let the input gases come in.
- Enable the microwave power supply when the system pressure reaches 5~10 Torr.
- Turn on the cooling fans.
- Slowly increase the input microwave power as pressure increases so that the ellipsoid-like discharge covers the entire substrate surface.
- Fine tune the cavity length,  $L_s$  and  $L_p$  to obtain the maximum absorption power.
- The experiment starts to run on its own under time control when the system pressure reaches the valued set in the plasma software.

When the experiment is completed, the system will perform the automatic shut down procedure as follows.

- Shut off the  $H_2$  and  $CH_4$  mass flow controllers.
- 3 minutes self-cleaning process with argon plasma.

- Turn off microwave power.
- Turn off the water to microwave power supply when the system is cooled.
- Turn off the argon mass flow controller.
- The automatic throttle valve will open to evacuate the chamber.

### **3.3.2.2 System II**

After loading the sample, the system is pumped down to less than mTorr range. Close the roughing valve and open the turbo isolation valve. Turn on the turbo molecular pump. Let the system pump for a few hours until the base pressure is about  $1\sim 2 \times 10^{-6}$  Torr. When the system reaches high vacuum status, turn off the turbo molecular pump and close the turbo isolation valve. Now, the experimental run is initiated by the follow steps.

- Turn on the water to microwave power supply.
- Turn on the microwave power supply. The power level control knob should be zero.
- Turn on the nitrogen purge to the pump.
- Turn on the Neslab chiller and set the temperature at 15°C.
- Set the experimental running time, input microwave power, pressure, and gas flows (During the start-up procedure, set the gas flows six times higher than the planned gas flows. Keep the same gas chemistry ratio and remember to set the value back to the desired gas flows.) for each channel in the plasma software.
- Set the experimental pressure on the pressure controller of the throttle valve.

- Adjust the cavity length to 21.7 cm by moving the sliding short position and set the probe depth at  $L_p=3.2$  cm.
- Open the process valve and turn on the mass flow controllers to let the input gases flow in. (Optional, flushing the chamber with Argon gas. So far, there is no quantitatively evidence that it changes the ultra-nanocrystalline diamond deposition result.)
- Open the roughing valve. Now the chamber pressure is controlled by the automatic throttle valve.
- Enable the microwave power supply when the system pressure reaches 10 Torr.
- Turn on the cooling fans.
- Slowly increase the input microwave power as pressure increases so that the ellipsoid-like discharge covers the entire substrate surface.
- Fine tune the cavity length,  $L_s$  and  $L_p$  to obtain the minimum reflected power.
- The experiment starts to run on its own under time control when the system pressure reaches the valued set in the pressure controller.

When the experiment is completed, the system will perform the shut down procedure as followed.

- No self-cleaning process.
- Turn off microwave power.
- Turn off the water to microwave power supply when the system is cooled.



- Turn off all the mass flow controllers.
- The automatic throttle valve will close at 10 torr below set point. If there is a leak in the system and the atmospheric air is forced into the system, the throttle will reopen at the set point pressure to let the system pressure remain at the set point, below atmosphere.

### **3.4 Experimental Parameter Space**

The performance of the microwave plasma reactor is closely related to the input, internal, and output variables (Fig. 3.18). The input variables include the controllable input variables ( $U_1$ ), reactor design variables ( $U_2$ ), and deposition process variables ( $U_3$ ). As the input parameters ( $U$ ) vary, internal variables ( $X$ ) also change. The output variables which can be subdivided into reactor performance variables ( $Y_1$ ) and film characteristics variables ( $Y_2$ ) are the outcome of input and internal variables.

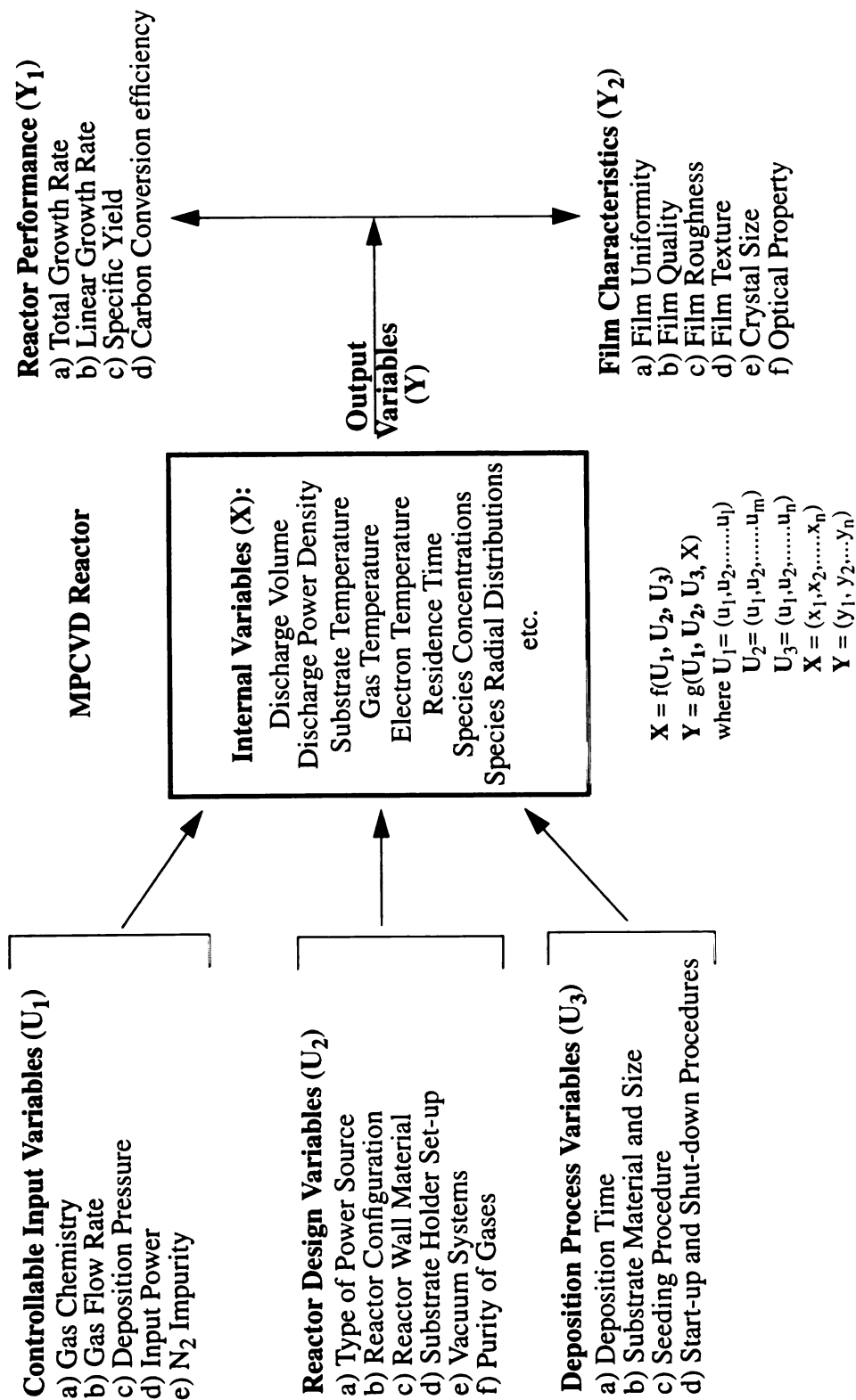


FIGURE 3.18 : RELATIONSHIP BETWEEN INPUT, INTERNAL, AND OUTPUT PARAMETERS IN A GENERIC MPCVD-SYSTEM.

Because of the complex relations between the large number of experimental variables, some of the variables are fixed to limit the experimental parameter space. Various operating conditions including pressure, gas chemistry, temperature, powers, and flow rate will be investigated and mapped to the attributes of film quality, film uniformity, and film growth rate (determined by weight gain). The relationships between macroscopically controllable input variables ( $U_1$ ), reactor design variables ( $U_2$ ), deposition process variables ( $U_3$ ), vs. internal variables ( $X$ ), and output variables ( $Y$ ) are investigated in this thesis. Table 3.1 and 3.2 specify the experimental variables chosen for systems I and II in this thesis research.

**TABLE 3.1: PARAMETER SPACE FOR EXPERIMENTS PERFORMED AT SYSTEM I**

	Controllable Input Variables $U_1$	a) Gas Chemistry, Ar/H <sub>2</sub> /CH <sub>4</sub> =99-91/1-7/0-2 (%) b) Total Gas Flow Rate, Ar=102.5-642 sccm c) Deposition Pressure, p=120-160 Torr d) Absorbed Microwave Power, P <sub>abs</sub> =691-1221W
Input Variables $U$	Reactor Design Variables $U_2$	a) 2.45 GHz Microwave Power, fixed b) Reactor Configuration, MPCR, fixed c) End Feed Excitation, fixed d) Electromagnetic Mode and Cavity Tuning, Fixed at TM <sub>013</sub> e) Reactor Wall Material, quartz dome, fixed, dia.=5” f) Substrate Holder Set-up, molybdenum holder, thermally floating stage g) Vacuum System, mechanical pump, 1~2x10 <sup>-2</sup> Torr, leak rate: 12.6 mTorr/hr h) Purity of gases, fixed, See Section 3.2.2.1
	Deposition Process Variables $U_3$	a) Deposition Time, 2-48 hours b) Substrate Material and Size, 3” Si (100) wafers c) Seeding Procedure, mechanically scratched by 0.1 μm natural diamond powder d) Start-up and Shut-down, fixed

**TABLE 3.2: PARAMETER SPACE FOR EXPERIMENTS PERFORMED AT SYSTEM II**

	Controllable Input Variables $U_1$	a) Gas Chemistry, Ar/H <sub>2</sub> /CH <sub>4</sub> =99-90/0-9/1 (%) b) Argon Flow Rate, Ar=101-630 sccm c) Deposition Pressure, p=60-240 Torr d) Absorbed Microwave Power, P <sub>abs</sub> =732-1518W e) N <sub>2</sub> impurity, 5-2500ppm
Input Variables $U$	Reactor Design Variables $U_2$	a) 2.45 GHz Microwave Power, fixed b) Reactor Configuration, MPCR, fixed c) End Feed Excitation, fixed d) Electromagnetic Mode and Cavity Tuning, Fixed at TM <sub>013</sub> e) Reactor Wall Material, quartz dome, fixed, dia.=5" f) Substrate Holder Set-up, molybdenum holder, thermally floating stage g) Vacuum System, turbo pump, 10 <sup>-7</sup> ~10 <sup>-6</sup> Torr, leak rate*: 4mTorr/hr h) Purity of gases, fixed, See Section 3.2.2.2
	Deposition Process Variables $U_3$	a) Deposition Time, 8-25 hours b) Substrate Material and Size, 3" Si (100) wafers c) Seeding Procedure, mechanically scratched by 0.1 μm natural diamond powder d) Start-up and Shut-down, fixed

\* Measurement of leak rate was done by Brian Wright.

## 3.5 Measurement Methodologies

### 3.5.1 Reactor Performance

#### 3.5.1.1 Total Growth Rate

The total growth rate of the film,  $G_T$  (mg/h) is determined by the weight gain,  $W$  (mg) of the substrate during the deposition process divided by the deposition time,  $t$  (hour).  $G_T = \frac{W}{t}$

#### 3.5.1.2 Average Growth Rate

The average growth rate,  $G_{ave}$  ( $\mu\text{m/h}$ ) is defined as the total growth rate divided by the deposition area  $A$  ( $A=45.60 \text{ cm}^2$ ) and the diamond density ( $D=3.515 \text{ g/cm}^3$ ) with the assumption that the whole wafer is covered with ultra-nanocrystalline diamond uniformly. This method includes a certain inaccuracy caused by the scale. Also, the CVD ultra-nanocrystalline diamond may not have the same density as natural diamond type II because of the numerous amount of grain boundaries.  $G_{ave} = \frac{G_T}{A \cdot D}$

#### 3.5.1.3 Specific Yield

The specific yield,  $S$  ( $\text{kw} \cdot \text{h/g}$ ) is given by the microwave power,  $P_{abs}$  (kw) versus the film total growth rate in the units of “g/h” to describe the energy efficiency of the diamond deposition process.  $S = \frac{P_{abs}}{G_T \times \frac{\text{g}}{10^3 \text{ mg}}}$

#### 3.5.1.4 Carbon Conversion Efficiency

The carbon conversion efficiency,  $C$  (%) is the percentage of the total carbon atoms provided by the input gases that are actually converted into the diamond film on the substrate.

For example, the number of carbon atoms which are converted into the diamond film for a total growth rate of 1 mg/h is:

$$1 \frac{\text{mg}}{\text{h}} \times \frac{\text{g}}{10^3 \text{ mg}} \times \frac{1 \text{ h}}{60 \text{ min}} \times \frac{\text{mole}}{12 \text{ g}} \times \frac{6.02 \times 10^{23} \text{ atom}}{\text{mole}} = 8,316 \times 10^{17} \frac{\text{atoms}}{\text{min}}$$

For a flow rate of 1 sccm methane, the total number of carbon atoms provided is:

$$1 \frac{\text{cm}^3}{\text{min}} \times \frac{\text{L}}{10^3 \text{ cm}^3} \times \frac{\text{mole}}{22.4 \text{ L}} \times \frac{6.02 \times 10^{23} \text{ atom}}{\text{mole}} = 2,6875 \times 10^{19} \frac{\text{atoms}}{\text{min}}$$

In this case, the carbon conversion efficiency would be:

$$\frac{8.316 \times 10^{17}}{2.6875 \times 10^{19}} \times 100 \% = 3.09 \%$$

So, for a total growth rate of  $G_T$  and  $f_M$  sccm of methane, the carbon conversion efficiency is:

$$C = \frac{G_T \times 8.316 \times 10^{17}}{f_M \times 2.6875 \times 10^{19}} \times 100 \%$$

## 3.5.2 Film Characteristics

### 3.5.2.1 Film Texture

The direction of the largest dimension (the direction of the most rapid growth) of crystals often determines the texture of the film. Usually the texture is determined by means of x-ray diffraction crystallography. With the information of the structure of crystalline phases from x-ray diffraction, x-ray diffraction crystallography was used to identify the presence of diamond. At the same time, x-ray diffraction crystallography becomes a

substitute tool for Raman spectroscopy. A two-theta scan of a film provides an indication of growth orientation/texture in the crystalline films by comparison the intensity of the peaks. However, a quantitative determination of the film texture can be better pursued by pole figures and inverse pole figures, which were not used in this thesis research. The x-ray diffractometer at Chemistry Department of MSU is a Rigaku 200 rotating anode powder diffractometer with maximum power: 60 kV and maximum current: 200 mA.

### **3.5.2.2 Film Roughness and Morphology**

The roughness and surface profile of the films were measured by AFM (Atomic Force Microscopy) with the technique of tapping mode. TappingMode AFM has the advantage of higher lateral resolution and virtually eliminates lateral forces (no scraping on sample). There is one minor disadvantage: slightly slower scan speed than Contact-Mode AFM. The AFM system at KMF (W. M. Keck Microfabrication Facility at Michigan State University, a NSF MRSEC facility) at PHY Department of MSU is a SPM (Scanning Probe Microscopy) model DI D3100.

### **3.5.2.3 Film Quality**

Raman Spectroscopy can identify the presence of various forms of carbon such as diamond, amorphous carbon, and graphite. It is a common method to determine the quality of CVD diamond films. The method of Raman spectroscopy is described in chapter 4.1. Different Raman systems were used in this thesis research. In the early stages of this research, when the films had larger crystal sizes, the Raman system at ECE Department of MSU with 30  $\mu\text{m}$  spot size could detect the diamond peak. The Raman system at ECE Department of MSU is: (1) an argon ion CW laser operates at 514.5 nm at multimode with



a spectral width of 10 GHz, (2) output intensity is automatically regulated within 1%, (3) a scanning 0.75 m double monochromator which is coupled with a photomultiplier tube (PMT) is used as the discriminating instrument, (4) a peltier element in the housing of the PMT assures cooling down to -23 °C for reduction of dark count, (5) the double monochromator has a spectral resolution of 1.08 nm/mm<sub>slitwidth</sub>, (6) slits are set accordingly to allow high discrimination and reasonable throughput for measuring CVD diamond films, (7) a 180° geometry, backscattering arrangement, is chosen to allow superior use of microscopic optics [Moss 1997]. In this research, the spectra resolution of the acquired spectra is 6.6 cm<sup>-1</sup>. The spectra are recorded in steps of 1 cm<sup>-1</sup>. The Raman spectra were taken from 1200-1600 cm<sup>-1</sup>. With a 60X objective lens of a optical microscope, the illuminated spot size is 30 µm in diameter.

As the research continued, the crystal size became smaller. Thus, the broadening effect of the small crystal size required the use of the UV Raman at ANL (Argonne National Laboratory). Unfortunately, the UV Raman became unavailable (since year 2000). Therefore, the measurements could not be performed for most of the films. The UV Raman system at Materials Science Division of Argonne National Lab is: (1) beginning wavelength is 266 x 4 nm (It is Nd YAG), (2) the doubling part is commercially available from Coherent (The Verdi laser), (3) the quadrupling part is an external cavity made by Laser Analytical Systems (LAS) that uses a BBO crystal, (4) spot size with present lens is about 100 µm wide by 200 to 300 µm wide.

#### **3.5.2.4 Crystal Size**

Because of the small crystal size of ultra-nanocrystalline diamond films, determining the crystal size is a difficult task with the available instruments. There are a few SEM-analysis equipments at Michigan State University. Because of the small crystal size of ultra-nanocrystalline diamond films, a high resolution SEM is required. The Hitachi S-4700II FESEM (Field Emission SEM) at W. M. Keck Microfabrication Facility in the Physics Department of MSU has the resolution in the order of tens of nanometers for diamond films. An Everhart-Thornley detector to acquire secondary electron images (SE detector) was used to take the SEM pictures. With an ultra-high resolution setting on a Hitachi S-4700II FESEM, a optimum resolution on the order of ten nanometers can be obtained for diamond films. Due to charging problems non-conducting of the diamond films and the beam damage caused by the bombardment of the energized electron beam, the images were often blurry and darkened during the scan.

Another approach was to use AFM technique. Using a tip with a nominal 5-10 nm radius of curvature, TappingMode AFM can achieve 1-5 nm of lateral resolution on most samples. However, in reality, the tip radius of curvature is more than 5-10 nm. In addition to that, the silicon probe wears out quickly during the scan on diamond samples. So, the radius of the curvature of the tip is constantly changing. As a result, it changes the lateral resolution of the tip as it scans. This makes the measurements of the crystal size inaccurate. Therefore, the AFM approach for determination of the crystal size was only applied to the films produced by the system I.

With the crystal size on the order of nanometers, like those synthesized in MSU-MPACVD system II, the Hitachi H-800 TEM (Transmission Electron Microscopy) with 200 kV in the CHEMS (Chemical Engineering and Materials Science) Department of MSU was used. Bright field, dark field imaging techniques, and SAD (Selected Area Diffraction) patterns were used in this study. The growth mechanism of ultra-nanocrystalline diamond was also studied with cross-section TEM images. Plan-view and cross-section TEM specimens were prepared for the study of crystal sizes and growth mechanism of ultra-nanocrystalline diamond films.

To prepare plan-view TEM specimens, a 3 mm diameter piece of the diamond sample was cut by a mechanical disc cutter, and a 3 mm diameter molybdenum ring was glued to the diamond film side using G-1 epoxy (cured at 130 °C for 10 minutes). The silicon substrate was mechanically polished to ~80  $\mu\text{m}$ . The center of the specimen was further thinned to ~10  $\mu\text{m}$  using a dimpler. Then the specimen was milled until perforation with 5 kV argon ions. Therefore, the specimen could be imaged in the TEM. The resulting specimen had a hole at the center of the electron transparent diamond film.

To prepare cross-section TEM specimens, two (4 mm x 8 mm) pieces of the sample were cut by a wafer saw and glued face-to-face with G1-epoxy. Two pieces of silicon were glued to the backs of the sample pieces if the silicon substrates were too thin to have a good mechanical support. A ~1.5 mm thick slice of this diamond sandwich was cut by a wafer saw. A 3 mm diameter disk was cut out from the slice with a mechanical disc cutter. One side of the cross-section specimen was polished with sand paper and followed with diamond lapping films of progressively finer grit size until a mirror finish was obtained. A

3 mm diameter molybdenum ring was glued to the polished side using G-1 epoxy (cured at 130 °C for 10 minutes). Then, the specimen was turned over and ground down to ~100  $\mu\text{m}$  mechanically. The center of the specimen was dimpled to ~10  $\mu\text{m}$  thickness. Then the specimen was ion milled until perforation with 5 kV argon ions. Then, the specimen was ready to be used for imaging in the TEM. The resulting specimen had a hole located at the boundary of silicon substrate and diamond film.

#### **3.5.2.5 Optical Property**

Transmission measurements were performed using a Beckman Spectrophotometer model IR4220 in the ECE Department of MSU. Ultra-nanocrystalline diamond films of different thickness were grown on both side polished silicon wafers. The diamond film was first deposited on one side, then on the backside. For the two layers, the silicon wafer went through an oxidation process in a furnace, then grew the ultra-nanocrystalline diamond film on the  $\text{SiO}_2$  film. The measured transmission data were compared to the theoretical calculations. The method of IR transmission measurements and theoretical calculations are described in Section 7.2.2 and 7.2.3.

and

and

and

and

and

and

X

and

and

and

and

and

and

and

and

and

## 4 MSU-MPACVD Reactor Experimental Output Variables-Reactor Performance ( $Y_1$ )

### 4.1 Introduction

The output variables ( $Y$ ) of the experimental parameter space can be subdivided into reactor performance variables ( $Y_1$ ) and film characteristics ( $Y_2$ ). The results of the experimental investigation of the reactor performance ( $Y_1$ ) of the two MSU-MPACVD systems for ultra-nanocrystalline diamond synthesis are presented in this chapter. The film characteristics ( $Y_2$ ) will be presented in next chapter. The theories that describe and predict the reactor behavior are still under development. Therefore, it's necessary to explore the experimental behavior of the MSU-MPACVD systems.

The output variable ( $Y$ ) is a function of many input ( $U=[U_1, U_2, U_3]$ ) and internal ( $X$ ) variables, i.e.,  $Y=g(U, X)$ , and the internal variables are dependent upon the input variables, i.e.,  $X=f(U)$ . Because of the large number of variables and the intricacy between the variables, the microwave plasma deposition process is very complicated and the reactor behavior is difficult to analyze. Thus in this chapter, a subset of the parameter space shown in Figure 3.18 and their relationships are investigated. Figure 4.1 illustrates this subset and Tables 4.1 and 4.2 display the input ( $U$ ), internal ( $X$ ), and output ( $Y$ ) variables considered and the associated experimental ranges that are explored in this chapter.

As shown in Figure 4.1, the input variables  $U$  are divided into three groups, (1) controllable input variables  $U_1$  which include (a) gas chemistry  $Ar/H_2/CH_4$ , (b) total gas flow rate  $f_t$ , (c) deposition pressure  $p$ , and (d) microwave power  $P_{abs}$ ; (2) reactor design

variables  
capacity  
rotation  
multiples  
state be  
system  
tion pro  
substrat  
tion 3.3  
describ  
holder  
gas the  
power  
impair  
sis of  
winter  
struc  
terus  
f. dep  
ment

variables  $U_2$  which are held constant and (a) include a 2.45 GHz microwave excitation frequency, (b) a cavity inner diameter of 17.78 cm, (c) a cavity tuned at electromagnetic excitation mode of  $TM_{013}$ , (d) a quartz dome with inner base diameter of 5 inches, (e) a molybdenum holder with thermally floating substrate holder set up (i.e., no external substrate heating or cooling), (f) a discharge diameter of approximately 10 cm, (g) a vacuum system (see Table 4.1 and 4.2), (h) purity of gases (see Table 4.1 and 4.2); and (3) deposition process variables  $U_3$  which include (a) a variable deposition time  $t$ , (b) Si (100) substrates with a diameter of 3 inches, (c) a substrate seeding procedure described in Section 3.3.1.2, and (d) a start up and shut down procedure described in Section 3.3.2. As described in Section 3.2.4.1, the reactor is operated with a thermally floating substrate holder set up. Therefore, the substrate temperature is not independently controlled. The gas chemistry, deposition time, total gas flow rate, deposition pressure, and microwave power are the input variables for the experiments presented in this chapter. One of the important internal variables  $X$  is the substrate temperature,  $T_s$ . Output variables ( $Y$ ) consist of (1) reactor performance variables  $Y_1$  such as growth rate, specific yield, and carbon conversion efficiency; and (2) film characteristics  $Y_2$  such as film roughness, morphology, structure quality, film texture and crystal size.

This chapter presents an overview of the MSU-MPACVD reactor performance  $Y_1$  versus a selected number of input variables: Ar/H<sub>2</sub>/CH<sub>4</sub> gas chemistry, total gas flow rate  $f_t$ , deposition pressure,  $p$ , microwave power,  $P_{abs}$ , and deposition time,  $t$ . It was experimentally determined that the relationships between input, internal, and output variables



were complex and non-linear, i.e.,  $Y_1 = g(\text{Ar}/\text{H}_2/\text{CH}_4, f_t, p, P_{\text{abs}}, T_s, t)$ , and  $T_s = f(\text{Ar}/\text{H}_2/\text{CH}_4, p, P_{\text{abs}})$ .

In Section 4.2 and Section 4.3, the influences of gas chemistry, deposition time, total gas flow rate, deposition pressure and microwave power on the reactor performance of system I and II respectively are investigated. Section 4.4 presents the experimental results of the influence of additional nitrogen impurities on reactor performance of system II. At the end, a summary of the reactor performance is presented in Section 4.5.

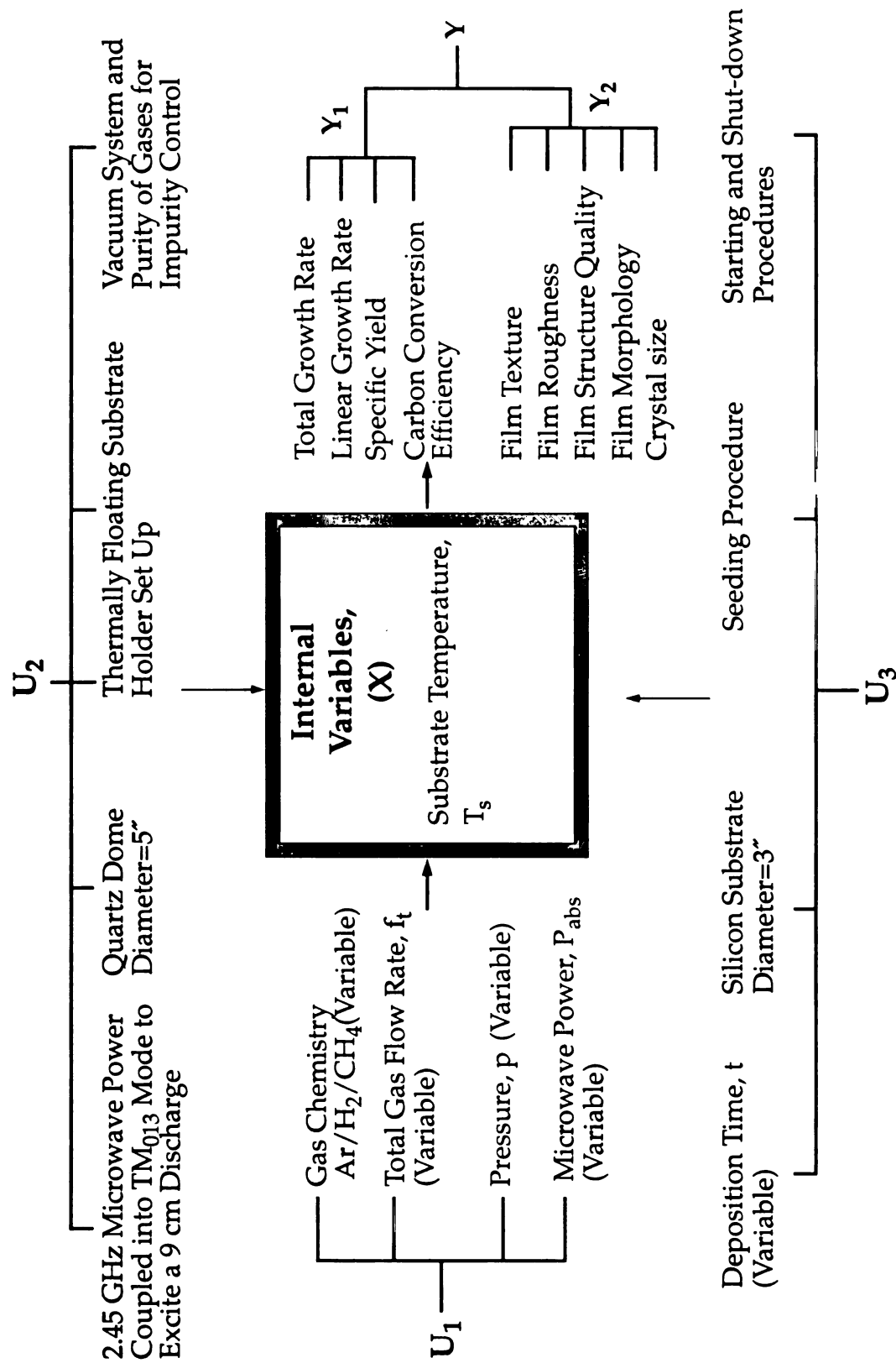


FIGURE 4.1 : MCPR BLOCK DIAGRAM FOR THE EXPERIMENTS

**TABLE 4.1: PARAMETER SPACE FOR EXPERIMENTS PERFORMED ON SYSTEM I**

	Controllable Input Variables $U_1$	a) Gas Chemistry, $Ar/H_2/CH_4=(99-91)/(1-7)/(0-2)$ (%) b) Total Gas Flow Rate, $f_t=102.5-642$ sccm c) Deposition Pressure, $p=120-160$ Torr d) Absorbed Microwave Power, $P_{abs}=691-1221$ W
Input Variables $U$	Reactor Design Variables $U_2$	a) 2.45 GHz Microwave Power, fixed b) Reactor Configuration, MPCR, fixed c) End Feed Excitation, fixed d) Electromagnetic Mode and Cavity Tuning, Fixed at $TM_{013}$ e) Reactor Wall Material, quartz dome, fixed, dia.=5" f) Substrate Holder Set-up, molybdenum holder, thermally floating stage g) Vacuum System, mechanical pump, $1\sim 2\times 10^{-2}$ Torr, leak rate: 12.6 mTorr/hr h) Purity of gases, fixed, See Section 3.2.2.1
	Deposition Process Variables $U_3$	a) Deposition Time, 2-48 hours b) Substrate Material and Size, 3" Si (100) wafers c) Seeding Procedure, mechanically scratched by 0.1 $\mu m$ natural diamond powder d) Start-up and Shut-down, fixed
Internal Variables $X$		Substrate Temperature, $T_s=750-950$ °C (by pyrometer, top side)
Output Variable $Y$	Reactor Performance $Y_1$	a) Total Growth Rate: 0.163-12.963 mg/hr b) Linear Growth Rate: 0.010-0.809 $\mu m/hr$ c) Specific Yield: 4411-69 kW*hr/g d) Carbon Conversion Efficiency: 0.504-33.382%

**TABLE 4.2: PARAMETER SPACE FOR EXPERIMENTS PERFORMED ON SYSTEM II**

	Controllable Input Variables $U_1$	a) Gas Chemistry, $Ar/H_2/CH_4=(99-90)/(0-9)/1$ (%) b) Total Gas Flow Rate, $f_t=101-630$ sccm c) Deposition Pressure, $p=60-240$ Torr d) Absorbed Microwave Power, $P_{abs}=732-1518$ W e) Controlled $N_2$ impurity, 5-2500ppm
Input Variables $U$	Reactor Design Variables $U_2$	a) 2.45 GHz Microwave Power, fixed b) Reactor Configuration, MPCR, fixed c) End Feed Excitation, fixed d) EM Mode and Cavity Tuning, Fixed at $TM_{013}$ e) Reactor Wall Material, quartz dome, fixed, dia.=5" f) Substrate Holder Set-up, molybdenum holder, thermally floating stage g) Vacuum System, turbo pump, $10^{-7} \sim 10^{-6}$ Torr, leak rate*: 4mTorr/hr h) Purity of gases, fixed, See Section 3.2.2.2
	Deposition Process Variables $U_3$	a) Deposition Time, 8-25 hours b) Substrate Material and Size, 3" Si (100) wafers c) Seeding Procedure, mechanically scratched by 0.1 $\mu m$ natural diamond powder d) Start-up and Shut-down, fixed
Internal Variables $X$		a) Substrate Temperature, $T_s=UFL-770$ °C (by pyrome- ter, back side)
Output Variable $Y$	Reactor Performance $Y_1$	a) Total Growth Rate: 0.175-14.25 mg/hr b) Linear Growth Rate: 0.011-0.889 $\mu m/hr$ c) Specific Yield: 4229-99 kW*hr/g d) Carbon Conversion Efficiency: 0.542-44.094%

\* Measurement of leak rate was done by Brian Wright.

**UFL:** Temperature is too low to be within the pyrometer measurement range.

## 4.2 System I

### 4.2.1 Introduction

The initial ultra-nanocrystalline diamond film synthesis experiments were performed using system I with argon-hydrogen-methane plasma chemistries. According to the results of Gruen et al. [Zuik 1995], the gas chemistry required for ultra-nanocrystalline diamond growth is a high concentration of argon (90 vol% and above), some methane, and no or little hydrogen. After many trial experiments, it was discovered that in order to stabilize the plasma for the entire experiment run and remove the flames inside the plasma (the flames often produce a graphitic by-product), the hydrogen to methane ratio could not be less than 3 at any gas flow rate, i.e.  $H_2/CH_4 \geq 3$ .

The thermally floating substrate holder setup utilized in this thesis research is shown in Fig. 3.9. With the setup displayed in Figure 3.9, quartz tubes of different heights can be used to change the position of the substrate with respect to the plasma to optimize the film deposition process. It was found that quartz tubes with about 50 mm height gave the best results. The quartz tube with 35 mm height had a reduced growth rate around 15%. The quartz tube with 57 mm height had not only reduced the growth rate by at least 47% but also made the plasma unstable which sometimes reduced the growth rate by 76%.

The substrate temperature measurements of the experiments conducted in system I were performed by using a pyrometer and aiming it at the surface of the substrate (see Figure 3.8). The top-side substrate temperature measurement was about 200 °C higher (see Tables 4.1 and 4.2) than the back-side substrate temperature measurement (see Figure

3.8). The intense emission from the plasma discharges influences the top-side temperature measurements which are thus inaccurate. The experimental data measured in system I is listed in Appendix 9.1. All data points presented in Section 4.3 are listed in Appendix 9.2.

#### **4.2.2 Total Growth Rate = $g(\text{Ar}/\text{H}_2/\text{CH}_4, t, f_t, p, P_{\text{abs}})$**

Figure 4.2 displays the total growth rate plotted versus hydrogen concentration (the percentage of hydrogen flow rate to the total gas flow rate). These experiments were performed at a constant pressure of 120 Torr and deposition time of 8 hours. The argon concentration was varied from 90.91-98.68%, the  $\text{H}_2$  concentration varied from 0.99-7.27%, and the  $\text{CH}_4$  concentration varied from 0.33-1.85% with the total gas flow rate varied from 102.5-642 sccm. The performance of the reactor's total growth rate versus hydrogen concentration is shown in Figure 4.2 and thus defines the experimental performance of the system I at the pressure of 120 Torr. Figure 4.2 shows (i) given a constant  $\text{CH}_4$  concentration, the growth rate increases as  $\text{H}_2$  concentration increases (if provided with enough methane concentration to supply carbon atoms for the diamond growth), (ii) given a constant  $\text{H}_2$  concentration, growth rate increases as  $\text{CH}_4$  concentration increases.

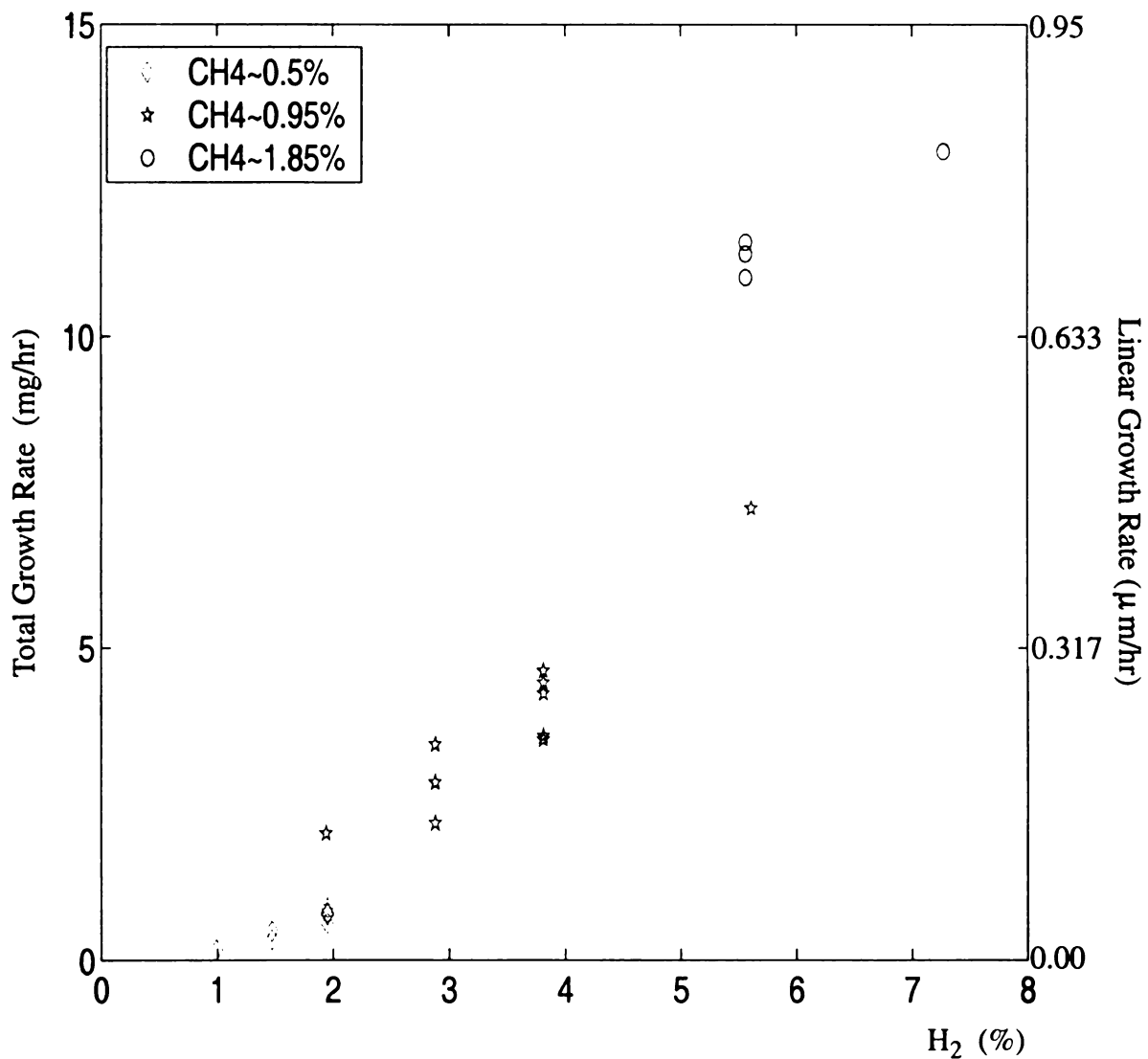


FIGURE 4.2 : TOTAL GROWTH RATE VS. HYDROGEN CONCENTRATION

Pressure=120 Torr, deposition time=8 hours,  
 Ar:H<sub>2</sub>:CH<sub>4</sub>=(90.91-98.68):(0.99-7.27):(0.33-1.85)%  
 and total gas flow rate varied from 102.5-642 sccm  
 by system I.

Figure 4.3 displays the total growth rate versus the deposition time,  $t$ , with a constant pressure of 120 Torr,  $\text{Ar:H}_2\text{:CH}_4=100:2:0.5$ , and  $f_t=615$  sccm. As shown, the growth rate increases about 25% from an 8 hour run to a 24 hour run. The lower growth rate at the shorter deposition time region may be due to the presence of impurities at the beginning of the experiments.

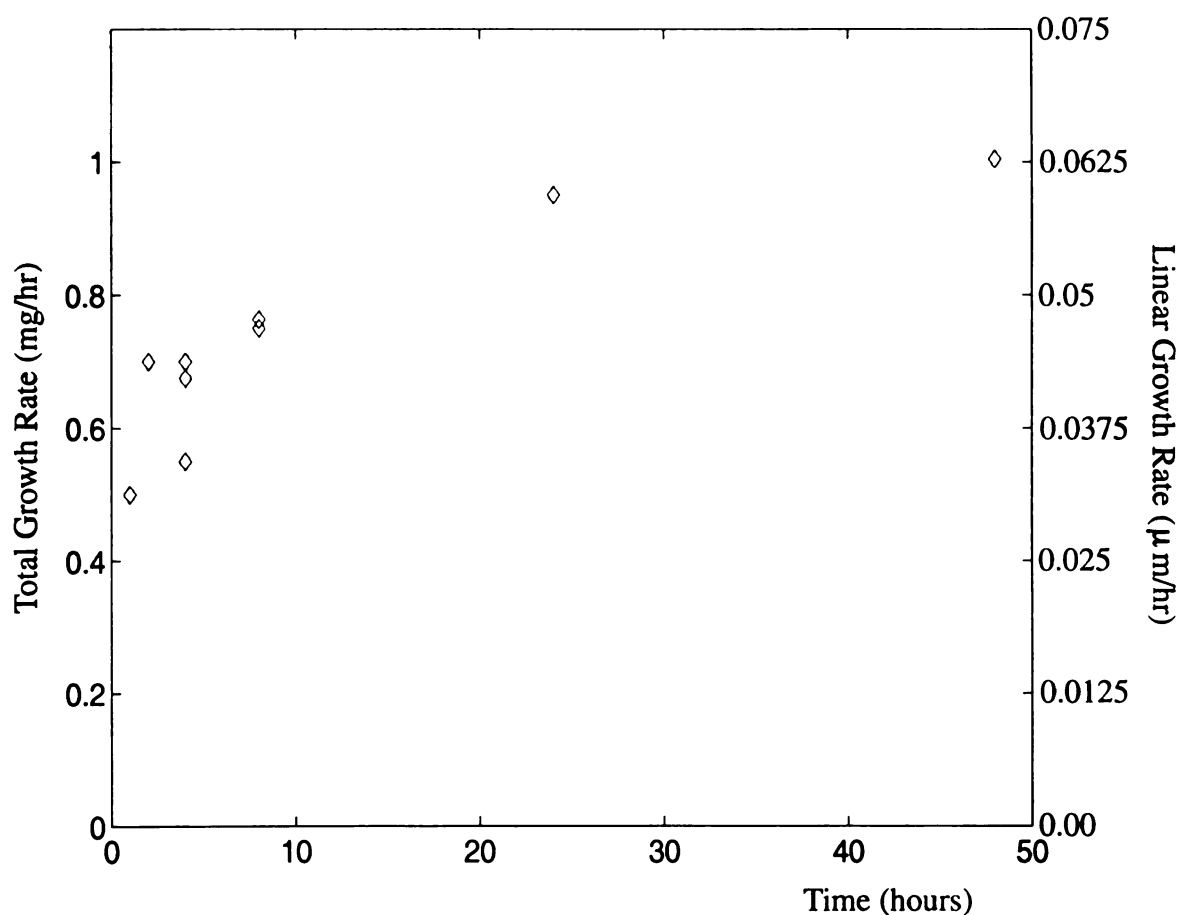


FIGURE 4.3 : TOTAL GROWTH RATE VS. DEPOSITION TIME  
Pressure=120 Torr and  $\text{Ar:H}_2\text{:CH}_4=100:2:0.5$ , and  $f_t=615$  sccm by system I



1. 100

2. 100

3. 100

4. 100

Total Growth Rate (comp/yr)

Figure 4.4 displays the total growth rate plotted as a function of total gas flow rate,  $f_t$ , with pressure at 140 Torr, deposition time of 8 hours, and three different gas chemistry ratios. Figure 4.4 indicates that the total gas flow rate does not influence the growth rate. With a fixed total gas flow rate, the growth rate is mainly affected by gas chemistry. In Figure 4.4, the gas chemistry is expressed as ratios.

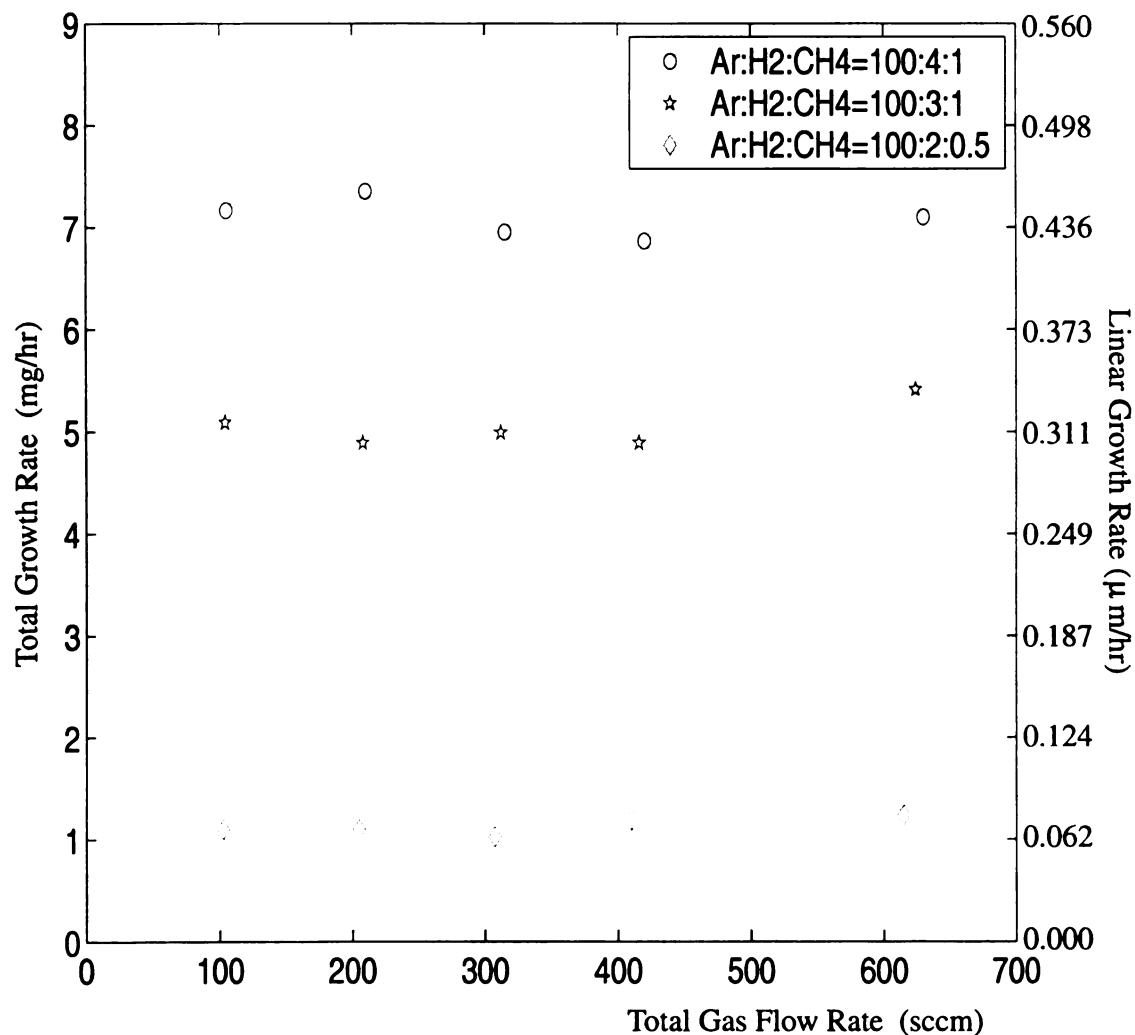


FIGURE 4.4 : TOTAL GROWTH RATE VS. TOTAL GAS FLOW RATE  
Pressure=140 Torr and deposition time=8 hours by system I

Figures 4.5 and 4.6 display the total growth rate versus deposition pressure,  $p$ , and absorbed microwave power,  $P_{\text{abs}}$ , respectively, with deposition time of 8 hours and  $f_t = 102.5\text{-}630$  sccm. Because at a constant input power, the discharge area  $A_d$  decreased with the deposition pressure,  $p$ . During the ultra-nanocrystalline diamond film synthesis with system I, the microwave power input was increased as the pressure increased to maintain a discharge area  $A_d$  that covered the three inch substrates.

As shown in Figure 4.5, the growth rate increases with increases in deposition pressure. With a fixed pressure, the higher hydrogen or methane concentration resulted in higher growth. This result is consistent with the data in Figure 4.2. In Figure 4.6, the growth rates of the experiments with gas chemistry ratio of  $\text{Ar:H}_2\text{:CH}_4 = 100\text{:}2\text{:}0.5$  approximately doubles as the absorbed microwave power increases from 702W to 903 W. The growth rates of those experiments with gas chemistry ratios of  $\text{Ar:H}_2\text{:CH}_4 = 100\text{:}3\text{:}1$  or  $100\text{:}4\text{:}1$  increase rapidly from 3.450 mg/hr to 8.675 mg/hr for  $\text{Ar:H}_2\text{:CH}_4 = 100\text{:}3\text{:}1$  and from 4.625 mg/hr to 10.788 mg/hr for  $\text{Ar:H}_2\text{:CH}_4 = 100\text{:}4\text{:}1$  as the absorbed microwave power increases from 795W to 1017 W. But at the same time, the deposition pressure is increased, too. The contribution can come from either deposition pressure or absorbed microwave power.

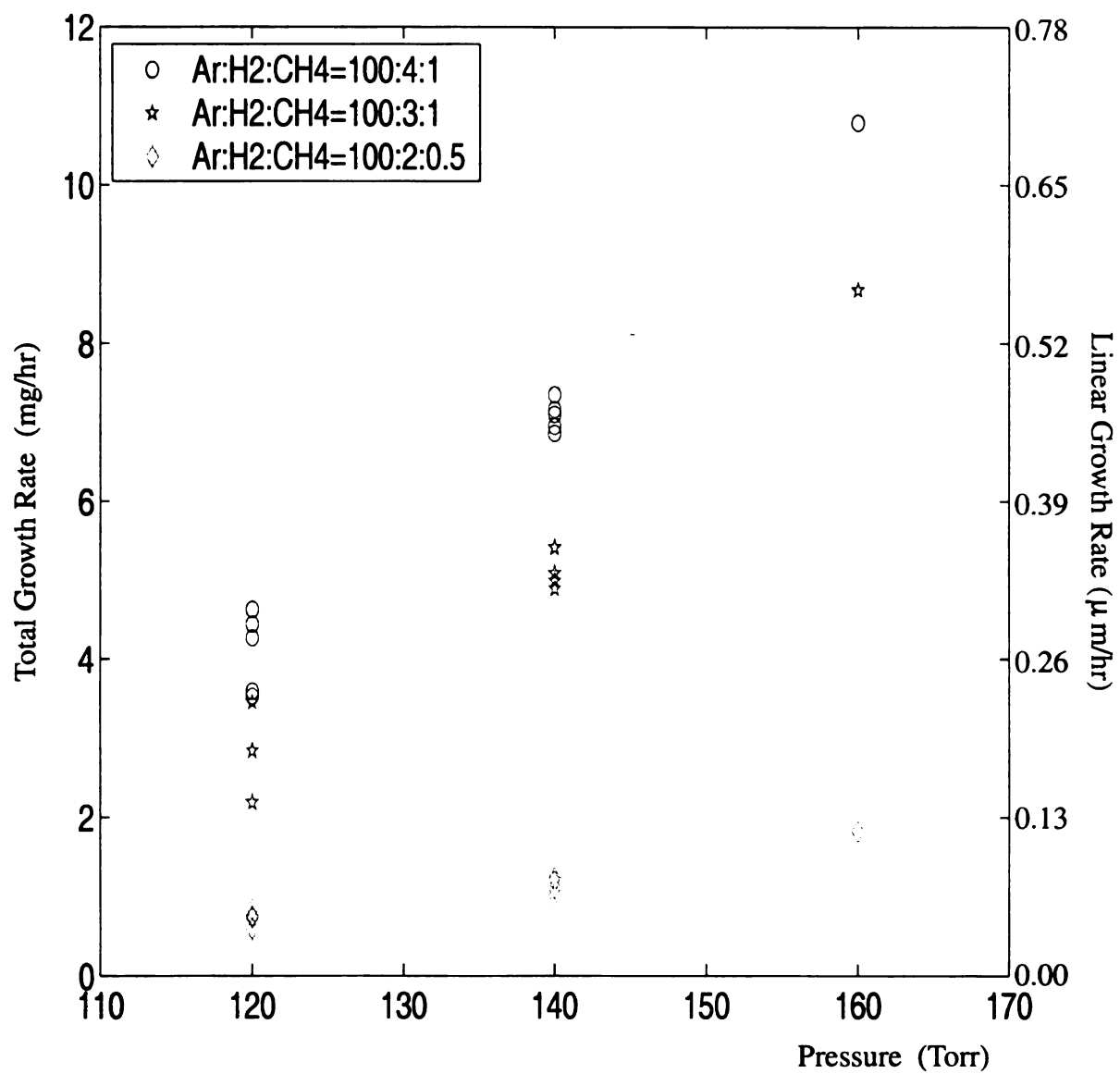
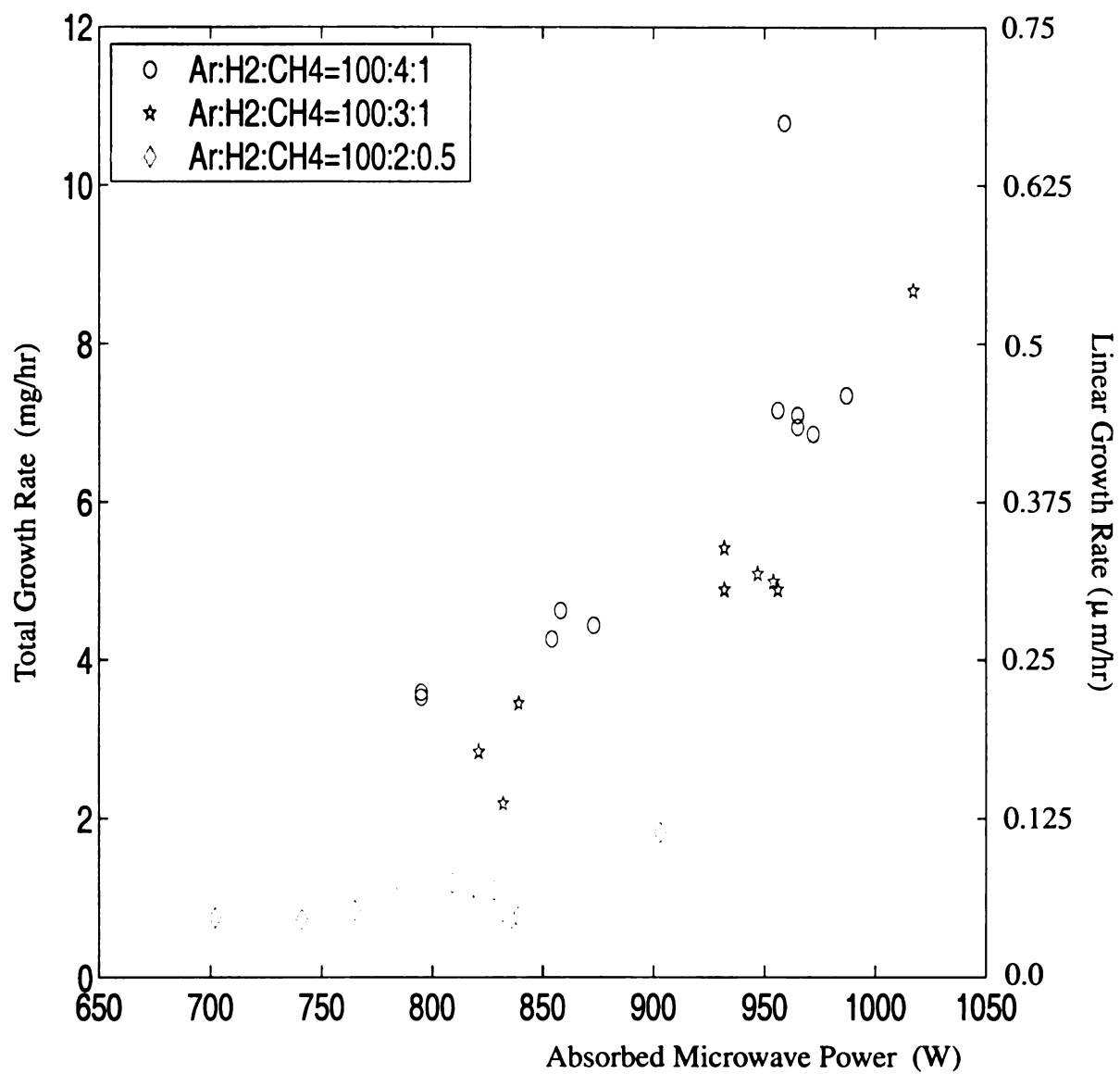


FIGURE 4.5 : TOTAL GROWTH RATE VS. DEPOSITION PRESSURE  
Deposition time=8 hours and total gas flow rate=100-600 sccm by system I



**FIGURE 4.6 : TOTAL GROWTH RATE VS. ABSORBED POWER**  
 Deposition time=8 hours and total gas flow rate=100-600 sccm by system I

### 4.2.3 Specific Yield = $g(\text{Ar}/\text{H}_2/\text{CH}_4, t, f_t, p, P_{\text{abs}})$

Specific yield is a measurement of the energy efficiency of the deposition process. The lower the specific yield, the less microwave power required to deposit a given weight of ultra-nanocrystalline diamond.

Figure 4.7 displays the specific yield versus the hydrogen concentration (the percentage of hydrogen flow rate to the total gas flow rate). These experiments were performed at a constant pressure of 120 Torr and deposition time of 8 hours. The argon concentration was varied from 90.91-98.68%, the  $\text{H}_2$  concentration varied from 0.99-7.27%, and the  $\text{CH}_4$  concentration varied from 0.33-1.85% with the total gas flow rate varied from 102.5-642 sccm. Figure 4.7 thus defines the microwave energy efficiency of the system I at the pressure of 120 Torr. In particular, Figure 4.7 shows (i) given a constant  $\text{CH}_4$  concentration, specific yield decreases as  $\text{H}_2$  concentration increases, (ii) given a constant  $\text{H}_2$  concentration, specific yield decreases as  $\text{CH}_4$  concentration increases (if  $\text{H}_2/\text{CH}_4 \geq 3$  to prevent the present of flames inside the plasma, which reduces the energy efficiency for diamond growth).

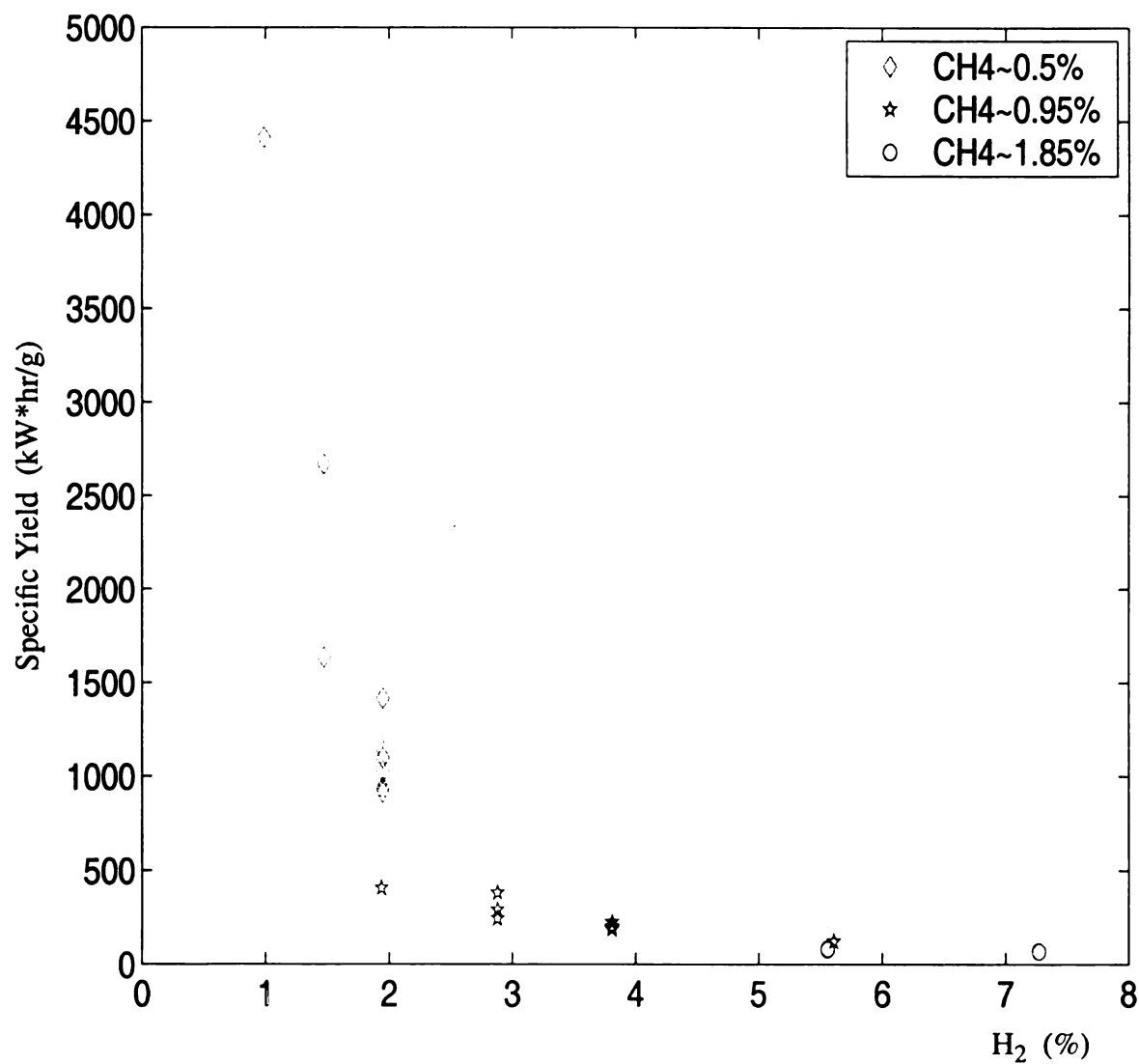


**FIGURE 4.7 : SPECIFIC YIELD VS. HYDROGEN CONCENTRATION**

Pressure=120 Torr, deposition time=8 hours,  
 Ar:H<sub>2</sub>:CH<sub>4</sub>=(90.91-98.68):(0.99-7.27):(0.33-1.85)%  
 and total gas flow rate varied from 102.5-642 sccm  
 by system I.

Figure 4.8 displays the specific yield versus the deposition time,  $t$ , with pressure at 120 Torr,  $\text{Ar:H}_2\text{:CH}_4 = 100/2/0.5$ , and  $f_t = 615$  sccm. As shown, the specific yield becomes lower as deposition time increases. Since specific yield is proportional to the reverse of total growth rate, the higher specific yield in the shorter deposition time region is a reflection of the lower growth rate.

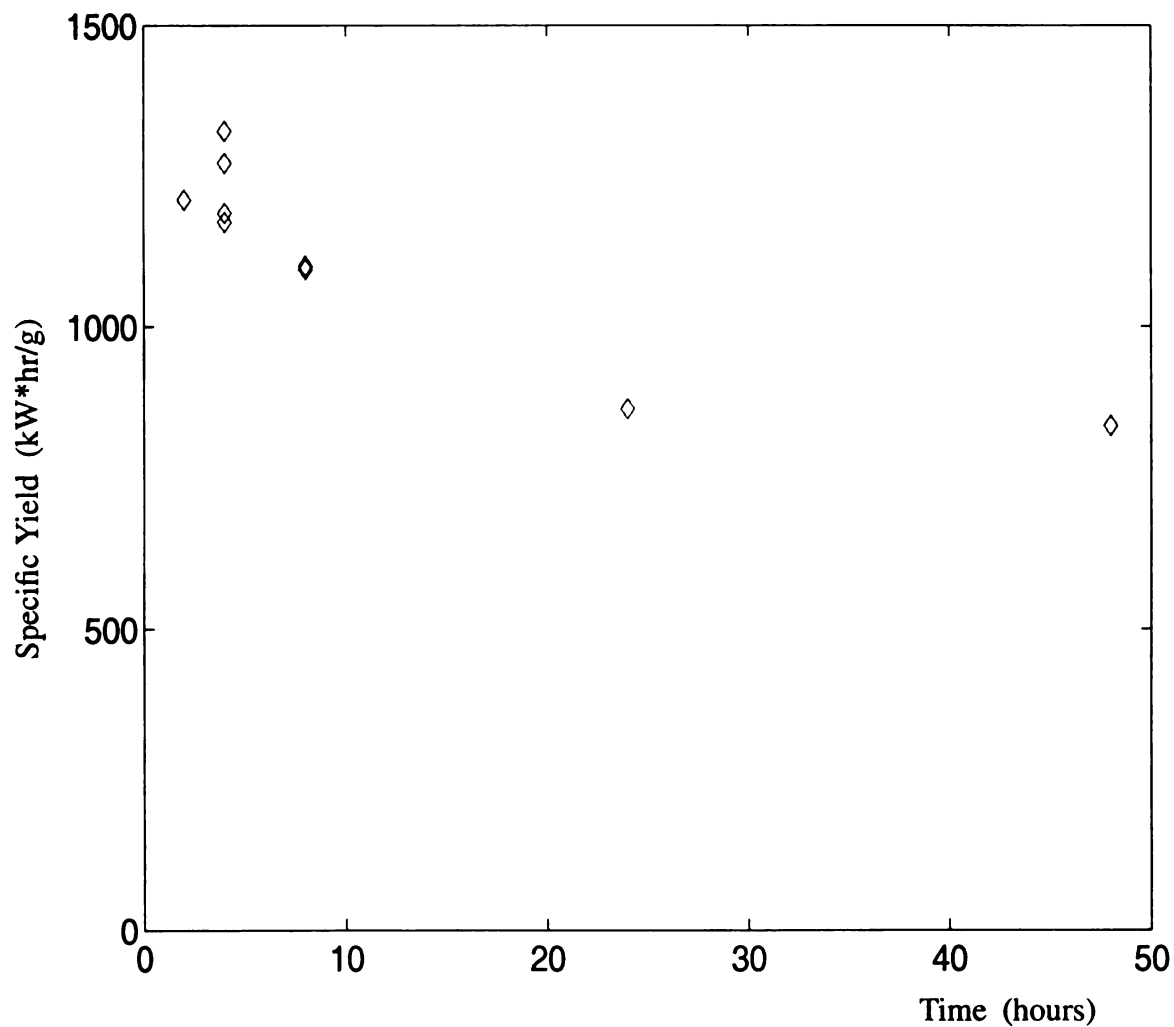


**FIGURE 4.8 : SPECIFIC YIELD VS. DEPOSITION TIME**  
 Pressure=120 Torr and  $\text{Ar:H}_2\text{:CH}_4 = 100:2:0.5$ ,  $f_t = 615$  sccm by system I



Figure 4.9 displays the specific yield versus total gas flow rate,  $f_t$ , with pressure at 140 Torr and deposition time of 8 hours. The data indicate that the total gas flow rate does not influence the specific yield when the plasma is stable and no flames are inside the plasma. With a fixed total gas flow rate, the specific yield is mainly influenced by gas chemistry.

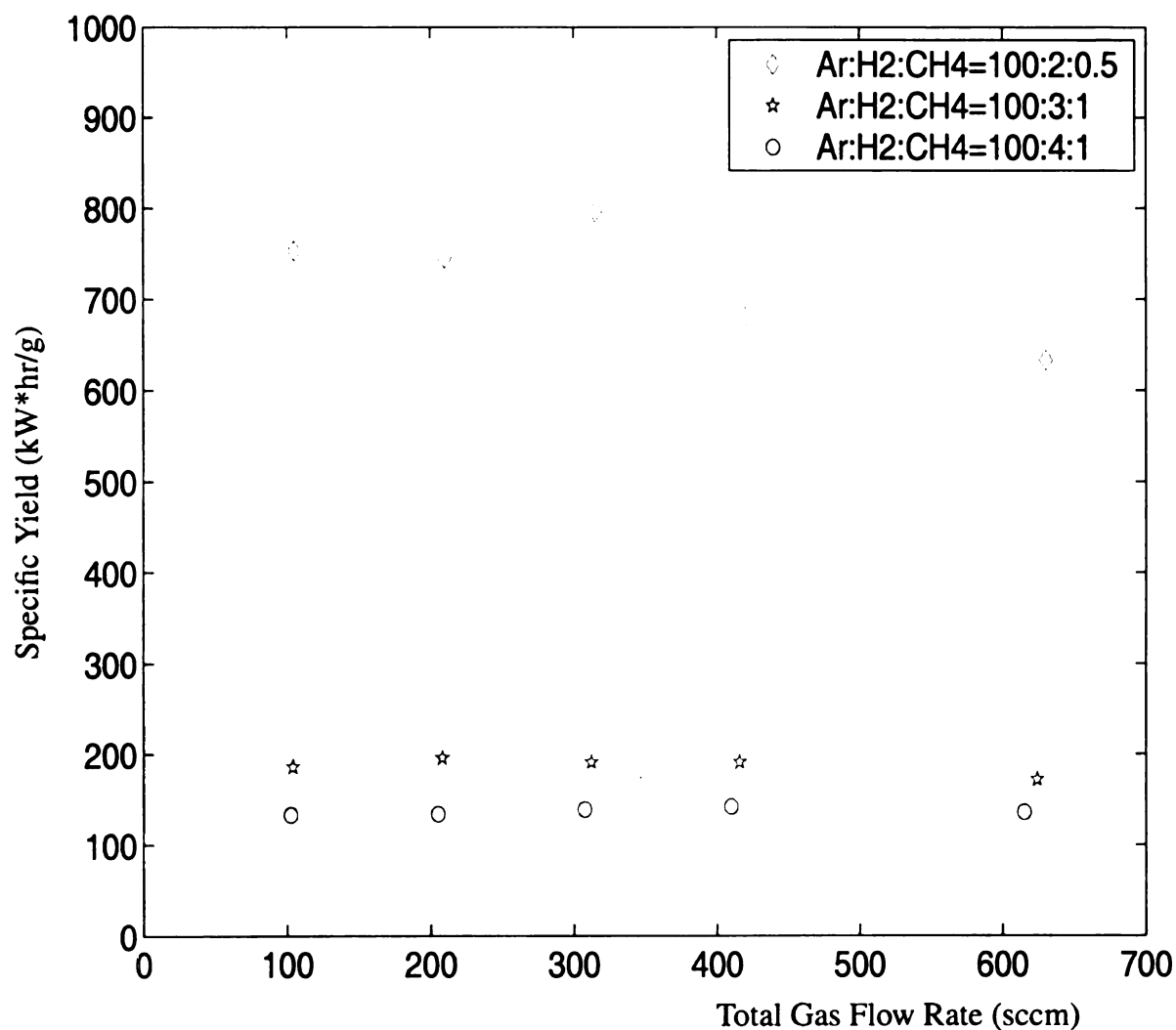


**FIGURE 4.9 : SPECIFIC YIELD VS. TOTAL GAS FLOW RATE**  
 Pressure=140 Torr and deposition time=8 hours by system I

Figure 4.10 and 4.11 display the specific yield versus deposition pressure,  $p$ , and absorbed microwave power,  $P_{\text{abs}}$ , respectively, with deposition time of 8 hours. As shown in Figure 4.10, the specific yield decreases with increases in deposition pressure. With a fixed pressure, higher hydrogen and methane concentration result in lower specific yield. This result is consistent with the data in Figure 4.7.

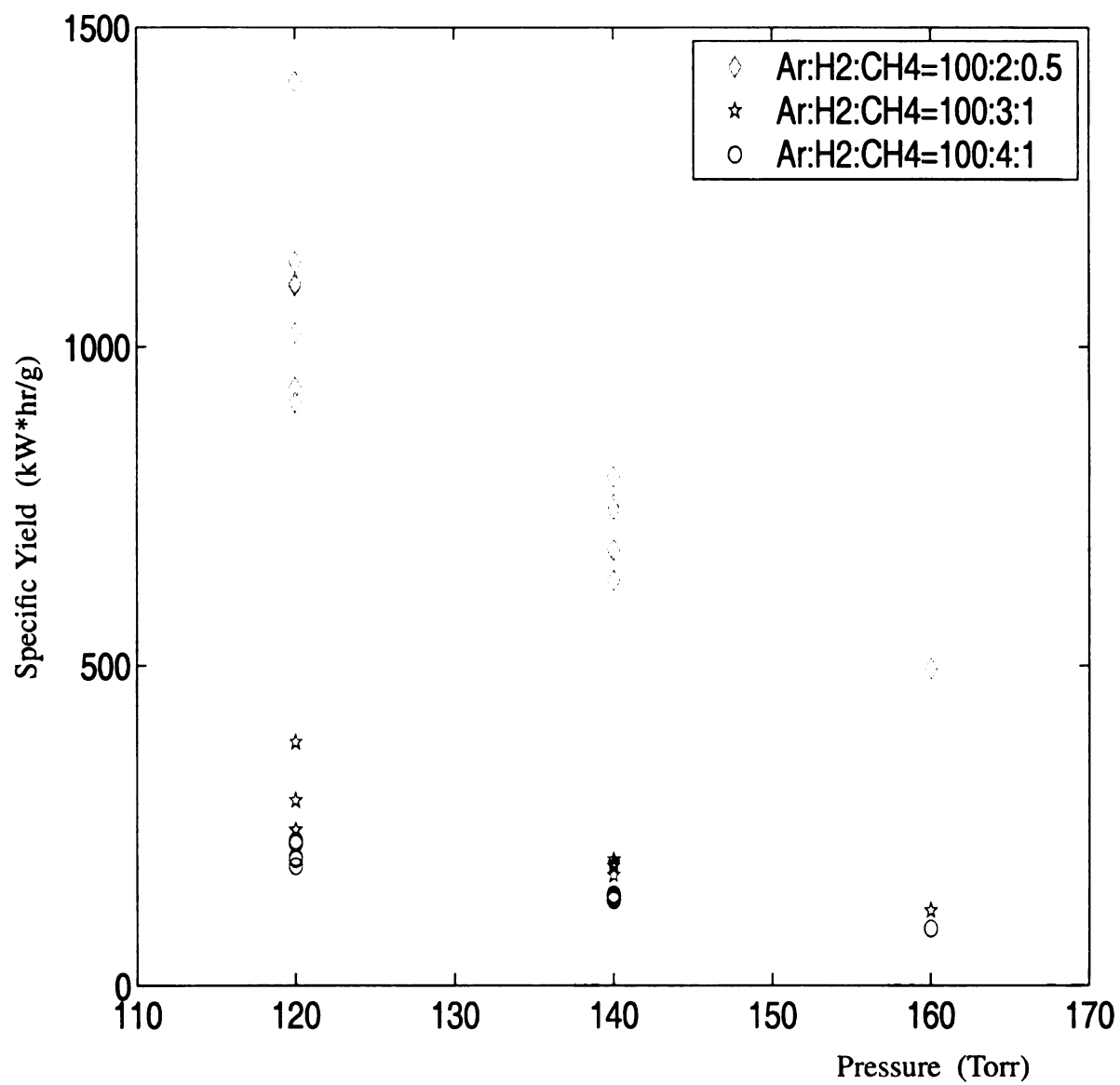


FIGURE 4.10 : SPECIFIC YIELD VS. DEPOSITION PRESSURE  
Deposition time=8 hours by system I

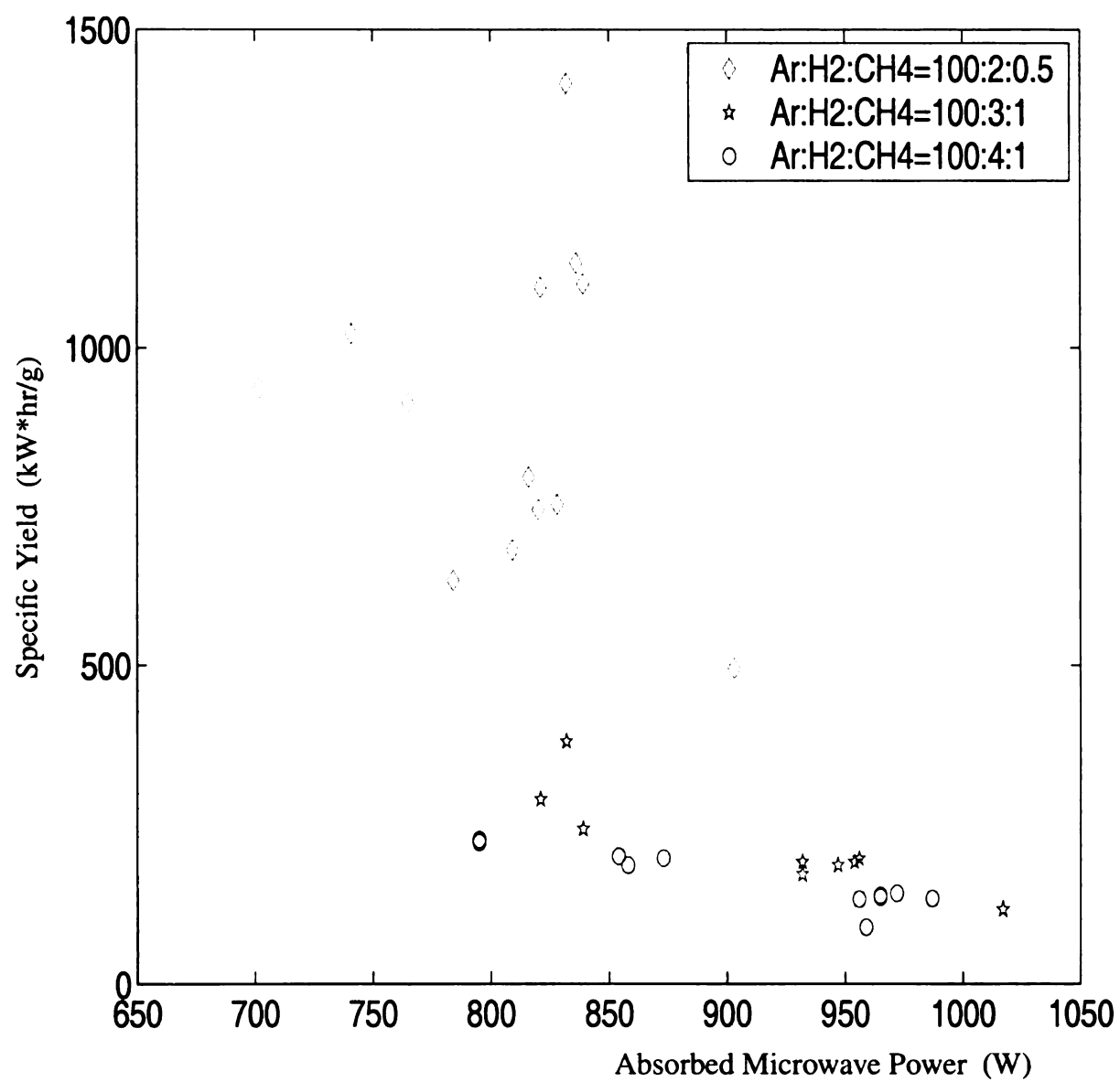


FIGURE 4.11 : SPECIFIC YIELD VS. MICROWAVE POWER  
Deposition time=8 hours by system I

#### 4.2.4 Carbon Conversion Efficiency = $g(\text{Ar}/\text{H}_2/\text{CH}_4, t, f_t, p, P_{\text{abs}})$

The carbon conversion efficiency is a measure of how many of the input carbon atoms that are actually converted to diamond in the ultra-nanocrystalline diamond films.

Figure 4.12 displays the carbon conversion efficiency versus the percentage of hydrogen input gas. These experiments were performed at a constant pressure of 120 Torr and deposition time of 8 hours. The argon concentration was varied from 90.91-98.68%, the  $\text{H}_2$  concentration varied from 0.99-7.27%, and the  $\text{CH}_4$  concentration varied from 0.33-1.85% with the total gas flow rate varied from 102.5-642 sccm. The performance of the reactor's carbon conversion efficiency versus hydrogen concentration is shown in Figure 4.12 and thus defines the carbon conversion efficiency of the system I at the pressure of 120 Torr. In particular, Figure 4.12 shows (i) given a constant  $\text{CH}_4$  concentration, carbon conversion efficiency increases as  $\text{H}_2$  concentration increases, (ii) given a constant  $\text{H}_2$  concentration, carbon conversion efficiency increases as  $\text{CH}_4$  concentration increases.

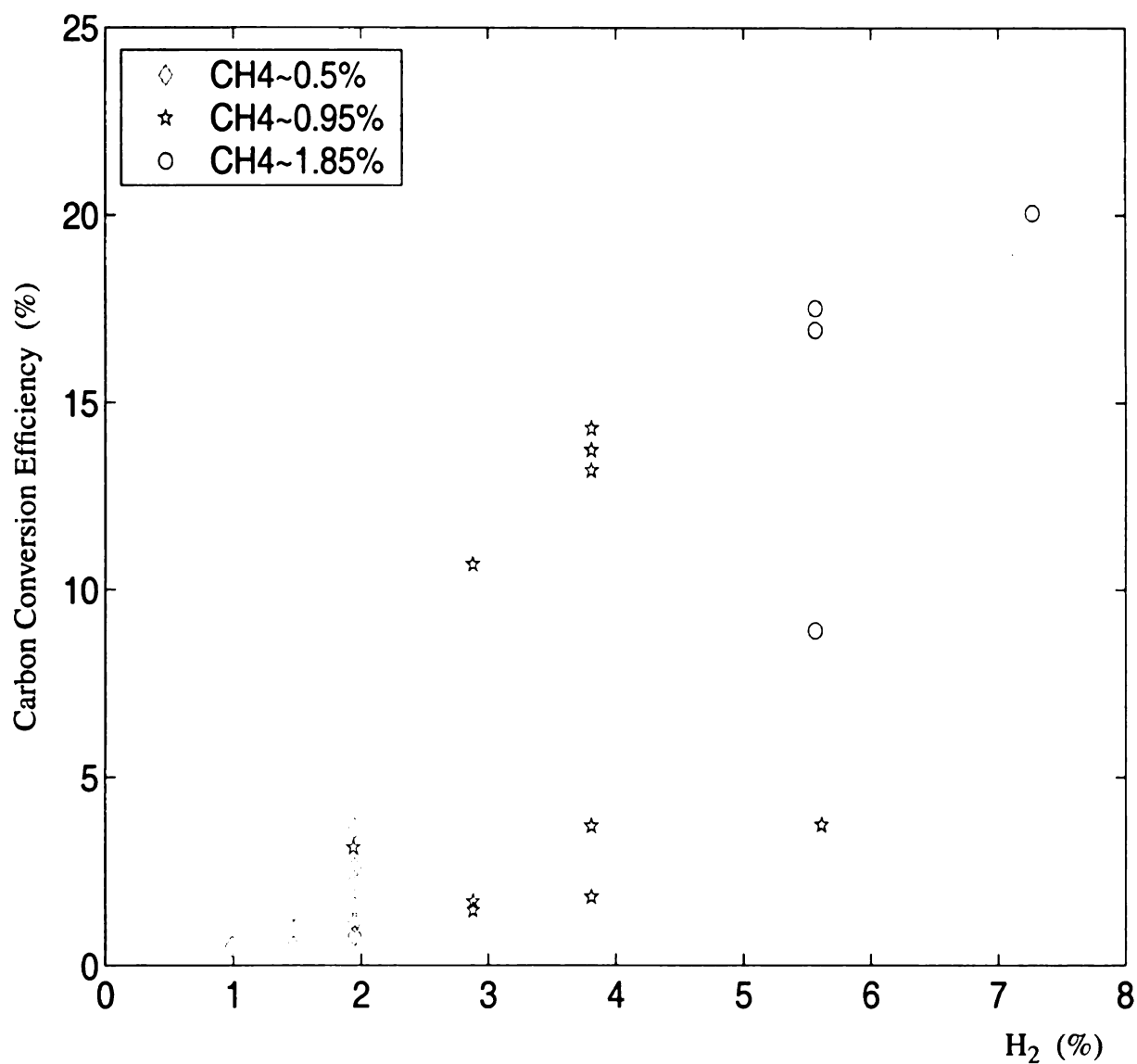


FIGURE 4.12 : CARBON CONVERSION EFFICIENCY VS. HYDROGEN CONCENTRATION

Pressure=120 Torr, deposition time=8 hours,  
 Ar:H<sub>2</sub>:CH<sub>4</sub>=(90.91-98.68):(0.99-7.27):(0.33-1.85)%  
 and total gas flow rate varied from 102.5-642 sccm  
 by system I.

Figure 4.13 displays the carbon conversion efficiency versus the deposition time,  $t$ , with pressure at 120 Torr,  $\text{Ar:H}_2\text{:CH}_4 = 100:2:0.5$ , and  $f_t = 615$  sccm. As shown, the carbon conversion efficiency increased about 20% from an 8 hour run to a 24 hour run. Since carbon conversion efficiency is proportional to total growth rate, the lower carbon conversion efficiency in the shorter deposition time region is a reflection of the lower growth rate.

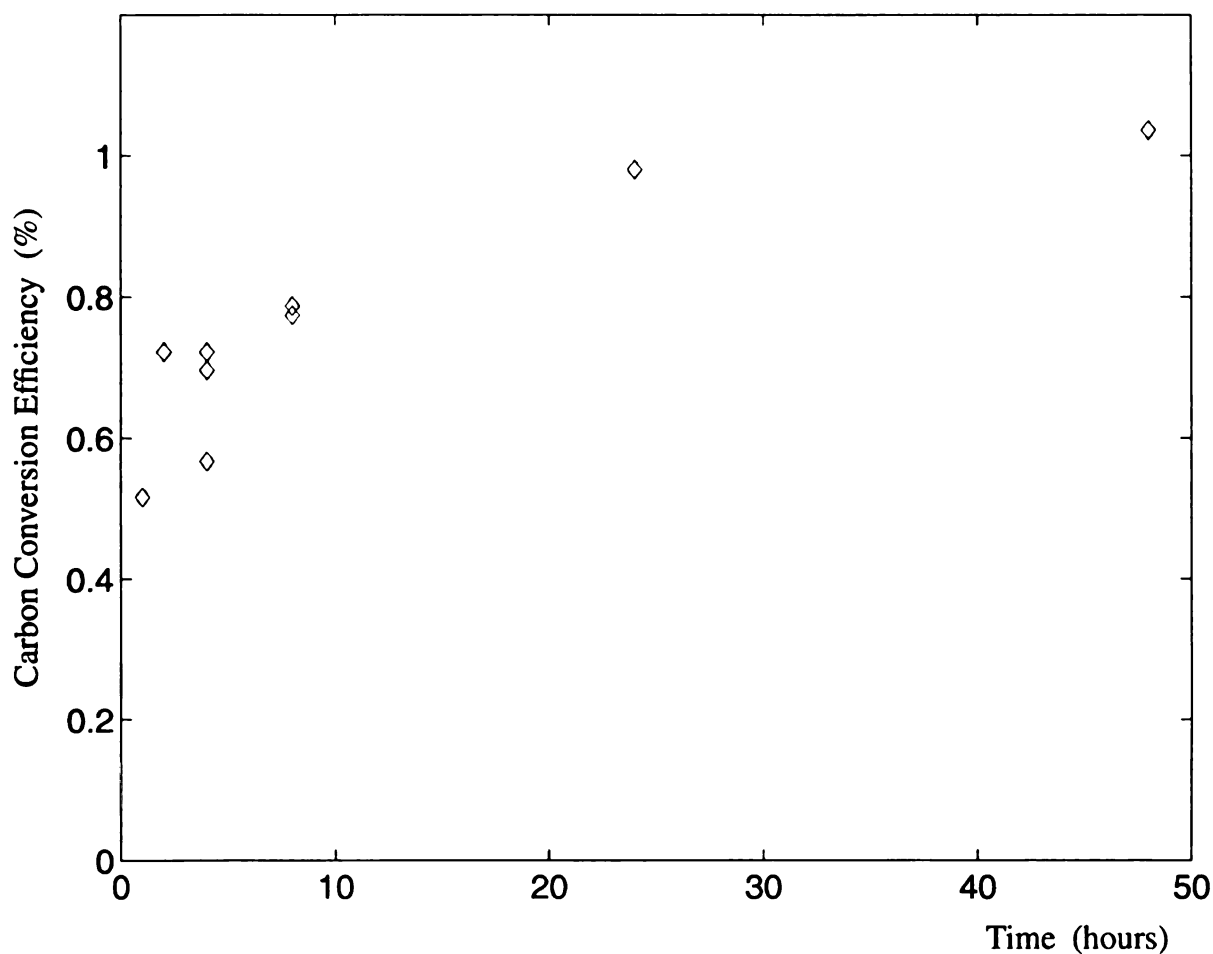


FIGURE 4.13 : CARBON CONVERSION EFFICIENCY VS.  
DEPOSITION TIME  
Pressure=120 Torr,  $\text{Ar:H}_2\text{:CH}_4 = 100:2:0.5$ , and  $f_t = 615$  sccm by system I

Figure 4.14 displays the carbon conversion efficiency versus total gas flow rate,  $f_t$ , with pressure at 140 Torr and deposition time of 8 hours and indicates that carbon conversion efficiency increases as total gas flow rate decreases. The carbon conversion efficiency increases dramatically at low-total-gas-flow-rates. The carbon conversion efficiency of 100 sccm total gas flow rate is over 5 times than 600 sccm total gas flow rate. The carbon conversion efficiency is affected by both gas chemistry and total gas flow rate.

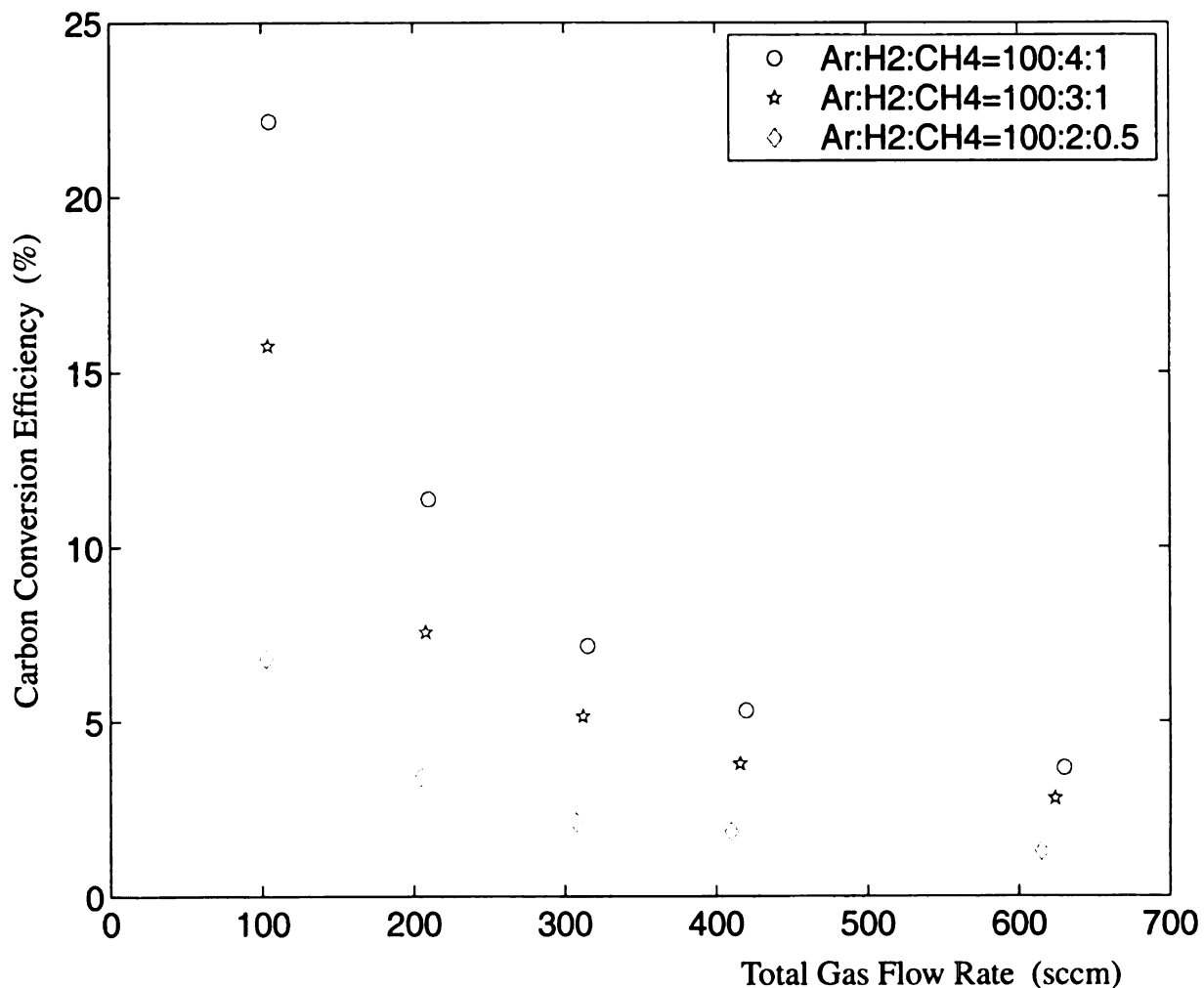


FIGURE 4.14 : CARBON CONVERSION EFFICIENCY VS.  
TOTAL GAS FLOW RATE  
Pressure=140 Torr and deposition time=8 hours by system I



Figure 4.15 and 4.16 display the carbon conversion efficiency versus deposition pressure,  $p$ , and absorbed microwave power,  $P_{\text{abs}}$ , respectively, with deposition time of 8 hours. As shown in Figure 4.15, the carbon conversion efficiency increases with increases in deposition pressure. With a fixed pressure, higher hydrogen and methane concentration usually result in higher carbon conversion efficiency. This result is consistent with the data in Figure 4.12. The fluctuation of the data points is caused by different total gas flow rates. In Figure 4.16, the carbon conversion efficiency of the experiments with gas chemistry ratio of  $\text{Ar:H}_2\text{:CH}_4=100:2:0.5$  increase as the absorbed microwave power increases from 702W to 903 W. The carbon conversion efficiency of those experiments with gas chemistry ratios of  $\text{Ar:H}_2\text{:CH}_4=100:3:1$  and  $100:4:1$  increase rapidly as the absorbed microwave power increases from 795W to 1017 W.

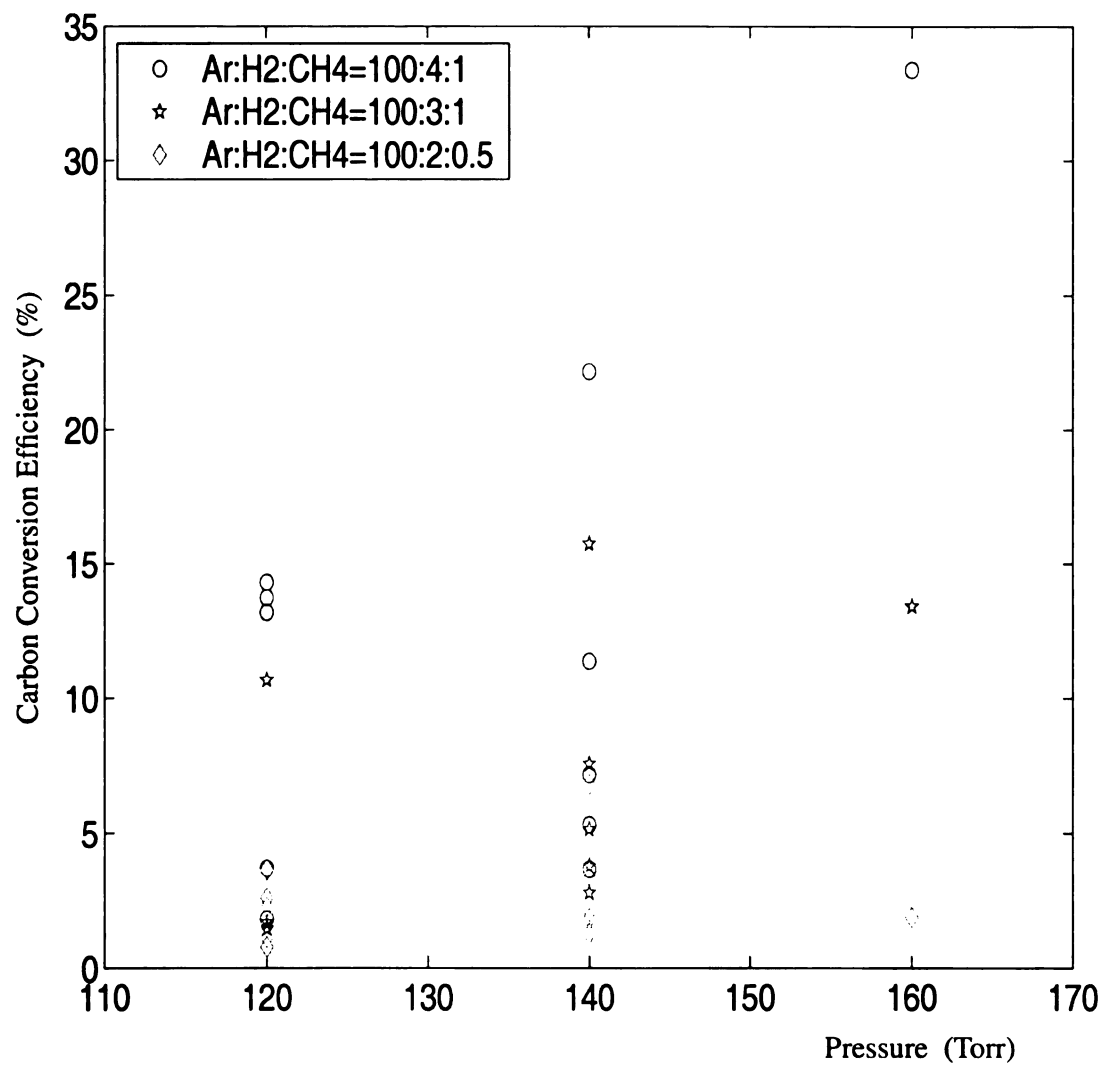


FIGURE 4.15 : CARBON CONVERSION EFFICIENCY VS.  
DEPOSITION PRESSURE  
Deposition time=8 hours by system I

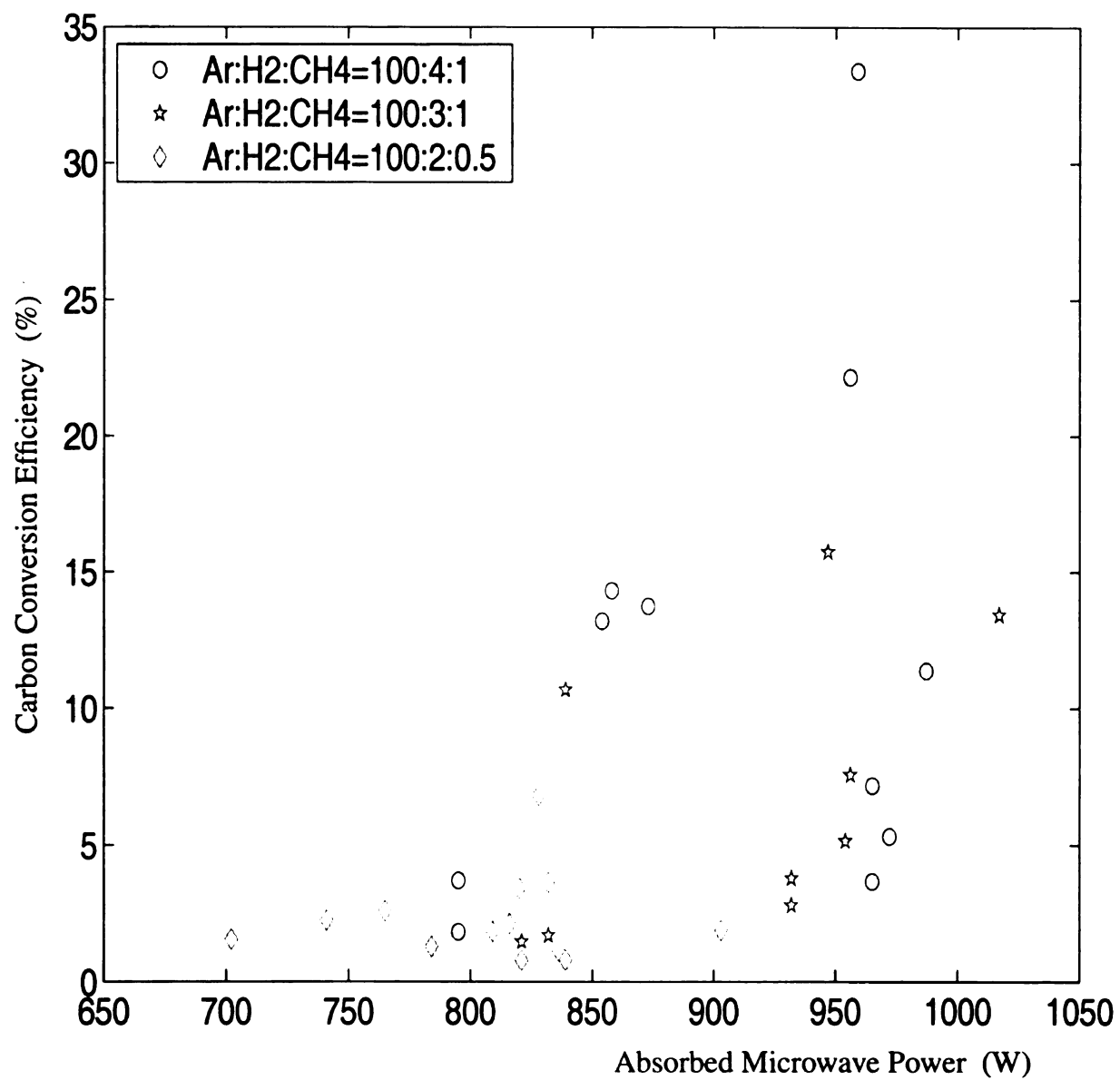


FIGURE 4.16 : CARBON CONVERSION EFFICIENCY VS.  
MICROWAVE POWER  
Deposition time=8 hours by system I

## 4.3 System II

### 4.3.1 Introduction

Based upon the “optimized” experimental results from system I, the thermally floating substrate holder setup with quartz tube height of about 50 mm was used for the synthesis of ultra-nanocrystalline diamond films in system II. The temperature of the Neslab chiller of system II was set at 15°C; i.e. it was set (1) to be close to the temperature of the water cooling in system I in order to provide a similar growth environment as system I, and (2) to provide a safe condition for the higher pressure regime experiments. The substrate temperature measurements of the experiments conducted in system II were performed by using a pyrometer directed at the mirror (see Figure 3.8). According to the results from system I, the higher total gas flow rate (1) does not increase the grow rate, and (2) has lower carbon conversion efficiency. Therefore, most of the experiments performed with system II had a total gas flow rate of ~100 sccm. The experimental data for Section 4.3 is given in detail in Appendix 9.2. Using the system II and operating under 240 Torr, the discharge is flame free.

### 4.3.2 Total Growth Rate = $g(\text{Ar}/\text{H}_2/\text{CH}_4, t, f_t, p, P_{\text{abs}}, T_s)$

Figure 4.17 displays the total growth rate versus hydrogen flow rate with all other variables held constant, i.e. argon flow rate is fixed at 100 sccm, methane flow rate is fixed at 1 sccm, the pressure is held constant at 120 Torr and deposition time is 8 hours. As shown, the total growth rate increases from 2.06 mg/hr to 5.4 mg/hr when the hydrogen flow rate is varied from 0 to 10 sccm.

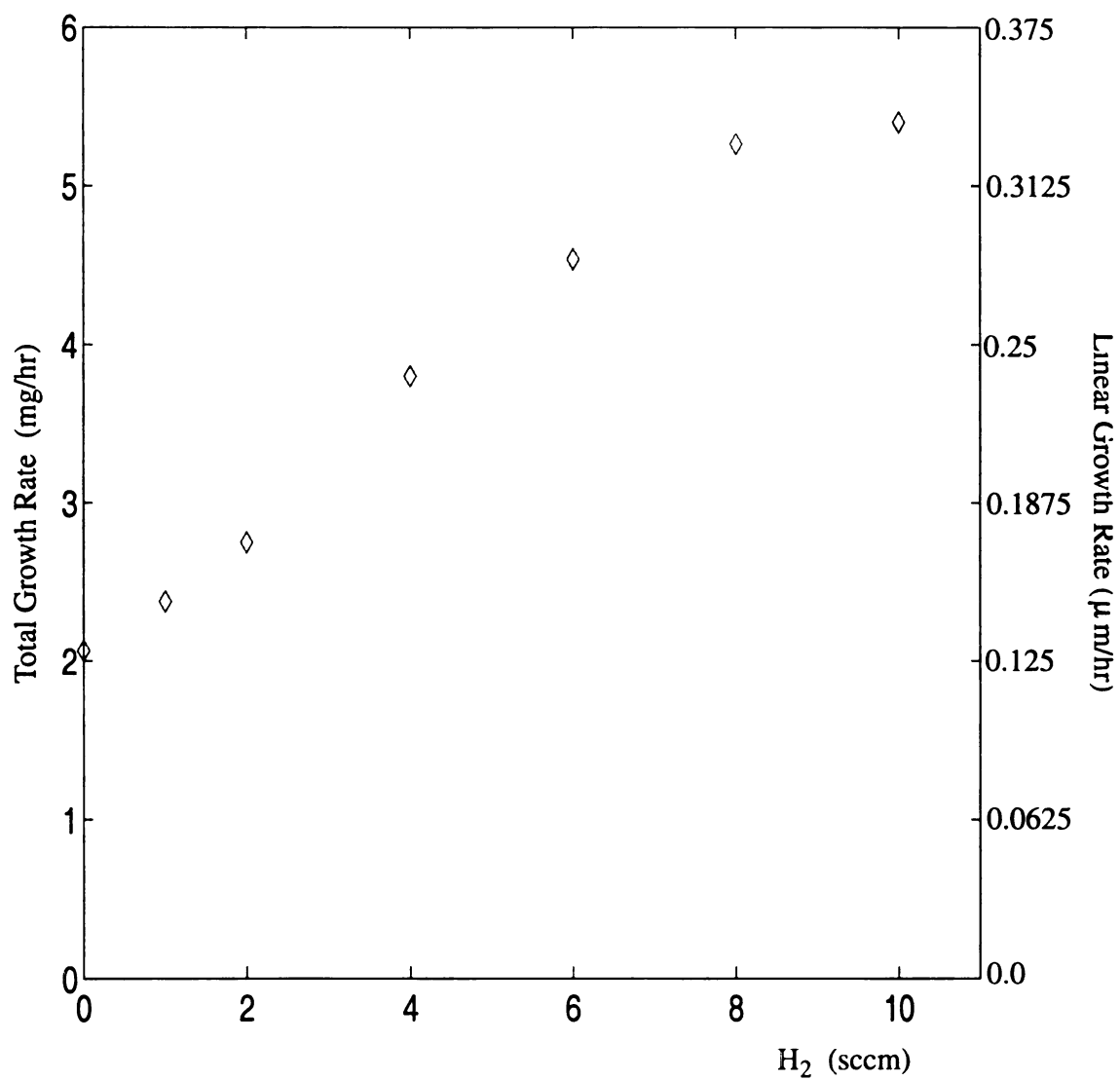


FIGURE 4.17 : TOTAL GROWTH RATE VS. H<sub>2</sub> FLOW RATE  
Pressure=120 Torr, Ar=100 sccm, CH<sub>4</sub>=1 sccm and deposition time=8 hours  
by system II

In order to understand why the hydrogen concentration had such a contribution to total growth rate of ultra-nanocrystalline diamond synthesis, the study of the influence of the hydrogen concentration on substrate temperature and absorbed microwave power was performed as shown in Figure 4.18. Figure 4.18(a) shows that the substrate temperature increases as hydrogen concentration increases. Figure 4.18(b) shows the absorbed microwave power increases as hydrogen flow rate increases. Overall, higher hydrogen concentration has increased the substrate temperature and absorbed microwave power directly and indirectly. The covered area by the plasma was about the same.

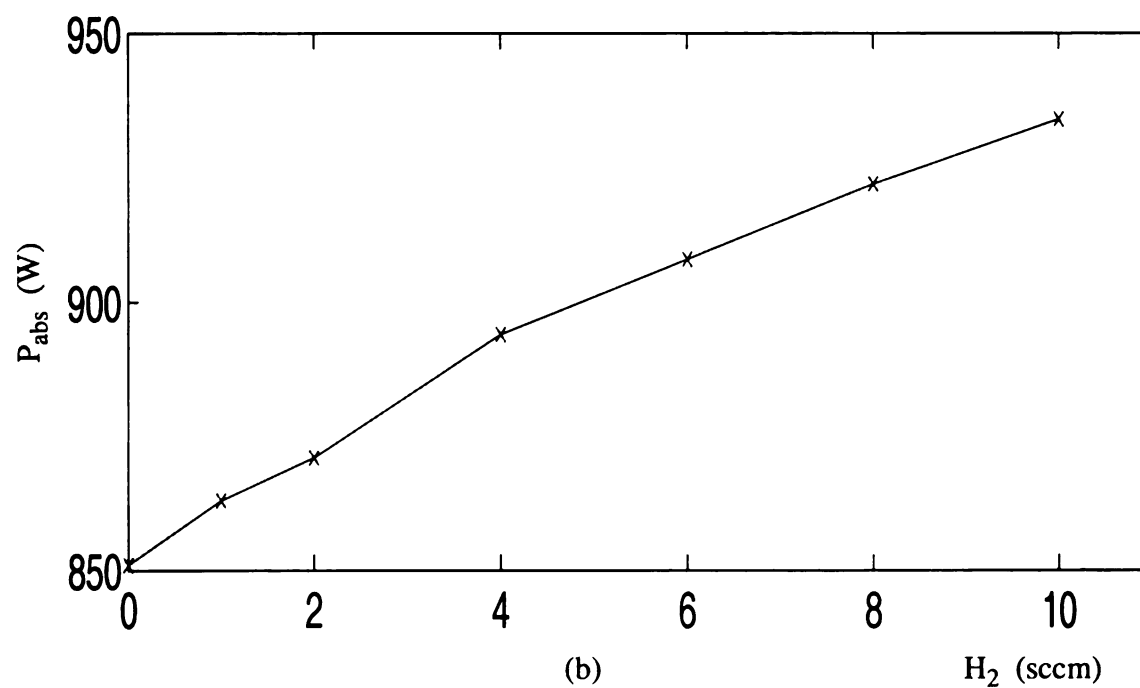
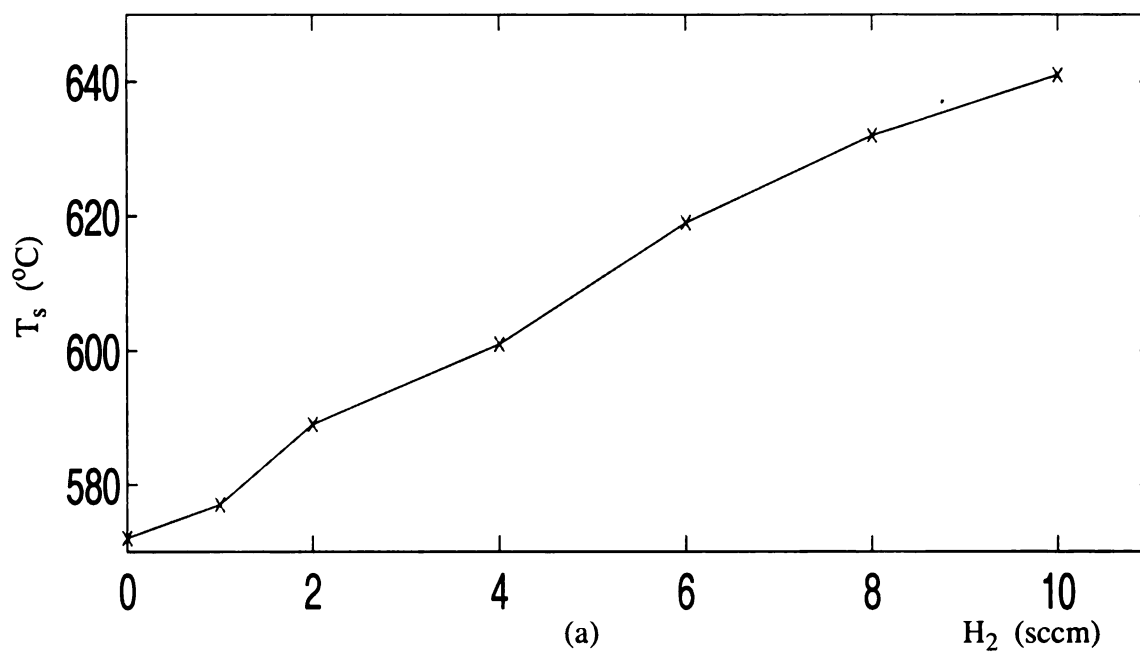


FIGURE 4.18 : THE INFLUENCE OF  $H_2$  FLOW RATE ON  $T_s$  AND  $P_{abs}$   
 $Ar=100$  sccm,  $CH_4=1$  sccm and pressure=120 Torr by system II

Figure 4.19 displays the total growth rate versus the deposition time,  $t$ , with pressure at 160 Torr and  $\text{Ar}/\text{H}_2/\text{CH}_4 = 100/4/1$  sccm. As shown, the growth rate is approximately constant between 8 hour and 25 hour experiments. The experiments here were not done with the same quartz dome and that could affect the growth rate slightly. Therefore, the data points fluctuate a little. With these exploratory experiments, one can notice that system II does not behave the same as system I (See Figure 4.3).

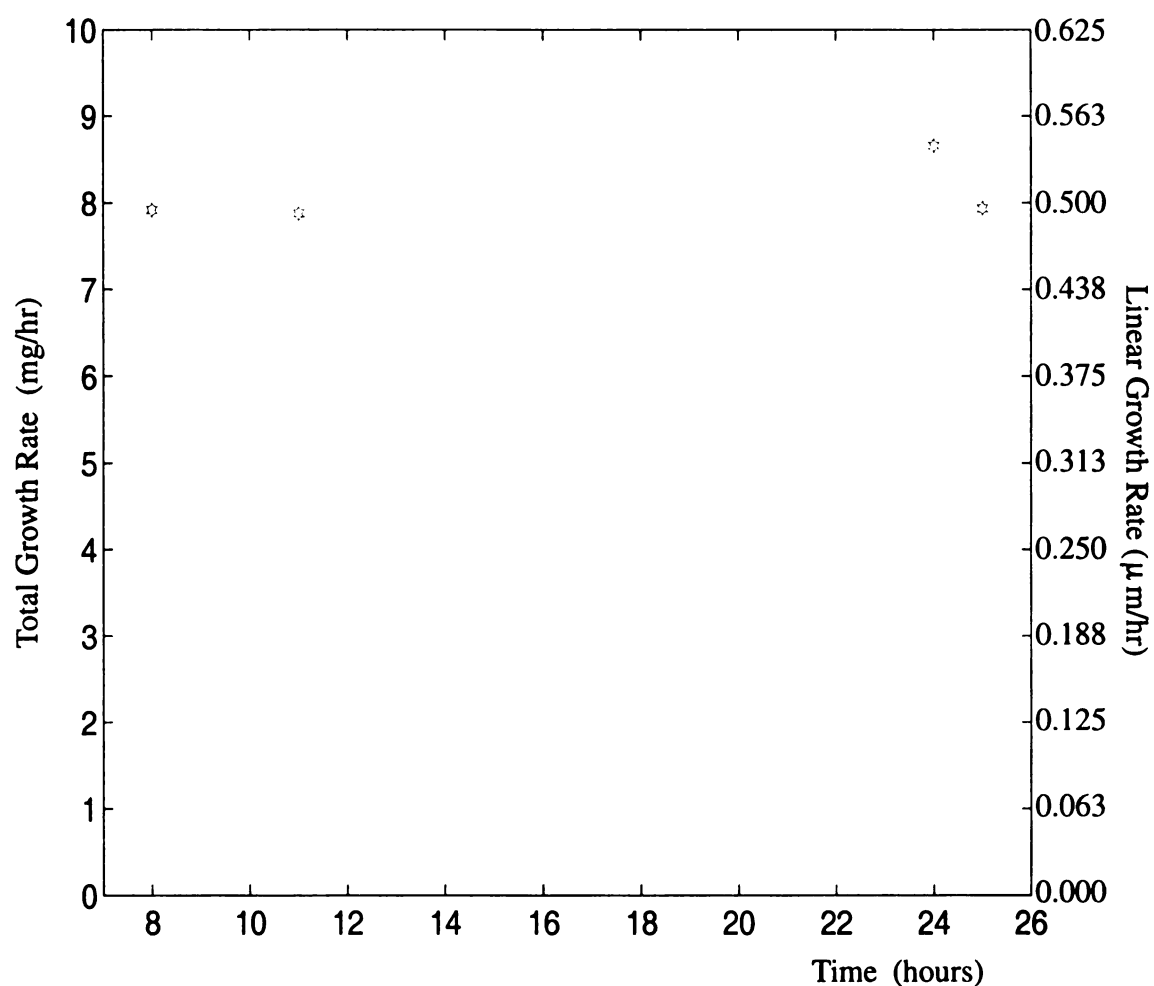
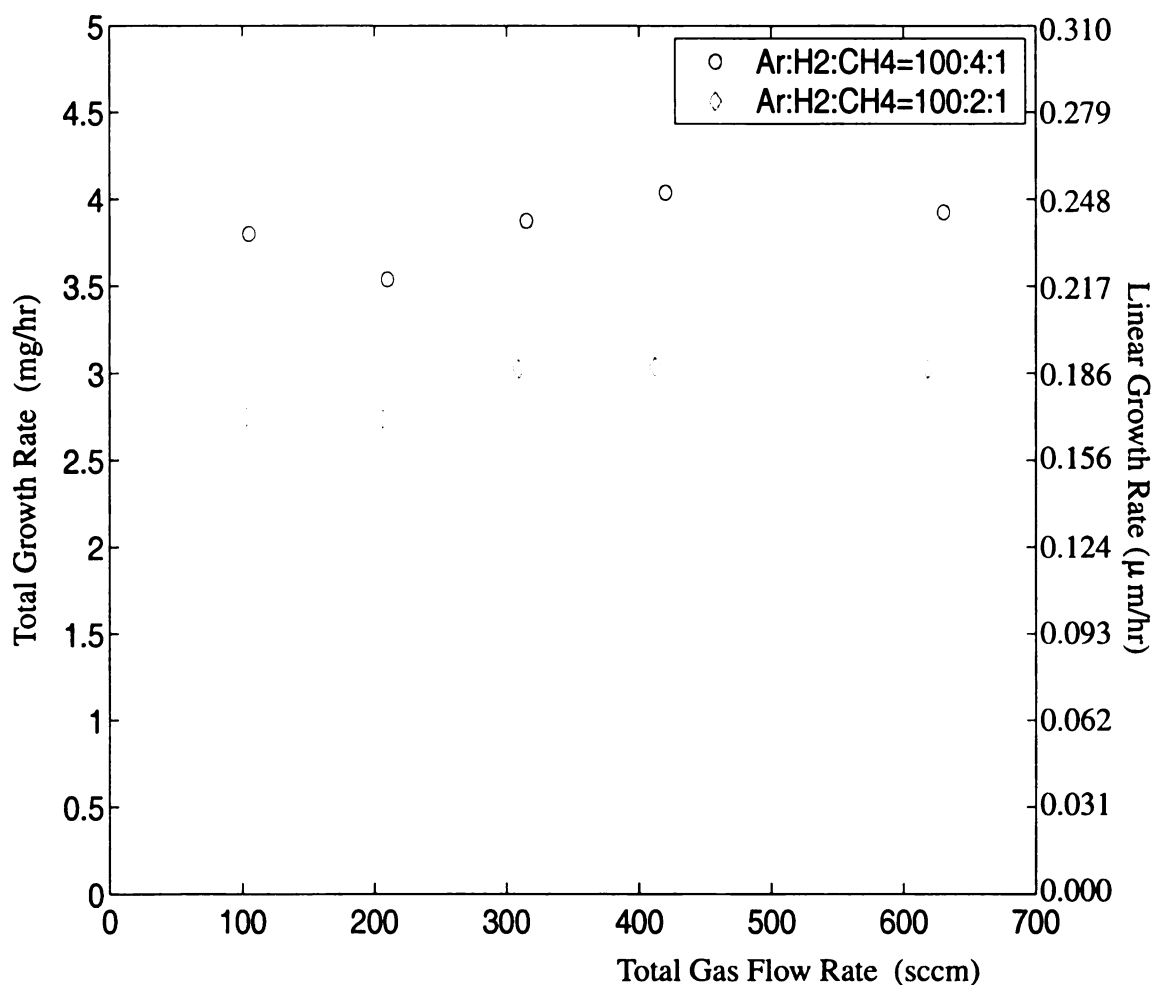


FIGURE 4.19 : TOTAL GROWTH RATE VS. DEPOSITION TIME  
Pressure=160 Torr and  $\text{Ar}/\text{H}_2/\text{CH}_4=100/4/1$  sccm by system II



Figure 4.20 displays the total growth rate versus total gas flow rate,  $f_t$ , with pressure at 120 Torr and deposition time of 8 hours and it indicates that the total gas flow rate does not influence the growth rate. This result is similar to system I but the high-total-gas-flow-rate experiments run at system II did not have flames in the plasma discharge as it sometimes happened in system I. Also, the plasma with this gas chemistry ratio,  $\text{Ar:H}_2\text{:CH}_4 = 100:2:1$  was unable to be stabilized in system I.



**FIGURE 4.20 : TOTAL GROWTH RATE VS. TOTAL GAS FLOW RATE**  
 Pressure=120 Torr and deposition time=8 hours by system II.

The study result of the influence of the total gas flow rate on substrate temperature and absorbed microwave power is shown in Figure 4.21. Figure 4.21(a) indicates that the total gas flow rate has little influence on substrate temperature. Figure 4.21(b) indicates that the total gas flow rate has no influence on absorbed microwave power. Total gas flow rate has no effect on absorbed microwave power and very little influence on substrate temperature.

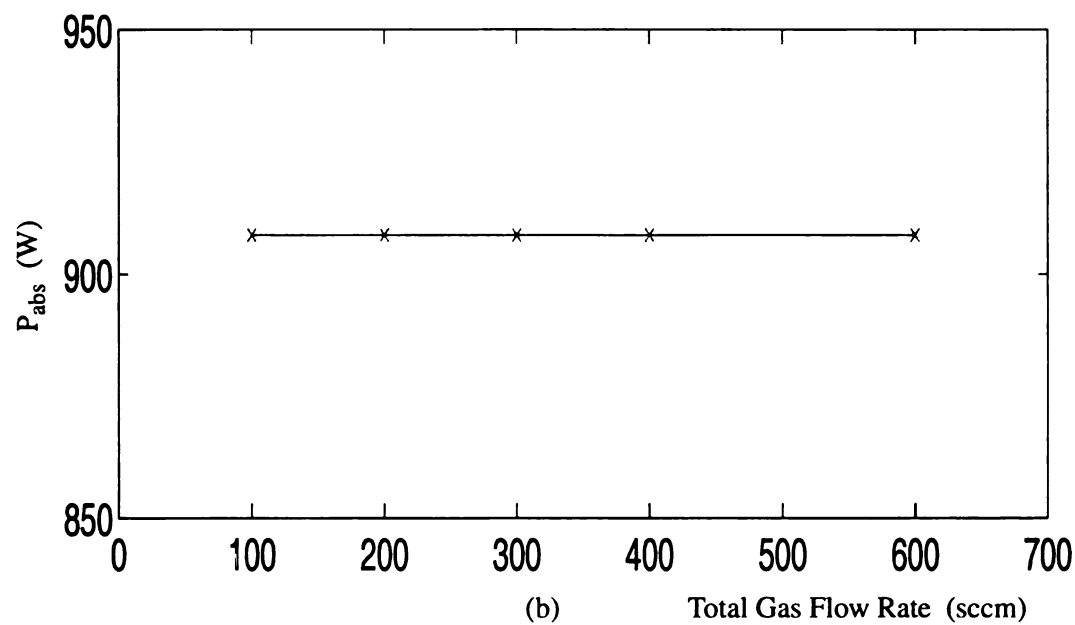
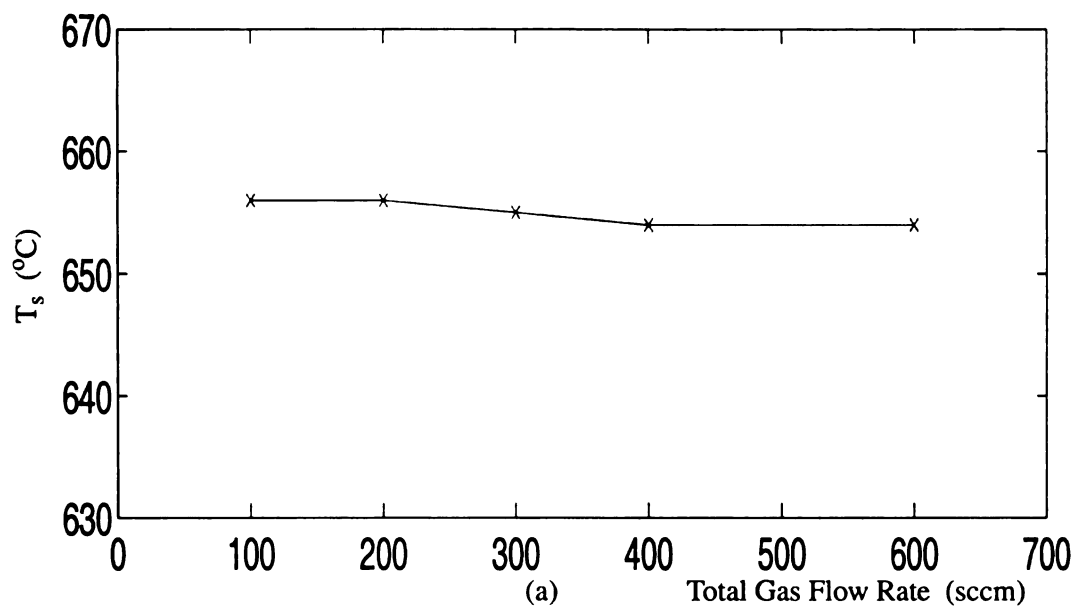


FIGURE 4.21 : THE INFLUENCE OF TOTAL GAS FLOW RATE ON  
 $T_s$  and  $P_{abs}$   
Ar:H<sub>2</sub>:CH<sub>4</sub>=100:4:1 and pressure=120 Torr by system II.

Figure 4.22 and 4.23 display the total growth rate versus deposition pressure,  $p$ , and absorbed microwave power,  $P_{\text{abs}}$ , respectively, with argon flow equal to 100 sccm, methane flow equal to 1 sccm and deposition time of 8 hours. Because at a constant input power, the discharge area  $A_d$  decreased with the deposition pressure,  $p$ . Same methodology as in system I, while the ultra-nanocrystalline diamond films were synthesized with system II, the microwave power input was increased as the pressure increased to maintain a discharge area  $A_d$  that covered the three inch substrates.

As shown in Figure 4.22, the total growth rate increases as pressure increases and the higher hydrogen concentrations generally produce higher growth rate at the same pressure. A small flame starts to show at the center of the plasma at different pressure for each different hydrogen gas flow rate. For the experiments of  $H_2=4$  sccm, it's around 240 Torr. For the experiments of  $H_2=2$  sccm, it's around 220 Torr. For the experiments of  $H_2=1$  and 0 sccm, it's around 200 Torr. It has been investigated that adding more power can reduce the flame but the operator should be careful not to overheat the reactor at higher pressure region. In Figure 4.23, the growth rate increases with increases in absorbed microwave power. But at the same time, the deposition pressure is increased, too. The contribution can come from either deposition pressure or absorbed microwave power. At a fixed pressure, those experiments with higher hydrogen concentration have higher absorbed microwave power.

As we have learned from Figure 3.12, the substrate temperature increases with increases in pressure and absorbed microwave power. This explains why the growth rate

increases with increases in pressure and absorbed microwave power. For the values of data points, please see appendix.

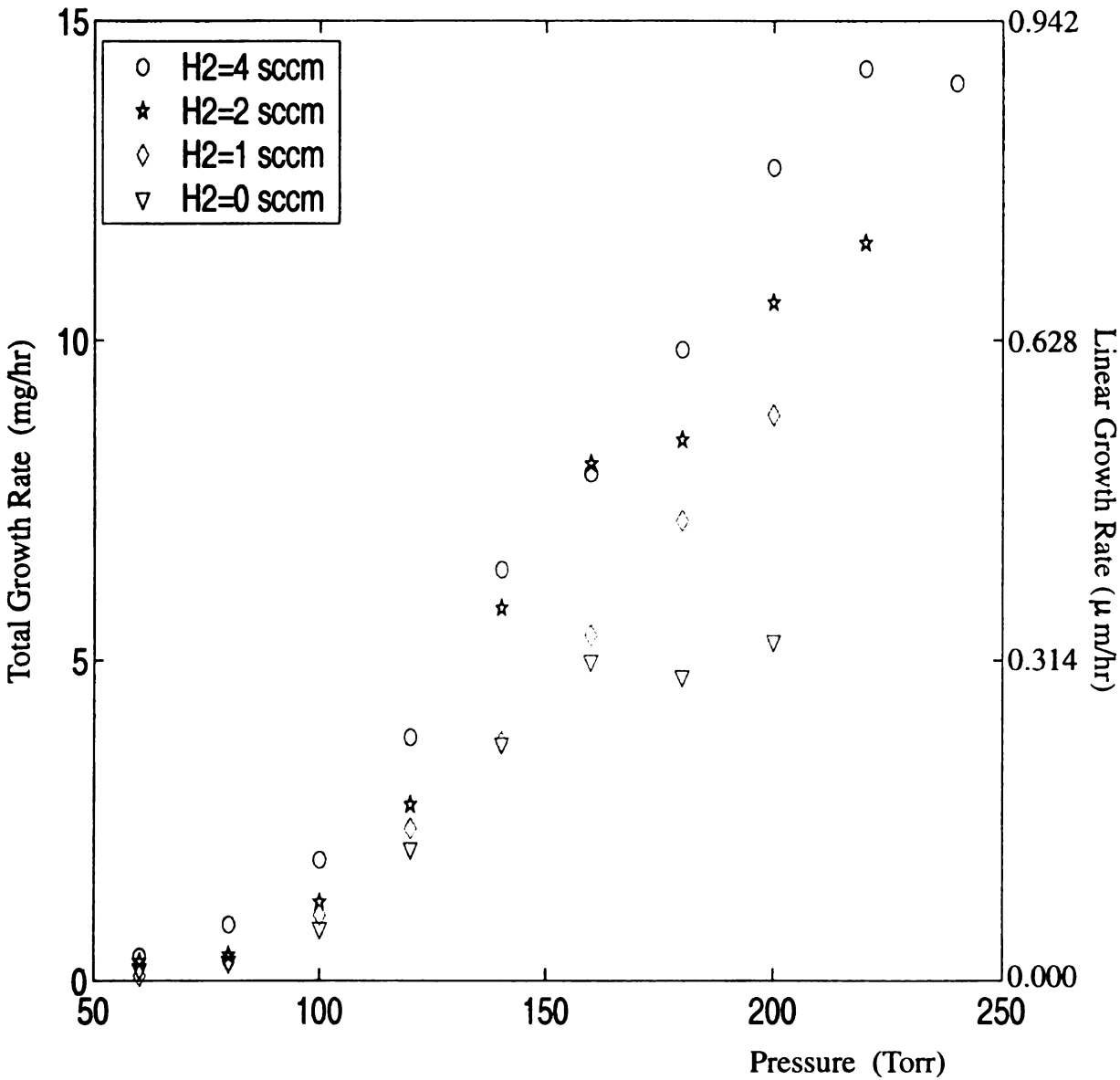


FIGURE 4.22 : TOTAL GROWTH RATE VS. PRESSURE  
Ar=100 sccm, CH<sub>4</sub>=1 sccm and deposition time=8 hours by system II.

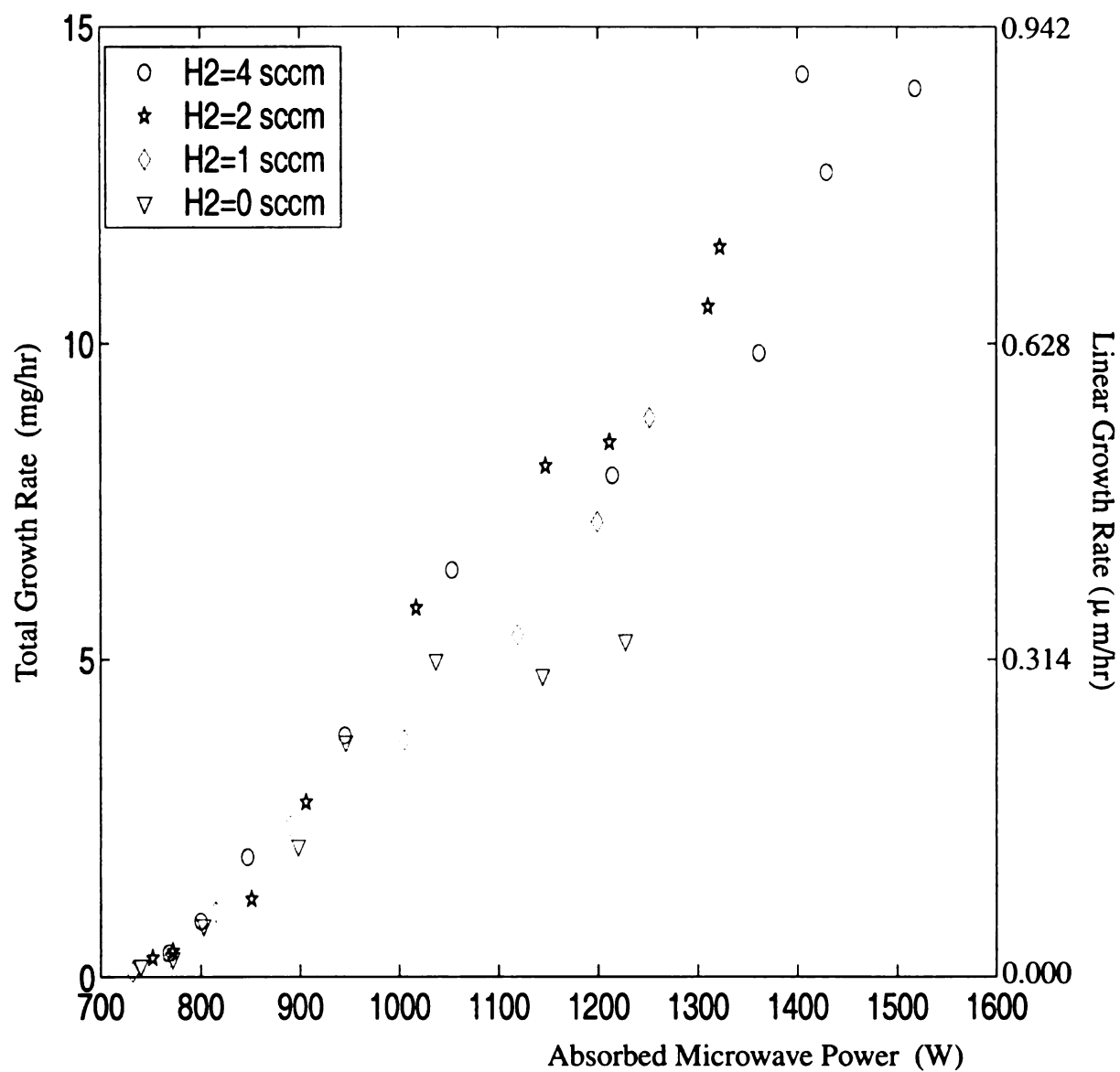


FIGURE 4.23 : TOTAL GROWTH RATE VS. MICROWAVE POWER  
Ar=100 sccm, CH<sub>4</sub>=1 sccm and deposition time=8 hours by system II.

### 4.3.3 Specific Yield= $g(\text{Ar}/\text{H}_2/\text{CH}_4, t, f_t, p, P_{\text{abs}})$

Figure 4.24 displays the specific yield versus hydrogen flow rate, with argon flow fixed at 100 sccm, methane flow fixed at 1 sccm, pressure at 120 Torr and deposition time of 8 hours by system II. As shown, the specific yield decreases with the increases in the hydrogen concentration.

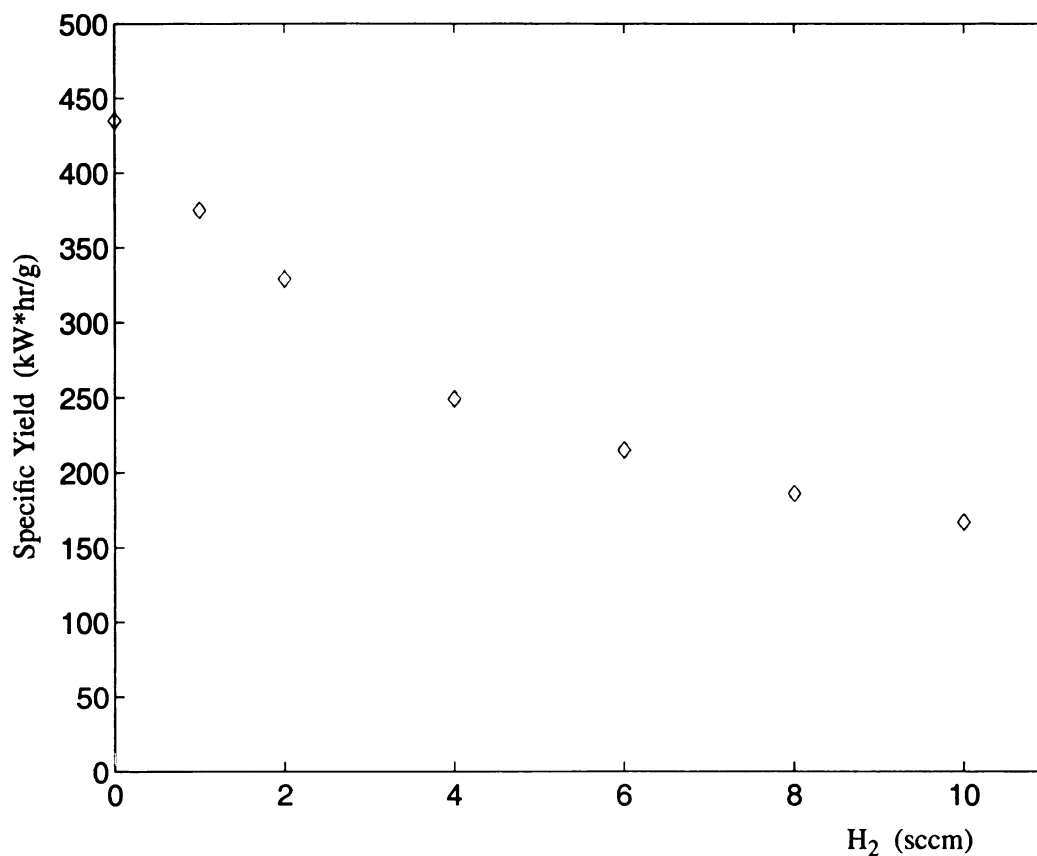
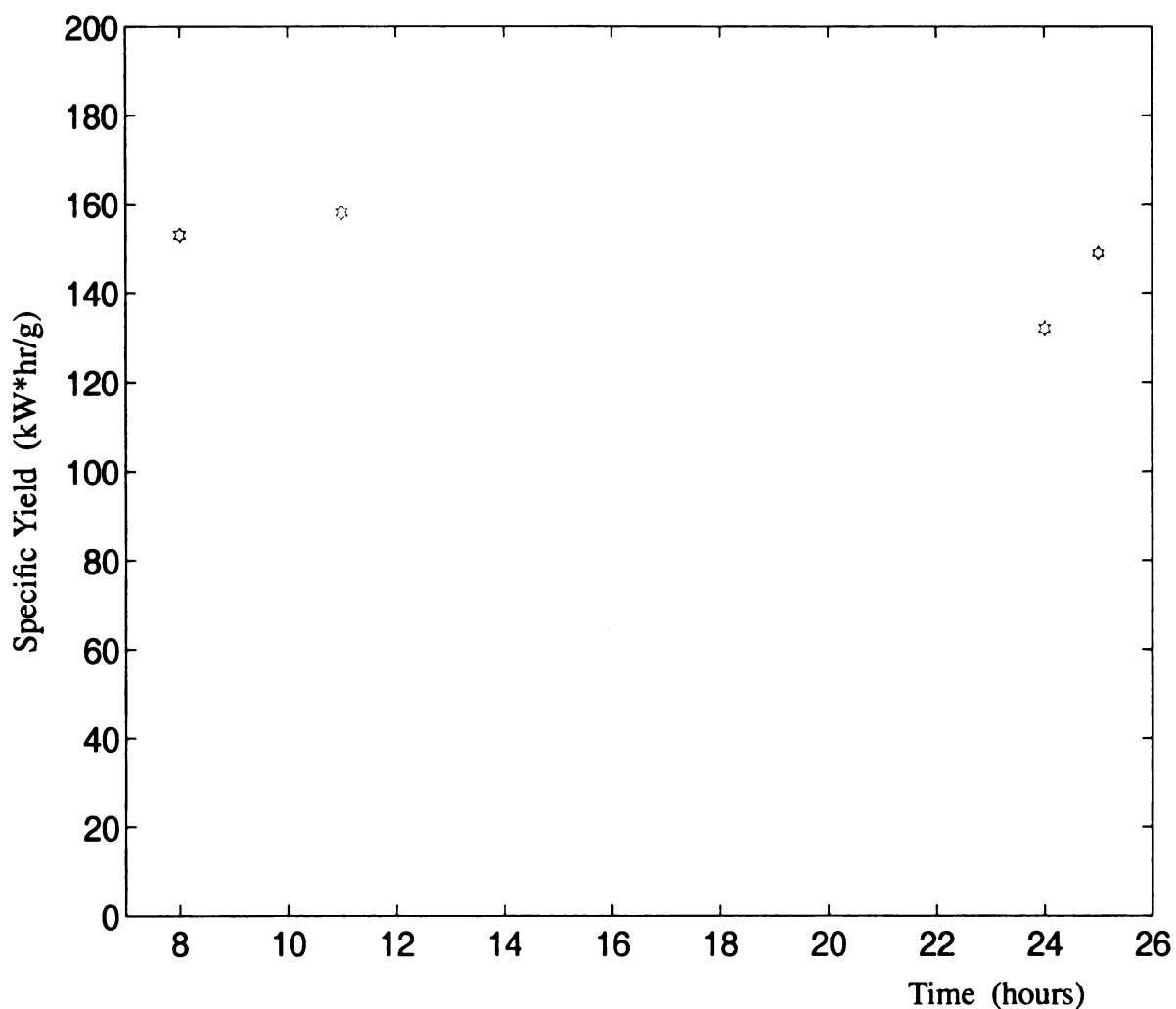


FIGURE 4.24 : SPECIFIC YIELD VS. H<sub>2</sub> FLOW RATE  
Pressure=120 Torr, Ar=100 sccm, CH<sub>4</sub>=1 sccm and deposition time=8 hours  
by system II

Figure 4.25 displays the specific yield versus the deposition time,  $t$ , with pressure at 160 Torr and  $\text{Ar}/\text{H}_2/\text{CH}_4 = 100/4/1$  sccm. As shown, the specific yield was constant between 8 hour and 25 hour experiments.



**FIGURE 4.25 : SPECIFIC YIELD VS. DEPOSITION TIME**  
Pressure=160 Torr and  $\text{Ar}/\text{H}_2/\text{CH}_4 = 100/4/1$  sccm by system II



Figure 4.26 displays the specific yield versus total gas flow rate,  $f_t$ , with pressure at 120 Torr and deposition time of 8 hours and it indicates that the total gas flow rate does not influence the specific yield. The fluctuation of the data points is because the experiments are not performed with the same quartz dome and they may not have the same energy efficiency.

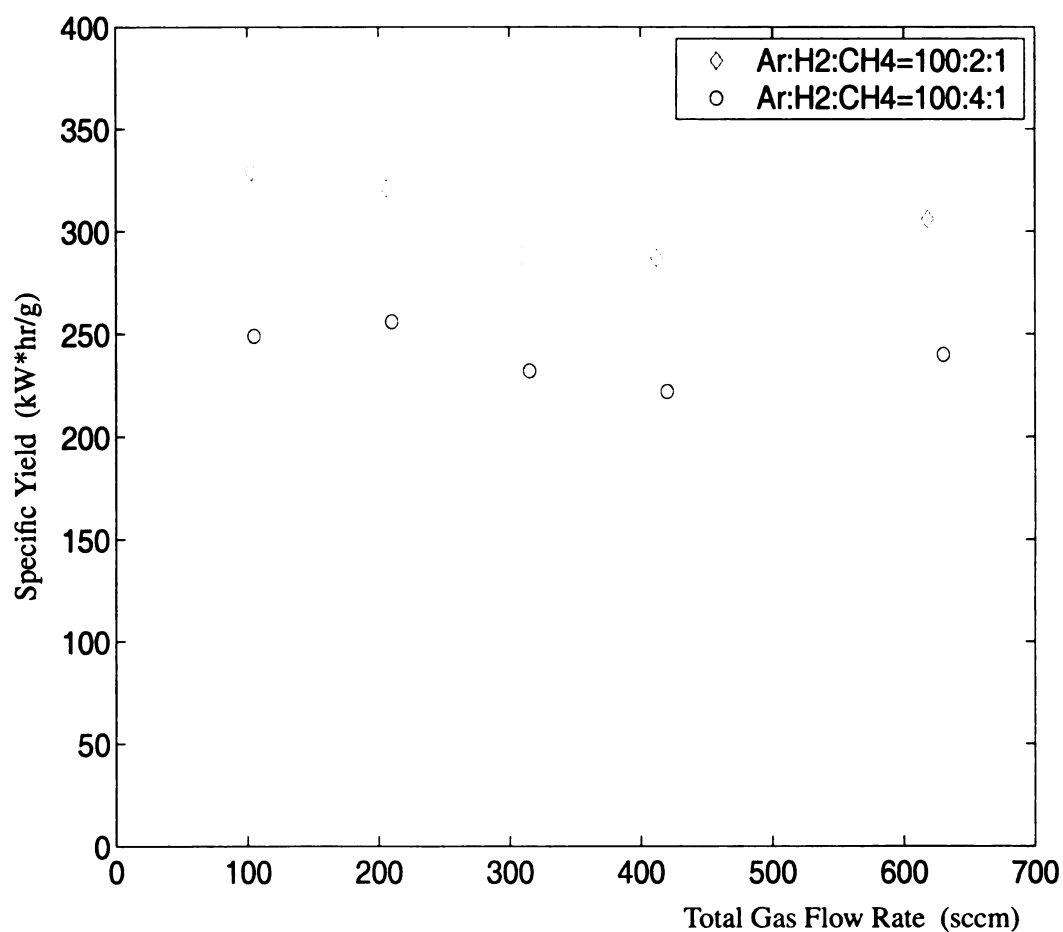


FIGURE 4.26 : SPECIFIC YIELD VS. TOTAL GAS FLOW RATE  
Pressure=120 Torr and deposition time=8 hours by system II.

Figure 4.27 and 4.28 display the specific yield versus deposition pressure,  $p$ , and absorbed microwave power,  $P_{\text{abs}}$ , respectively, with argon flow equal to 100 sccm, methane flow equal to 1 sccm and deposition time of 8 hours. As shown in Figure 4.27, the specific yield decreases as pressure increases. The higher hydrogen concentrations have lower specific yield at a fixed pressure. As a result, the microwave energy efficiency is higher. This result is consistent with the data in Figure 4.24. In Figure 4.28, the specific yield decreases with increases in absorbed microwave power. But meanwhile, the deposition pressure is increased, too. The contribution can come from either deposition pressure or absorbed microwave power.

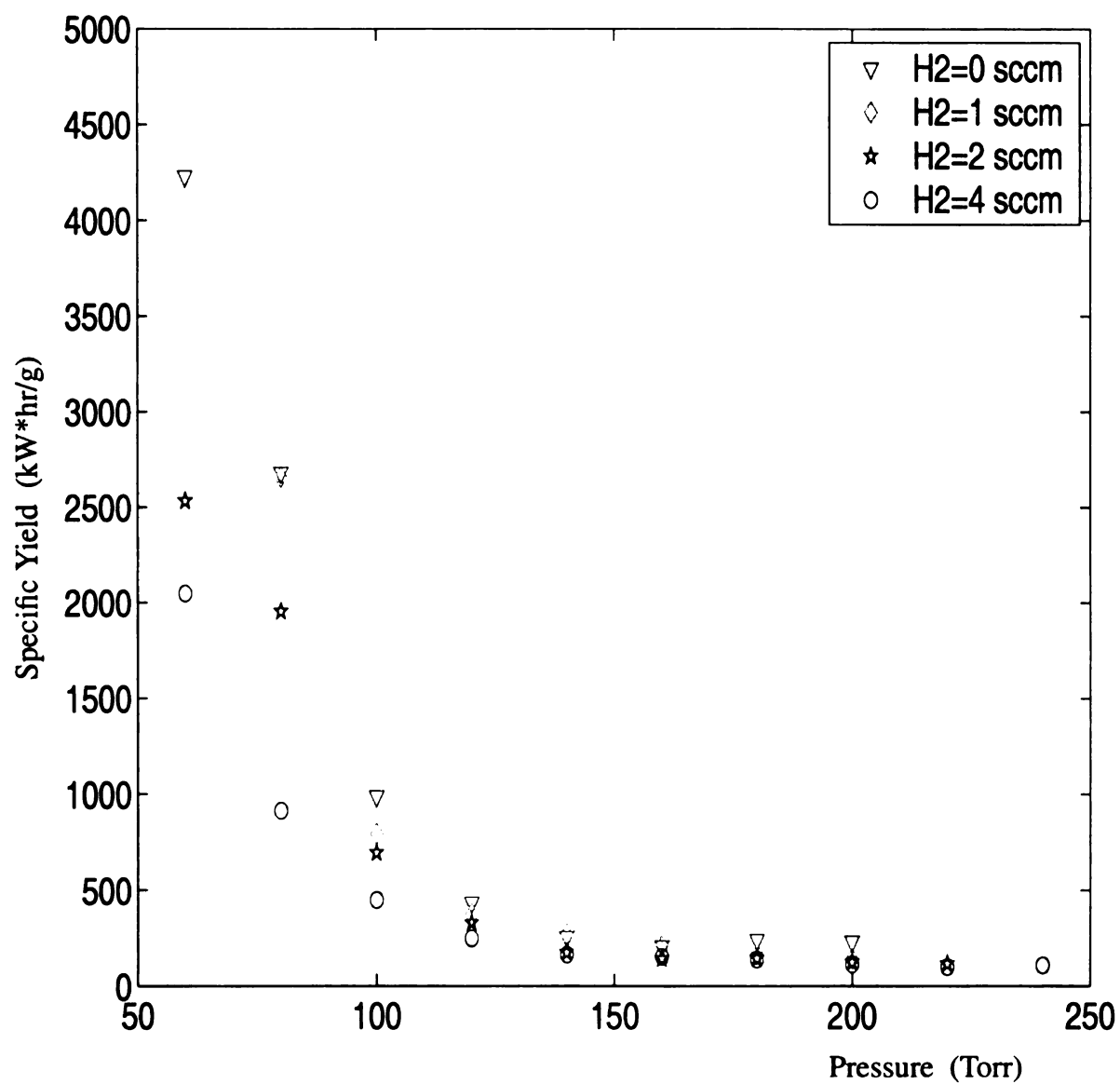


FIGURE 4.27 : SPECIFIC YIELD VS. PRESSURE  
Ar=100 sccm, CH<sub>4</sub>=1 sccm and deposition time=8 hours by system II.

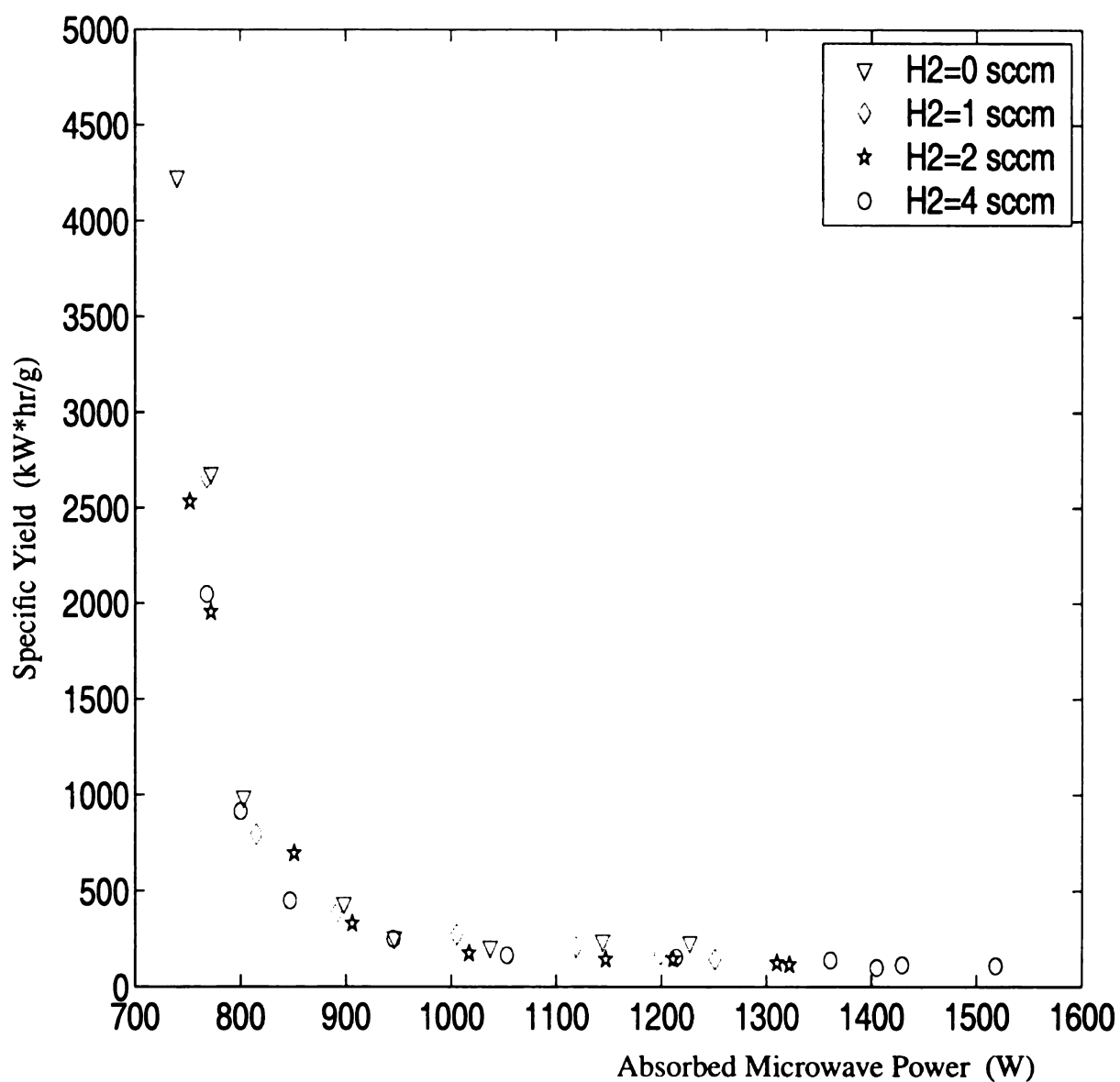


FIGURE 4.28 : SPECIFIC YIELD VS. MICROWAVE POWER  
Ar=100 sccm, CH<sub>4</sub>=1 sccm and deposition time=8 hours by system II.

#### 4.3.4 Carbon Conversion Efficiency = $g(\text{Ar}/\text{H}_2/\text{CH}_4, t, p, P_{\text{abs}})$

Figure 4.29 displays the carbon conversion efficiency versus hydrogen flow rate, with argon flow fixed at 100 sccm, methane flow fixed at 1 sccm, pressure at 120 Torr and deposition time of 8 hours by system II. As shown, the carbon conversion efficiency increases with the increases in the hydrogen concentration.

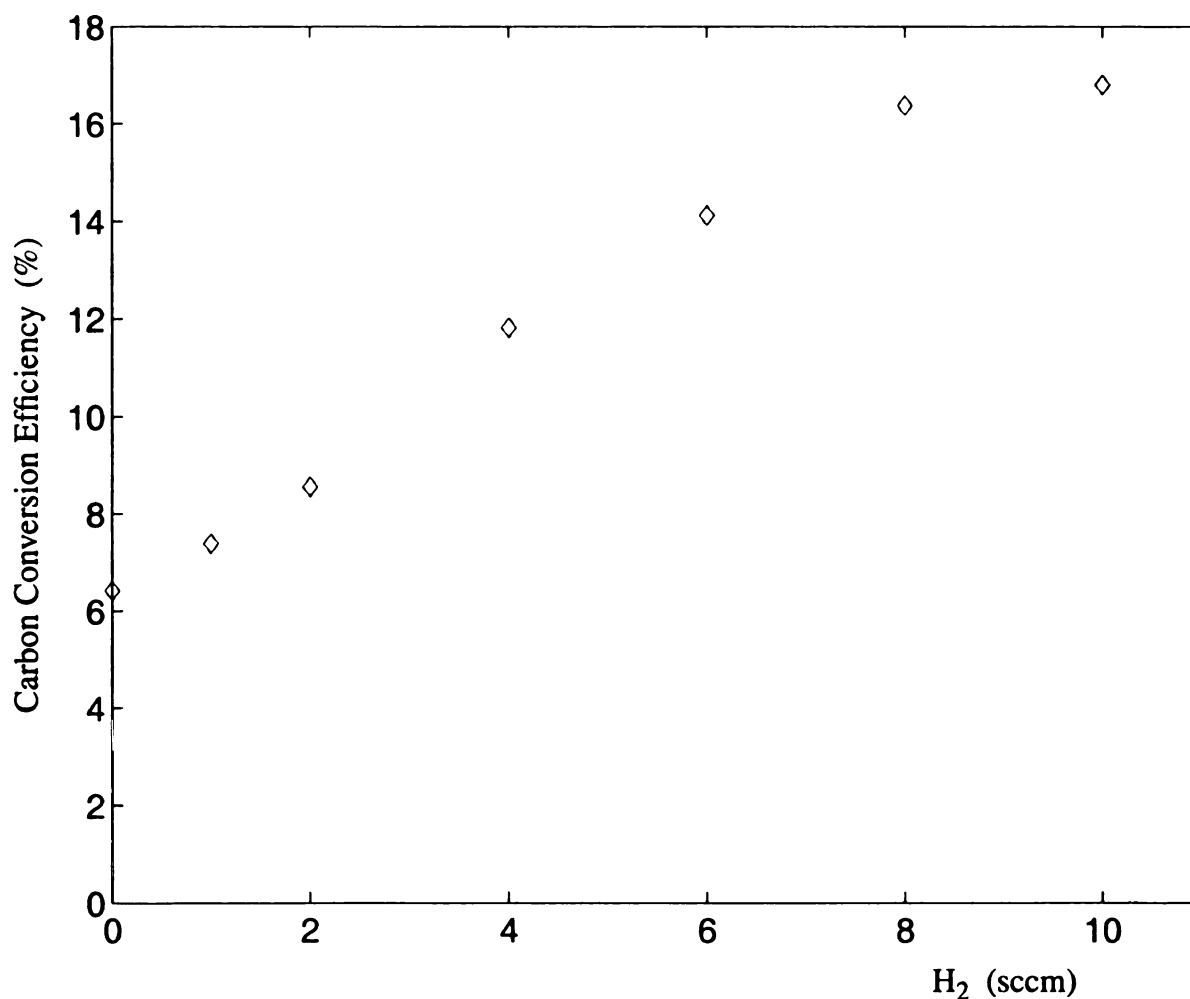


FIGURE 4.29 : CARBON CONVERSION EFFICIENCY VS. H<sub>2</sub> FLOW RATE  
Pressure=120 Torr, Ar=100 sccm, CH<sub>4</sub>=1 sccm and deposition time=8 hours  
by system II

Figure 4.30 displays the carbon conversion efficiency versus the deposition time,  $t$ , with pressure at 160 Torr and  $\text{Ar}/\text{H}_2/\text{CH}_4 = 100/4/1$  sccm. As shown, the carbon conversion efficiency remains constant between 8 hour and 25 hour experiments. The experiments here were not done with the same quartz dome and that could affect the carbon conversion efficiency slightly. Therefore, the data points fluctuate a little.

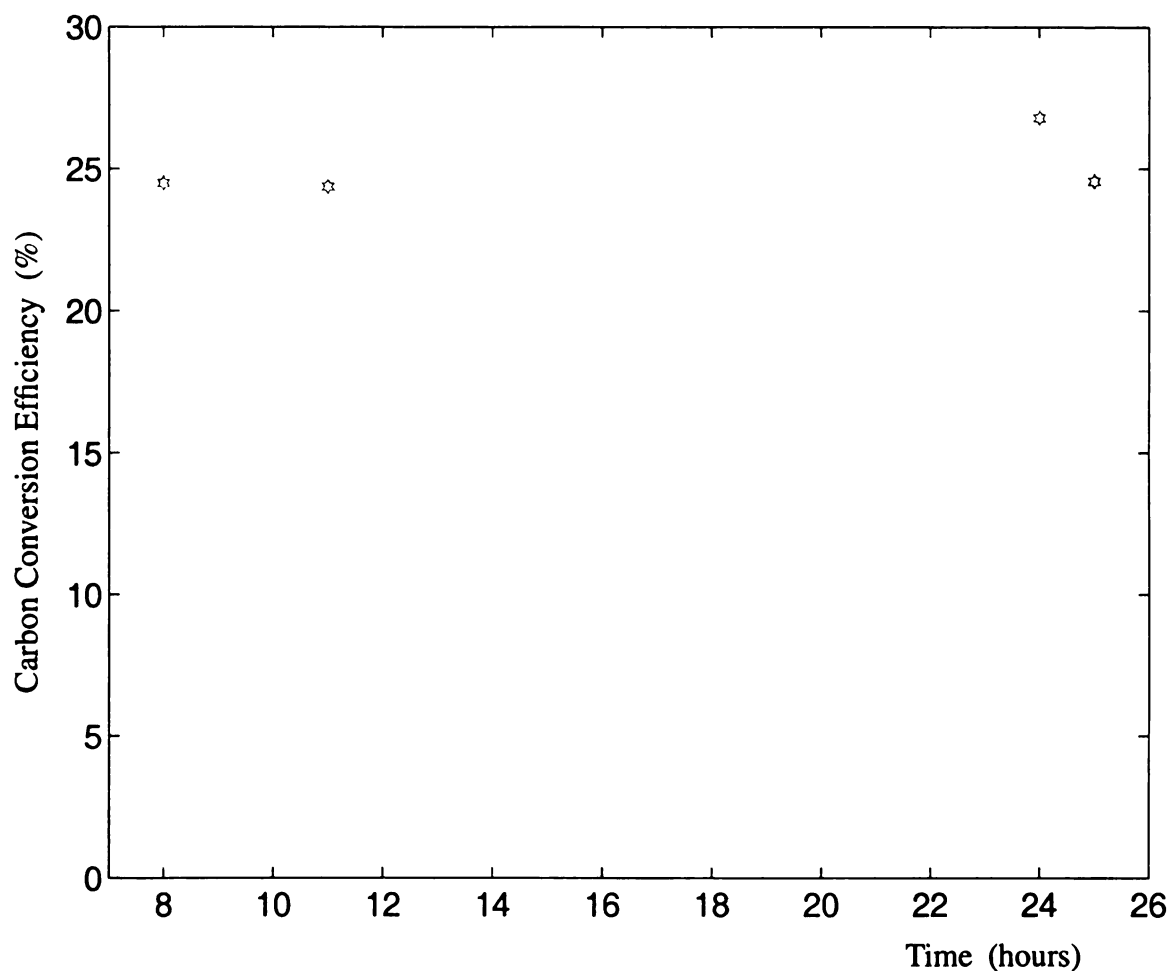


FIGURE 4.30 : CARBON CONVERSION EFFICIENCY VS. DEPOSITION TIME

Pressure=160 Torr and  $\text{Ar}/\text{H}_2/\text{CH}_4 = 100/4/1$  sccm by system II

Figure 4.31 displays the carbon conversion efficiency versus total gas flow rate,  $f_t$ , with pressure at 120 Torr and deposition time of 8 hours and indicates that carbon conversion efficiency increases as total gas flow rate decreases. This result is similar to system I but the plasma with this gas chemistry,  $\text{Ar:H}_2\text{:CH}_4 = 100:2:1$  was unable to be stabilized in system I.

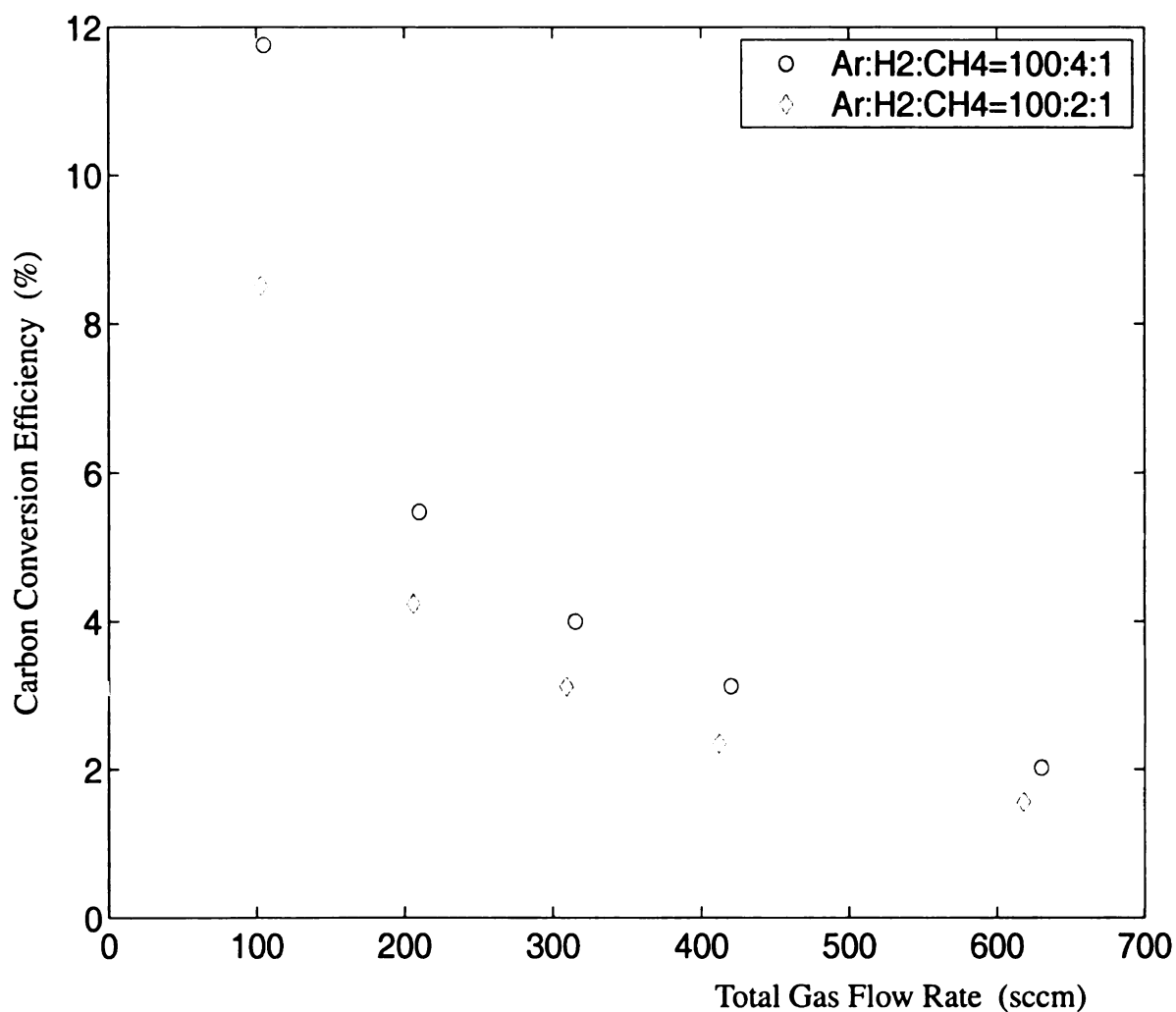


FIGURE 4.31 : CARBON CONVERSION EFFICIENCY VS. TOTAL GAS FLOW RATE

Pressure=120 Torr and deposition time=8 hours by system II.

Figure 4.32 and 4.33 display the carbon conversion efficiency versus deposition pressure,  $p$ , and absorbed microwave power,  $P_{\text{abs}}$ , respectively, with argon flow equal to 100 sccm, methane flow equal to 1 sccm and deposition time of 8 hours. As shown in Figure 4.32, the carbon conversion efficiency increases as pressure increases. Also higher hydrogen concentrations generally produce higher carbon conversion efficiency at the same pressure. In Figure 4.33, the carbon conversion efficiency increases with increases in absorbed microwave power. But at the same time, the deposition pressure is increased, too. The contribution can come from either deposition pressure or absorbed microwave power.



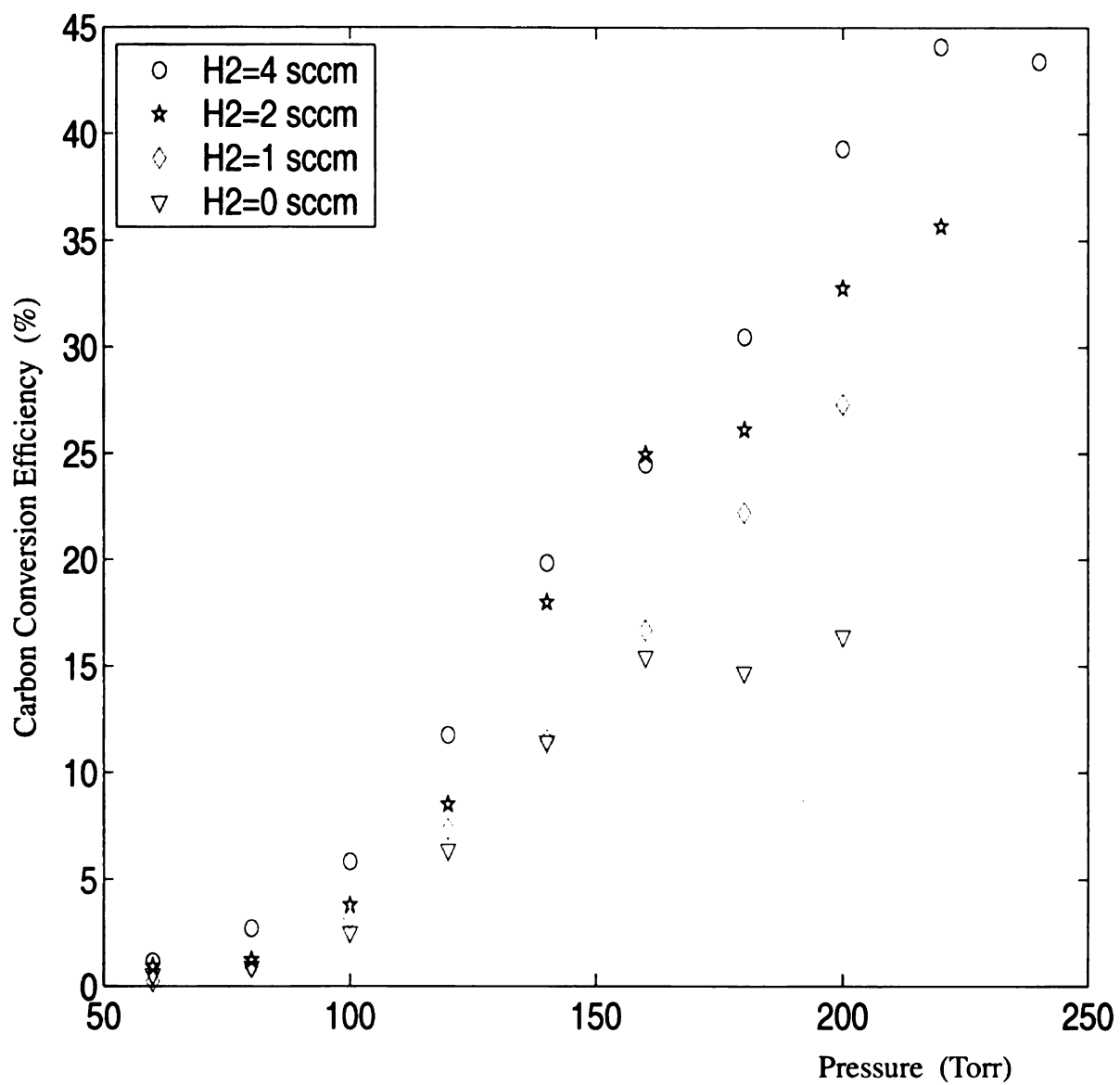


FIGURE 4.32 : CARBON CONVERSION EFFICIENCY VS. PRESSURE  
Ar=100 sccm, CH<sub>4</sub>=1 sccm and deposition time=8 hours by system II.

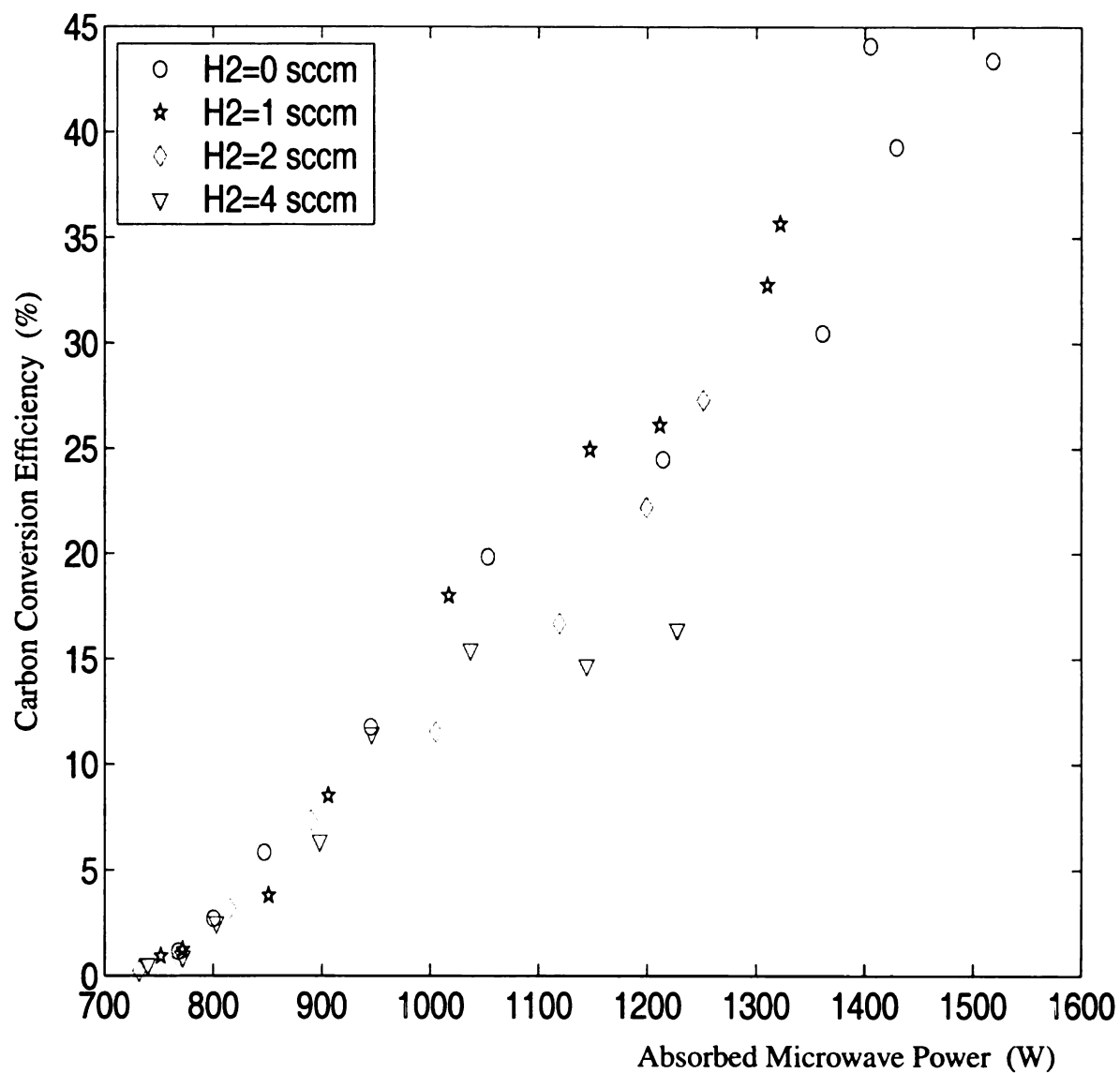


FIGURE 4.33 : CARBON CONVERSION EFFICIENCY VS. MICROWAVE POWER

Ar=100 sccm, CH<sub>4</sub>=1 sccm and deposition time=8 hours by system II.

## 4.4 Controlled Nitrogen Impurity Study By System II

Figure 4.14 displays the total growth rate versus nitrogen impurities with pressure at 120 Torr, gas chemistry fixed at  $\text{Ar:H}_2\text{:CH}_4=100:4:1$ ,  $f_t=105$  sccm and deposition time of 8 hours. As shown, the addition of nitrogen impurity decreases the growth rate approximately 38% as nitrogen impurity increases from a few ppm to 2500 ppm.

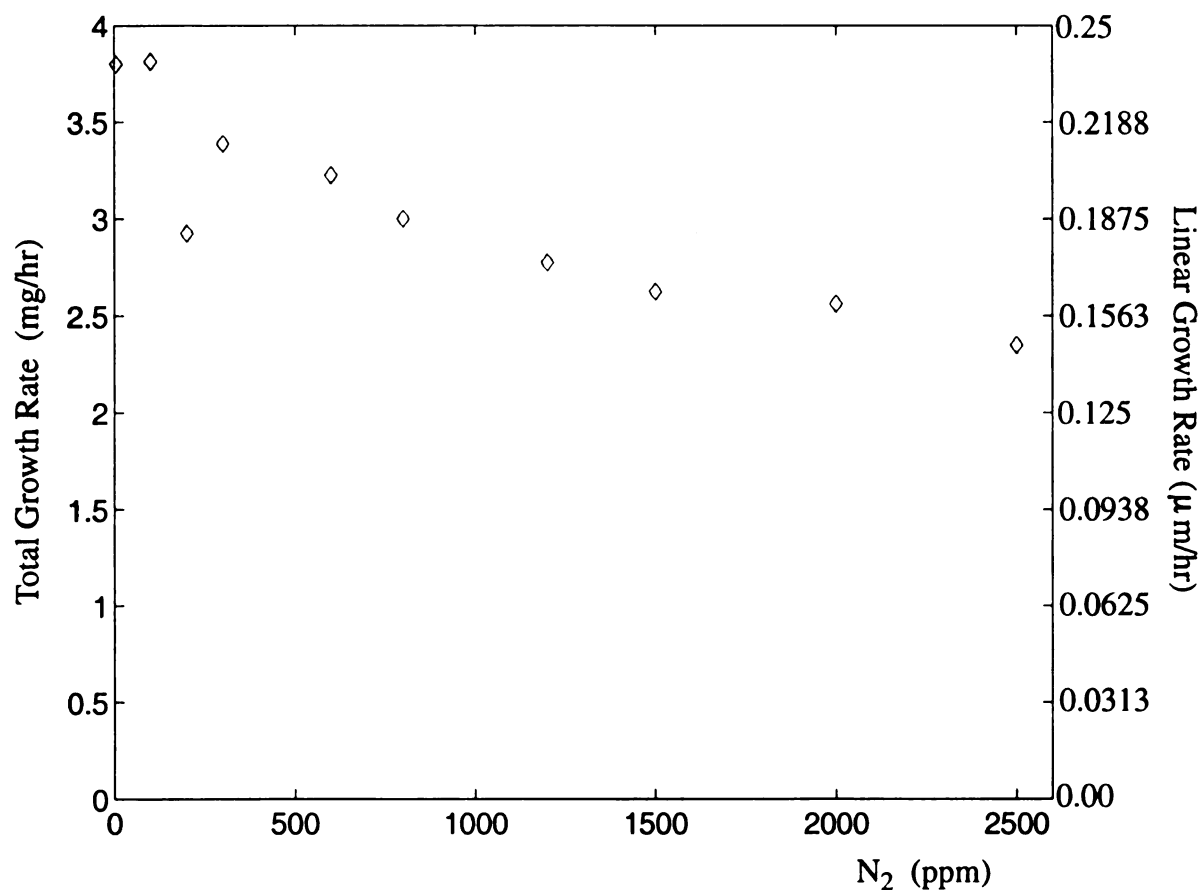


FIGURE 4.34 : TOTAL GROWTH RATE VS.  $\text{N}_2$  IMPURITIES  
Pressure=120 Torr,  $\text{Ar:H}_2\text{:CH}_4=100:4:1$ ,  $f_t=105$  sccm  
and deposition time=8 hours by system II.

Unfortunately, with the current set up of system II, the study of nitrogen impurity on substrate temperature and absorbed microwave power can only be done from 0 to 1500ppm in one experiment. The nitrogen impurity pre-mixed gas tank will need to be switched to a different tank to run higher nitrogen impurity experiments. To change the gas tanks, the plasma will have to be shut down and the system will need to be pumped down then restart the experiment. Therefore, the data presented here is only from 5 to 1500ppm of nitrogen impurity. The study of the influence of the nitrogen impurities on substrate temperature and absorbed microwave power is shown in Figure 4.35. Figure 4.35(a) shows that nitrogen impurities (up to 1500ppm) have only a minor effect on substrate temperature. Figure 4.35(b) shows that there is no changes in absorbed microwave power as nitrogen impurities increase (up to 1500ppm). Nitrogen impurities have no effect on absorbed microwave power and very little influence on substrate temperature.

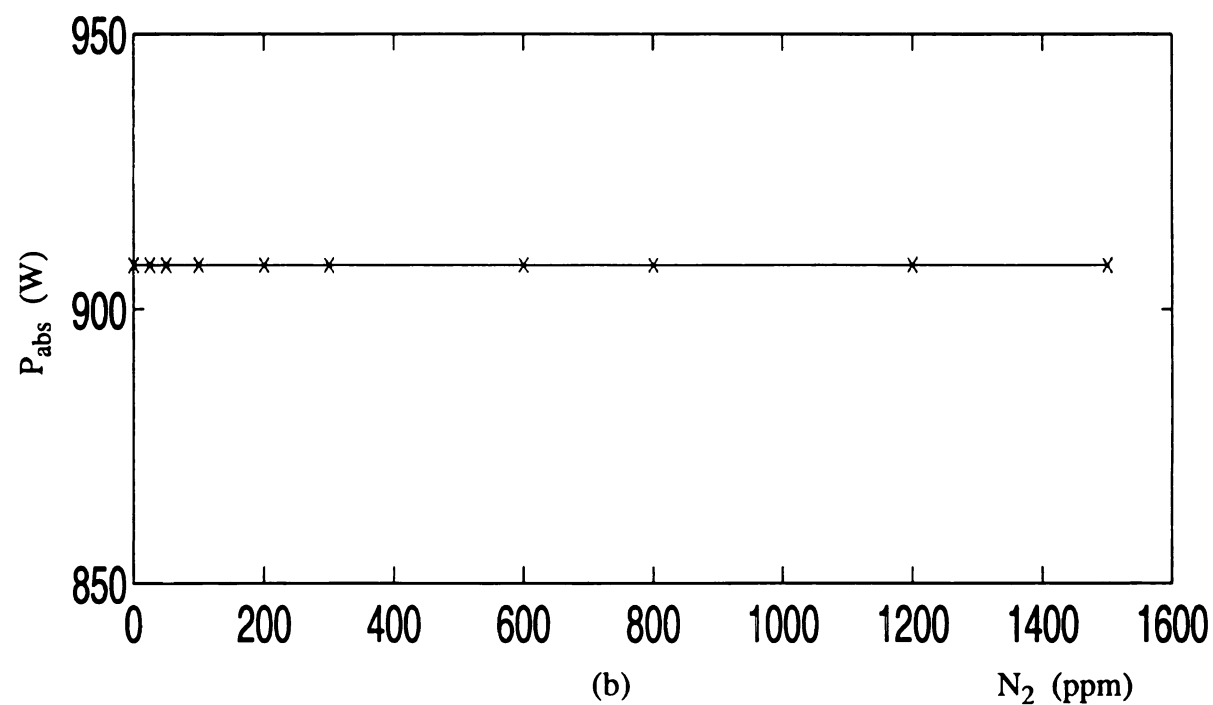
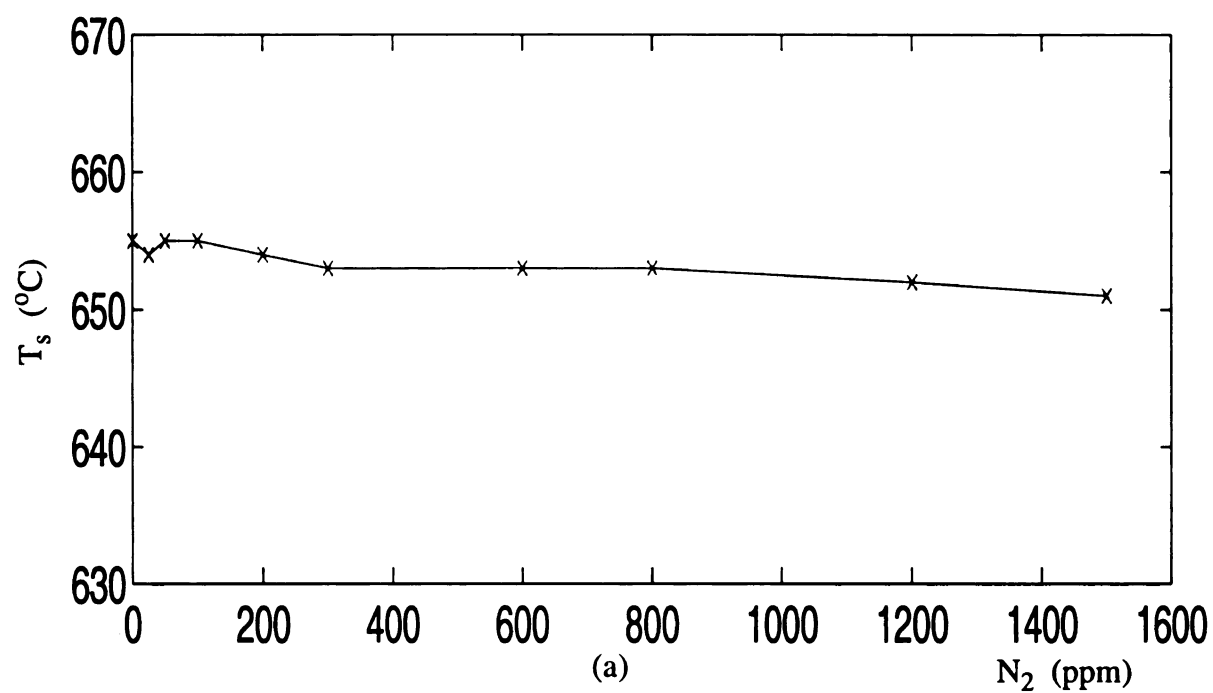
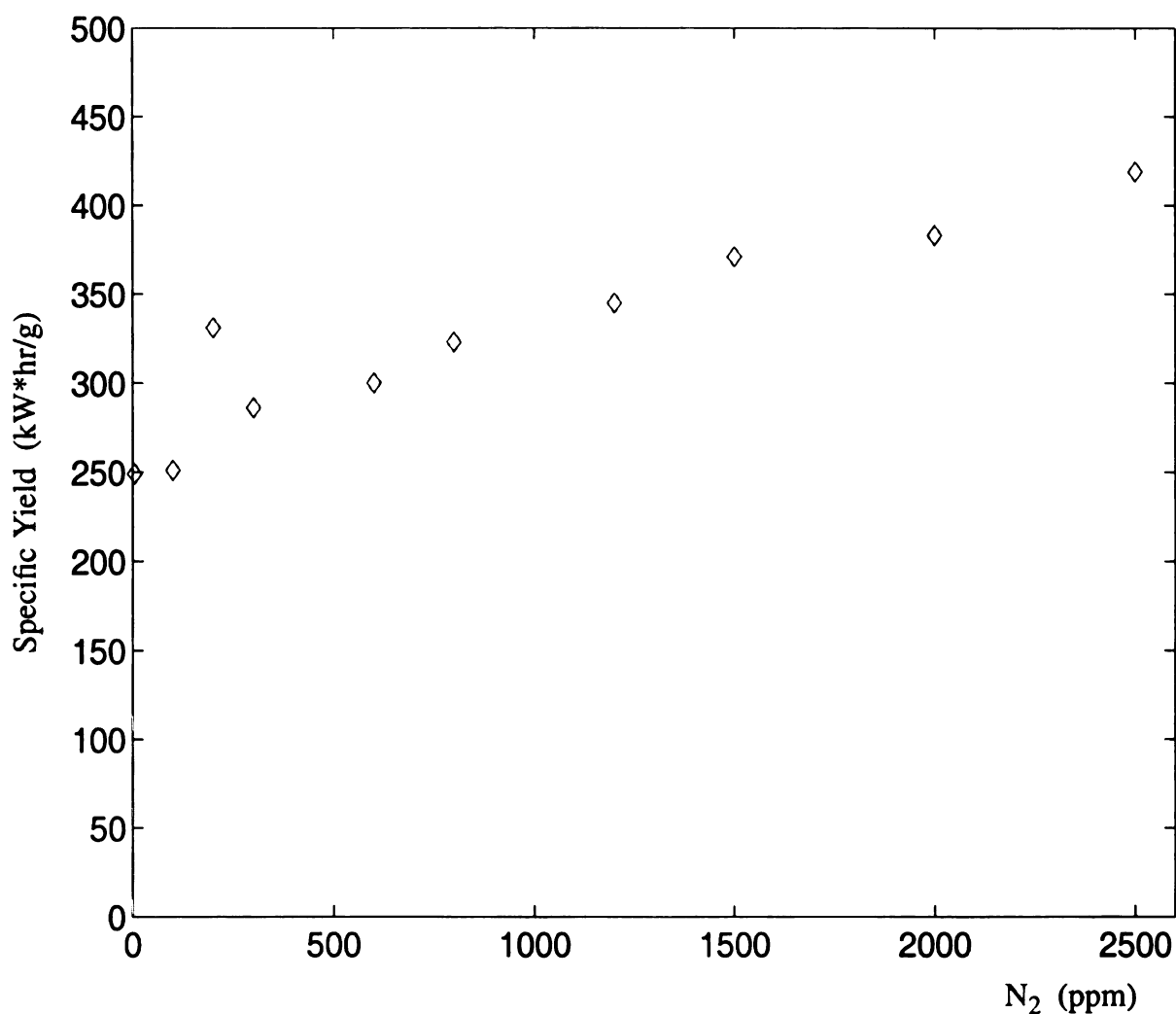


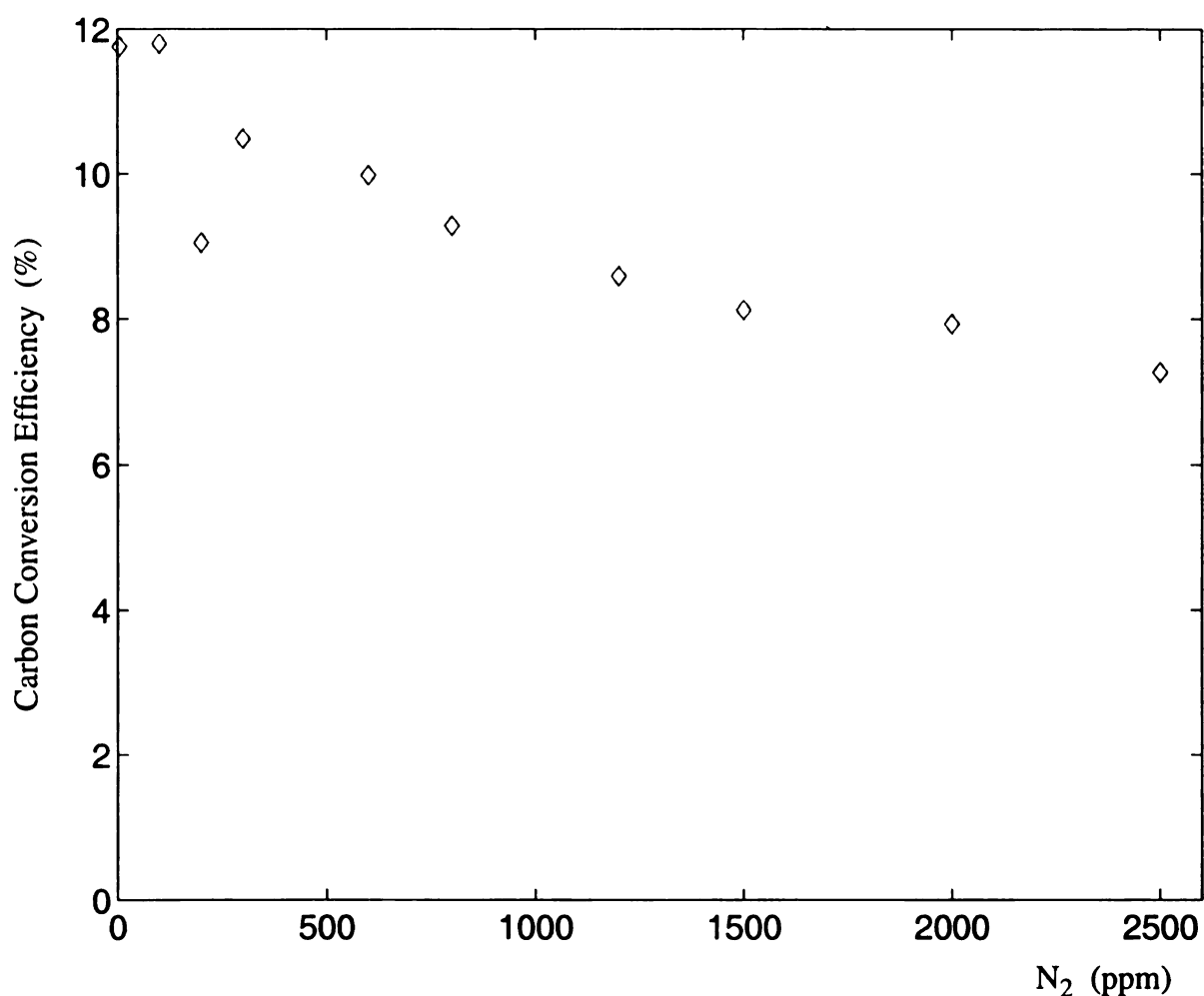
FIGURE 4.35 : THE INFLUENCE OF  $N_2$  IMPURITIES ON  $T_s$  and  $P_{abs}$   
Pressure=120 Torr and Ar/ $H_2$ / $CH_4$ =100/4/1 by system II.

Figure 4.14 displays the specific yield versus nitrogen impurities with pressure at 120 Torr, gas chemistry fixed at Ar/H<sub>2</sub>/CH<sub>4</sub>=100/4/1 sccm and deposition time of 8 hours. As shown, the addition of nitrogen impurities increase the specific yield approximately 68% as nitrogen impurity increases from a few ppm to 2500 ppm.



**FIGURE 4.36 : SPECIFIC YIELD VS. N<sub>2</sub> IMPURITIES**  
 Pressure=120 Torr, Ar/H<sub>2</sub>/CH<sub>4</sub>=100/4/1 sccm and deposition time=8 hours  
 by system II.

Figure 4.14 displays the carbon conversion efficiency versus nitrogen impurities with pressure at 120 Torr, gas chemistry fixed at  $\text{Ar}/\text{H}_2/\text{CH}_4=100/4/1$  sccm and deposition time of 8 hours. As shown, the addition of nitrogen impurity decreases the carbon conversion efficiency approximately 38% as nitrogen impurity increases from a few ppm to 2500 ppm.



**FIGURE 4.37 : CARBON CONVERSION EFFICIENCY VS. N<sub>2</sub> IMPURITIES**  
 Pressure=120 Torr,  $\text{Ar}/\text{H}_2/\text{CH}_4=100/4/1$  sccm and deposition time=8 hours  
 by system II.

## 4.5 Summary

Smooth ultra-nanocrystalline diamond film synthesis was investigated with argon, hydrogen, and methane gases by using MSU-MPACVD reactor systems I and II. The variables for reactor performance ( $Y_1$ ) of both systems are listed in Tables 4.1 and 4.2 respectively. We have learned that systems I and II behave in similar fashion as shown in Figures 4.2 to 4.34. The results for both systems are summarized below.

- (1) As hydrogen (and methane) concentration increases, the growth rate increases, the specific yield decreases, and the carbon conversion efficiency increases. Film growth rate and the carbon conversion efficiency increases (the specific yield decreases) dramatically with small increases in  $H_2$ .
- (2) Total gas flow rate has no influence on growth rate and specific yield (It's only true as hydrogen to methane ratio is equal or greater than three for system I.) but a higher total gas flow rate reduces the carbon conversion efficiency.
- (3) Higher pressure or absorbed microwave power increases growth rate and carbon conversion efficiency and lower the specific yield.
- (4) The experiments performed in systems I and II were both reproducible over a long period of time. Even in system II, there were six users sharing the reactor and it did not affect the reproducibility of system II. Several multiple data-point examples of reproducibility of experiments are listed in Tables 4.3 (system I) and 4.4 (system II).



**TABLE 4.3: REPRODUCIBLE EXPERIMENT DATA FOR SYSTEM I**

Ar (%)	H <sub>2</sub> (%)	CH <sub>4</sub> (%)	f <sub>t</sub> (sccm)	p (Torr)	t (hr)	T <sub>s</sub> (°C)	P <sub>abs</sub> (W)	G <sub>t</sub> (mg/hr)	G <sub>ave</sub> (μm/hr)	S (kWh/g)	C (%)
97.56	1.95	0.49	205	120	8	813	765	0.838	0.052	913	2.593
97.56	1.95	0.49	205	120	8	806	741	0.725	0.045	1022	2.243
97.56	1.95	0.49	615	120	8	830	821	0.750	0.047	1095	0.774
97.56	1.95	0.49	615	120	8	807	839	0.763	0.048	1100	0.787
97.56	1.95	0.49	615	120	4	810	821	0.700	0.044	1173	0.722
97.56	1.95	0.49	615	120	4	840	858	0.675	0.042	1271	0.696
97.56	1.95	0.49	615	120	4	830	802	0.675	0.042	1188	0.696
96.39	2.89	0.72	622.5	120	8	850	895	2.163	0.135	414	1.487
96.39	2.89	0.72	622.5	120	8	850	899	2.313	0.144	389	1.590
95.24	3.81	0.95	105	120	8	844	858	4.625	0.289	186	14.311
95.24	3.81	0.95	105	120	8	855	854	4.263	0.266	200	13.191
95.24	3.81	0.95	105	120	8	850	858	4.625	0.289	186	14.311
95.24	3.81	0.95	105	120	8	850	873	4.438	0.277	197	13.733
92.59	5.56	1.85	108	120	8	900	876	10.950	0.683	80	16.941
92.59	5.56	1.85	108	120	8	890	925	11.325	0.707	82	17.522

**TABLE 4.4: REPRODUCIBLE EXPERIMENT DATA FOR SYSTEM II**

Ar/H <sub>2</sub> /CH <sub>4</sub> (sccm)	p (Torr)	t (hr)	T <sub>s</sub> (°C)	P <sub>abs</sub> (W)	G <sub>t</sub> (mg/hr)	G <sub>ave</sub> (μm/hr)	S (kWh/g)	C (%)
100/4/1	120	8	626	945	3.800	0.237	249	11.758
100/4/1	120	8	650	973	3.663	0.228	266	11.335
100/4/1	120	16	629	965	3.881	0.242	249	12.009
100/4/1	120	16	642	965	3.825	0.239	252	11.836
100/4/1	160	8	709	1214	7.913	0.494	153	24.485
100/4/1	160	8	697	1223	8.238	0.514	148	25.491
100/2/1	160	8	696	1147	8.063	0.503	142	24.950
100/2/1	160	8	706	1160	7.575	0.473	153	23.440
100/1/1	120	8	594	890	2.375	0.148	375	7.349
100/1/1	120	8	601	894	2.238	0.140	399	6.925
100/1/1	200	8	673	1251	8.825	0.551	142	27.307
100/1/1	200	8	677	1314	8.838	0.551	149	27.348
100/0/1	200	8	611	1227	5.300	0.331	232	16.400
100/0/1	200	8	604	1220	6.038	0.377	202	18.684

There are some distinctive differences between the two systems. These are:

- (1) For System I, the plasma can not be stabilized and/or flame free if hydrogen to methane ratio is under three because of the impurity in the system. But system II can run the experiments with hydrogen to methane ratio approaches to zero.
- (2) The reactor performance: growth rate, specific yield, and carbon conversion efficiency are affected by deposition time about 20% to 25% between 8 and 24 hours for the films produced by system I but are not influenced by deposition time between 8 and

25 hours for the films produced by system II. The impurity in the system I seems to affect the growth mechanism of ultra-nanocrystalline diamond.

- (3) A quantitative comparison of the reactor performance of the two reactors with Ar/H<sub>2</sub>/CH<sub>4</sub>=100/4/1 sccm, and deposition time of 8 hours is listed in table 4.3.

**TABLE 4.5: QUANTITATIVE COMPARISON OF THE REACTOR PERFORMANCE OF SYSTEMS I AND II**

P	P <sub>abs</sub> <sup>I</sup>	P <sub>abs</sub> <sup>II</sup>	G <sub>T</sub> <sup>I</sup>	G <sub>T</sub> <sup>II</sup>	G <sub>ave</sub> <sup>I</sup>	G <sub>ave</sub> <sup>II</sup>	S <sub>y</sub> <sup>I</sup>	S <sub>y</sub> <sup>II</sup>	C <sup>I</sup>	C <sup>II</sup>
120	861	945	4.488	3.800	0.280	0.237	192	249	13.887	11.758
140	956	1053	7.163	6.413	0.447	0.400	133	164	22.165	19.844
160	959	1214	10.788	7.913	0.673	0.494	89	153	33.382	24.485

The ratios of microwave power of system I to system II at 120 Torr, 140 Torr, and 160 Torr are as follows:

$$\frac{(P_{abs})^I}{(P_{abs})^{II}} = 0.911, \frac{(P_{abs})^I}{(P_{abs})^{II}} = 0.908, \text{ and } \frac{(P_{abs})^I}{(P_{abs})^{II}} = 0.790.$$

Surprisingly, the microwave power of system I is lower than the microwave power of system II. This tells us that system I is more energy efficient than system II. This can be caused by a different quartz dome height or a difference in the size of the cooling base-plate of the two microwave cavity plasma reactors or substrate temperature. To improve the energy efficiency of system II, the operator can (1) use the same size quartz dome as system I, and (2) increase the temperature set point of the Neslab chiller of system II from 15°C to a higher degree (lowering the cooling efficiency).

The addition of nitrogen impurity decreases the growth rate and carbon conversion efficiency approximately 38%, and increases the specific yield approximately 68% as nitrogen impurity increases from a few ppm to 2500 ppm.

**Microwave Plasma Assisted Chemical Vapor Deposition of  
Ultra-nanocrystalline Diamond Films**

**VOLUME II**

**By**

**Wen-Shin Huang**

**A DISSERTATION**

**Submitted to  
Michigan State University  
in partial fulfillment of the requirements  
for the degree of**

**DOCTOR OF PHILOSOPHY**

**Department of Electrical and Computer Engineering**

**2004**

## **5 MSU-MPACVD Reactor Experimental Output Variables-Film Characteristics ( $Y_2$ )**

### **5.1 Introduction**

Chapter 4 described the ultra-nanocrystalline diamond film synthesis performance ( $Y_1$ ) for systems I and II. The results of the experimental investigation of the film characteristics ( $Y_2$ ) are presented in this chapter. The parameter space investigated in this chapter is the same as in Chapter 4 and is illustrated in Figure 4.1. The input ( $U$ ), internal ( $X$ ), and output ( $Y$ ) variables considered and their associated experimental range explored are displayed in Table 5.1 and 5.2 (Input and internal variables are the same as Table 4.1 and 4.2.). In system I, the residence time inside (1) the quartz dome is 9.31-77.74 seconds, and (2) the system is 11.82-98.72 minutes. In system II, the residence time inside (1) the quartz dome is 9.49-113.83 seconds, and (2) the system is 13.05-156.59 minutes. In this chapter, an overview of the MSU-MPACVD film characteristics ( $Y_2$ ) as a function of a selected number of input variables is presented: Ar/H<sub>2</sub>/CH<sub>4</sub> gas chemistry, total gas flow rate  $f_t$ , deposition pressure,  $p$ , and deposition time,  $t$ . Output variables-film characteristics ( $Y_2$ ) consist of film roughness, morphology, structure quality, film texture and crystal size. Section 5.2 and Section 5.3 describe the influence of gas chemistry, deposition time, total gas flow rate, and deposition pressure on the film characteristics of system I and II respectively. The controlled nitrogen impurity investigation using system II is presented in Section 5.4. In Section 5.5, the summary of the film characterization results of systems I and II discussed in this chapter is presented in Section 5.4.

**TABLE 5.1: PARAMETER SPACE FOR EXPERIMENTS PERFORMED ON SYSTEM I**

	Controllable Input Variables $U_1$	a) Gas Chemistry, $\text{Ar}/\text{H}_2/\text{CH}_4=(99-91)/(1-7)/(0-2)$ (%) b) Total Gas Flow Rate, $f_t=102.5-642$ sccm c) Deposition Pressure, $p=120-160$ Torr d) Absorbed Microwave Power, $P_{\text{abs}}=691-1221\text{W}$
Input Variables $U$	Reactor Design Variables $U_2$	a) 2.45 GHz Microwave Power, fixed b) Reactor Configuration, MPCR, fixed c) End Feed Excitation, fixed d) Electromagnetic Mode and Cavity Tuning, Fixed at $\text{TM}_{013}$ e) Reactor Wall Material, quartz dome, fixed, $\text{dia.}=5''$ f) Substrate Holder Set-up, molybdenum holder, thermally floating stage g) Vacuum System, mechanical pump, $1\sim 2\times 10^{-2}$ Torr, leak rate: 12.6 mTorr/hr h) Purity of gases, fixed, See Section 3.2.2.1
	Deposition Process Variables $U_3$	a) Deposition Time, 2-48 hours b) Substrate Material and Size, 3" Si (100) wafers c) Seeding Procedure, mechanically scratched by $0.1\ \mu\text{m}$ natural diamond powder d) Start-up and Shut-down, fixed
Internal Variables $X$		Substrate Temperature, $T_s=750-950\ ^\circ\text{C}$ (by pyrometer, top side)
	Film Characteristics $Y_2$	a) Film texture: $I(220)/I(111)=0.06-4.04$ b) Film roughness: 14-149 nm c) Morphology: mostly (111) d) Crystal size: 30-2700 nm

**TABLE 5.2: PARAMETER SPACE FOR EXPERIMENTS PERFORMED ON SYSTEM II**

	Controllable Input Variables <b>U<sub>1</sub></b>	a) Gas Chemistry, Ar/H <sub>2</sub> /CH <sub>4</sub> =(99-90)/(0-9)/1 (%) b) Total Gas Flow Rate, f <sub>t</sub> =101-630 sccm c) Deposition Pressure, p=60-240 Torr d) Absorbed Microwave Power, P <sub>abs</sub> =732-1518W e) Controlled N <sub>2</sub> impurity, 5-2500ppm
Input Variables <b>U</b>	Reactor Design Variables <b>U<sub>2</sub></b>	a) 2.45 GHz Microwave Power, fixed b) Reactor Configuration, MPCR, fixed c) End Feed Excitation, fixed d) EM Mode and Cavity Tuning, Fixed at TM <sub>013</sub> e) Reactor Wall Material, quartz dome, fixed, dia.=5" f) Substrate Holder Set-up, molybdenum holder, thermally floating stage g) Vacuum System, turbo pump, 10 <sup>-7</sup> ~10 <sup>-6</sup> Torr, leak rate*: 4mTorr/hr h) Purity of gases, fixed, See Section 3.2.2.2
	Deposition Process Variables <b>U<sub>3</sub></b>	a) Deposition Time, 8-25 hours b) Substrate Material and Size, 3" Si (100) wafers c) Seeding Procedure, mechanically scratched by 0.1 μm natural diamond powder d) Start-up and Shut-down, fixed
Internal Variables <b>X</b>		Substrate Temperature, T <sub>s</sub> =UFL-770 °C (by pyrometer, back side)
	Film Characteristics <b>Y<sub>2</sub></b>	a) Film texture: most (220); I(220)/I(111)=0.13-9.31 b) Film roughness: 11-50 nm c) Morphology: featureless d) Crystal size: 3-30 nm

UFL: Temperature is too low to be detected by the pyrometer.



## 5.2 System I

### 5.2.1 Film Texture = $g(\text{Ar}/\text{H}_2/\text{CH}_4, t, f_t, p)$

Figure 5.1 displays the XRD (X-ray Diffraction) ratio of integrated intensities of diamond  $\langle 220 \rangle$  and  $\langle 111 \rangle$  peaks plotted as a function of hydrogen concentration (the percentage of hydrogen flow rate to the total gas flow rate). These experiments were performed at a constant pressure of 120 Torr and deposition time of 8 hours. The argon concentration was varied from 90.91-98.68%, the  $\text{H}_2$  concentration varied from 0.99-7.27%, and the  $\text{CH}_4$  concentration varied from 0.33-1.85% with the total gas flow rate varied from 102.5-642 sccm. According to ASTM (American Society for Testing Materials) and JCPDS (Joint Committee on Powder Diffraction Standard) - International Center for Diffraction Data, using diamond powder sample with no preferred orientation, the XRD ratio of intensities of diamond  $\langle 220 \rangle$  and  $\langle 111 \rangle$  peaks is 0.25. (For statistics reasons,  $\langle 111 \rangle$  and  $\langle 220 \rangle$  peaks are chosen.) A ratio larger than 0.25 means the film has (220) preferred orientation. A ratio less than 0.25 indicates the film has (111) preferred orientation.

As hydrogen concentration rises above 4%, the films clearly have (220) preferred orientation. Generally, the films synthesized with higher hydrogen concentration (or higher methane concentration) have the (220) preferred orientation. At lower hydrogen concentration (below 4%), the value of  $I(220)/I(111)$  scatters between 0 and 0.47. The film corresponding to a zero ratio is too thin (average film thickness=81 nm) and is masked under the large Si(400) peak.

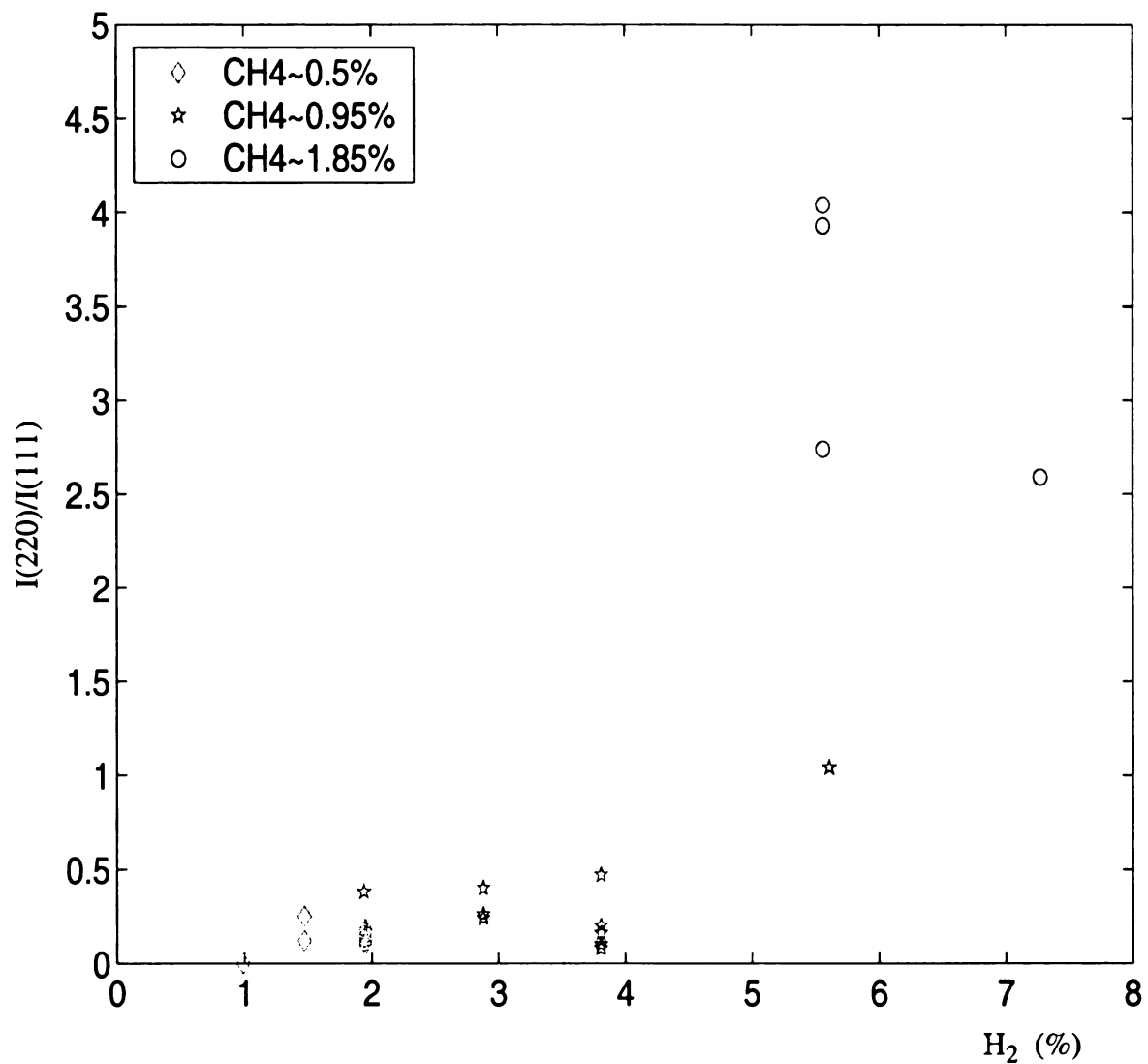


FIGURE 5.1 :  $I(220)/I(111)$  VS. HYDROGEN CONCENTRATION

Pressure=120 Torr, deposition time=8 hours,  
 $Ar:H_2:CH_4=(90.91-98.68):(0.99-7.27):(0.33-1.85)\%$   
 and total gas flow rate varied from 102.5-642 sccm  
 by system I.

Figure 5.2 displays the XRD ratio of integrated intensities of diamond <220> and <111> peaks plotted as a function of the deposition time,  $t$ , with pressure at 120 Torr  $\text{Ar:H}_2\text{:CH}_4 = 100:2:0.5$ , and  $f_t=615$  sccm. Using this deposition condition, the films have the (111) preferred orientation. The film corresponding to zero ratio is too thin (average film thickness=87 nm) and is masked under the big Si(400) peak.

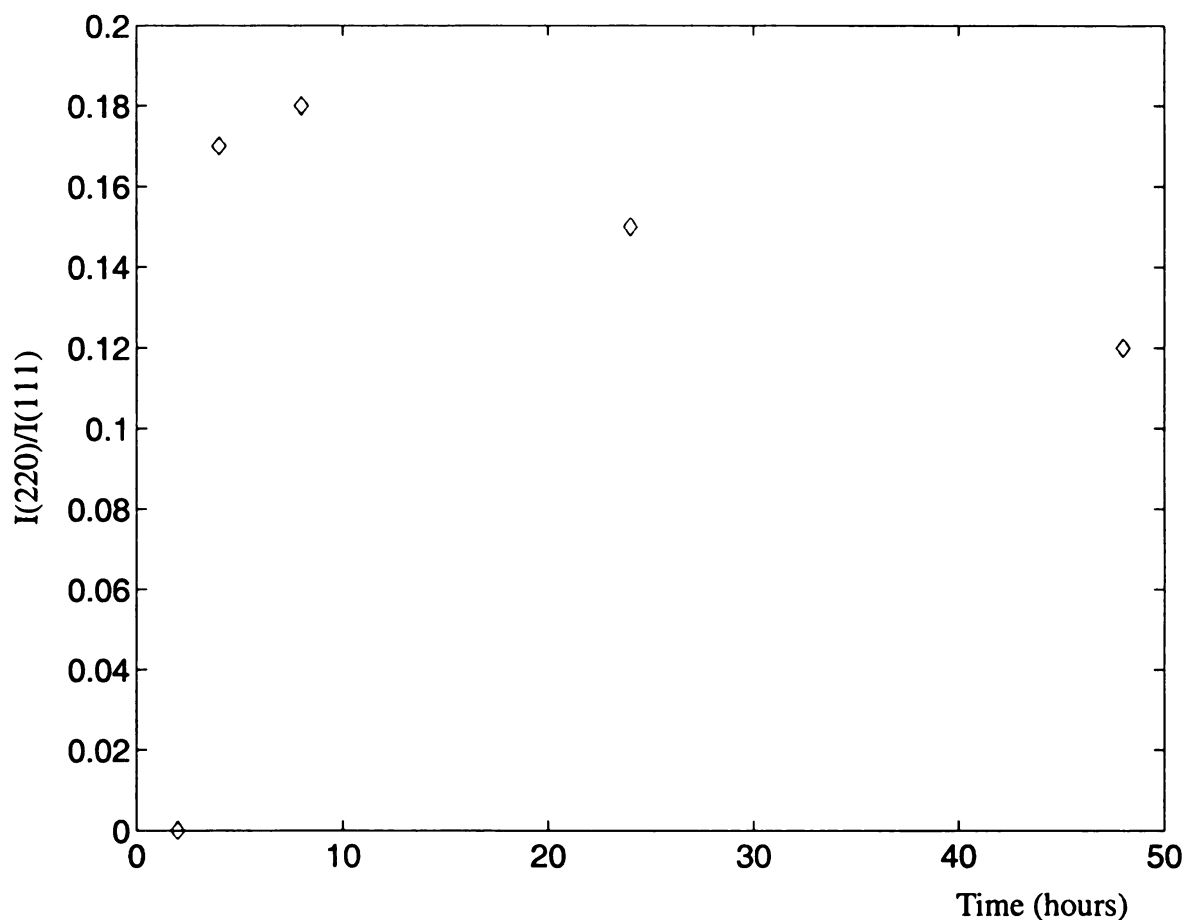
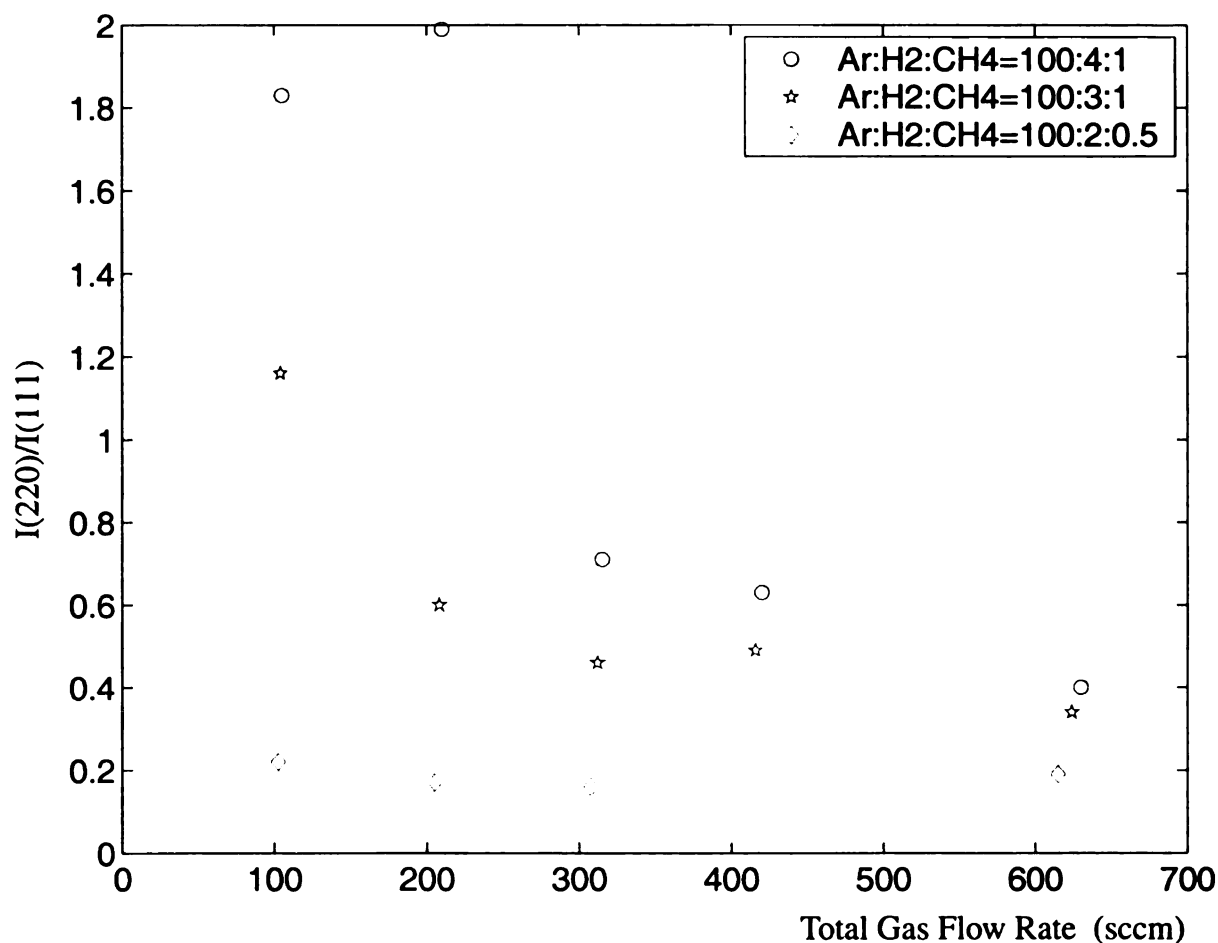


FIGURE 5.2 :  $I(220)/I(111)$  VS. DEPOSITION TIME  
Pressure=120 Torr,  $\text{Ar:H}_2\text{:CH}_4=100:2:0.5$ , and  $f_t=615$  sccm by system I

Figure 5.3 displays the XRD ratio of integrated intensities of diamond <220> and <111> peaks plotted as a function of total gas flow rate,  $f_t$ , with pressure at 140 Torr and deposition time of 8 hours. Only the films synthesized with Ar:H<sub>2</sub>:CH<sub>4</sub>=100:2:0.5 gas chemistry ratio have the (111) preferred orientation. The films synthesized with the gas chemistry ratios of Ar:H<sub>2</sub>:CH<sub>4</sub>=100:3:1 and Ar:H<sub>2</sub>:CH<sub>4</sub>=100:4:1 have the (220) preferred orientation. At higher total gas flow rates, the films' (220) preferred orientation tends to be weaker.



**FIGURE 5.3 :  $I(220)/I(111)$  VS. TOTAL GAS FLOW RATE**  
 Pressure=140 Torr and deposition time=8 hours by system I

Figure 5.4 display the XRD ratio of integrated intensities of diamond <220> and <111> peaks plotted as a function of deposition pressure, p, with deposition time of 8 hours and  $f_t = 102.5\text{-}630$  sccm. Between the deposition pressure of 120 to 160 Torr, only the films synthesized with  $\text{Ar:H}_2\text{:CH}_4=100\text{:}2\text{:}0.5$  gas chemistry ratio have the (111) preferred orientation. As the deposition pressure equal to or greater than 140 Torr, the films synthesized with the gas chemistry ratios of  $\text{Ar:H}_2\text{:CH}_4=100\text{:}3\text{:}1$  and  $\text{Ar:H}_2\text{:CH}_4=100\text{:}4\text{:}1$  mostly have the (220) preferred orientation;  $I(220)/I(111)=0.34\text{-}3.62$ . As the deposition pressure equal to 120 Torr and the films were synthesized with the gas chemistry ratios of  $\text{Ar:H}_2\text{:CH}_4=100\text{:}3\text{:}1$  and  $\text{Ar:H}_2\text{:CH}_4=100\text{:}4\text{:}1$ , the ratio of  $I(220)/I(111)$  scatters between 0.08-0.47. Figure 5.4 shows that the increase of the deposition pressure has more effect on the films grown with the gas chemistry ratios of  $\text{Ar:H}_2\text{:CH}_4=100\text{:}3\text{:}1$  and  $\text{Ar:H}_2\text{:CH}_4=100\text{:}4\text{:}1$  than those grown with  $\text{Ar:H}_2\text{:CH}_4=100\text{:}2\text{:}0.5$  gas chemistry ratio. The effect caused an increase in the (220) preferred orientation for the films synthesized with the gas chemistry ratios of  $\text{Ar:H}_2\text{:CH}_4=100\text{:}3\text{:}1$  and  $\text{Ar:H}_2\text{:CH}_4=100\text{:}4\text{:}1$ .

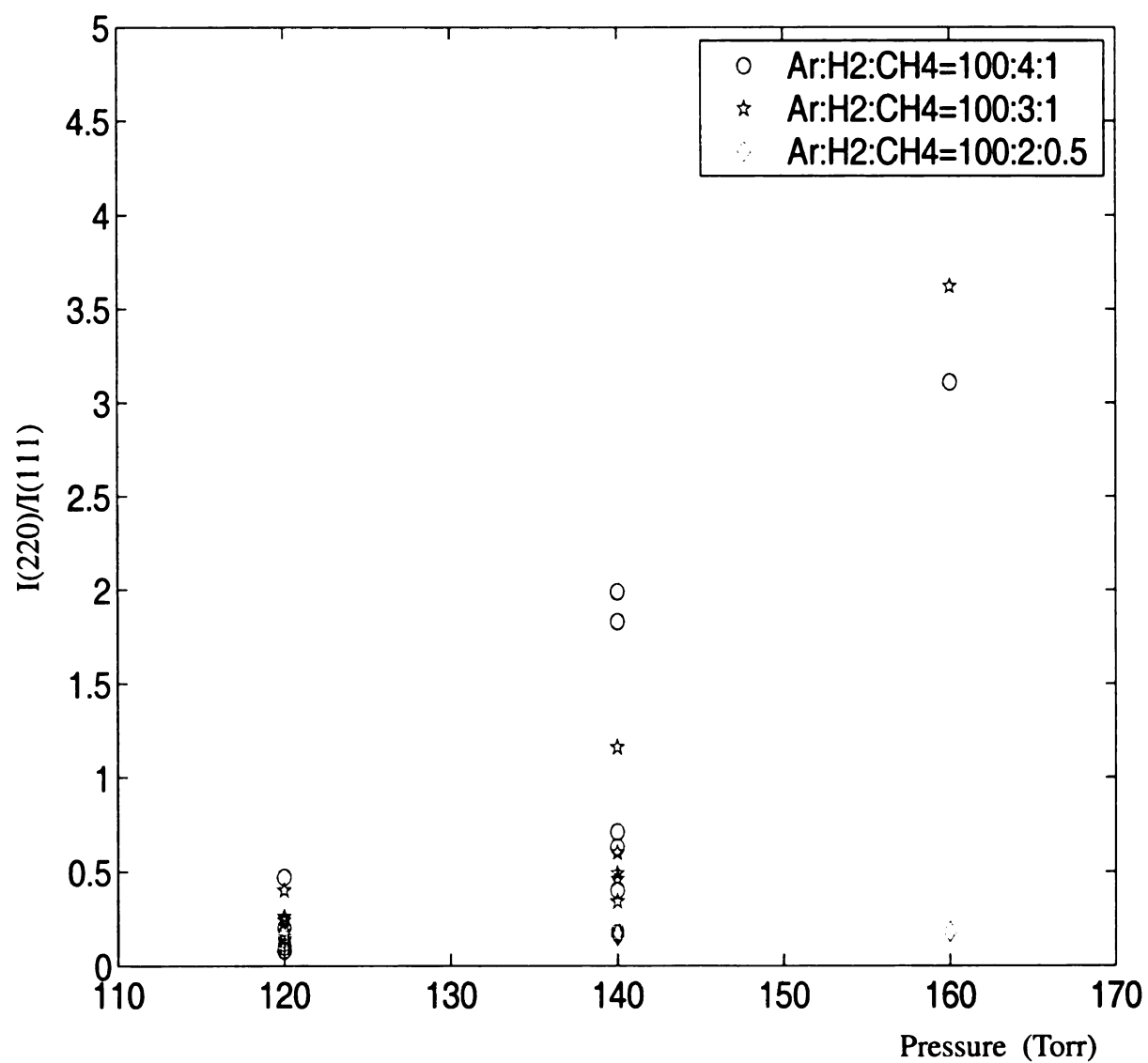


FIGURE 5.4 :  $I(220)/I(111)$  VS. DEPOSITION PRESSURE  
Deposition time=8 hours by system I

### 5.2.2 Film Roughness = $g(\text{Ar}/\text{H}_2/\text{CH}_4, t, f_t, p)$

Figure 5.5 displays the film roughness plotted as a function of hydrogen concentration, (the percentage of argon, hydrogen, and methane gases), with a constant pressure of 120 Torr,  $\text{Ar}:\text{H}_2:\text{CH}_4 = 100:2:0.5$ ,  $\text{Ar}:\text{H}_2:\text{CH}_4 = 100:3:1$ ,  $\text{Ar}:\text{H}_2:\text{CH}_4 = 100:4:1$ , and with (a)  $f_t = 102.5\text{--}105$  sccm, (b)  $f_t = 615\text{--}630$  sccm, and deposition time of 8 hours. The film roughness increases with the increases in hydrogen concentration.

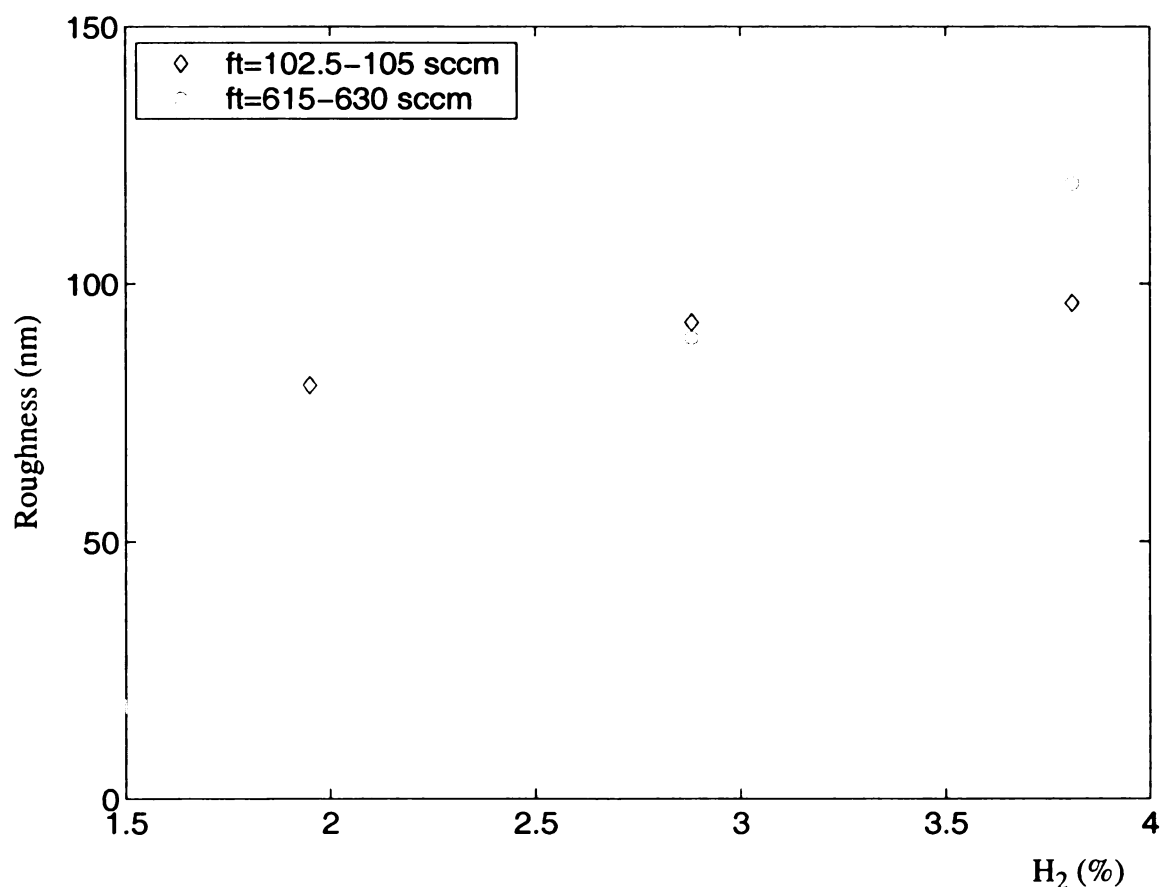
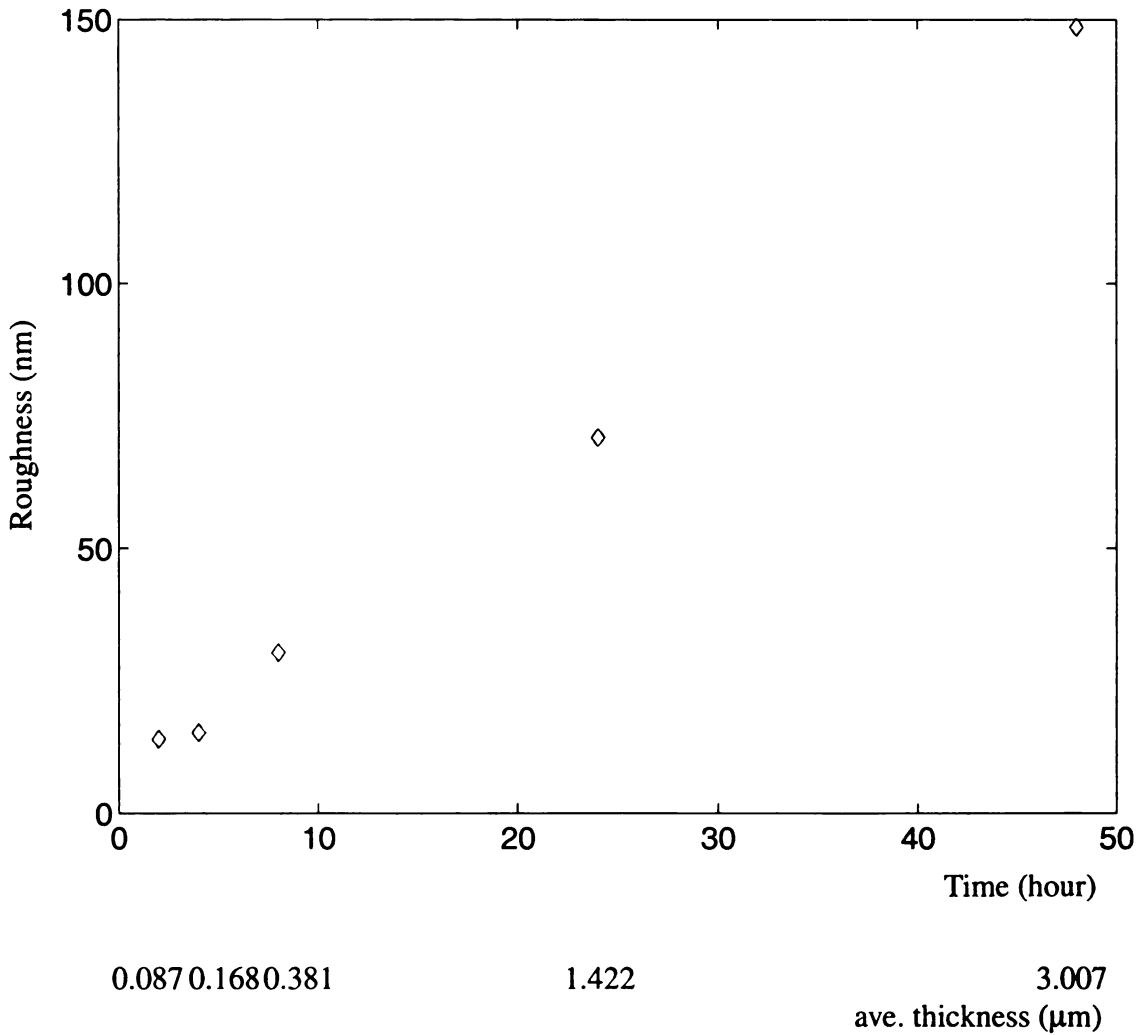


FIGURE 5.5 : RMS ROUGHNESS VS. HYDROGEN CONCENTRATION  
Pressure=120 Torr and deposition time=8 hours by system I

Figure 5.6 displays the film roughness plotted as a function of different deposition times, with the pressure of 120 Torr, Ar:H<sub>2</sub>:CH<sub>4</sub> =100:2:0.5, and f<sub>t</sub>=615 sccm. The film roughness increases as the deposition time increases.



**FIGURE 5.6 : RMS ROUGHNESS VS. DEPOSITION TIME**  
 Pressure=120 Torr, Ar:H<sub>2</sub>:CH<sub>4</sub>=100:2:0.5, f<sub>t</sub>=615 sccm by system I.



Figure 5.7 displays the film roughness plotted as a function of different deposition pressure, with  $\text{Ar:H}_2\text{:CH}_4 = 100:2:0.5$ ,  $f_t = 615$  sccm and a deposition time of 8 hours. The film roughness increases as the deposition pressure increases.

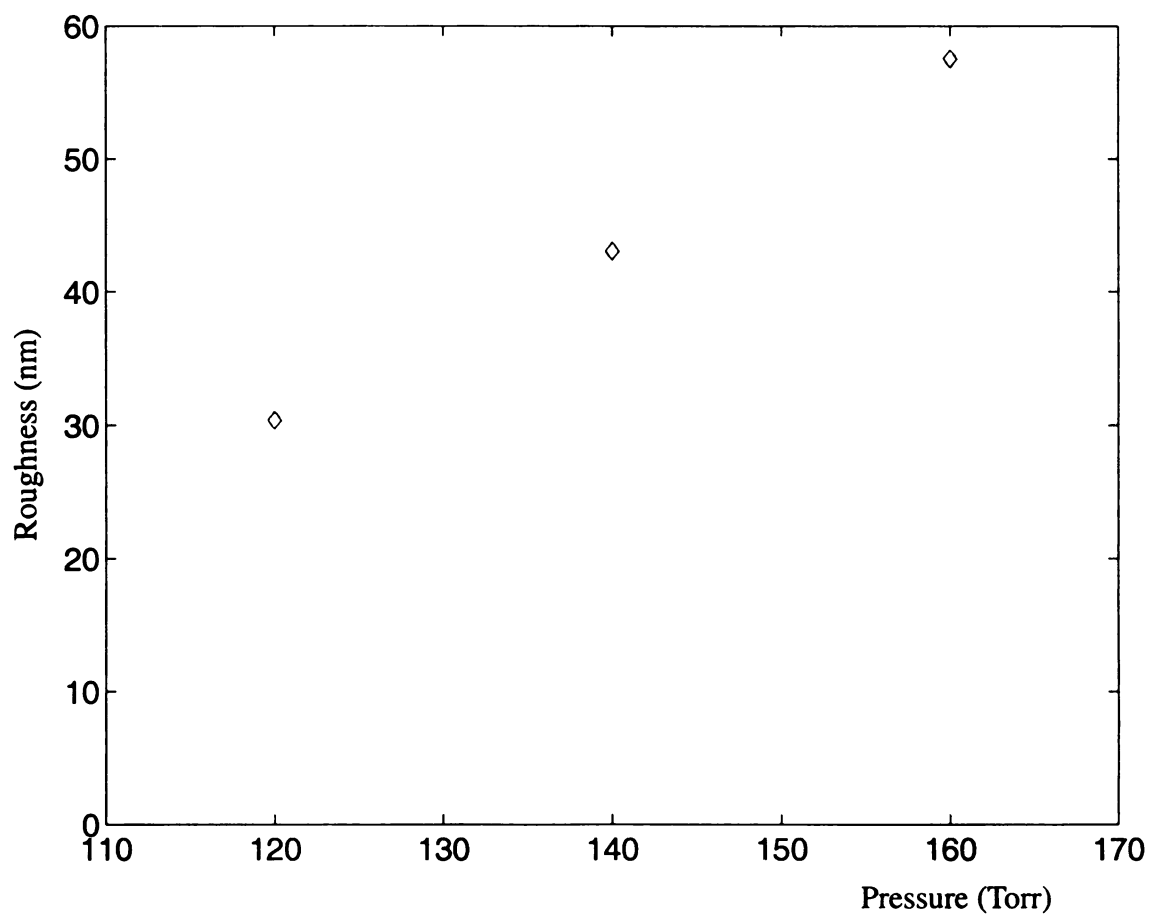
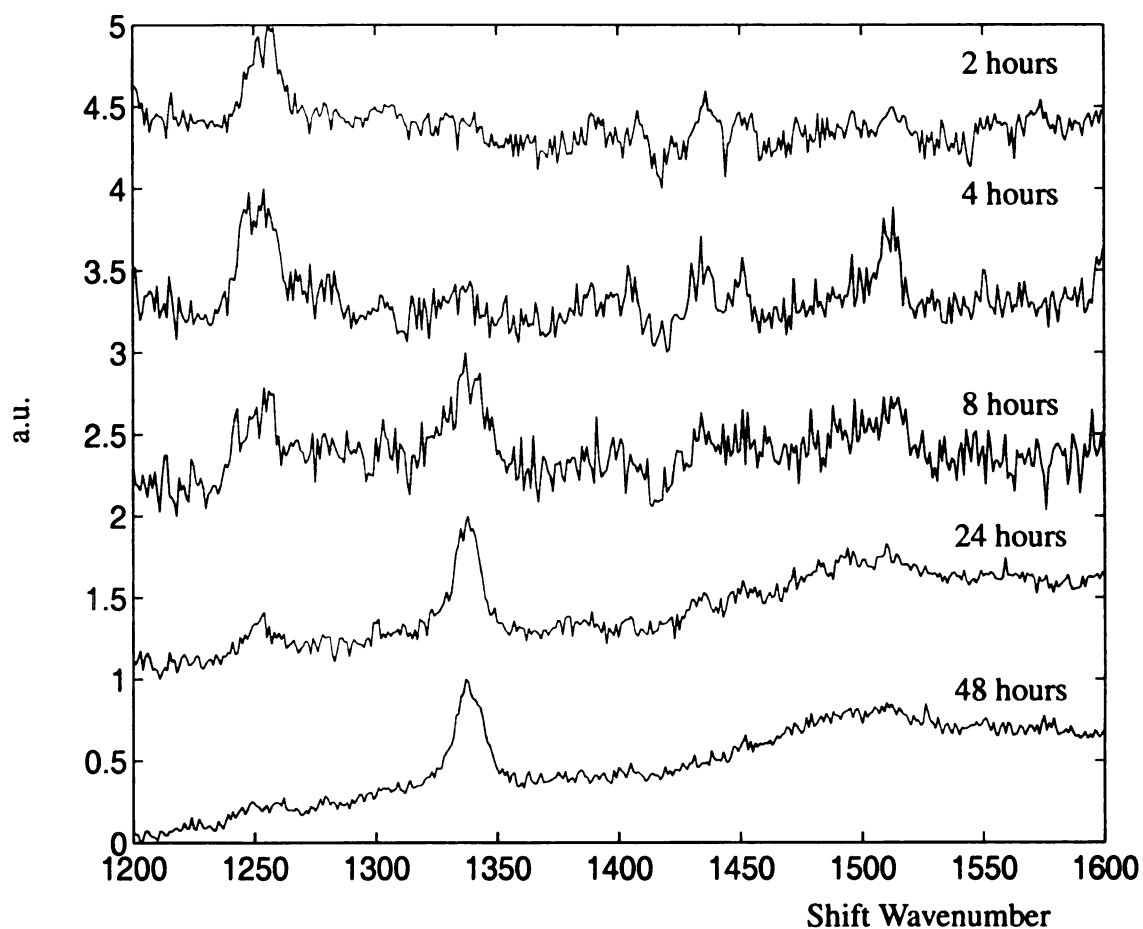


FIGURE 5.7 : RMS ROUGHNESS VS. DEPOSITION PRESSURE  
 $\text{Ar:H}_2\text{:CH}_4 = 100:2:0.5$ ,  $f_t = 615$  sccm and deposition time = 8 hours  
by system I.

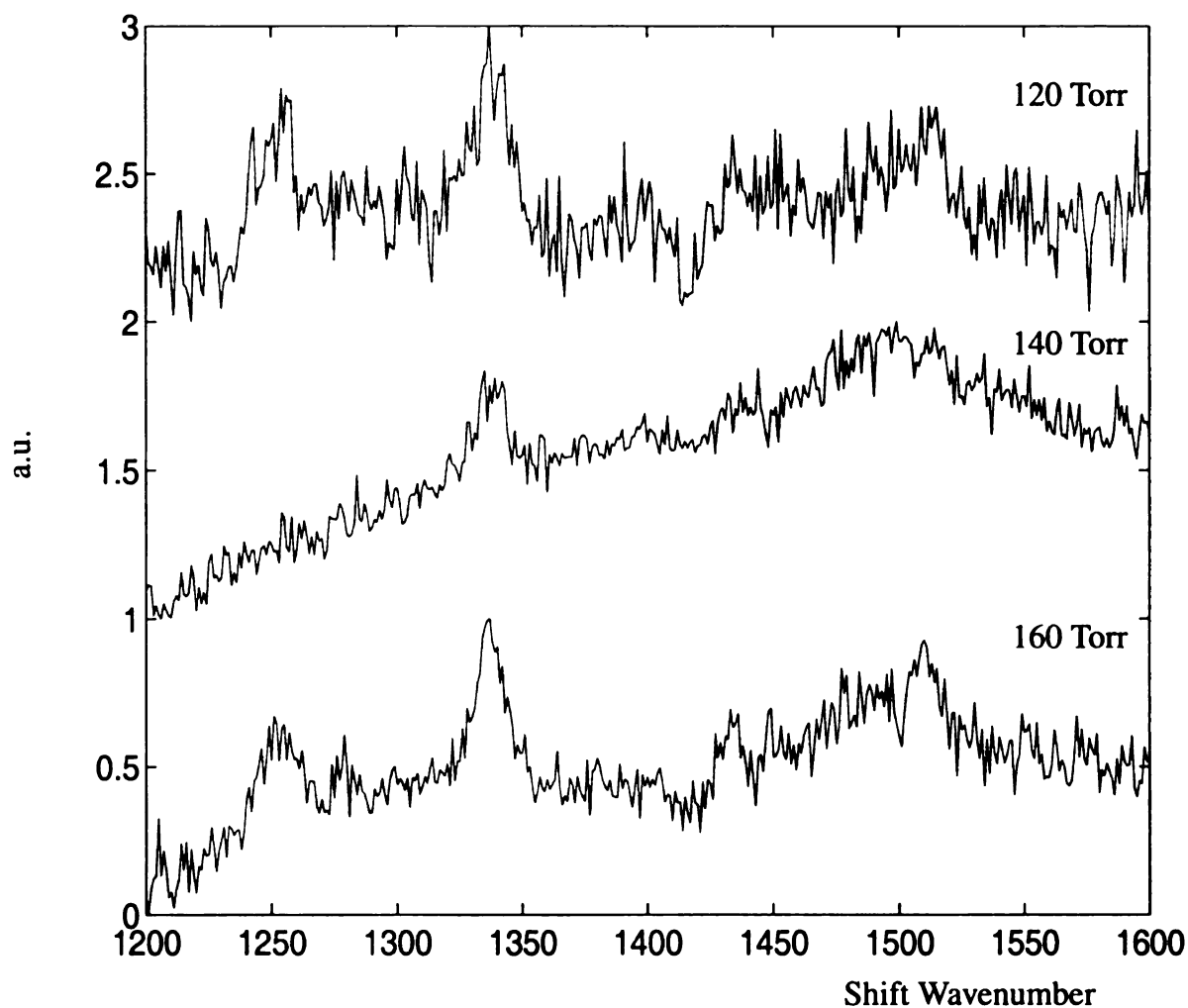
### 5.2.3 Film Quality = $g(t, p)$

Figure 5.8 displays the Raman Spectra for different deposition times, with the pressure of 120 Torr,  $\text{Ar:H}_2\text{:CH}_4 = 100:2:0.5$ , and  $f_t = 615$  sccm. The diamond peak at  $1332 \text{ cm}^{-1}$  becomes sharper as deposition time becomes longer. This may be caused by the fact that crystal size becomes larger as time increases.



**FIGURE 5.8 : RAMAN SPECTRA**  
Pressure=120 Torr,  $\text{Ar:H}_2\text{:CH}_4 = 100:2:0.5$ , and  $f_t = 615$  sccm by system I.  
Spectra Taken by Raman System (Ar 514.5nm Laser) at MSU, ECE

Figure 5.9 displays the Raman Spectra for different deposition pressures, with  $\text{Ar}/\text{H}_2/\text{CH}_4 = 600/12/3$  sccm and deposition time of 8 hours. The diamond peak at  $1332\text{ cm}^{-1}$  becomes sharper as deposition pressure becomes larger. This may be caused by the fact that crystal size increases as pressure increases.



**FIGURE 5.9 : RAMAN SPECTRA**  
 $\text{Ar}:\text{H}_2:\text{CH}_4=100:2:0.5$ ,  $f_t=615$  sccm and deposition time=8 hours  
by system I.  
Spectra Taken by Raman System (Ar 514.5nm Laser) at MSU, ECE.

#### 5.2.4 Morphology and Crystal Size= $g(\text{Ar}/\text{H}_2/\text{CH}_4, t, f_t, p)$

The AFM probes used in this research were TESP (TappingMode Etched Silicon Probe) which had nominal tip radius of curvature of 5 -10 nm. For this thesis research, 5  $\mu\text{m}$  x 5  $\mu\text{m}$  images were acquired with the number of samples parameter set to 512. Then the pixel size is 9.8 nm (5  $\mu\text{m}/512=0.0098 \mu\text{m}=9.8 \text{ nm}$ ). Thus, features smaller than 9.8 nm can not be resolved. As AFM scan is performing, the tip becomes dull and the radius of curvature increases. A dull tip with a larger radius of curvature will not be able to laterally resolve as small a feature as a sharp tip does. Therefore, the resolution decreases as the radius of curvature increases because of the scanning. Thus, an AFM is not a good tool to determine the crystal size when the crystal size is small because it can not distinguish the individual crystal's boundary. But it's an excellent tool to examine the film morphology without film destruction and estimate the crystal size when the crystal is large enough. Although the crystal sizes of the films deposited by system I are larger than desired, it offers an opportunity to study the relationship between the crystal size and the input variables for system I.

Figure 5.10 displays the film morphology for different gas chemistries,  $\text{Ar}/\text{H}_2/\text{CH}_4$ , (the percentage of argon, hydrogen, and methane gases), with the pressure of 120 Torr and deposition time of 8 hours. Figure 5.10(b) and Figure 5.10(c) have (111) triangular morphology.

Figure 5.10(a) ( $\text{Ar}:\text{H}_2:\text{CH}_4=100:2:0.5$  and  $f_t=102.5 \text{ sccm}$ ) shows that the crystal sizes range from roughly 30 nm to 1  $\mu\text{m}$ . In Figure 5.10(b) ( $\text{Ar}:\text{H}_2:\text{CH}_4=100:3:1$  and  $f_t=104 \text{ sccm}$ ), the crystal sizes range from roughly 100 nm to 1.5  $\mu\text{m}$ . In Figure 5.10(c),

(Ar:H<sub>2</sub>:CH<sub>4</sub>=100:4:1 and f<sub>t</sub>=105 sccm) the crystal sizes range from roughly 100 nm to 1.7 μm. With the pressure of 120 Torr, f<sub>t</sub>=102.5-105 sccm and deposition time of 8 hours, increasing hydrogen concentration from 1.95% to 3.81% increases the low end of crystal size around 3.3 times and 1.7 times for the high end.

Figure 5.10(a)

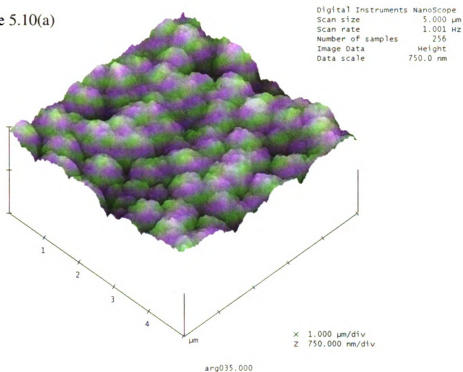


Figure 5.10(b)

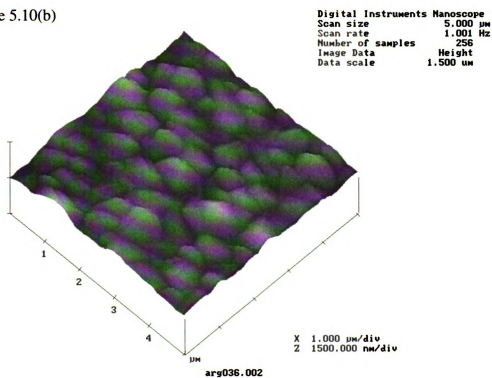


FIGURE 5.10 : FILM MORPHOLOGY VS. GAS CHEMISTRY  
 Pressure=120 Torr and deposition time=8 hours by system I.

Figure 5.10(c)

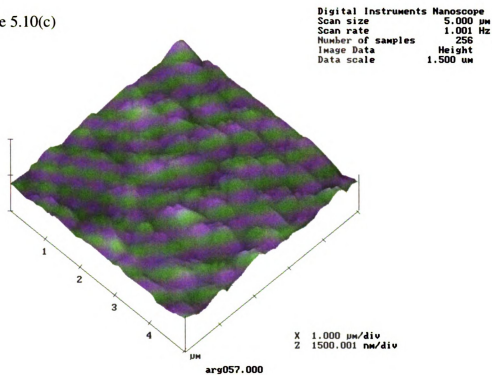


Figure 5.10(a): Ar:H<sub>2</sub>:CH<sub>4</sub>=100:2:0.5 and  $f_t=102.5$  sccm

Figure 5.10(b): Ar:H<sub>2</sub>:CH<sub>4</sub>=100:3:1 and  $f_t=104$  sccm

Figure 5.10(c): Ar:H<sub>2</sub>:CH<sub>4</sub>=100:4:1 and  $f_t=105$  sccm

FIGURE 5.10 (cont'd)

Figure 5.11 displays the film morphology for different gas chemistries, i.e. for different percentages of argon, hydrogen, and methane gases, with the pressure of 120 Torr and deposition time of 8 hours. Figure 5.11(a), Figure 5.11(b) and Figure 5.10(c) have (111) triangular morphology. In Figure 5.11(a) ( $\text{Ar:H}_2\text{:CH}_4=100:2:0.5$  and  $f_t=615$  sccm), the crystal sizes range from roughly 80 nm to 600 nm. In Figure 5.11(b) ( $\text{Ar:H}_2\text{:CH}_4=100:3:1$  and  $f_t=624$  sccm), the crystal sizes range from roughly 120 nm to 1  $\mu\text{m}$ . In Figure 5.11(c) ( $\text{Ar:H}_2\text{:CH}_4=100:4:1$  and  $f_t=630$  sccm), the crystal sizes range from roughly 120 nm to 1.3  $\mu\text{m}$ . With the pressure of 120 Torr,  $f_t=615$ -630 sccm and deposition time of 8 hours, by increasing the hydrogen concentration from 1.95% to 3.81% increases the low end of crystal size 1.5 times and almost 2.2 times for the high end.



Figure 5.11(a)

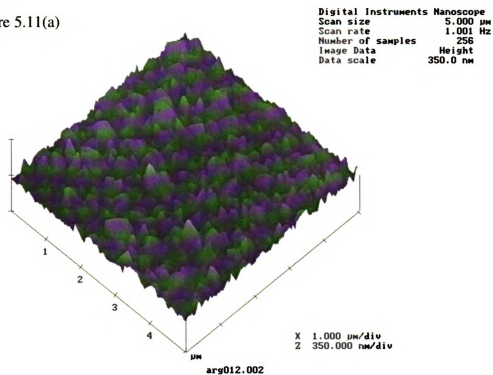


Figure 5.11(b)

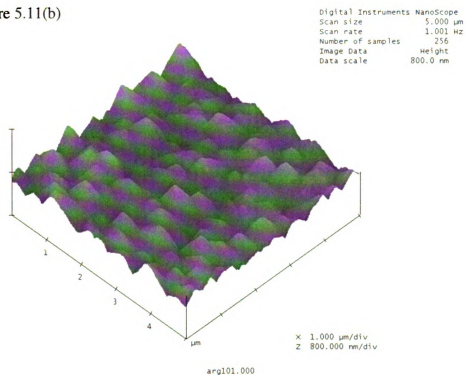


FIGURE 5.11 : FILM MORPHOLOGY VS. GAS CHEMISTRY  
Pressure=120 Torr and deposition time=8 hours by system I.

Figure 5.11(c)

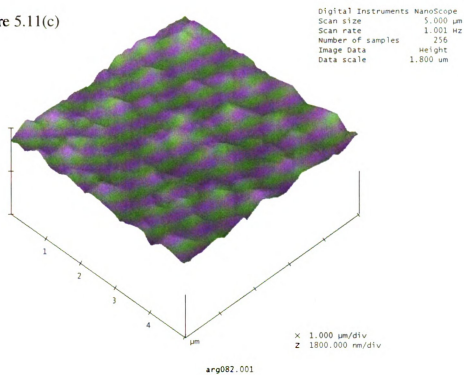


Figure 5.10(a):  $\text{Ar:H}_2\text{:CH}_4=100:2:0.5$  and  $f_t=615$  sccm

Figure 5.10(b):  $\text{Ar:H}_2\text{:CH}_4=100:3:1$  and  $f_t=624$  sccm

Figure 5.10(c):  $\text{Ar:H}_2\text{:CH}_4=100:4:1$  and  $f_t=630$  sccm

FIGURE 5.11 (cont'd)

Figure 5.12 displays the film morphology of different deposition times, with the pressure of 120 Torr,  $\text{Ar:H}_2\text{:CH}_4 = 100:2:0.5$ , and  $f_t = 615$  sccm. Figures 5.12(a), 5.12(b), and 5.12(c) have (111) triangular morphology. Figure 5.12(d) and Figure 5.12(e) have mixed morphology. In Figure 5.12(a) (deposition time = 2 hours), the crystal sizes range from 30 nm to 120 nm roughly. In Figure 5.12(b) (deposition time = 4 hours), the crystal sizes range from 50 nm to 200 nm roughly. In Figure 5.12(c) (deposition time = 8 hours), the crystal sizes range from 80 nm to 600 nm roughly. Figure 5.12(d) (deposition time = 24 hours), the crystal sizes range from 140 nm to 1.4  $\mu\text{m}$  roughly. In Figure 5.12(e) (deposition time = 48 hours), the crystal sizes range from 200 nm to 2.7  $\mu\text{m}$  roughly. With the pressure fixed at 120 Torr,  $\text{Ar:H}_2\text{:CH}_4 = 100:2:0.5$ , and  $f_t = 615$  sccm, and by varying the deposition time from 2 hours to 48 hours increases the low end of the crystal size almost 7 times and 22.5 times for the high end.

Figure 5.12(a)

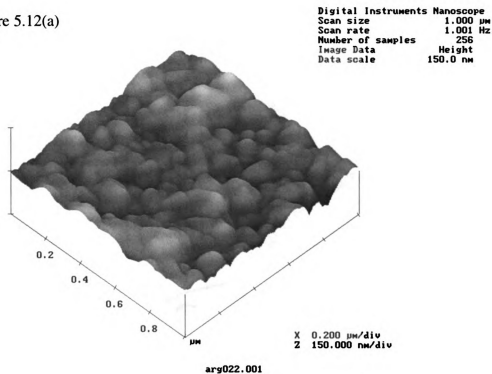


Figure 5.12(b)

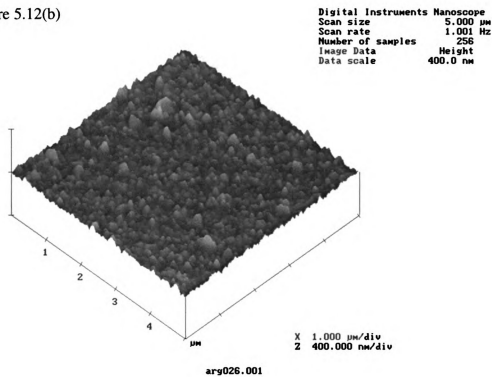


FIGURE 5.12 : FILM MORPHOLOGY VS. DEPOSITION TIME  
Pressure=120 Torr, Ar:H<sub>2</sub>:CH<sub>4</sub>=100:2:0.5, and  $f_t$ =615 sccm by system I.

Figure 5.12(c)

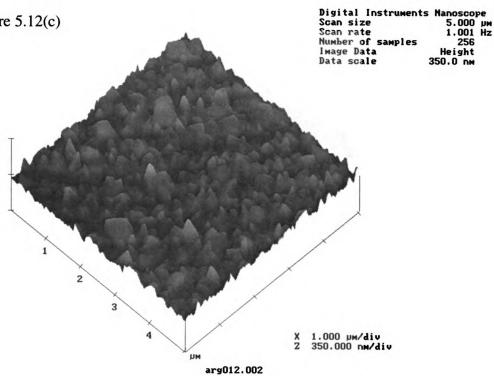


Figure 5.12(d)

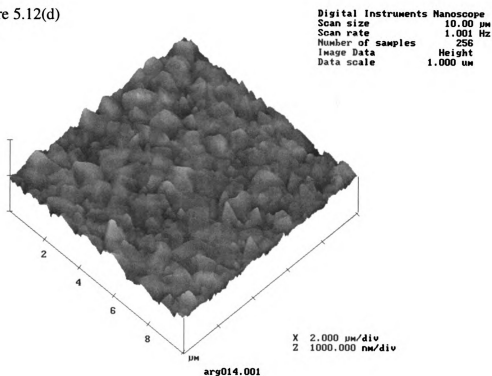
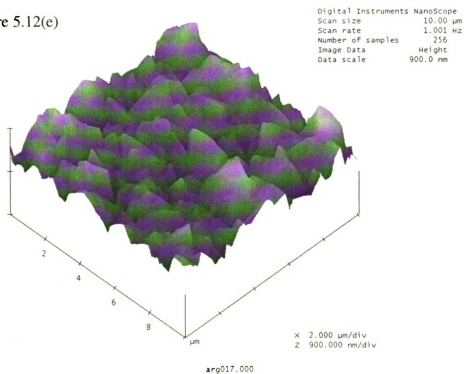


FIGURE 5.12 (cont'd)

Figure 5.12(e)



#### Deposition Time & AFM Scan Size:

Figure 5.12(a): 2 hours;  $1 \times 1 \mu\text{m}^2$

Figure 5.12(b): 4 hours;  $5 \times 5 \mu\text{m}^2$

Figure 5.12(c): 8 hours;  $5 \times 5 \mu\text{m}^2$

Figure 5.12(d): 24 hours;  $10 \times 10 \mu\text{m}^2$

Figure 5.12(e): 48 hours;  $10 \times 10 \mu\text{m}^2$

FIGURE 5.12 (cont'd)

Figure 5.13 displays the film morphology versus different deposition pressures, with  $\text{Ar:H}_2\text{:CH}_4 = 100:2:0.5$ , and  $f_t=615$  sccm and deposition time of 8 hours. Figure 5.13(a), Figure 5.13(b) and Figure 5.13(c) have mostly (111) triangular morphology. In Figure 5.13(a) (deposition pressure = 120 Torr), the crystal sizes range from roughly 80 nm to 600 nm. In Figure 5.13(b) (deposition pressure = 140 Torr), the crystal sizes range from roughly 100 nm to 700 nm. In Figure 5.13(c) (deposition pressure = 160 Torr), the crystal sizes range from roughly 100 nm to 1.2  $\mu\text{m}$ . With  $\text{Ar:H}_2\text{:CH}_4 = 100:2:0.5$ ,  $f_t=615$  sccm and deposition time of 8 hours, by varying the deposition pressure from 120 Torr to 160 Torr increases the low end of the crystal size 1.25 times and almost 2 times for the high end.

Figure 5.13(a)

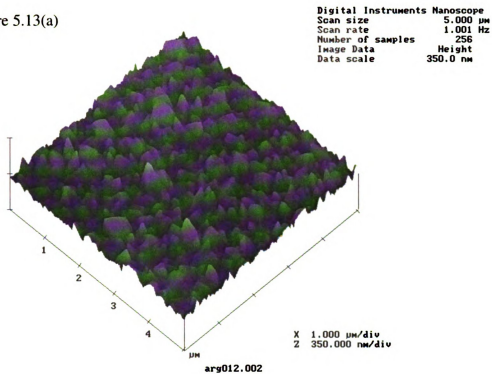


Figure 5.13(b)

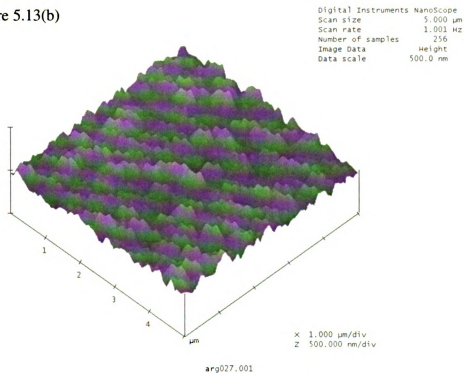


FIGURE 5.13 : FILM MORPHOLOGY VS. DEPOSITION PRESSURE

Deposition Pressure: (a): 120 Torr, (b): 140 Torr, (c): 160 Torr  
Ar:H<sub>2</sub>:CH<sub>4</sub>=100:2:0.5,  $f_t$ =615 sccm and deposition time=8 hours  
by system I.



Figure 5.13(c)

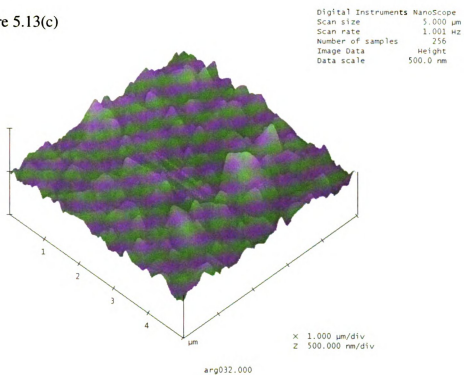


FIGURE 5.13 (cont'd)

## 5.3 System II

### 5.3.1 Film Texture = $g(\text{Ar}/\text{H}_2/\text{CH}_4, f_t, p)$

Figure 5.14 displays the XRD ratio of integrated intensities of diamond  $\langle 220 \rangle$  and  $\langle 111 \rangle$  peaks plotted as a function of the hydrogen flow rate, with argon flow fixed at 100 sccm, methane flow fixed at 1 sccm, pressure of 120 Torr and deposition time of 8 hours. The XRD ratios of intensities of diamond  $\langle 220 \rangle$  and  $\langle 111 \rangle$  peaks are all above 0.25. Therefore, all the films have the (220) preferred orientation.

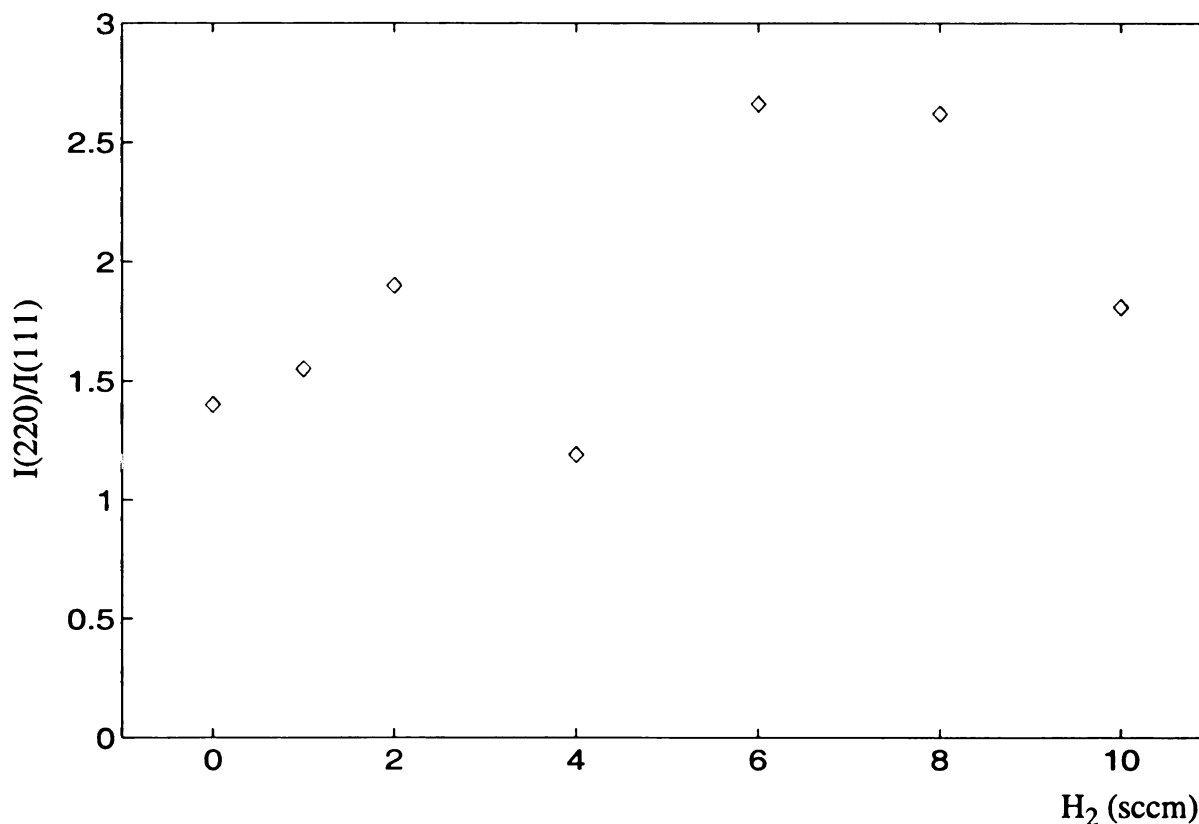


FIGURE 5.14 :  $I(220)/I(111)$  VS.  $\text{H}_2$  FLOW RATE  
Pressure=120 Torr, Ar=100 sccm,  $\text{CH}_4$ =1 sccm and deposition time=8 hours  
by system II

Figure 5.15 displays the XRD ratio of integrated intensities of diamond <220> and <111> peaks plotted as a function of total gas flow rate,  $f_t$ , with pressure of 120 Torr and deposition time of 8 hours. Only the films synthesized with Ar:H<sub>2</sub>:CH<sub>4</sub>=100:4:1 gas chemistry ratio and total gas flow rates equal to 400 sccm or 600 sccm have the (111) preferred orientation. The films synthesized with the gas chemistry ratios of (a) Ar:H<sub>2</sub>:CH<sub>4</sub>=100:2:1; and (b) Ar:H<sub>2</sub>:CH<sub>4</sub>=100:4:1 and total gas flow rate equal to 100 or 200 all have the (220) preferred orientation. At higher total gas flow rates, the films' (220) preferred orientation tends to be weaker.

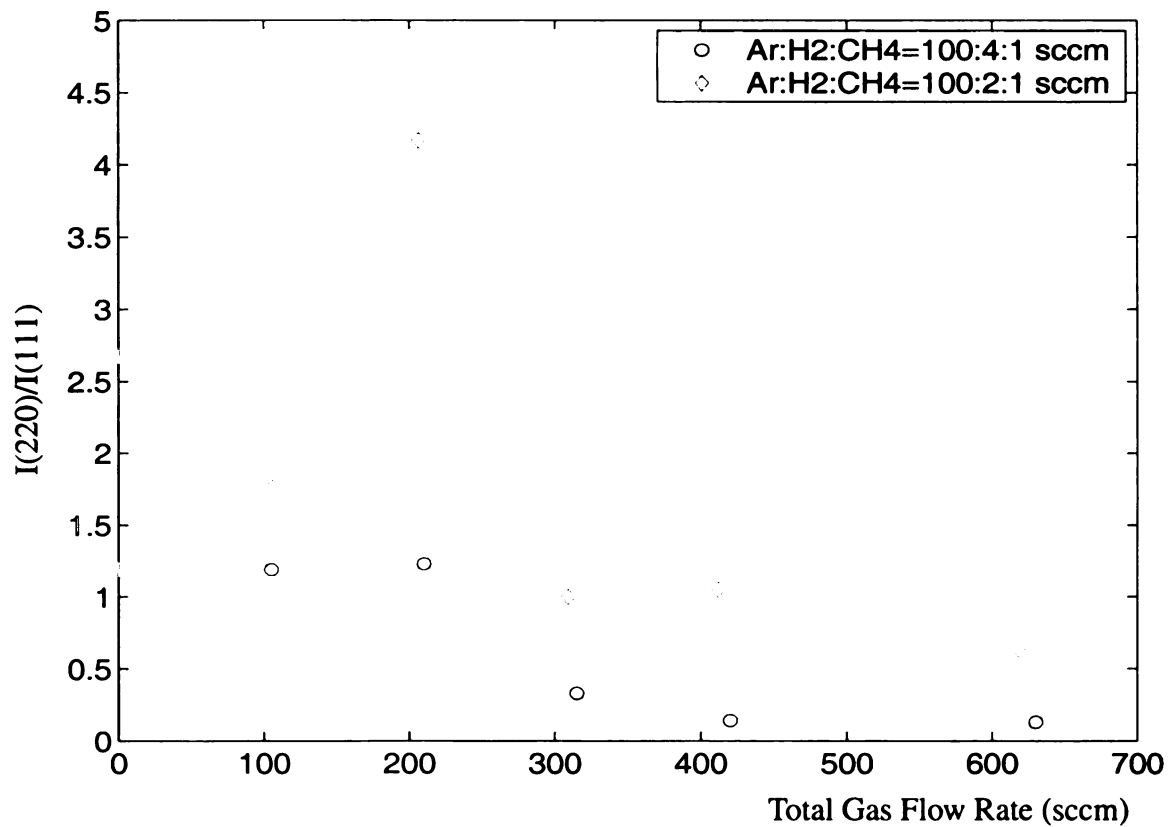


FIGURE 5.15 :  $I(220)/I(111)$  VS. TOTAL GAS FLOW RATE  
Pressure=120 Torr and deposition time=8 hours by system II

Figure 5.16 display the XRD ratio of integrated intensities of diamond <220> and <111> peaks plotted as a function of deposition pressure, with argon flow equal to 100 sccm, methane flow equal to 1 sccm and deposition time of 8 hours. The film corresponds to zero ratio is too thin and is masked under the big Si(400) peak. The XRD ratios of integrated intensities of diamond <220> and <111> peaks usually have a maximum around 140 Torr or 160 Torr except when the hydrogen flow equal to 1 sccm.

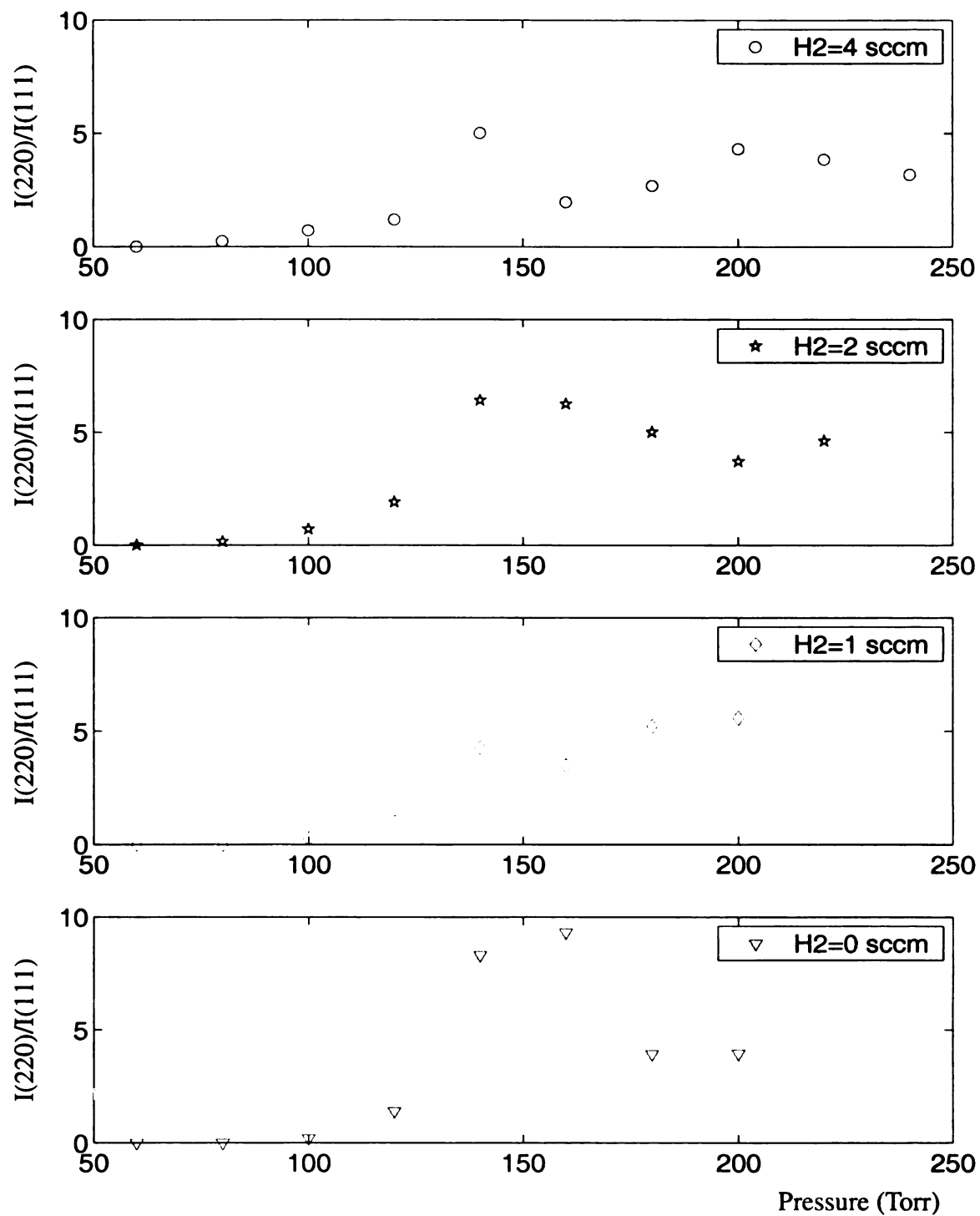


FIGURE 5.16 :  $I(220)/I(111)$  VS. DEPOSITION PRESSURE  
 $Ar/CH_4=100/1$  sccm and deposition time=8 hours by system II

### 5.3.2 Film Roughness = $g(\text{Ar}/\text{H}_2/\text{CH}_4, t, f_t, p)$

Figure 5.17 displays the film roughness plotted as a function of hydrogen flow rate, with argon flow fixed at 100 sccm, methane flow fixed at 1 sccm, pressure at 120 Torr and deposition time of 8 hours. The film roughness increases dramatically with the increases in hydrogen concentration.

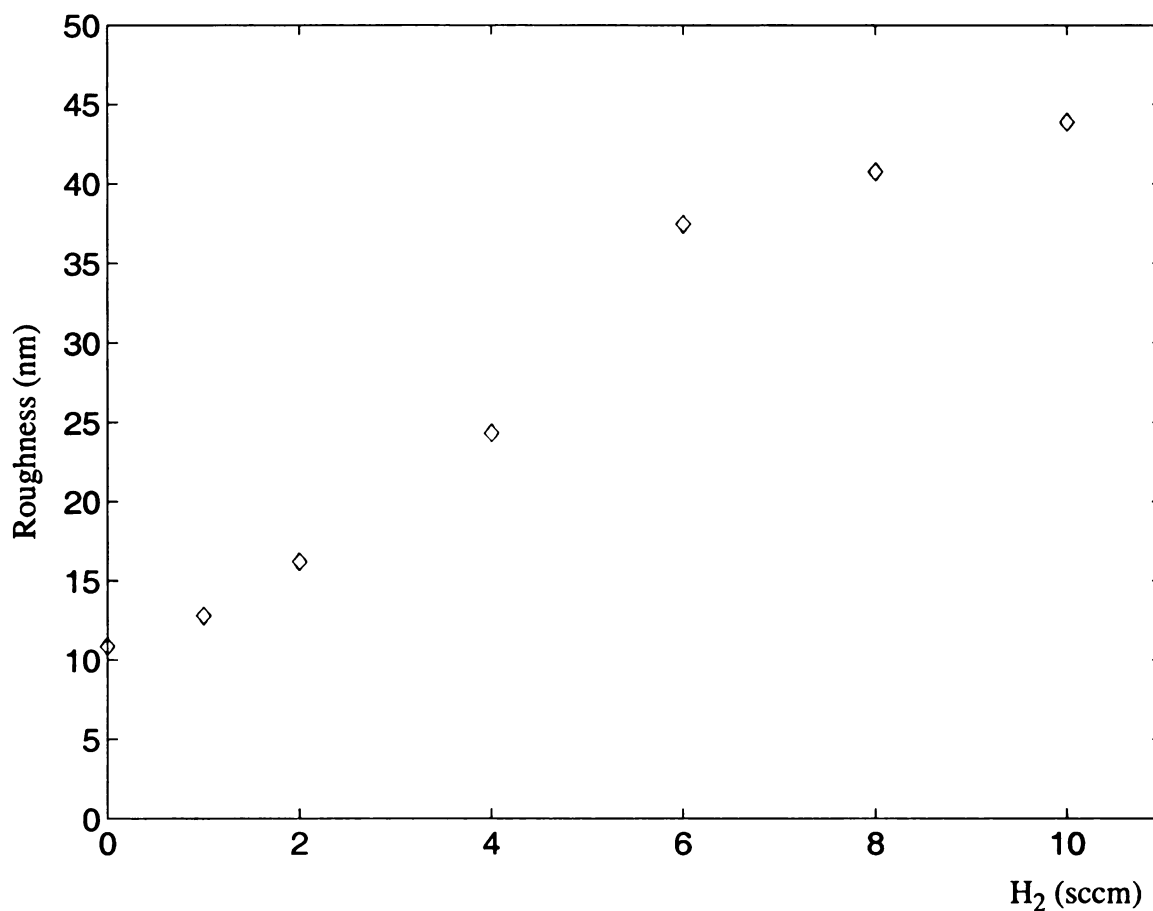


FIGURE 5.17 : RMS ROUGHNESS VS. H<sub>2</sub> FLOW RATE  
Pressure=120 Torr, Ar=100 sccm, CH<sub>4</sub>=1 sccm and deposition time=8 hours  
by system II

Figure 5.18 displays the film roughness plotted as a function of the deposition time,  $t$ , with pressure of 160 Torr and  $\text{Ar}/\text{H}_2/\text{CH}_4 = 100/4/1$  sccm. As shown, the film roughness increases as deposition time increases.

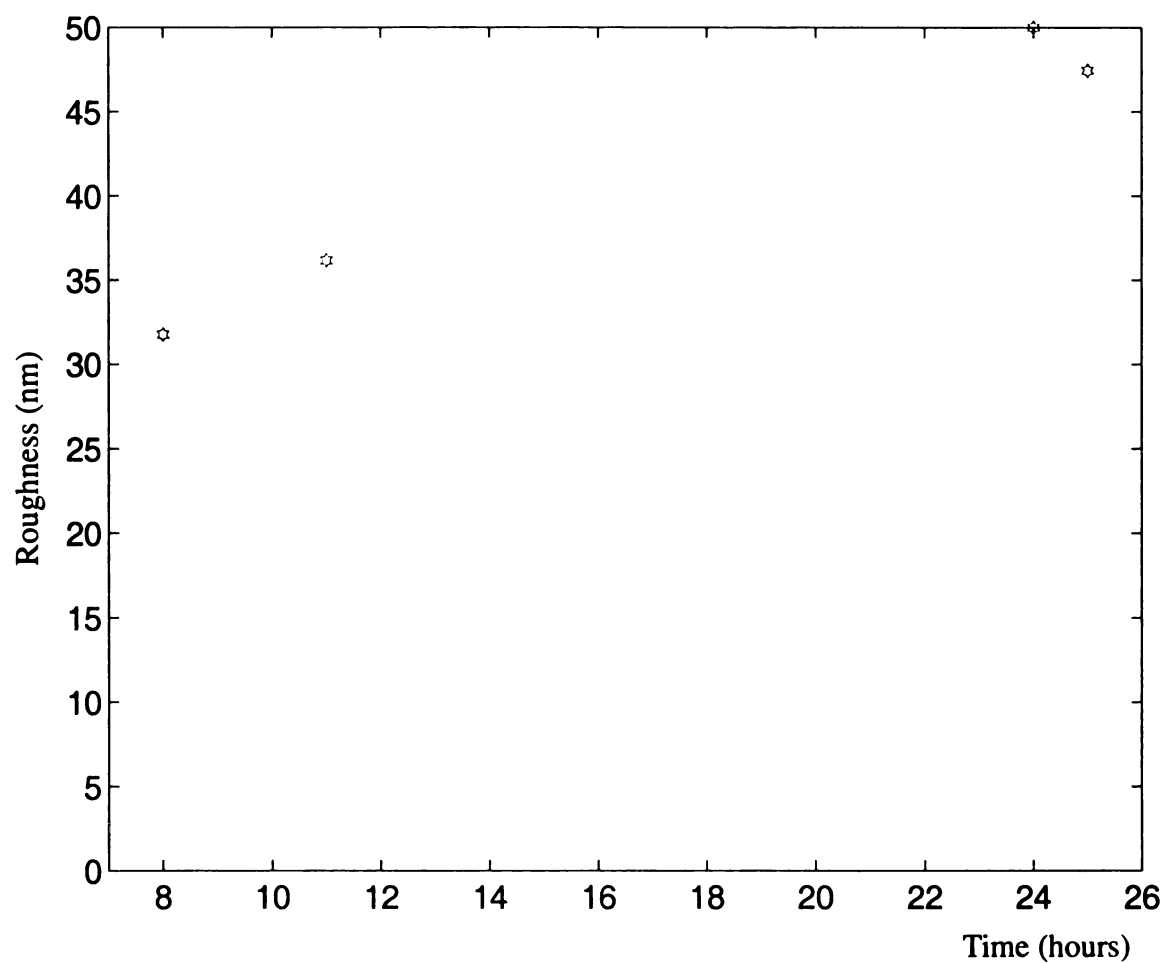
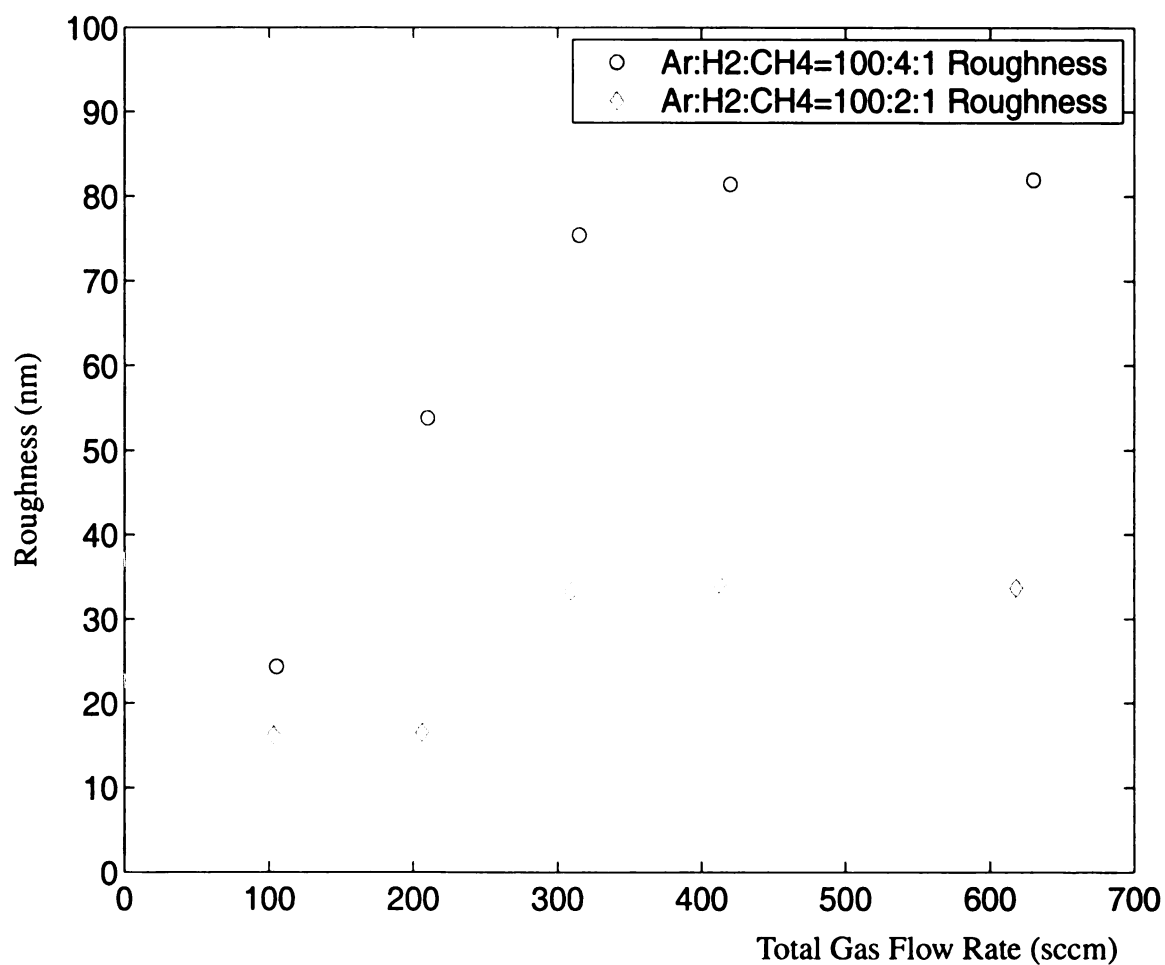


FIGURE 5.18 : RMS ROUGHNESS VS. DEPOSITION TIME  
Pressure=160 Torr,  $\text{Ar}/\text{H}_2/\text{CH}_4=100/4/1$  sccm by System II

Figure 5.19 displays the film roughness plotted as a function of total gas flow rate,  $f_t$ , with pressure of 120 Torr and deposition time of 8 hours. the data indicate that the film roughness increases as total gas flow rate increases.



**FIGURE 5.19 : RMS ROUGHNESS VS. TOTAL GAS FLOW RATE**  
 Pressure=120 Torr and deposition time=8 hours by System II



Figure 5.20 display the film roughness plotted as a function of deposition pressure,  $p$ , with argon flow constant at 100 sccm, methane flow equal to 1 sccm and deposition time of 8 hours. Figure 5.20 shows that between 100-120 Torr, the film roughness achieves minimum. As pressure increases beyond 160 Torr, the film roughness increases. Between 60 to 100 torr, usually, the film roughness decreases as the deposition pressure increases. The smoothest films have a surface roughness of 10-15 nm between 100-160 Torr.

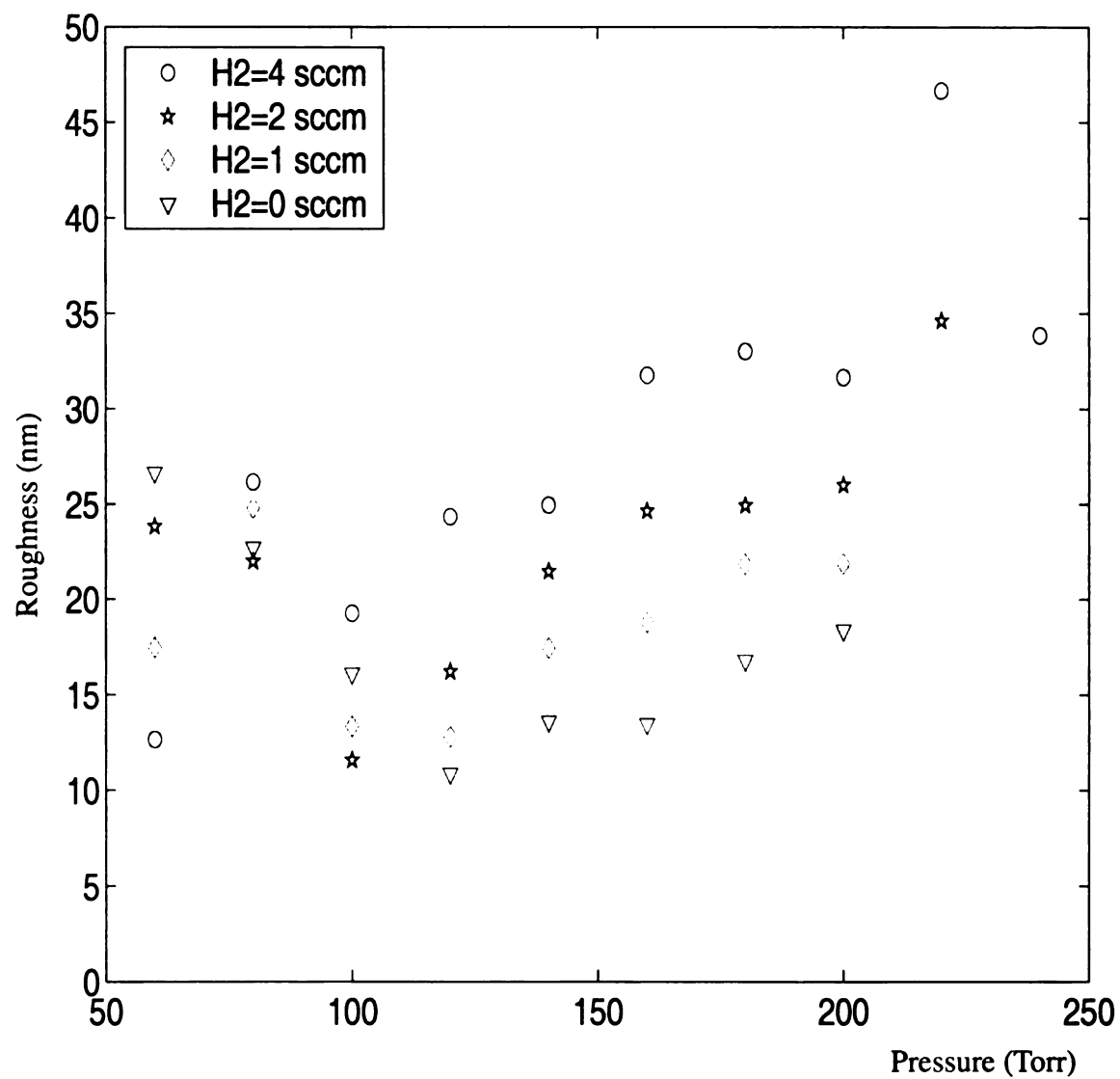
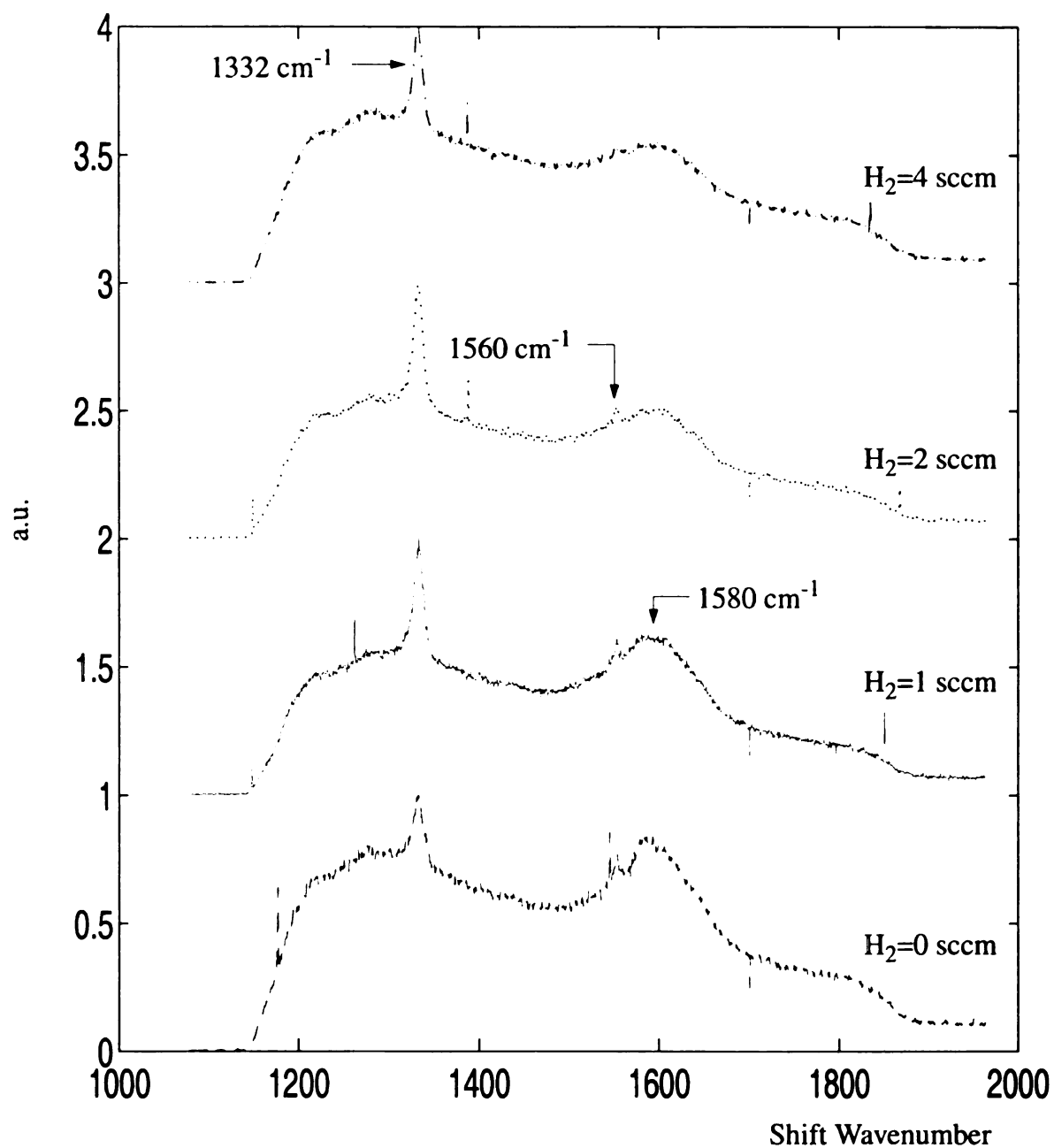


FIGURE 5.20 : RMS ROUGHNESS VS. DEPOSITION PRESSURE  
Ar/CH<sub>4</sub>=100/1 sccm and deposition time=8 hours by System II

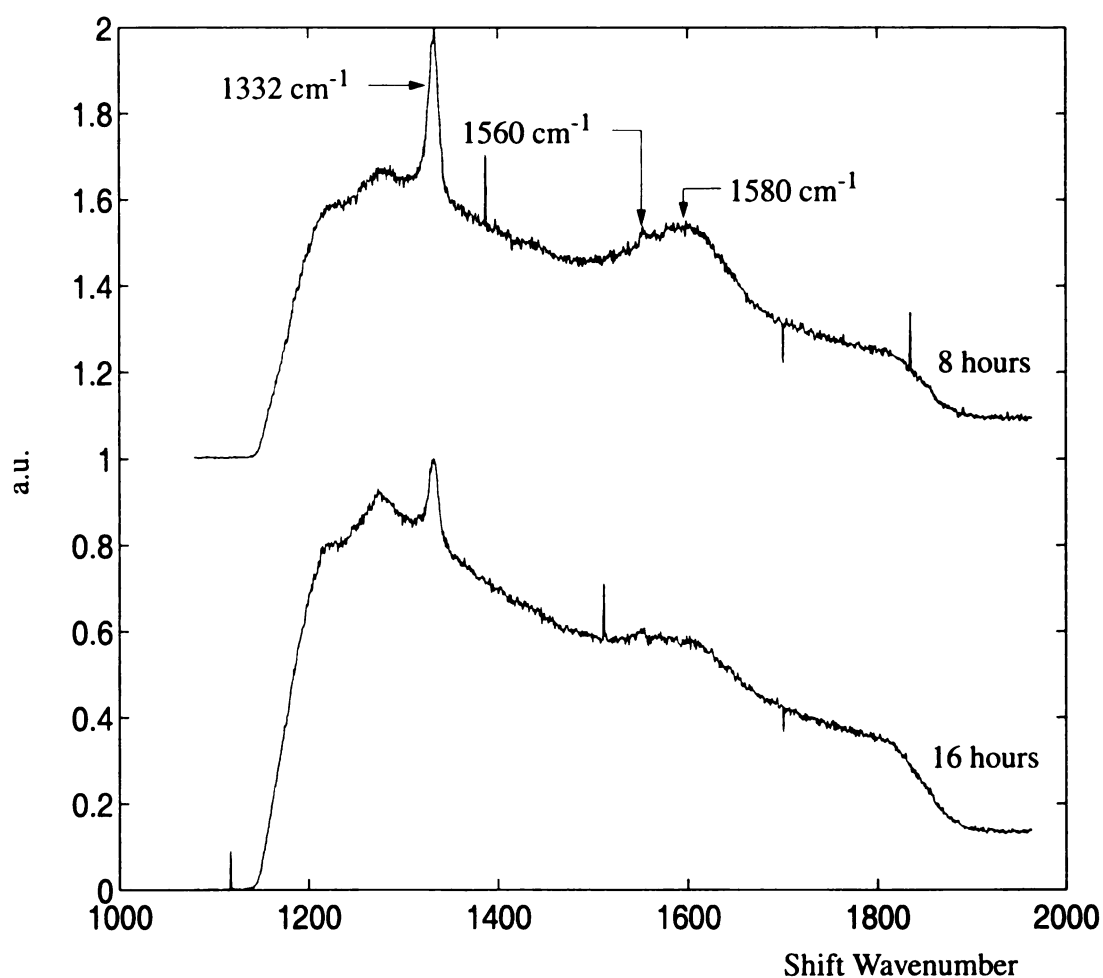
### 5.3.3 Film Quality = $g(\text{Ar}/\text{H}_2/\text{CH}_4, t, p)$

Figure 5.21 displays the Raman Spectra for different hydrogen flow rates, with argon flow fixed at 100 sccm, methane flow fixed at 1 sccm, pressure held constant at 120 Torr and deposition time of 8 hours by system II [Huan 2000]. The intensity of the graphitic/amorphous carbon peak around  $1560\text{ cm}^{-1}$  increases as the input  $\text{H}_2$  concentration decreases. By varying the  $\text{H}_2$  concentration, the variation of the graphitic peak at  $1580\text{ cm}^{-1}$  has been observed. Lower  $\text{H}_2$  concentrations tend to have a higher graphitic peak. This usually indicates more graphite content in the ultra-nanocrystalline diamond films. The FWHM of the  $1332\text{ cm}^{-1}$  diamond peaks are the same. This may be an indication that the crystal size remains the same.



**FIGURE 5.21 : RAMAN SPECTRA**  
Pressure=120 Torr and Ar=100 sccm, CH<sub>4</sub>=1 sccm and deposition time =8 hours  
by system II.  
Spectra Taken by UV-Raman System at Argonne National Lab.

Figure 5.22 displays the Raman Spectra for different deposition times, with pressure held constant at 120 Torr and  $\text{Ar}/\text{H}_2/\text{CH}_4 = 100/4/1$  sccm. The FWHM of the  $1332\text{ cm}^{-1}$  diamond peaks are the same. This may be an indication that the crystal size remains the same.



**FIGURE 5.22 : RAMAN SPECTRA**  
Pressure=120 Torr and  $\text{Ar}/\text{H}_2/\text{CH}_4=100/4/1$  sccm by system II.  
Spectra Taken by UV-Raman System at Argonne National Lab.

Figure 5.23 displays the Raman Spectra for different deposition pressures, with  $\text{Ar}/\text{H}_2/\text{CH}_4 = 100/2/1$  sccm and deposition time of 8 hours. The FWHM of the diamond peaks are the same. This may be an indication that the crystal size remains the same.

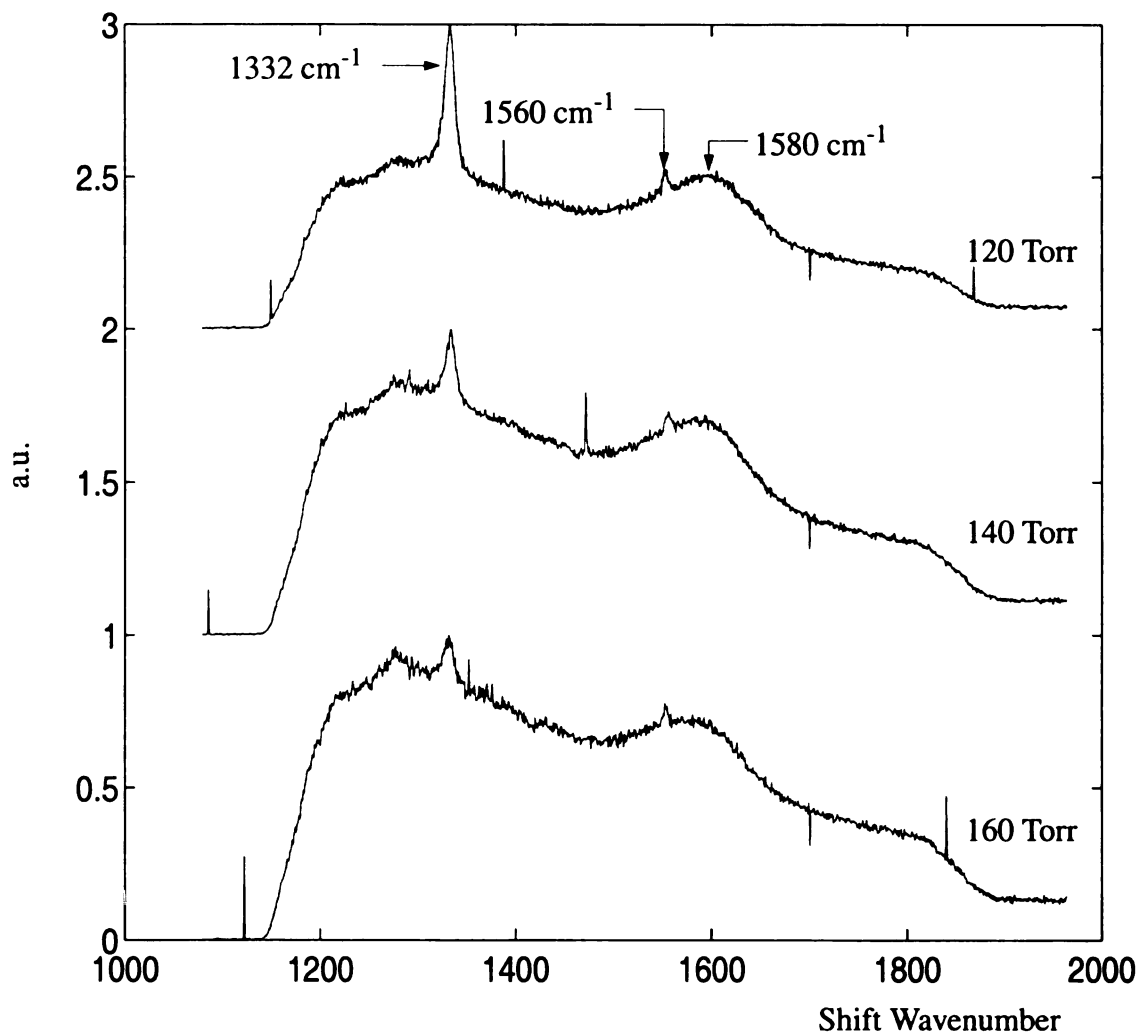


FIGURE 5.23 : RAMAN SPECTRA  
 $\text{Ar}/\text{H}_2/\text{CH}_4 = 100/2/1$  sccm and deposition time=8 hours  
by system II.  
Spectra Taken by UV-Raman System at Argonne National Lab.

### 5.3.4 Morphology = $g(\text{Ar}/\text{H}_2/\text{CH}_4, t, f_t, p)$

The films deposited by system II are fine grained with small smooth projections. The small crystal sizes of the films make it inaccurate to use AFM to determine the crystal size.

Figure 5.24 displays the film morphology for different hydrogen flow rate with argon flow fixed at 100 sccm, methane flow fixed at 1 sccm, pressure held constant at 120 Torr and deposition time of 8 hours. From Figure 5.24(a) to Figure 5.24(g), the films all have a featureless (not showing any crystalline facets) morphology. Therefore, the morphology does not vary with changes in gas chemistry. However, the contour of the film is affected by the gas chemistry. They change from numerous small round protrusions (Figure 5.24(a), (b), (c), and (d)) to many small and medium-sized mounds (Figure 5.24(e), (f), and (g)). The film roughness (See Figure 5.17.) is higher for those films which have more irregular surface contours.

Figure 5.24(a)  
H<sub>2</sub>=0 sccm

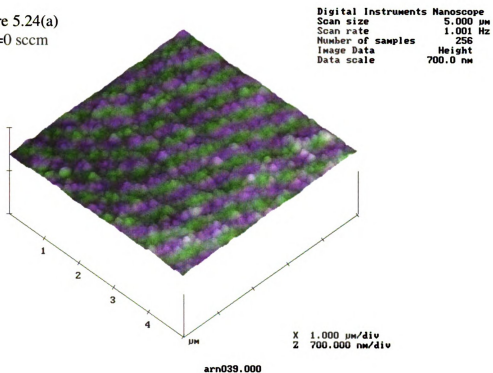


Figure 5.24(b)  
H<sub>2</sub>=1 sccm

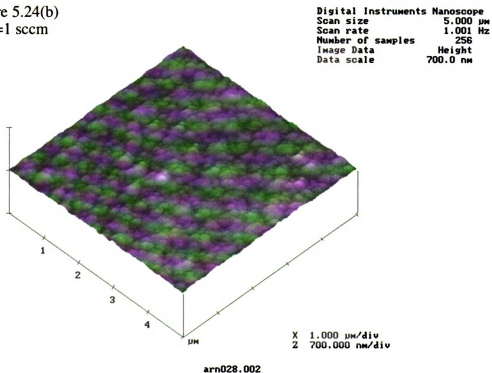


FIGURE 5.24 : FILM MORPHOLOGY VS. H<sub>2</sub> FLOW RATE  
Pressure=120 Torr, Ar=100 sccm, CH<sub>4</sub>=1 sccm and deposition time=8 hours  
by system II.



Figure 5.24(c)  
H<sub>2</sub>=2 sccm

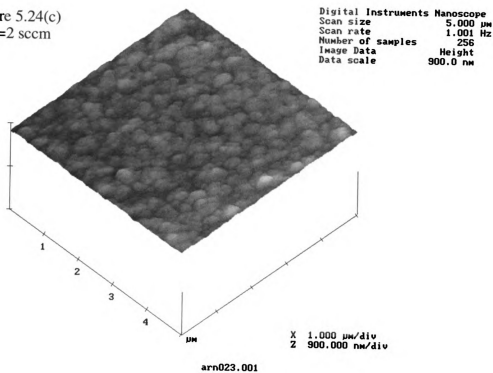


Figure 5.24(d)  
H<sub>2</sub>=4 sccm

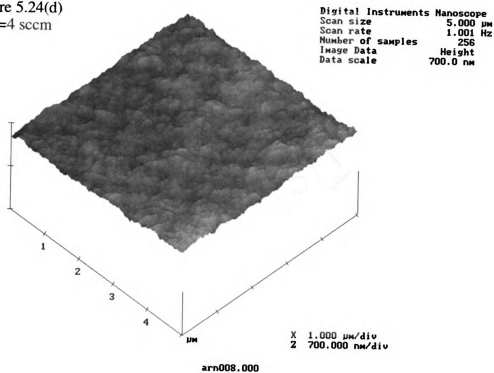


FIGURE 5.24 (cont'd)

Figure 5.24(e)  
H<sub>2</sub>=6 sccm

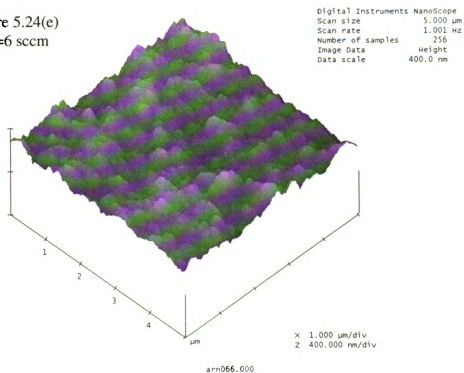


Figure 5.24(f)  
H<sub>2</sub>=8 sccm

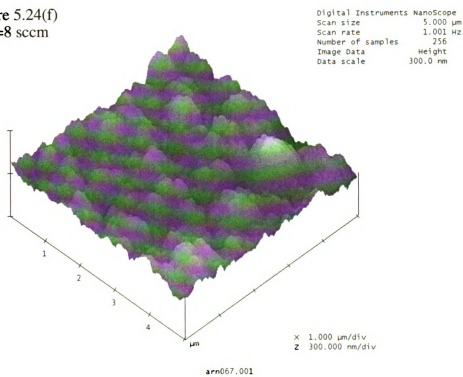


FIGURE 5.24 (cont'd)

Figure 5.24(g)  
 $H_2=10$  sccm

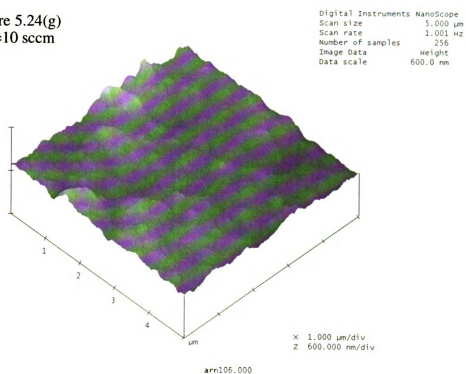


FIGURE 5.24 (cont'd)

Figure 5.25 displays the film morphology for different deposition times with pressure held constant at 160 Torr and  $\text{Ar}/\text{H}_2/\text{CH}_4 = 100/4/1$  sccm. From Figure 5.25(a) to Figure 5.25(c), the films all have a featureless morphology. Therefore, the morphology does not vary with changes in deposition time. However, the contour of the film is different for each film. The contour of the film changes from many round protrusions (Figure 5.25(a)) to numerous small smooth projections (Figure 5.25(b)) and to small and medium-sized mounds (Figure 5.25(c)). The film roughness (See Figure 5.18.) is higher for those films which have more irregular surface contours.

Figure 5.25(a)  
t=8 hours

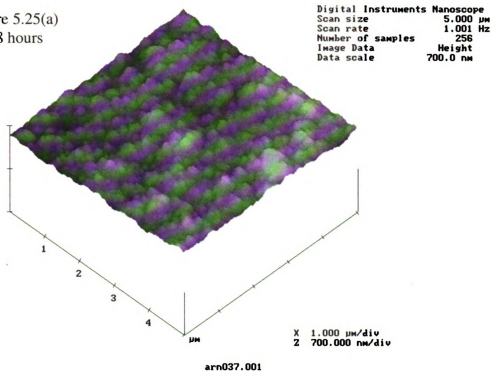


Figure 5.25(b)  
t=11 hours

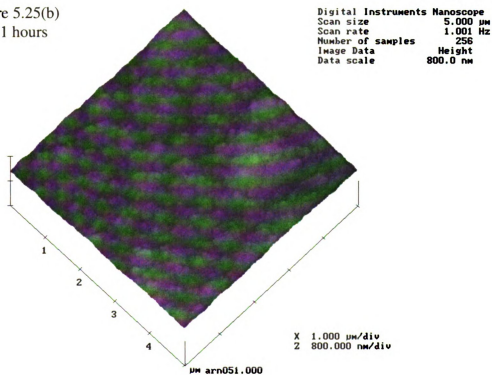


FIGURE 5.25 : FILM MORPHOLOGY VS. DEPOSITION TIME  
 Pressure=160 Torr,  $\text{Ar}/\text{H}_2/\text{CH}_4=100/4/1$  sccm by system II

Figure 5.25(c)  
t=25 hours

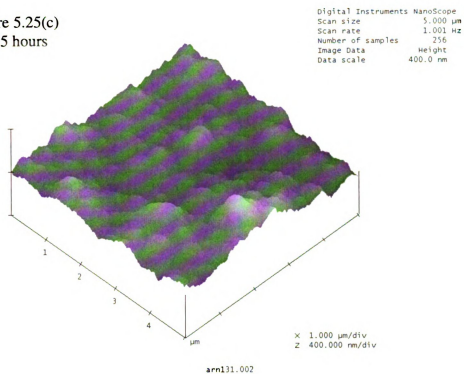


FIGURE 5.25 (cont'd)

Figure 5.26 displays the film morphology for different total gas flow rates with the pressure held constant at 120 Torr, Ar:H<sub>2</sub>:CH<sub>4</sub>=100:2:1 sccm and deposition time of 8 hours. From Figure 5.26(a) to Figure 5.26(e), the films all have featureless morphology. Therefore, the morphology is not affected by total gas flow rate. However, the total gas flow rate does affect the contour of the film. The contour of the film changes from small smooth projections (Figure 5.26(a)) to small round protrusions (Figure 5.26(b)) and to small and medium-sized mounds (Figure 5.26(c), (d), and (e)). The film roughness (See Figure 5.19.) is higher for those films which have more irregular surface contours.

Figure 5.26(a)  
 $f_t=103$  sccm

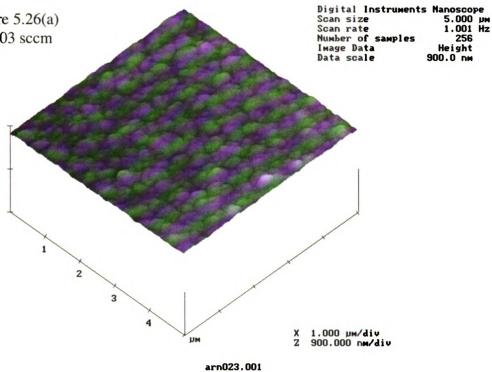


Figure 5.26(b)  
 $f_t=206$  sccm

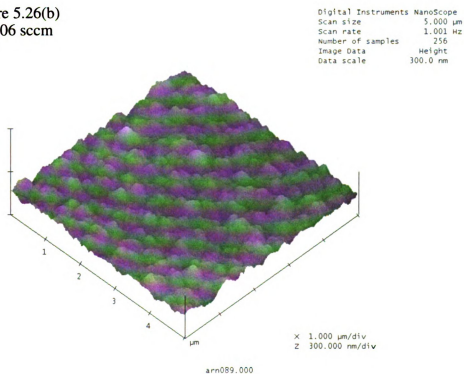


FIGURE 5.26 : FILM MORPHOLOGY VS. TOTAL GAS FLOW RATE  
 Pressure=120 Torr, Ar:H<sub>2</sub>:CH<sub>4</sub>=100:2:1 sccm and deposition time=8 hours  
 by system II



Figure 5.26(c)  
 $f_i=309$  sccm

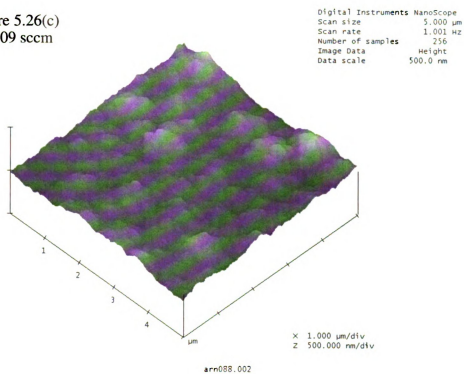


Figure 5.26(d)  
 $f_i=412$  sccm

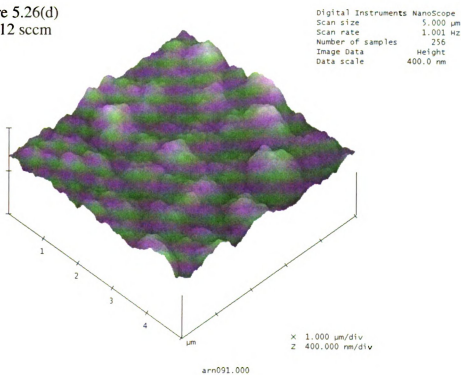


FIGURE 5.26 (cont'd)

Figure 5.26(e)  
 $f_t=618$  sccm

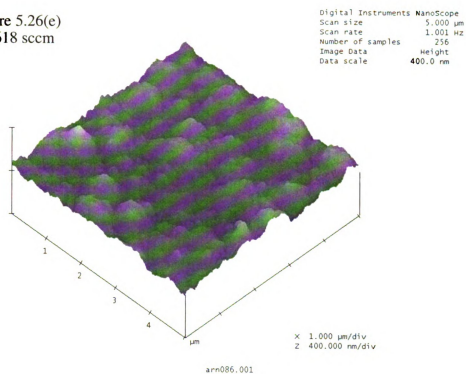


FIGURE 5.26 (cont'd)

Figure 5.27 display the film morphology for different deposition pressures with  $\text{Ar}/\text{H}_2/\text{CH}_4=100/4/1$  sccm and deposition time of 8 hours. As shown in Figures 5.27(a) to 5.27(j), the films all have featureless morphology. Therefore, the morphology does not vary with changes in deposition pressure. However, the contour of the films are somewhat different as the deposition pressure changes. The contour of the film changes from numerous smooth projections (Figure 5.27(a)) to small-sized mounds (Figure 5.27(b)) to tiny and small-sized protrusions (Figure 5.27(c)) to numerous small smooth projections (Figure 5.27 (d)) to small smooth protrusions (Figure 5.27(e), (f), (g), and (h)) to small and medium-sized hills (Figure 5.27(i)) and to small and medium-sized mounds (Figure 5.27(j)). The film roughness (See Figure 5.20.) is higher for those films which have more irregular surface contours.

Figure 5.27(a): 60 Torr

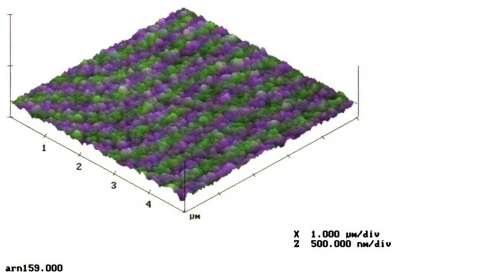


Figure 5.27(b): 80 Torr

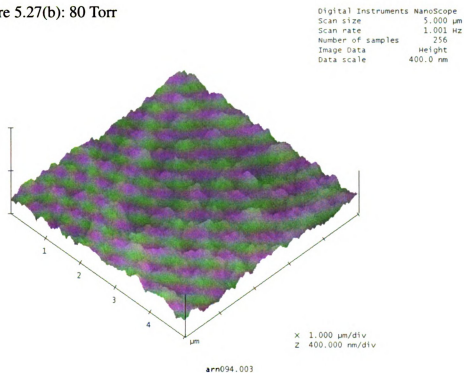


FIGURE 5.27 : FILM MORPHOLOGY VS. DEPOSITION PRESSURE  
 $\text{Ar}/\text{H}_2/\text{CH}_4=100/4/1$  sccm and deposition time=8 hours  
 by system II.

Figure 5.27(c): 100 Torr

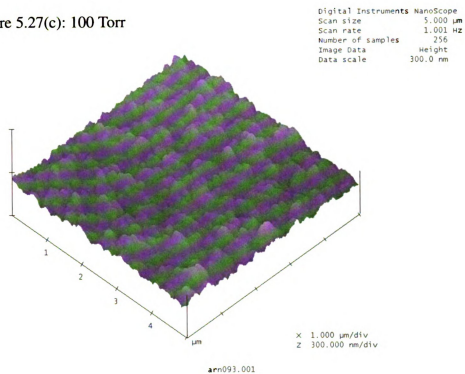


Figure 5.27(d): 120 Torr

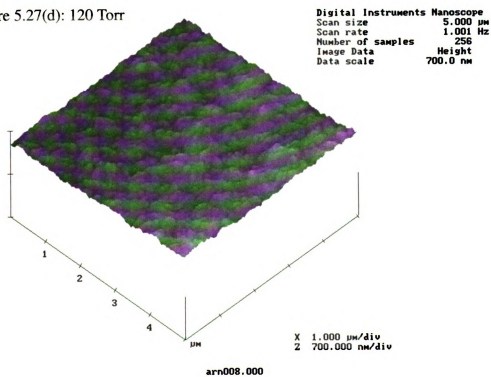


FIGURE 5.27 (cont'd)

Figure 5.27(e): 140 Torr

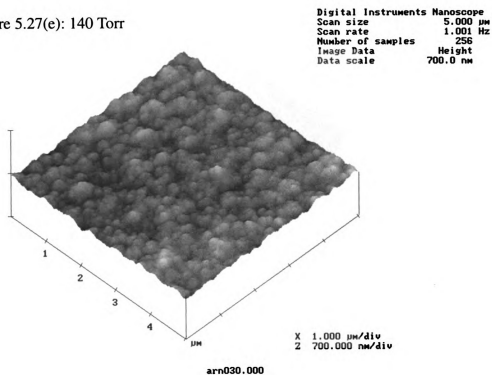


Figure 5.27(f): 160 Torr

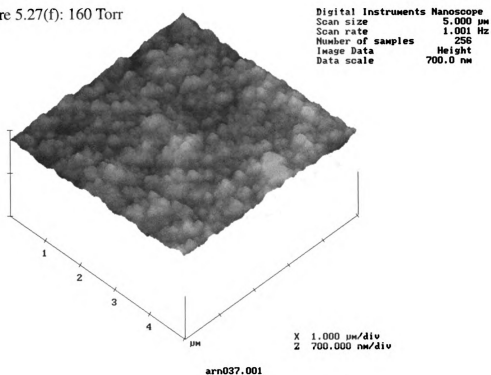


FIGURE 5.27 (cont'd)

Figure 5.27(g): 180 Torr

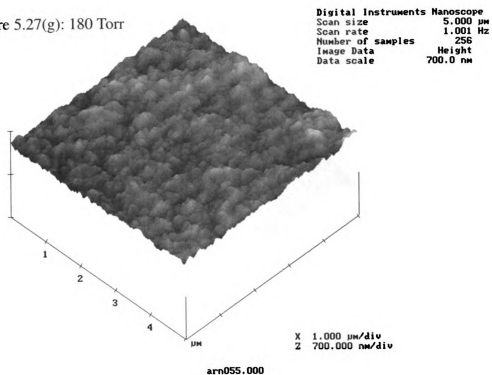


Figure 5.27(h): 200 Torr

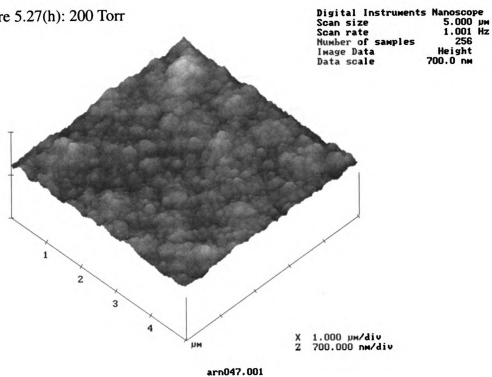


FIGURE 5.27 (cont'd)

Figure 5.27(i): 220 Torr

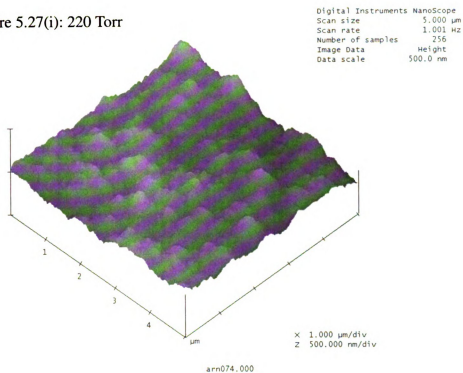


Figure 5.27(j): 240 Torr

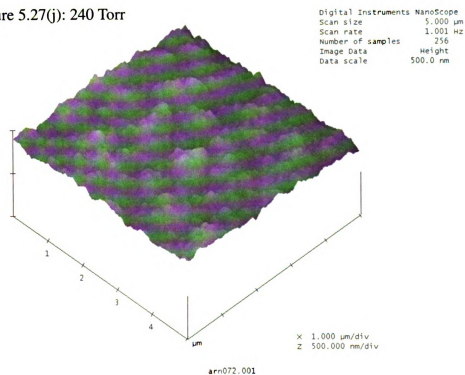


FIGURE 5.27 (cont'd)



Figure 5.28 display the film morphology for different deposition pressures with  $\text{Ar}/\text{H}_2/\text{CH}_4=100/0/1$  sccm and deposition time of 8 hours. As shown in Figure 5.28(a) to 5.28(h), the films all have a featureless morphology. Therefore, the morphology does not vary with changes in deposition pressure. However, the contour of the films varies as deposition pressure changes. The contour of the film changes from small round protrusions (Figure 5.28(a) and (b)) to small-sized hills (Figure 5.28(c)) and to small smooth projections (Figure 5.28(d), (e), (f), (g), and (h)). The film roughness (See Figure 5.21.) is higher for those films which have more irregular surface contours.

Figure 5.28(a): 60 Torr

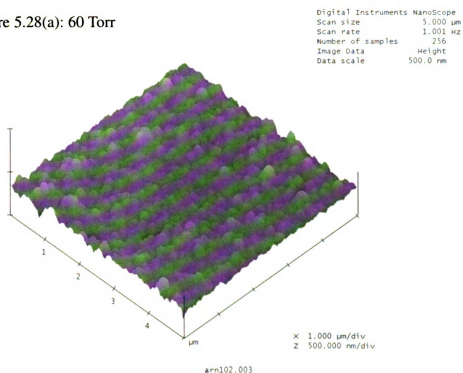
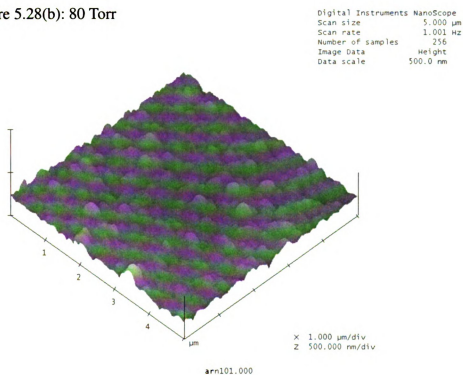


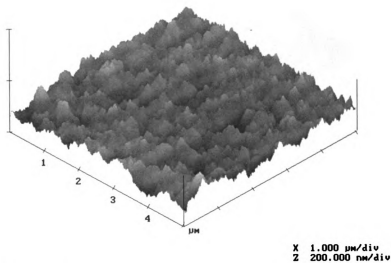
Figure 5.28(b): 80 Torr



**FIGURE 5.28 : FILM MORPHOLOGY VS. DEPOSITION PRESSURE**  
 $\text{Ar}/\text{H}_2/\text{CH}_4=100/0/1$  sccm and deposition time=8 hours  
 by system II

Figure 5.28(c): 100 Torr

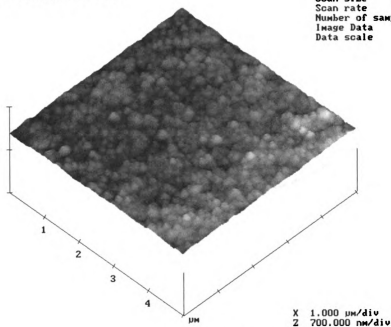
Digital Instruments Nanoscope  
 Scan size 5.000  $\mu\text{m}$   
 Scan rate 1.001 Hz  
 Number of samples 256  
 Image Data Height  
 Data scale 200.0 nm



arn100.002

Figure 5.28(d): 120 Torr

Digital Instruments Nanoscope  
 Scan size 5.000  $\mu\text{m}$   
 Scan rate 1.001 Hz  
 Number of samples 256  
 Image Data Height  
 Data scale 700.0 nm



arn039.000

FIGURE 5.28 (cont'd)

Figure 5.28(e): 140 Torr

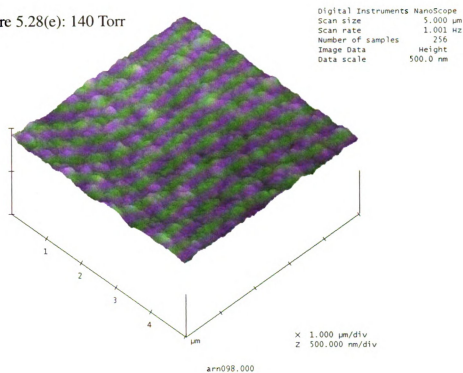


Figure 5.28(f): 160 Torr

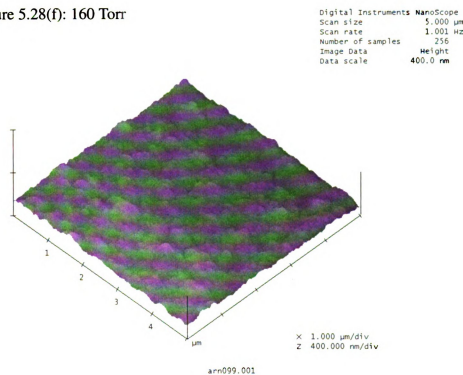


FIGURE 5.28 (cont'd)

Figure 5.28(g): 180 Torr

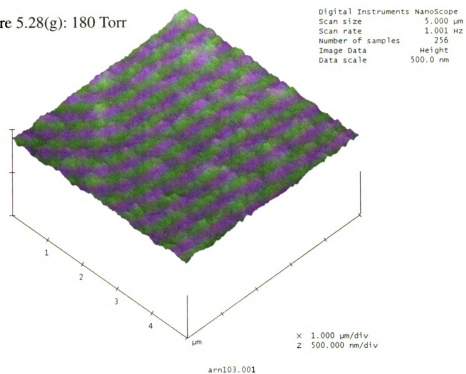


Figure 5.28(h): 200 Torr

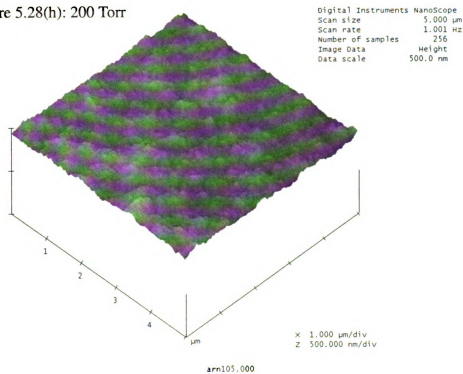


FIGURE 5.28 (cont'd)

### 5.3.5 Growth Mechanism & Crystal Size= g(Ar/H<sub>2</sub>/CH<sub>4</sub>)

To investigate the growth mechanism and to observe the microstructure of the ultra-nanocrystalline diamond film on the silicon substrate, cross-section TEM images were taken. The ultra-nanocrystalline diamond film was deposited in system II with the following experimental conditions: pressure=120 Torr, argon flow rate=100 sccm, hydrogen flow rate=4 sccm, methane flow rate=1 sccm, time=8 hours, and no additional nitrogen.

A cross-section TEM bright field image of the diamond film on a silicon substrate is displayed in Figure 5.29. It is clearly shown in the image that there is a transitional layer (~50 nm) between the silicon substrate and the diamond film. The nature of this interlayer is unknown. Further probing using EELS (Electron Energy Loss Spectroscopy) is recommended to identify the nature of this interlayer. Further away from the silicon boundary and the transitional interlayer (around 280 nm to the right, see the white arrow), there seems to be some cone-shaped features. According to the results of the researchers from ANL (Argonne National Laboratory), the cone-shaped features (see the black arrow) that appear in Figure 5.29 are not columnar-type single crystals. It actually consists of many nanosized grains [Jiao 1999]. From Figure 5.29, diamond appears to deposit on the silicon substrate directly (black arrow), in the transitional layer, and also in the film beyond the transitional layer (re-nucleation).

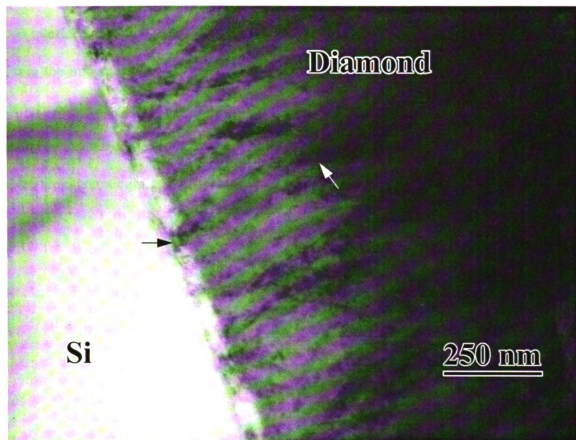


FIGURE 5.29 : BRIGHT FIELD TEM IMAGE

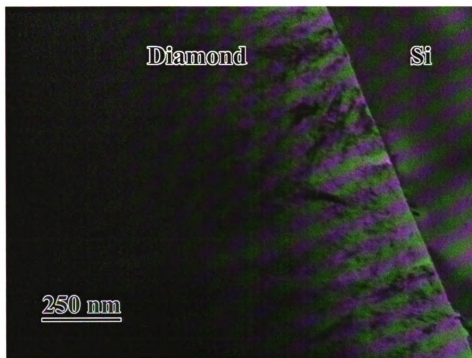
Black arrow: interlayer, white arrow: cone-shaped feature.

Sample: Deposition pressure=120 Torr, Ar/H<sub>2</sub>/CH<sub>4</sub>=100/4/1 sccm and  
deposition time=8 hours by system II

A pair of bright field and dark field cross-section TEM images of the diamond/silicon interface taken in the different area of the same specimen are displayed in Figure 5.30. From the images, the transitional interlayer is invisible at this area. Diamond appears to deposit on the silicon substrate directly. In the images, the MSU-ultra-nanocrystalline diamond grains are equiaxed and aspect ratio. From Figure 5.30 (B), it is clearly shown that there are diamond grains which re-nucleate after the boundary of silicon and diamond.



(A)



(B)

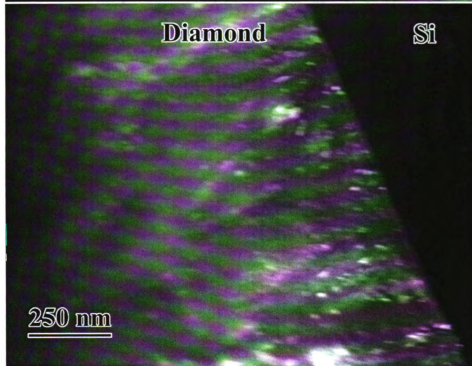


FIGURE 5.30 : BRIGHT FIELD(A) & DARK FIELD(B) TEM IMAGES  
Sample: Deposition pressure=120 Torr,  $\text{Ar}/\text{H}_2/\text{CH}_4=100/4/1$  sccm and  
deposition time=8 hours by system II

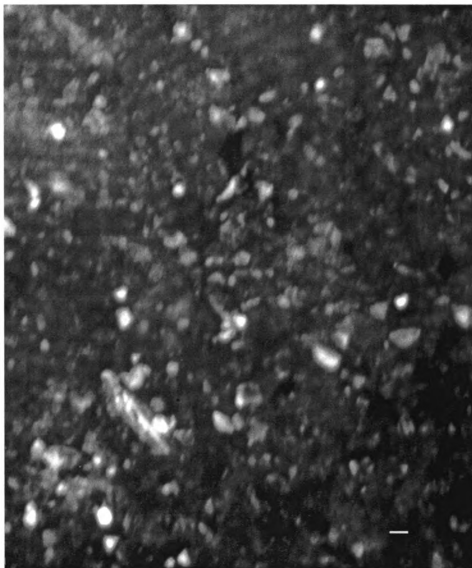
Figure 5.31 displays a cross-section TEM dark field image of Figure 5.30 at higher magnification. It shows many small diamond grains agglomerated together. The comet-tailed features (see the white arrow) are not single crystals because there are many spots inside one tail. The spot inside the tails can be an individual crystal or groups of crystals with the same orientation with respect to the diffraction condition.



FIGURE 5.31 : DARK FIELD TEM IMAGE  
Sample: Deposition pressure=120 Torr, Ar/H<sub>2</sub>/CH<sub>4</sub>=100/4/1 sccm and  
deposition time=8 hours by system II

The crystal sizes of the films deposited by system II are very small. Plan-view TEM (Transmission Electron Microscopy) images were taken to observe the microstructure and to measure the crystal sizes. Based on the results by cross-section TEM, the cone-shaped and comet-tailed features (conglomerate structures) are not big single crystals. Then the crystal size determined by plan-view TEM is meaningful.

A dark field TEM image, Figure 5.32, was obtained by selecting a fraction of the (111) ring of the SAD (Selected Area Diffraction) with an objective aperture. It shows different orientations of the ultra-nanocrystalline diamond [Huan 2000]. Crystallinities contributing to this fraction of diffraction illuminate brightly over the dark background. The differences in the orientation with respect to the diffraction condition has caused the differences in the contrast between the individual grains in the image. The upper bound limit of the crystal sizes is about 20 nm.



Scale Bar=10 nm

FIGURE 5.32 : DARK FIELD TEM IMAGE BY ANL [HUAN 2000]  
Sample: Deposition pressure=120 Torr, Ar/H<sub>2</sub>/CH<sub>4</sub>=100/4/1 sccm and  
deposition time=8 hours by system II

Figure 5.33 is a HRTEM (High Resolution TEM) image which shows planar defects such as stacking faults (on the order of angstroms) and twinning [Huan 2000]. It appears that there is not much amorphous carbon in the intergranular boundaries and there is no evidence of segregation. The microtwins in the film have been interpreted as a secondary nucleation mechanism. Such a secondary nucleation mechanism could be the cause of the high nucleation rate which in turn produces nano-sized diamond grains [Luo]. In Figure 5.33, the crystal sizes range from 1-15 nm.

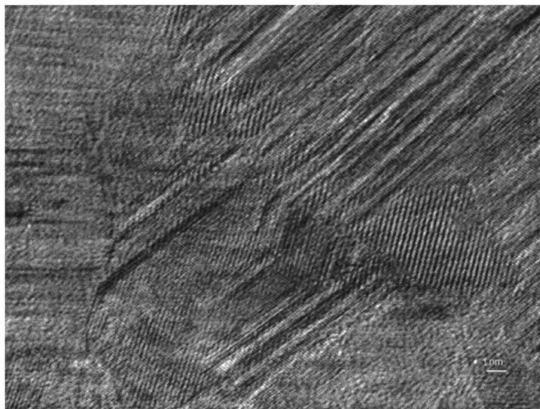


FIGURE 5.33 : HIGH RESOLUTION TEM IMAGE BY ANL [HUAN 2000]

Sample: Deposition pressure=120 Torr, Ar/H<sub>2</sub>/CH<sub>4</sub>=100/4/1 sccm and  
deposition time=8 hours by system II

Due to the better contrast (than bright field TEM) and higher statistics (capable of covering hundreds or thousands of crystals rather than several in a typical HRTEM), a dark field image is used to determine grain size distribution for ultra-nanocrystalline materials. Figure 5.34 shows an automapping of histogram of grain size distribution of the film in Figure 5.32. The data was obtained with NIH imaging analysis software, showing that the crystals are predominantly of the size  $\leq 7$  nm [Huan 2000], [Huan 2001].

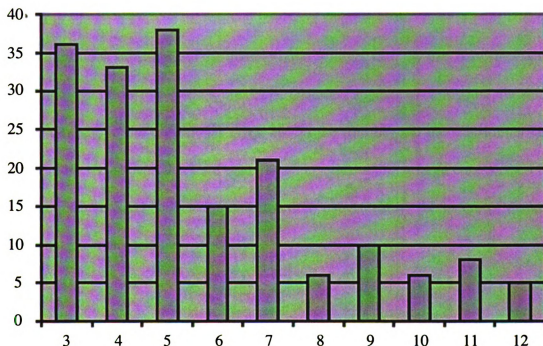


FIGURE 5.34 : A HISTOGRAM OF FIGURE 5.32 BY ANL [HUAN 2000]

Grain size distribution of MSU ultra-nanocrystalline diamond film  
 Sample: Deposition pressure=120 Torr, Ar/H<sub>2</sub>/CH<sub>4</sub>=100/4/1 sccm and  
 deposition time=8 hours by system II

To investigate the influence of additional hydrogen on the growth mechanism, another ultra-nanocrystalline diamond film was deposited by system II with the following experimental conditions: pressure=120 Torr, argon flow rate=100 sccm, methane flow rate=1 sccm, time=8 hours, and no additional nitrogen. To observe the microstructure of the ultra-nanocrystalline diamond film on the silicon substrate, cross-sectional TEM images were taken.

A dark field cross-section TEM image of the diamond film on a silicon substrate is displayed in Figure 5.35. The transitional interlayer (between two white arrows, ~70 nm) between the silicon substrate and the diamond film is larger than the film deposited with 4 sccm of hydrogen flow rate (see Figure 5.29). Diamond appears to deposit on the silicon substrate directly, in the transitional layer, and in the film beyond the transitional layer (re-nucleation). As shown, there are many small crystals within a large cone-shaped features. The inserted SAD (selected area diffraction) pattern shows the nature of diamond but does not show any texture.

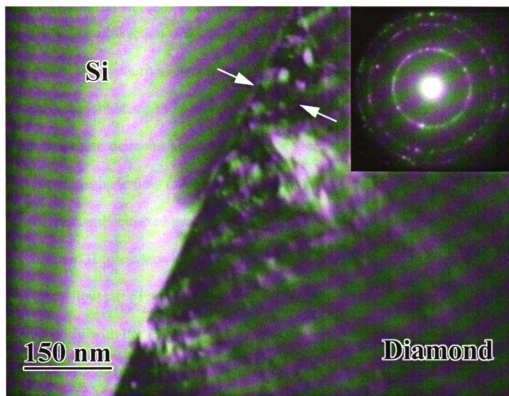


FIGURE 5.35 : DARK FIELD TEM IMAGE  
Sample: Deposition pressure=120 Torr, Ar/CH<sub>4</sub>=100/1 sccm and  
deposition time=8 hours by system II



A bright field plan-view TEM image with a corresponding SAD pattern is displayed in Figure 5.36. The diffraction rings, indexed as diamond, are visible up to (531). Both the image and the SAD pattern show the polycrystalline nature of the ultra-nanocrystalline diamond film and indicate the randomness of the crystal orientations. As shown, the ultra-nanocrystalline diamond grains grown by system II (pressure=120 Torr, argon flow rate=100 sccm, methane flow rate=1 sccm, time=8 hours, and no additional nitrogen) has both aspect ratio and equiaxed grains. Similar to the ultra-nanocrystalline diamond grains grown by system II (pressure=120 Torr, argon flow rate=100 sccm, hydrogen flow rate=4 sccm, methane flow rate=1 sccm, time=8 hours, and no additional nitrogen). The comparison of this study with the results of similar research at ANL shows the film grown with Ar/CH<sub>4</sub>=100/1 sccm (other deposition conditions are the same) has fewer aspect ratio grains [Jiao 1999].

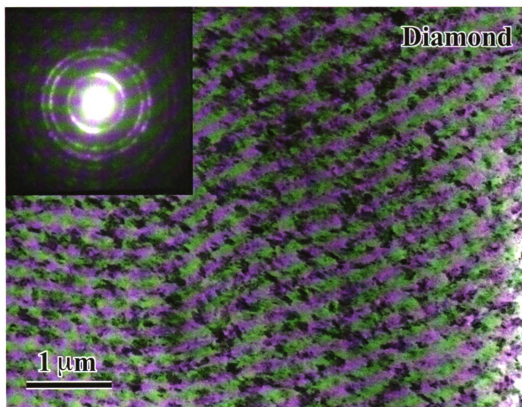


FIGURE 5.36 : PLAN VIEW BRIGHT FIELD TEM IMAGE  
Sample: Deposition pressure=120 Torr, Ar/CH<sub>4</sub>=100/1 sccm and  
deposition time=8 hours by system II

## 5.4 Controlled Nitrogen Impurity Study By System II

Figure 5.37 display the XRD ratio of integrated intensities of diamond <220> and <111> peaks plotted as a function of nitrogen impurities with pressure at 120 Torr, gas chemistry fixed at  $\text{Ar}/\text{H}_2/\text{CH}_4=100/4/1$  sccm and deposition time of 8 hours. The XRD ratios of intensities of diamond <220> and <111> peaks are all above 0.25. Therefore, most of the films have the (220) preferred orientation. Between 0 and 2500 ppm of nitrogen impurity, the XRD ratios of intensities of diamond <220> and <111> peaks reach the minimum as nitrogen impurity equal to 1200 ppm.

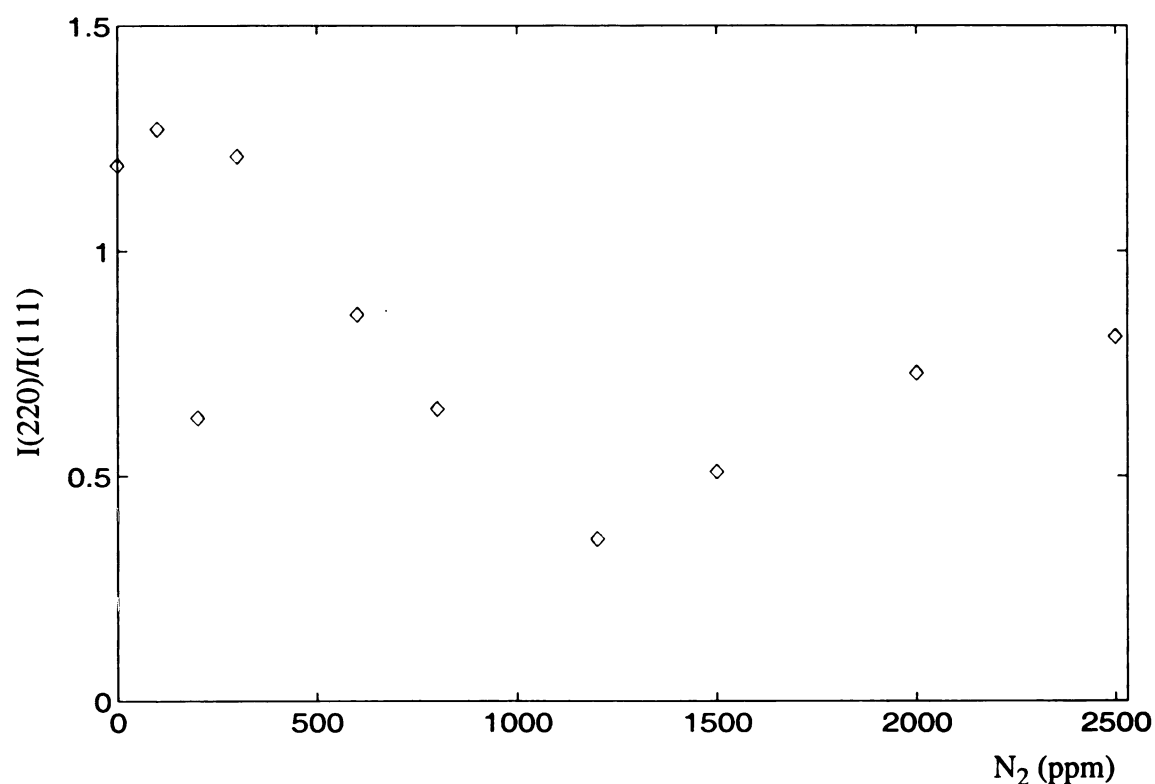
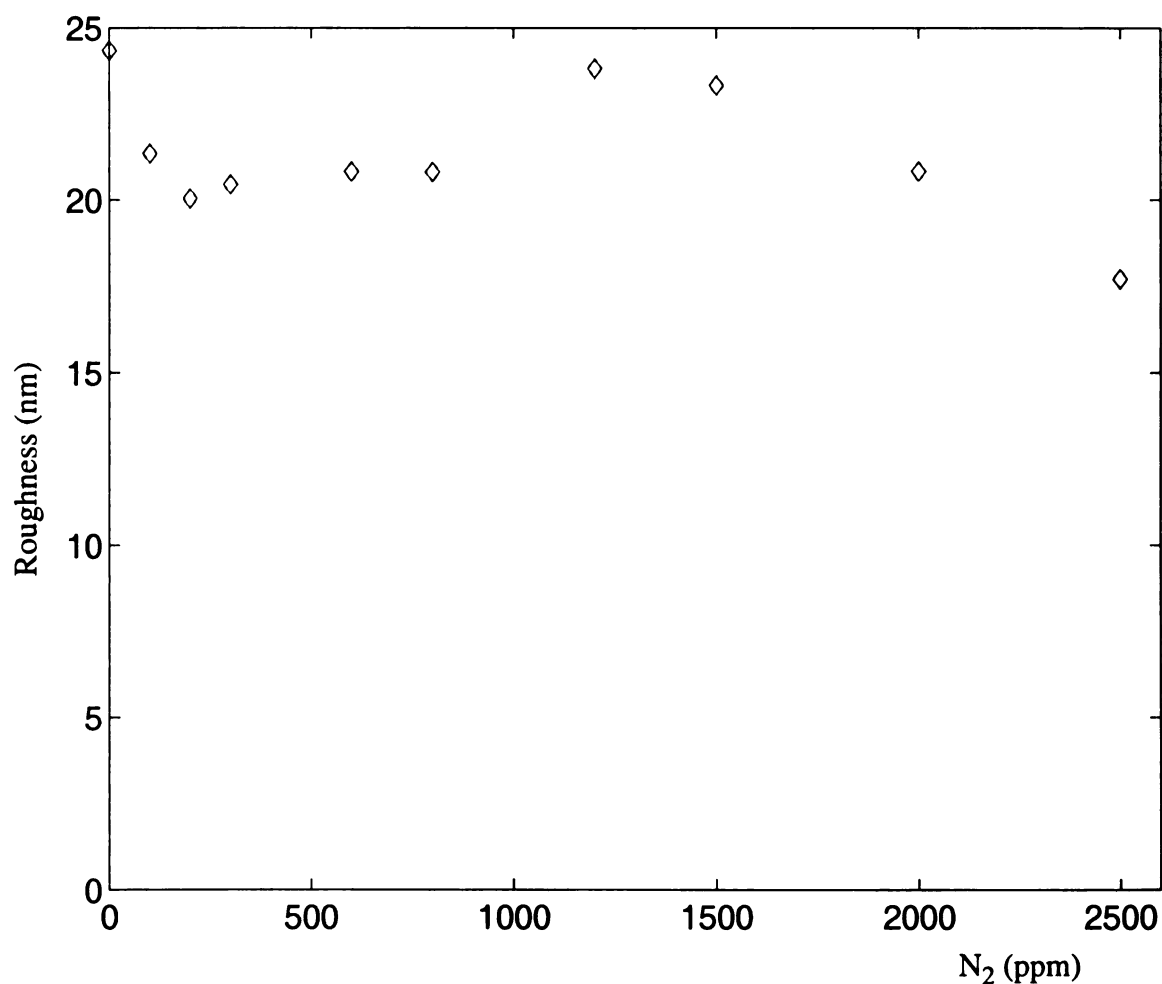


FIGURE 5.37 :  $I(220)/I(111)$  VS. NITROGEN IMPURITIES  
Pressure=120 Torr,  $\text{Ar}/\text{H}_2/\text{CH}_4=100/4/1$  sccm and deposition time=8 hours

Figure 5.38 displays the film roughness plotted as a function of nitrogen impurities with pressure held constant at 120 Torr, gas chemistry fixed at  $\text{Ar}/\text{H}_2/\text{CH}_4=100/4/1$  sccm and deposition time of 8 hours. As shown, between 0 and 2500 ppm of nitrogen impurity, the film roughness scatters between 18 to 25 nm.



**FIGURE 5.38 : RMS ROUGHNESS VS. NITROGEN IMPURITIES**  
Pressure=120 Torr,  $\text{Ar}/\text{H}_2/\text{CH}_4=100/4/1$  sccm and deposition time=8 hours  
by System II.

Figure 5.39 displays the film morphology versus different nitrogen impurities, with pressure held constant at 120 Torr, gas chemistry fixed at  $\text{Ar}/\text{H}_2/\text{CH}_4=100/4/1$  sccm and deposition time of 8 hours. From Figures 5.39(a) to 5.39(j), the films all have featureless morphology. Therefore, the morphology does not change by adding nitrogen impurity up to 2500 ppm. The contour of the films varies slightly as different nitrogen impurity concentrations are added. The contours of the films are mostly small smooth projections. The film roughness (See Figure 5.38.) does not change much within these films because the contours of the film are quite similar.

The influence of nitrogen on the growth, morphology, and crystalline quality of MPACVD diamond films has been studied by Asmussen et al. [Asmu 1998]. It was found nitrogen impurities as low as 20 ppm could affect the morphology and quality of the films. Based on the results of controlled nitrogen impurity study, there is no observable morphology changes of ultra-nanocrystalline diamond up to 2500 ppm. This may be because the very small crystal sizes of UNCD. Therefore, one can not tell from the AFM inspections. However, the films do begin to look opaque. Therefore, the optical properties of UNCD have been influenced by the additional nitrogen impurities.

Figure 5.39(a)  
N<sub>2</sub>:5 ppm

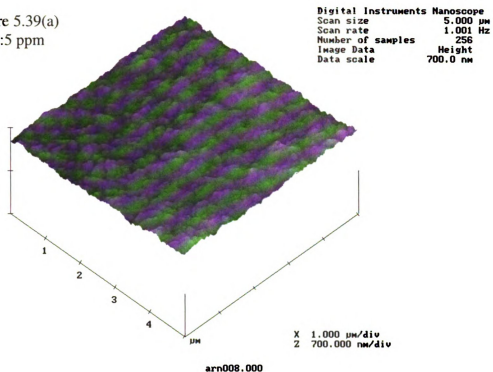


Figure 5.39(b)  
N<sub>2</sub>:100 ppm

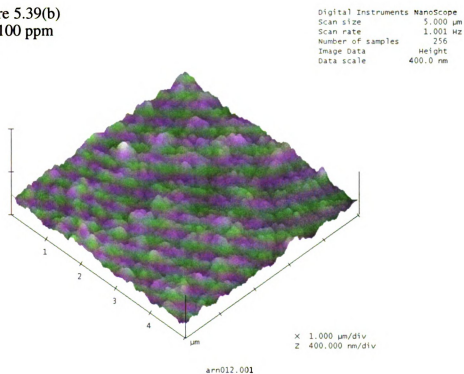


FIGURE 5.39 : FILM MORPHOLOGY VS. NITROGEN IMPURITIES  
 Ar/H<sub>2</sub>/CH<sub>4</sub>=100/4/1 sccm and deposition time=8 hours  
 by system II

Figure 5.39(c)  
N<sub>2</sub>:200 ppm

Digital Instruments NanoScope  
Scan size 5.000  $\mu\text{m}$   
Scan rate 1.001 Hz  
Number of samples 256  
Image Data Height  
Data scale 300.0 nm

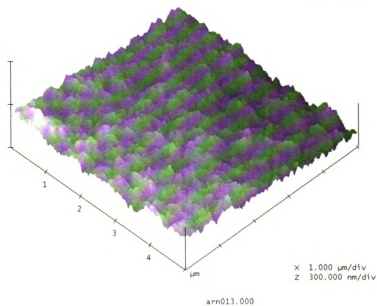


Figure 5.39(d)  
N<sub>2</sub>:300 ppm

Digital Instruments NanoScope  
Scan size 5.000  $\mu\text{m}$   
Scan rate 1.001 Hz  
Number of samples 256  
Image Data Height  
Data scale 700.0 nm

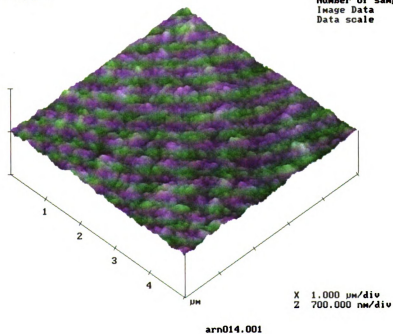


FIGURE 5.39 (cont'd)

Figure 5.39(e)  
N<sub>2</sub>:600 ppm

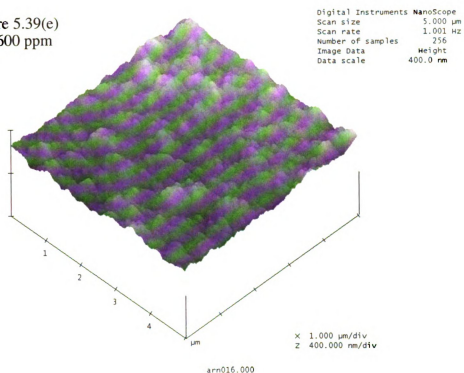


Figure 5.39(f)  
N<sub>2</sub>:800 ppm

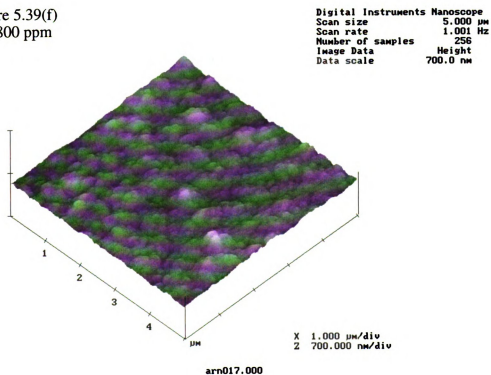


FIGURE 5.39 (cont'd)



Figure 5.39(g)  
N<sub>2</sub>:1200 ppm

Digital Instruments NanoScope  
Scan size 5.000  $\mu\text{m}$   
Scan rate 1.001 Hz  
Number of samples 256  
Image Data Height  
Data scale 400.0 nm

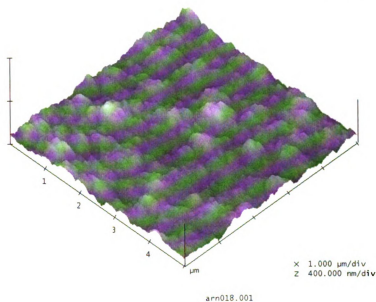


Figure 5.39(h)  
N<sub>2</sub>:1500 ppm

Digital Instruments NanoScope  
Scan size 5.000  $\mu\text{m}$   
Scan rate 1.001 Hz  
Number of samples 256  
Image Data Height  
Data scale 700.0 nm

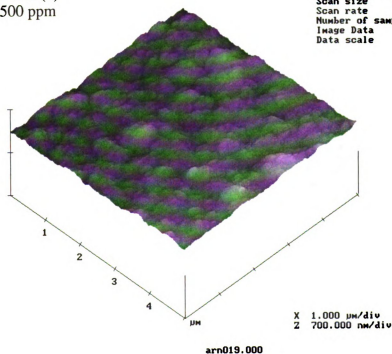


FIGURE 5.39 (cont'd)

Figure 5.39(i)  
N<sub>2</sub>:2000 ppm

Digital Instruments Nanoscope	
Scan size	5.000 $\mu\text{m}$
Scan rate	1.001 Hz
Number of samples	256
Image Data	Height
Data scale	700.0 nm

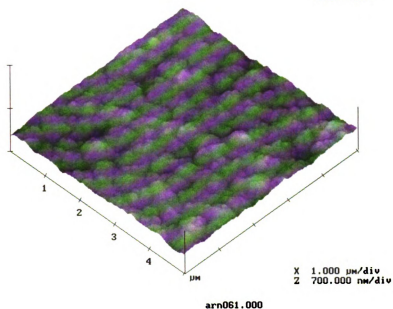


Figure 5.39(j)  
N<sub>2</sub>:2500 ppm

Digital Instruments Nanoscope	
Scan size	5.000 $\mu\text{m}$
Scan rate	1.001 Hz
Number of samples	256
Image Data	Height
Data scale	700.0 nm

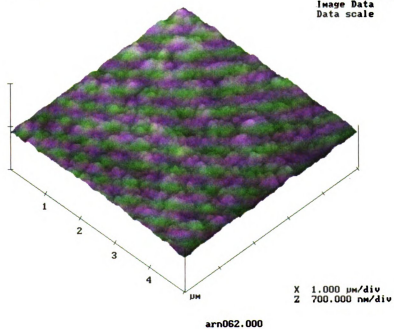


FIGURE 5.39 (cont'd)

## 5.5 Summary

Ultra-nanocrystalline diamond films synthesized by systems I and II have a variety of film textures, surface roughness, film structure qualities, morphologies, and crystal sizes. The comparisons of the film characteristics of these two systems are presented as follows.

### 5.5.1 System I

#### (a) Effect of gas chemistry

At deposition pressure of 120 Torr and deposition time of 8 hours, the films have preferred orientation in (220) direction when hydrogen concentrations are between 5-8%. At deposition pressure of 120 Torr and deposition time of 8 hours, increasing hydrogen concentration from 1.95% to 3.81% has increased the film roughness 1.2 times for  $f_t=102.5-105$  sccm experiments and 3.9 times for  $f_t=615-630$  sccm experiments. As hydrogen concentration increases, the film's crystal size increases. The films have (111) triangular morphology with a deposition pressure of 120 Torr, deposition time of 8 hours, and hydrogen concentration between 1.95% and 3.81%.

#### (b) Effect of deposition time

With deposition pressure at 120 Torr,  $\text{Ar:H}_2\text{:CH}_4=100:2:0.5$ ,  $f_t=615$  sccm, the film's preferred orientation did not change as the deposition time varied between 2 and 48 hours, but the film roughness increased 10.6 times as the deposition time increased from 2 to 48 hours. As the deposition time increased, from 2 to 8 hours, the crystal size increased

and the morphology was kept constant at a (111) triangular morphology. After 8 hours of deposition time, the film morphology became mixed morphology.

(c) Effect of total gas flow rate

The film's (220) preferred orientation became weaker with higher total gas flow rates. The crystal size variation became larger as total gas flow rate was reduced.

(d) Effect of deposition pressure

Film roughness increases 1.9 times as deposition pressure increases from 120 to 160 Torr with Ar:H<sub>2</sub>:CH<sub>4</sub>=100:2:0.5,  $f_t=615$  sccm and deposition time of 8 hours. The crystal size increased when deposition pressure increased. This was also supported by the films' Raman Spectra. With Ar:H<sub>2</sub>:CH<sub>4</sub>=100:2:0.5,  $f_t=615$  sccm and deposition time of 8 hours, the film has (111) triangular morphology between the deposition pressure of 120 to 160 Torr.

### 5.5.2 System II

(a) Effect of gas chemistry

At deposition pressure of 120 Torr, deposition time of 8 hours, Ar=100 sccm, CH<sub>4</sub>=1 sccm, and  $f_t=101-111$  sccm, the films have (220) preferred orientation. When hydrogen flow rate was increased from 0 to 10 sccm, the film roughness increased 4 times, and the films had a featureless morphology. The morphology did not vary with changes in gas chemistry. The surface contour of the films became more irregular as hydrogen con-

centration increased. As hydrogen flow rate increased from 0 to 4 sccm, the films had less graphitic/amorphous material.

(b) Effect of deposition time

With deposition pressure at 160 Torr and  $\text{Ar}/\text{H}_2/\text{CH}_4=100/4/1$  sccm, the film roughness increases 1.5 times as the deposition time increases from 8 to 25 hours, but the morphology remained featureless. Therefore, the morphology did not vary with changes in deposition time. However, the surface contour of the films was more irregular as deposition time increased.

(c) Effect of total gas flow rate

The film's preferred orientation in (220) direction became weaker with higher total gas flow rates. At a deposition pressure of 120 Torr and deposition time of 8 hours, as total gas flow rate increases, the film roughness increased 3.4 times for  $\text{Ar}:\text{H}_2:\text{CH}_4=100:4:1$  gas chemistry ratio. At a deposition pressure of 120 Torr and deposition time of 8 hours, as total gas flow rate increases, the film roughness increased 2.1 times for  $\text{Ar}:\text{H}_2:\text{CH}_4=100:2:1$  gas chemistry ratio. The film morphology was featureless and the surface contour of the films was more irregular with higher total gas flow rates. The morphology was not affected by total gas flow rate.

(d) Effect of deposition pressure

When the argon flow rate=100 sccm, methane flow rate=1 sccm, and deposition time of 8 hours, the films have (220) preferred orientation. The (220) preferred orientation was maintained as the deposition pressure was varied between 100 and 240 Torr. A maximum occurs around 140 or 160 Torr except for hydrogen flow rate of 1 sccm. As the deposition pressure increased, the film roughness dropped at the beginning and then continuously increased. The film morphology is featureless despite the variation of the deposition pressure. The surface contour of the films becomes more irregular as the deposition pressure increases.

(e) Effect of nitrogen impurity

The minimum of  $I(220)/I(111)$  occurs at 1200 ppm of added nitrogen impurity and the films all have (220) preferred orientation between nitrogen impurities of 0-2500 ppm. There is no significant effect on film roughness with nitrogen impurity concentrations up to 2500 ppm. The films all have featureless morphology. Therefore, the morphology does not change by adding nitrogen impurity up to 2500 ppm. The contour of the films varies slightly as different nitrogen impurity is added.

(e) Growth mechanism and crystal size study by TEM

Based on TEM observation, the ultra-nanocrystalline diamond films synthesized by system II consist of equiaxed and aspect ratio grains. The existence of a transitional interlayer between the silicon substrate and diamond film is clearly shown by the TEM cross-section images. Diamond appears to be able to nucleate on the silicon, in the transitional layer, on the diamond powder residue from the mechanical scratch process, and

continues to re-nucleate as the film grows. The SAD patterns indicate that ultra-nanocrystalline diamond has random orientation. However, the XRD results show mostly preferred (220) orientation. Neither SAD pattern nor the X-ray two-theta scan is able to quantitatively determine the texture of the films. Therefore, to verify the texture of ultra-nanocrystalline diamond films quantitatively, a more detailed study by X-ray pole figures and inverse pole figures is recommended.

Planar defects of ultra-nanocrystalline diamond are shown by HRTEM technique. Not much amorphous carbon was shown in the intergranular boundaries. The small activation energy involved in defect formation attributed to the forming of these structure imperfections [Zhu 1983]. The interaction of twins in diamond crystals has been studied by Shechtman et al. and it's been found that the meeting points of twins could play a very important role for the nucleation and growth of diamond crystals [Shec 1993], [Luo], [Grue 1994]. It's been demonstrated and claimed that the vertices, or edges of such twinned regions provide the nucleation sites for the new planes [Rang 1966] [Hami 1960]. The planar faults are likely formed during growth of secondary renucleation crystallinities [Qin 1998].

Because TEM is a two dimensional imaging technique applied to see a three dimensional structure. The grain overlapping may give rise to uncertainties in distinguish the grain boundary which leads to grain size determination. Besides that, the grain visibility with a diffraction condition relies on the resolution of the diffraction contrast which is attributed to the differences in crystals' orientations with respected to the incident electron beams. Therefore, combining the information from Figure 5.32, 5.33, and 5.34, the crystal

size of the ultra-nanocrystalline diamond is in the range of 3-20 nm with an average of 7 nm.

(e) Film uniformity study by SEM

Film uniformity was determined by breaking the wafer and measuring the thickness of the film using the cross-sectional SEM imaging technique at the following locations: (1) center, (2) one inch away from the center, (2) two inches away from the center, and (4) edge of the substrate. Percent uniformity is defined by the minimum thickness divided by maximum thickness. The uniformity and the corresponding deposition conditions are listed in Table 5.3.



**TABLE 5.3: FILM UNIFORMITY STUDY**

Ar/H <sub>2</sub> /CH <sub>4</sub> (sccm)	Pressure (Torr)	t (hr)	T <sub>s</sub> (°C)	P <sub>abs</sub> (W)	Uniformity (%)
100/4/1	60	8	UFL	768	94
100/0/1	80	8	UFL	772	100
100/1/1	80	8	UFL	768	100
100/2/1	80	8	UFL	772	95
100/0/1	100	8	UFL	803	88
100/1/1	120	8	594	890	76
100/2/1	120	8	616	906	70
100/1/1	140	8	621	1005	89
100/0/1	160	8	608	1037	80
100/1/1	160	8	655	1119	74
100/2/1	160	8	696	1147	71
100/4/1	160	8	709	1214	77
100/2/1	180	8	681	1211	77
100/4/1	180	8	709	1361	88
100/1/1	200	8	673	1251	75
100/4/1	200	8	770	1429	87
100/4/1	240	8	730	1518	70*

\*: There is a spot at the center of the deposited film caused by the small flame at the center of the discharge with this deposition condition.

## 6 Plasma Diagnostics

### 6.1 Introduction

Knowledge of the internal variables is important in order to develop an understanding of the ultra-nanocrystalline diamond deposition process and to relate the experimental data to the theoretical simulations of the conditions. MSU ultra-nanocrystalline diamond films were deposited with a mainly carbon containing argon plasma and with only a small fraction of hydrogen feed gas. The presence of argon in the input gases has been found to influence the plasma chemistry. Therefore, it indirectly influences the characteristics of diamond films, such as surface morphology, grain size, and even affects diamond growth mechanism [Zhou 1998], [Grue 1995]. In particular, it was found by Zhu et al. [Zhu 1990] that argon has an important influence on the plasma chemistry, including ionization and dissociation of reactant molecules. The carbon dimer, produced by the dissociation of methane molecules in a low hydrogen content argon plasma, is hypothesized to be the primary growth species in ultra-nanocrystalline diamond synthesis. Goyette et al. [Goy1 1998], [Goy2 1998] have shown that the  $C_2$  emission intensity is linearly proportional to the absolute carbon dimer density (as measured by a high-sensitivity white-light absorption spectroscopy apparatus) in the Ar-H<sub>2</sub>-CH<sub>4</sub> plasma discharges.

In order to understand the deposition process, a study of the  $C_2$  emission intensity versus various process conditions was performed in system II and the results are described in this chapter. The deposition process is sensitive to the gas kinetic temperature. The dependence of substrate temperature versus various input parameters have been presented in Chapter 3 (Figure 3.12 and Figure 3.13) and Chapter 4 (Figure 4.18 and Figure 4.21).

Therefore, only the gas neutral temperature versus various operating conditions is presented in this chapter. The theory of OES used in the gas temperature measurement is described in Section 6.3 and the experimental method and measurements are described in Section 6.4. The experimental data, including  $C_2$  emission intensity, gas temperature, and controlled nitrogen impurities are presented in Section 6.5. The kinetic gas temperature of discharges was measured by observing Swan band (0,0) emission intensity using OES (optical emission spectroscopy). Section 6.6 summarizes the plasma diagnostics measurements.

The influence of controlled input nitrogen impurities on  $Ar-H_2-CH_4$  plasma is also presented at the end of this chapter. The motivation for this set of measurements was to understand how the addition of nitrogen influences the gas chemistry. It has been shown that the nitrogen additions produce changes in the bulk plasma properties [Clay 1996] and [Hong 1995]. However, one should not overlook that the nitrogen has an influence on gas phase chemistry as well as the deposition surface [Hong 1995] and [Moss 1999]. The OES measurements presented in Section 6.5 investigate the bulk plasma property changes.

## **6.2 Background Fundamental of $C_2$ Emission Spectroscopy**

The optical emission intensity of the  $d^3\Pi-a^3\Pi$  (0,0) vibrational band of the  $C_2$  Swan system as a function of  $C_2$  concentration in an argon-hydrogen-methane microwave plasma was studied by Goyette et al. [Goye 1998]. The argon-hydrogen-methane plasma was created in a commercial ASTeX PDS-17 MPECVD system. The substrate tempera-

ture was independently controlled by a rf-heater. The ranges of plasma processing parameters used in the measurements are listed in Table 6.1.

**TABLE 6.1: EXPERIMENTAL PARAMETERS [Goy1 1998], [Goy2 1998]**

Ar sccm	H <sub>2</sub> sccm	CH <sub>4</sub> sccm	Pressure Torr	Substrate °C	Power W
97	2	1	55-150	800	800
97	2	1	100	800	500-1500
79-99	0-20	1	100	800	800
97	2	2	85	400-900	800
97	2	2	100	400-900	800

In Goyette's experiments, two viewports equipped with fused silica windows provide in situ optical access. The emission intensity is measured using the (0,0) bandhead. A typical spectrum of the carbon dimer  $d^3\Pi-a^3\Pi$  Swan band emission intensity around 516.5 nm is shown in Figure 6.1. The absolute density of  $C_2$  is measured using high-sensitivity white-light absorption spectroscopy obtained from the continuum source of a stabilized high-pressure Xe lamp. The absolute densities of  $C_2$  in the  $a^3\Pi$  state was carried out using the (0,0) vibrational band of the Swan system and used 1300 °C (1573 K, rotational temperature determined from  $d^3\Pi-a^3\Pi$  (0,0) vibrational band transition of  $C_2$ , the conditions, such as pressure, gas chemistry, microwave power, etc. of the measurements were not reported) in determining the Boltzmann factors (Among the vibrational levels of the  $d^3\Pi_u$  state, this statistical fraction includes the relative population distribution [Goye 1998].)

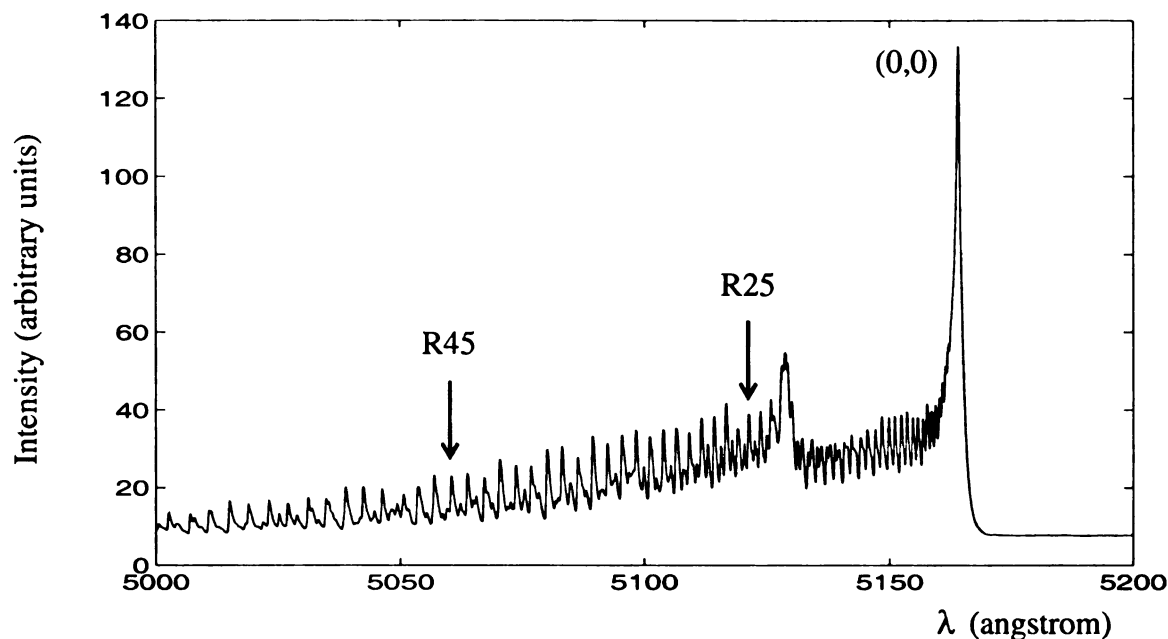


FIGURE 6.1 : CARBON DIMER  $d^3\Pi - a^3\Pi$  SWAN BAND EMISSION

As the various plasma parameters were varied, the spectroscopically determined  $C_2$  densities were correlated with the observed Swan band emission intensity from the microwave discharge. Goyette et al. [Goye 1998] observed a strong linear correlation between the experimentally measured bandhead emission intensity and the experimentally measured  $C_2$  concentrations. They observed the  $C_2$  densities were linearly related to  $C_2$  emission intensity as chamber pressure, substrate temperature,  $H_2$  percentage in the feed gas were varied over the experimental parameter range shown in Table 6.1.

Based on the work of Goyette et al., in this thesis, it is assumed that  $C_2$  emission intensity measurements are linearly related to  $C_2$  concentrations in the discharge. This may not be a valid assumption since the experimental parameter space, i.e. pressure,

microwave, and reactor geometry were quite different from those used by Goyette et al. and were performed across a larger parameter space. Thus,  $C_2$  emission intensity may not be exactly linearly related to  $C_2$  concentrations. In the future, this should be verified for the experimental conditions presented in this thesis.

### **6.3 Gas Kinetic Temperature Measurement Theory**

The rotational temperature was measured by OES and then was used to determine the gas temperature. The energy separations between rotational levels in a given vibrational state are relatively small. Typically they are about a few hundred  $\text{cm}^{-1}$ . In contrast, the vibrational frequency corresponds to an energy of the order  $1000 \text{ cm}^{-1}$  and the total changes in vibrational energy may be up to an order higher [Gayd 1968].

Nearly all gas kinetic collisions produce a change in the rotational quantum number of diatomic molecules, whereas collisions producing a change in the vibrational or electronic quantum numbers occur far less frequently. The relative rotational population distribution in a sufficiently long-lived vibrational state is a Boltzmann distribution function which reflects the gas kinetic temperature. In the Boltzmann distribution, the temperature parameter may be measured in many ways, depending on the plasma constituents, the temperature, etc. Generally, emission methods are the most applicable [Thor 1988] and thus the methodology applied in this chapter is confined to emission. The relative emission intensities of rotational lines within a single vibrational band is described by [Thor 1988]:

$$I = K\nu^4 S_{J'J''} \exp\left[\frac{-hcB_v J'(J'+1)}{kT_{\text{rot}}}\right] \quad (6.1)$$

Here,

K is a constant for all lines originating from the same electronic and vibrational level.

$\nu$  is the frequency of the radiation.

$S_{J'J''}$  is the appropriate Honl-London factor.

h is the Planck's constant.

c is the speed of light.

$B_v$  is the molecular rotational constant for the upper vibrational level.

J is the rotational quantum number. J' represents the upper level and J'' represents the lower level.

k is the Boltzmann constant.

$T_{\text{rot}}$  is the rotational temperature.

By fitting the experimental data to the expression  $I \sim S_{J'J''} \exp[-B_v J'(J'+1)/(kT_{\text{rot}})]$  using the R<sub>25</sub> to R<sub>45</sub> emission lines [Goye 1998], [Pras 1994], [Grot 1999], [Huan 2000], [Huan 2001], the rotational temperature is determined. The rotational temperature was measured for the d<sup>3</sup>Π - a<sup>3</sup>Π (0,0) vibrational band transition of C<sub>2</sub>. The a<sup>3</sup>Π level of C<sub>2</sub> is very long-lived and almost surely equilibrated. But the upper

electronic level,  $d^3\Pi$ , of this transition radiates and is short-lived. At the pressure range investigated in this chapter, it is likely that the collision rate is high enough to equilibrate the rotational modes of this electronic excited state and the rotational populations of this electronic state equilibrate to the gas kinetic temperature [Goye 1998] and [Gicq 1996].

## 6.4 Experimental Method and Measurement

The experiments were performed in the MSU-MPACVD reactor system II shown in Figure 6.2. Since in these experimental measurements, the  $C_2$  emission intensity depends on the volume of plasma discharges. Therefore, the discharge volume was kept constant. The details of the reactor were previously described in Section 3.2, Section 3.2.1, Section 3.2.2.2, Section 3.2.3.2, and Section 3.2.4.1. The starting procedure was described in Section 3.3.2.2. The operating pressure is 60-240 Torr, the gas chemistry is confined:  $Ar/H_2/CH_4=99-90/0-9/1$  (%), the absorbed microwave power is between 681-1520 W, and the total gas flow rate is 100-600 sccm.

The plasma is very bright, therefore, there is no need to perform any optical arrangement to focus the emission into the core of the fiber (dia.=0.8mm). A spectrometer: Spex I, 1 meter, f/9 plane grating scanning monochromator with 1200 grooves/mm grating and an EMI-GENCOM FACT-50 MKIII 3010 photomultiplier tube were used to detect the signal. The entrance slit was set to 100  $\mu m$  for acquiring CN spectrum, 20  $\mu m$  for acquiring  $C_2$  spectrum, and 2-5  $\mu m$  for rotational temperature measurements. The photomultiplier tube is mounted at the exit slit. For all the experiments, a bias voltage of -800 Volts by an EMI-GENCOM high voltage power supply model 3000R was applied to



the photomultiplier tube in order to obtain a good signal-to-noise ratio. The output current from the photomultiplier tube was read by a Keithley 480 Autoranging picoammeter. The output current was usually in the range of a few nanoamperes and should not exceed a microampere. The picoammeter was interfaced to a computer. The data acquisition and processing were carried out by the computer. The software consisted of a Quick-Basic program [Moss 1998] and was used to collect the data at the desired interval. The data analysis applying the intensity function of Boltzmann distribution with R25 to R45 emission lines was used to fit the experimental data to determine the rotational temperature is written in MATLAB [Grot 1999], [Huan 2000], [Huan 2001]. The molecular rotational constant for the upper vibrational level is 1.7456 and for the lower vibrational level is 1.62405 [Pras 1994]. The Honl-London factor is,  $S=(J'+1)(J'-1)/J'$ .

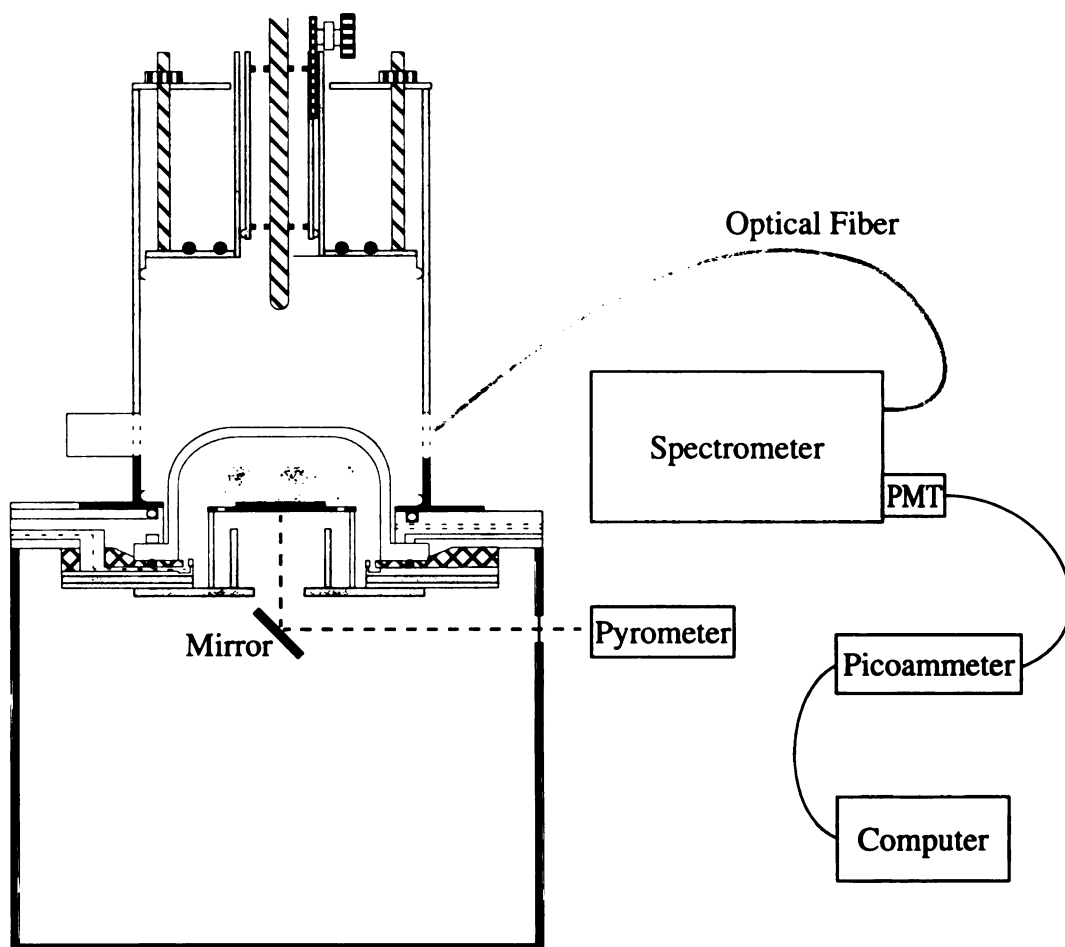


FIGURE 6.2 : EXPERIMENTAL SET-UP FOR OES MEASUREMENTS

System II: 2.45 GHz resonant cavity reactor,  
Thermal floating substrate holder,  
Ar-H<sub>2</sub>-CH<sub>4</sub> plasma discharges

## 6.5 Experimental Results

### 6.5.1 C<sub>2</sub> Emission Intensity

Figure 6.3 displays the C<sub>2</sub> emission intensity plotted as a function of hydrogen flow rate with argon flow at 100 sccm, methane flow at 1 sccm, and pressure at 120 Torr. As shown, starting from the hydrogen flow of 2 sccm, the C<sub>2</sub> emission intensity decreases with the increases in the hydrogen concentration. However, when hydrogen flow is below 2 sccm, the C<sub>2</sub> emission intensity increases as the hydrogen concentration increases.

The intensity that is detected depends not only on the plasma emission but also upon the visibility of the quartz dome. At low hydrogen flow experiments, i.e. H<sub>2</sub>=0 sccm experiment, a smoke-like vapor was produced. This smoke-like vapor deposits a film on the quartz dome which inhibits the transmission of plasma emission through the quartz dome. Part of the emission was blocked by the film and the measurements were affected. The quartz dome was clear by the time when the hydrogen flow reached 2 sccm. From 0 to 20% of H<sub>2</sub> (vol.%), there is a strong linear correlation between emission intensity and C<sub>2</sub> density in Ar-H<sub>2</sub>-CH<sub>4</sub> plasma [Goye 1998]. Therefore, the result indicates that the C<sub>2</sub> concentration decreases with increases in hydrogen percentage in the input gases between 2-9% of H<sub>2</sub>.

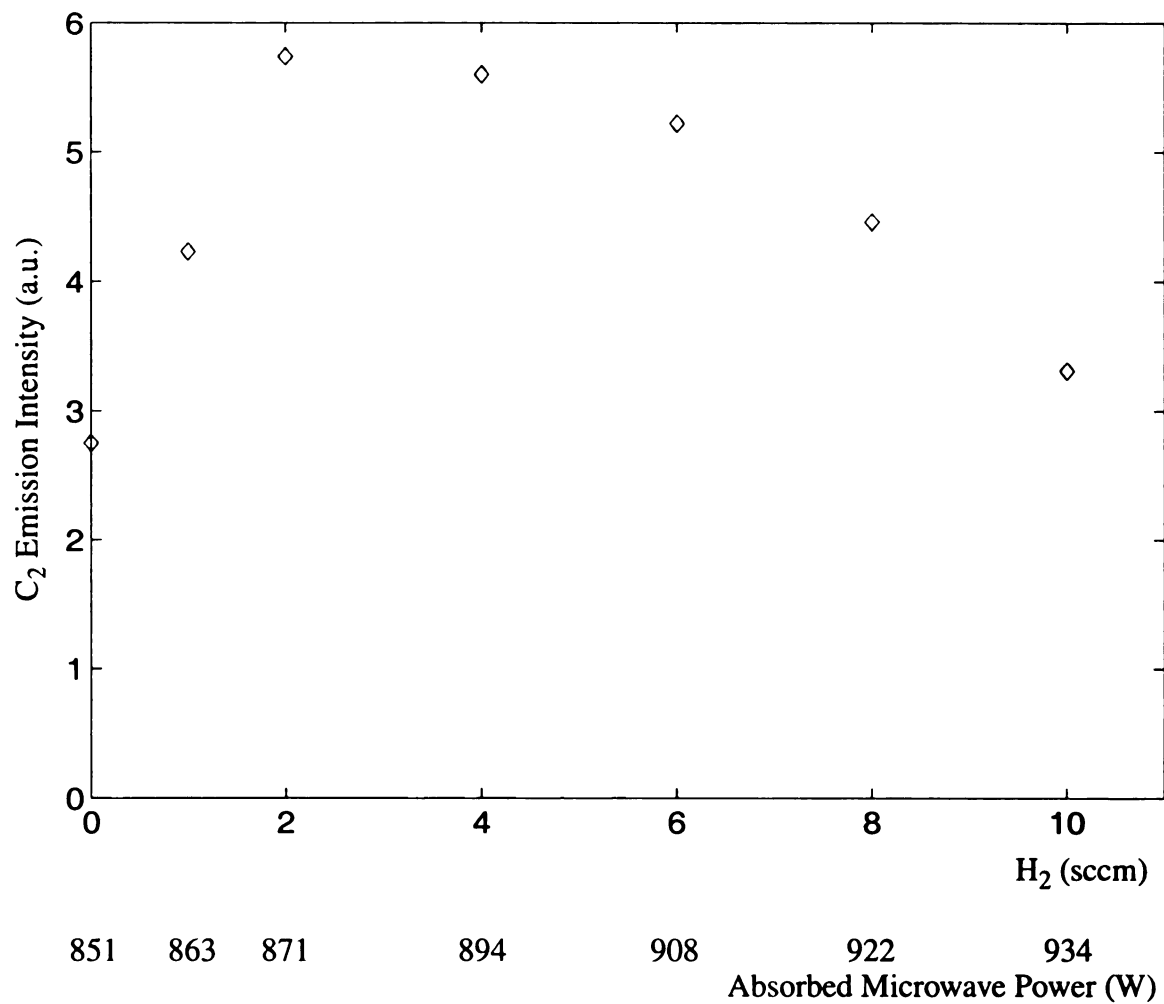


FIGURE 6.3 :  $C_2$  EMISSION INTENSITY VS.  $H_2$  FLOW RATE  
Pressure=120 Torr, Ar=100 sccm and  $CH_4$ =1 sccm by system II.

Figure 6.4 displays the  $C_2$  emission intensity plotted as a function of total gas flow rate,  $f_t$ , with  $Ar:H_2:CH_4=100:4:1$ , pressure at 120 Torr, and  $f_t=105-630$  sccm. It indicates that the  $C_2$  emission intensity is essentially constant as the total gas flow rate increases.

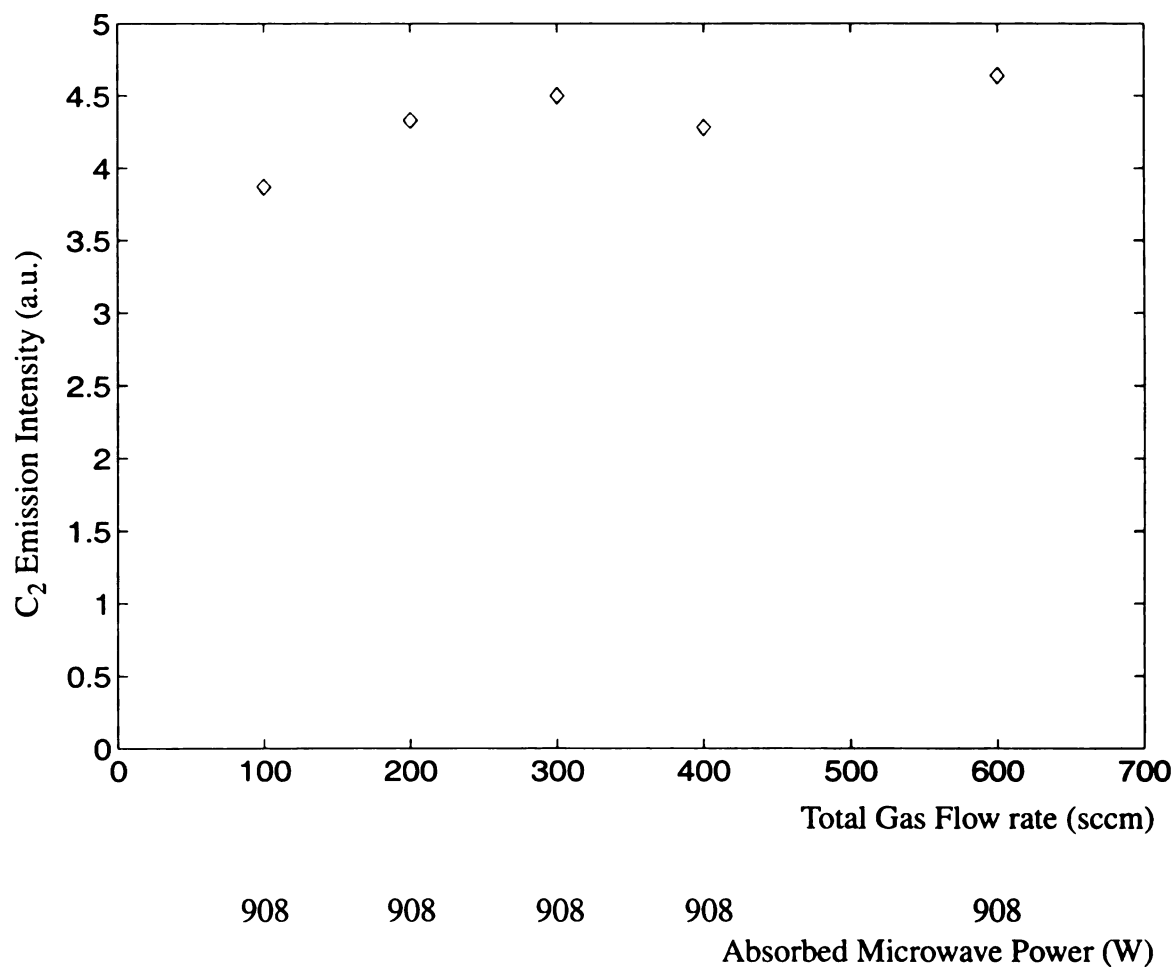


FIGURE 6.4 :  $C_2$  EMISSION INTENSITY VS. TOTAL GAS FLOW RATE  
Pressure=120 Torr,  $Ar:H_2:CH_4=100:4:1$ ,  $f_t=105-630$  sccm by system II.

Figure 6.5 and 6.6 display the  $C_2$  emission intensity plotted as a function of pressure,  $p$ , and absorbed microwave power,  $P_{abs}$ , respectively, with argon flow rate and methane flow rate held constant at 100 sccm and 1 sccm, respectively. The microwave power input was adjusted (increased) as the pressure increases to maintain a discharge area  $A_d$  that covered the three inch substrates because the discharge area  $A_d$  was varied with the deposition pressure,  $p$ , and the absorbed microwave power,  $P_{abs}$ .

As shown in Figure 6.5, the  $C_2$  emission intensity generally increases as pressure increases. A small flame starts to show at the center of the plasma at a different pressure for each different hydrogen gas flow rate. For the experiments of  $H_2=4$  sccm, it's around 240 Torr. For the experiments of  $H_2=2$  sccm, it's around 220 Torr. For the experiments of  $H_2=1$  and 0 sccm, it's around 200 Torr. For the experiments with  $H_2=0$  sccm, the quartz dome got quite dirty toward the end of the experiments. Therefore, the decreasing transmittance of the quartz dome decreased the emission intensity measurements at higher pressure regime of this set of measurements. For the measurements of the experiments of  $H_2=4$  sccm, the flame appeared at 240 Torr. It could have influenced the plasma emission. From 55 to 150 Torr, there is a strong linear correlation between emission intensity and  $C_2$  density in Ar- $H_2$ - $CH_4$  plasma [Goye 1998]. Therefore, the result indicates that the  $C_2$  concentration increases with increases between 60-160 Torr [Goye 1998], [Grot 1999]. The data between 180-240 Torr could have the similar behavior. Nevertheless, a verification by an absorption spectrum from a high-sensitivity absorption spectroscopy apparatus is recommended. As shown in Figure 6.6, the  $C_2$  emission intensity increases with increases in absorbed microwave power.

The same experimental data points that are shown in Figure 6.6 are also displayed in Figure 6.5. Thus, it is important to note that as microwave power increases in Figure 6.6, the deposition pressure is also increasing.

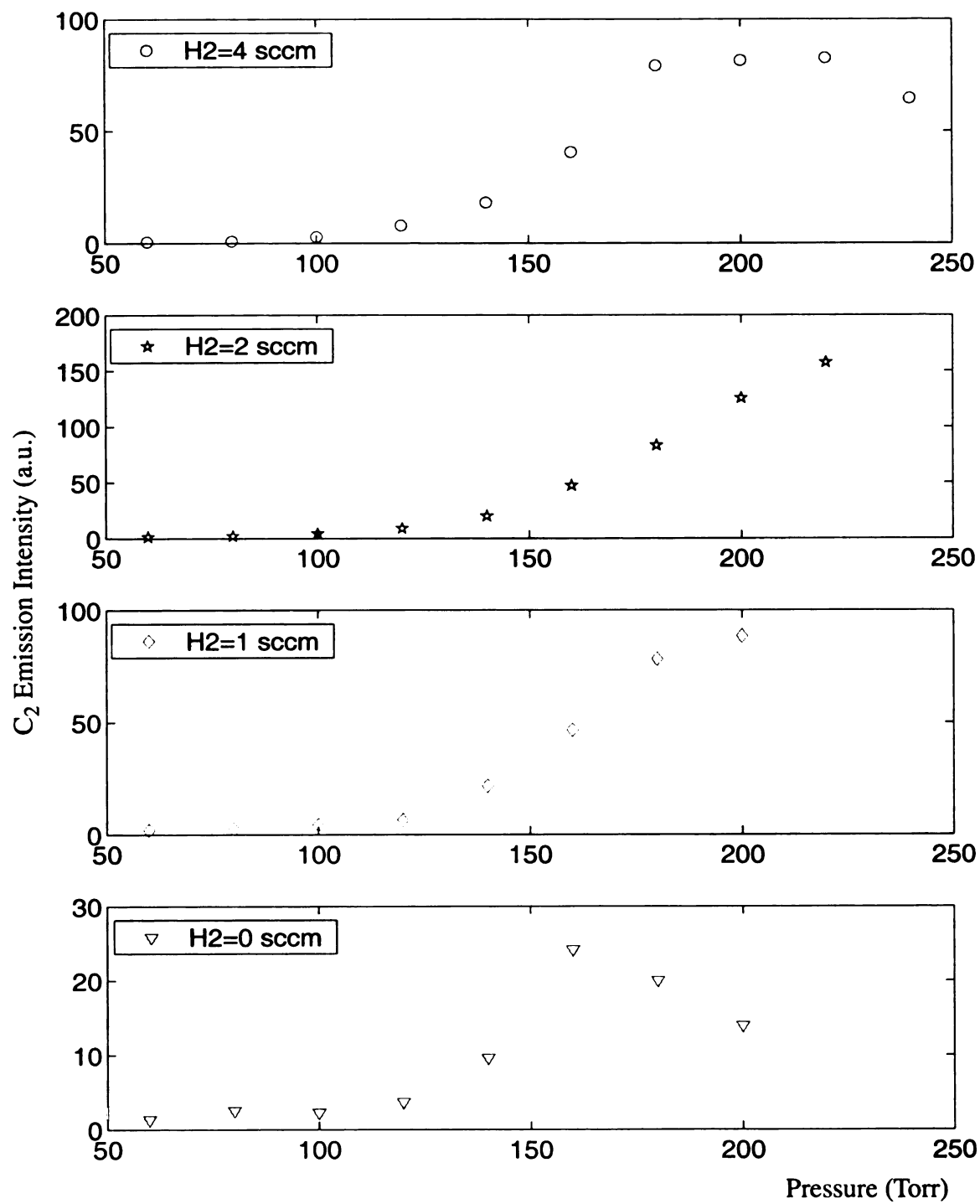


FIGURE 6.5 : C<sub>2</sub> EMISSION INTENSITY VS. PRESSURE  
Ar=100 sccm and CH<sub>4</sub>=1 sccm by system II.



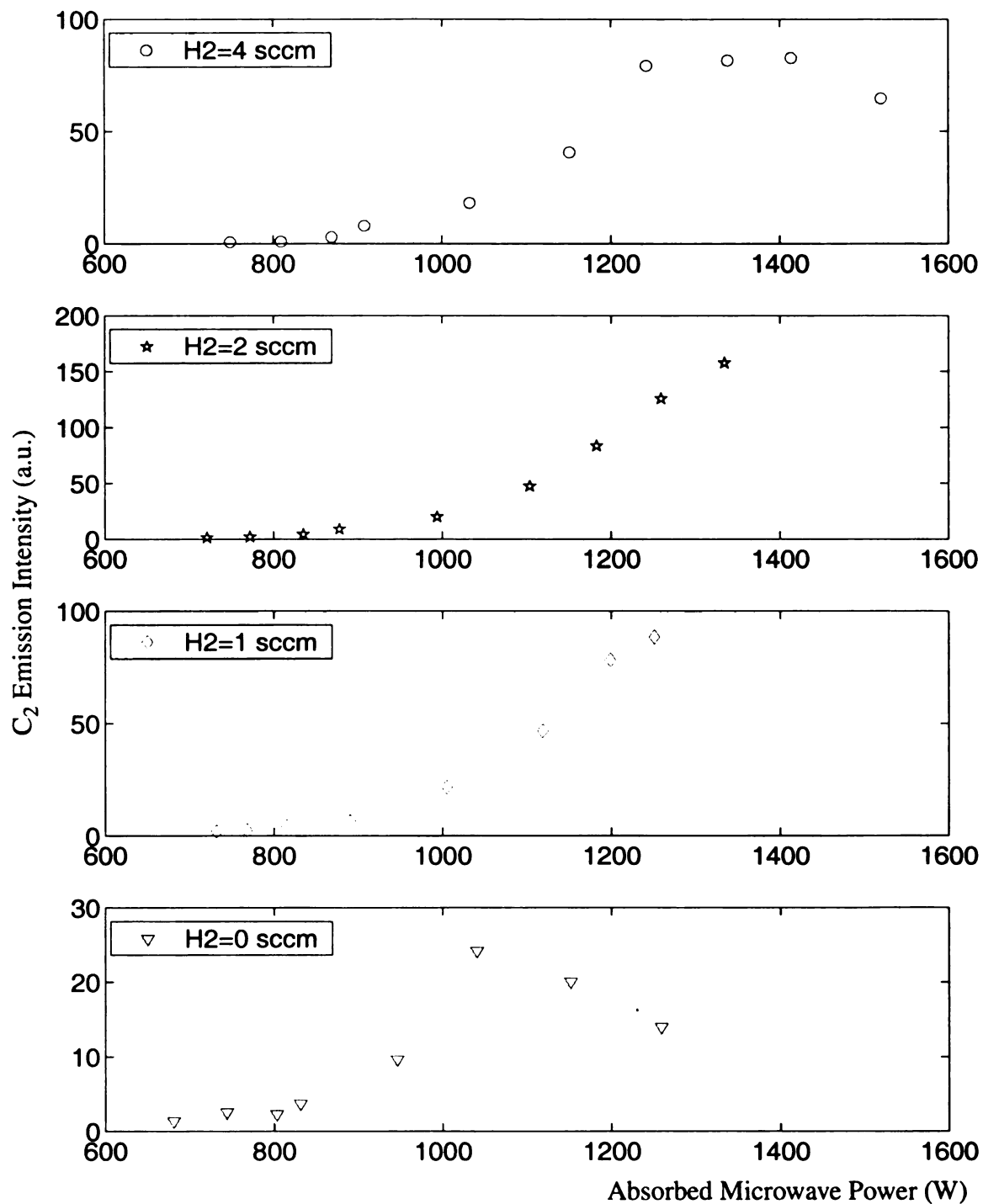


FIGURE 6.6 : C<sub>2</sub> EMISSION INTENSITY VS. MICROWAVE POWER  
Ar=100 sccm and CH<sub>4</sub>=1 sccm by system II.

Figure 6.7 displays the growth rate plotted as a function of  $C_2$  emission intensity with an argon flow rate of 100 sccm, a methane flow rate of 1 sccm,  $t = 8$  hrs, hydrogen flow rate of 2 sccm (Figure 6.7 (a)) and 1 sccm (Figure 6.7(b)). The same experimental data points that are shown in Figure 6.7 are also displayed in Figures 6.5 and 6.6. thus, it is important to note that as  $C_2$  emission increases in Figure 6.7, the microwave power and pressure are also increasing. Figure 6.7 shows the close relationship between the growth rate and  $C_2$  concentrations, and suggests that the concentration of  $C_2$  in the argon-methane plasma may be an important factor in determining the film growth rate under the low and constant hydrogen concentrations.

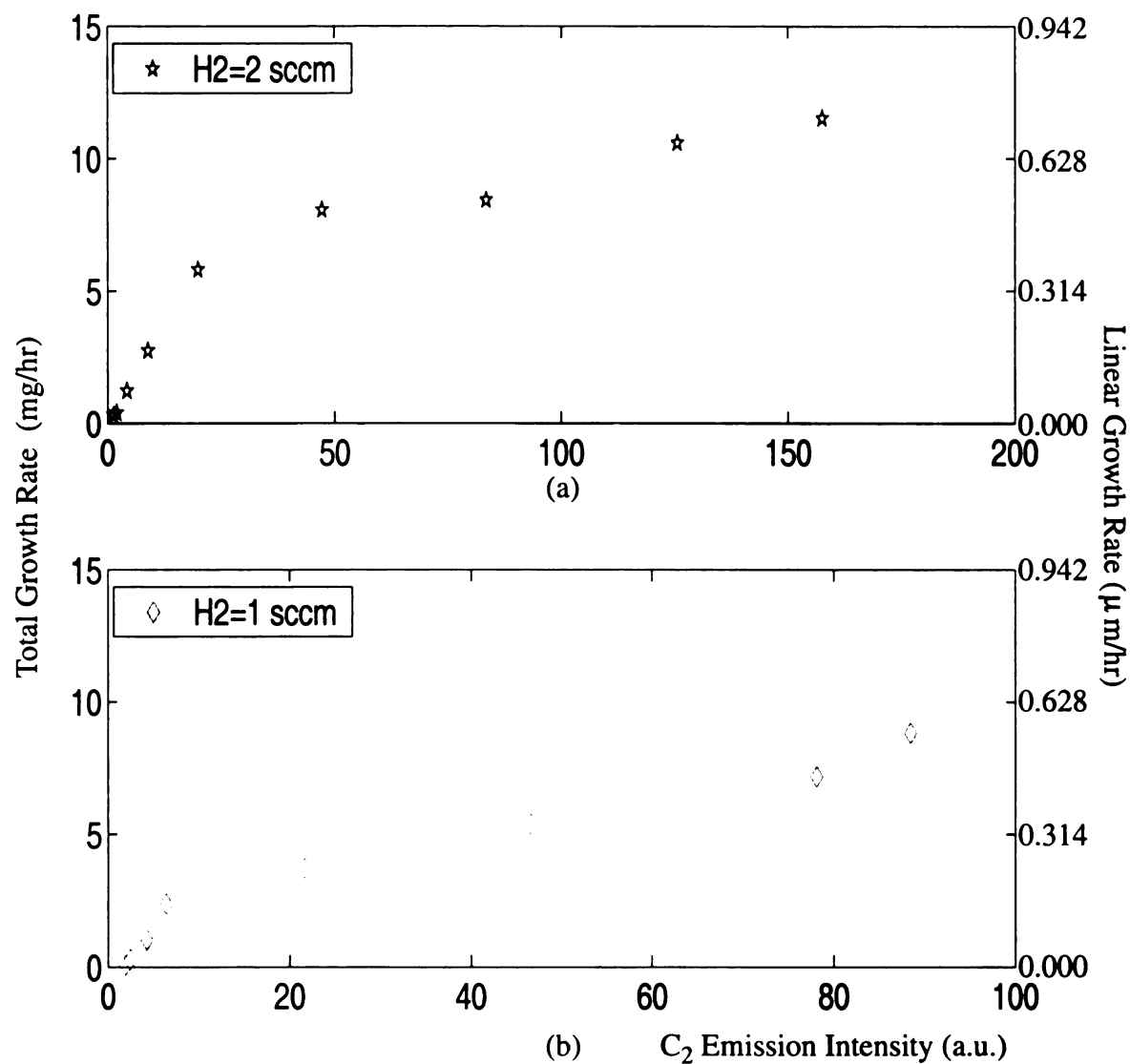


FIGURE 6.7 : GROWTH RATE VS. C<sub>2</sub> EMISSION INTENSITY  
Ar=100 sccm, CH<sub>4</sub>=1 sccm, and t=8 hours by system II.

## 6.5.2 Gas Temperature

Figure 6.8 displays the gas temperature plotted as a function of hydrogen flow rate, with argon flow fixed at 100 sccm, methane flow fixed at 1 sccm, and pressure at 120 Torr. As shown, the gas temperature increases with the increases in the hydrogen concentration. The substrate temperature and the absorbed microwave power versus hydrogen flow rate are shown in Figure 4.18. The uncertainty of the gas temperature is 100K.

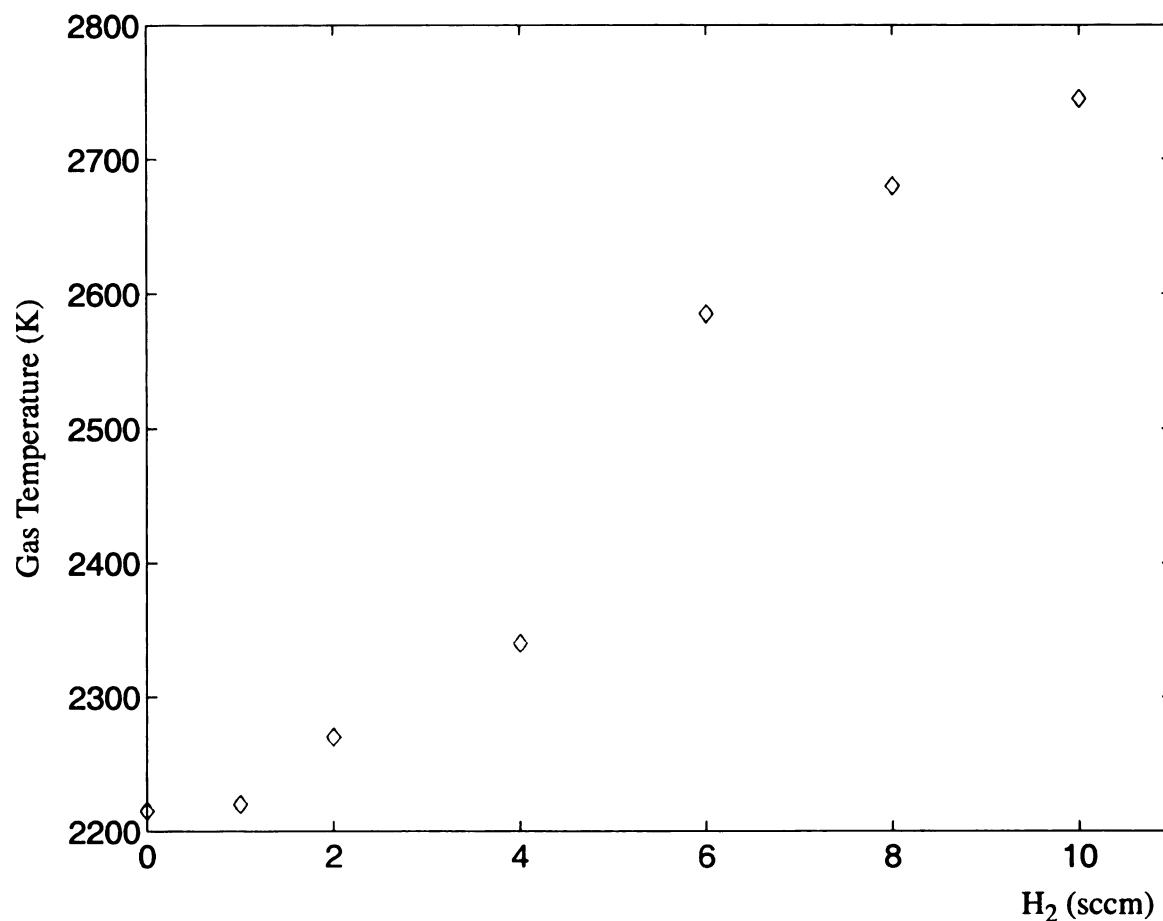


FIGURE 6.8 : GAS TEMPERATURE VS. H<sub>2</sub> FLOW RATE  
Pressure=120 Torr, Ar=100 sccm and CH<sub>4</sub>=1 sccm by system II.

Figure 6.9 displays growth rate plotted as a function of gas temperature with an argon flow rate of 100 sccm, a methane flow rate of 1 sccm,  $t=8$  hours. Hydrogen concentration increased from 0-9% (See Figure 6.8). The data shown in Figure 6.9 indicates that as the gas temperature increases from 2215-2745 K, the growth rate increases.

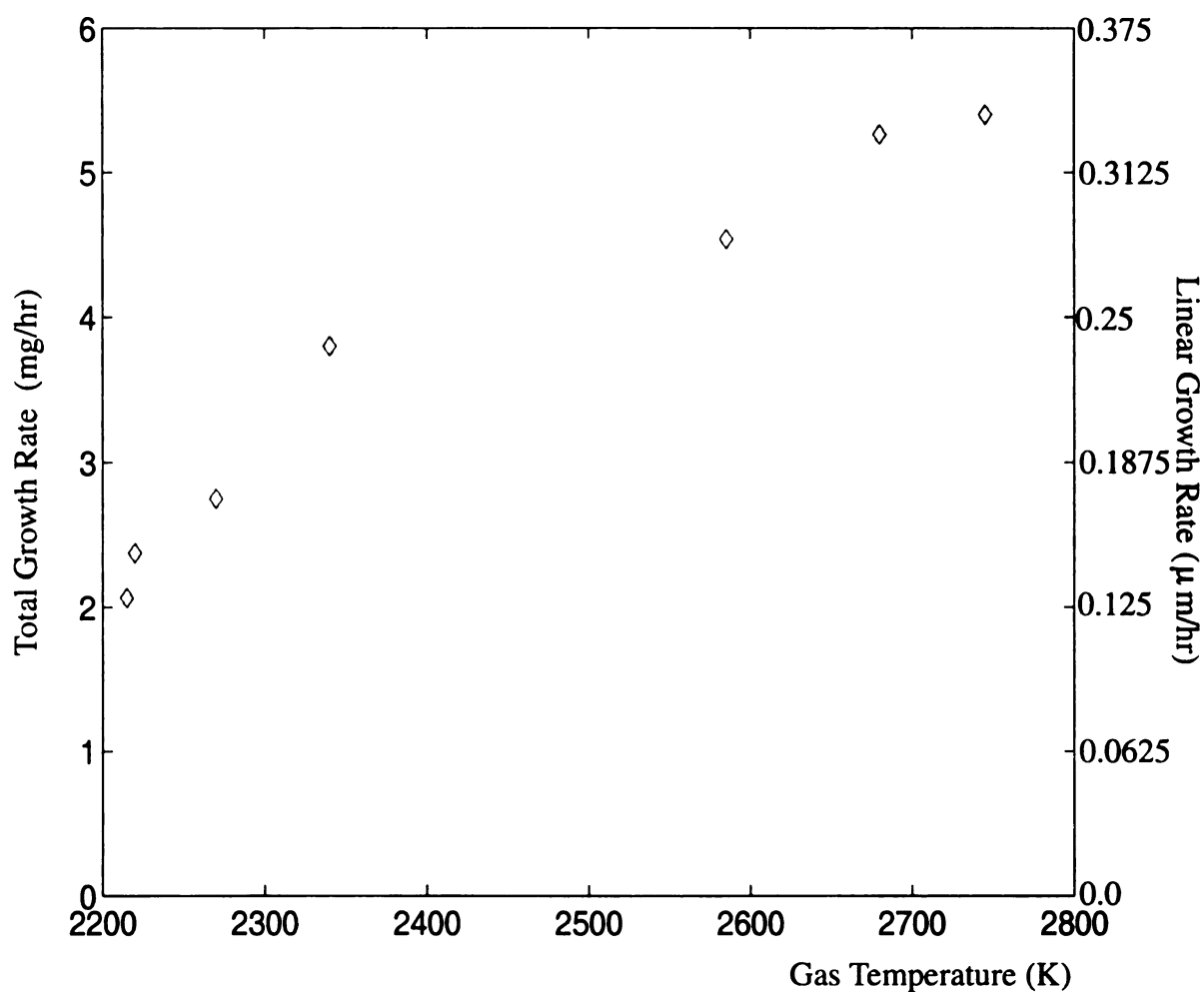


FIGURE 6.9 : GROWTH RATE VS. GAS TEMPERATURE  
Ar=100 sccm, CH<sub>4</sub>=1 sccm,  $t=8$  hours by system II.

Figure 6.10 displays the gas temperature plotted as a function of total gas flow rate,  $f_t$ , with  $\text{Ar:H}_2\text{:CH}_4=100:4:1$ ,  $f_t=105\text{-}630$  sccm and pressure at 120 Torr. The gas temperature fluctuates around 2330 K. As shown in Figure 4.21, the absorbed microwave power and substrate temperature versus total gas flow rate are constant under the same experimental conditions displayed in Figure 6.10. The uncertainty of the gas temperature is 100K.

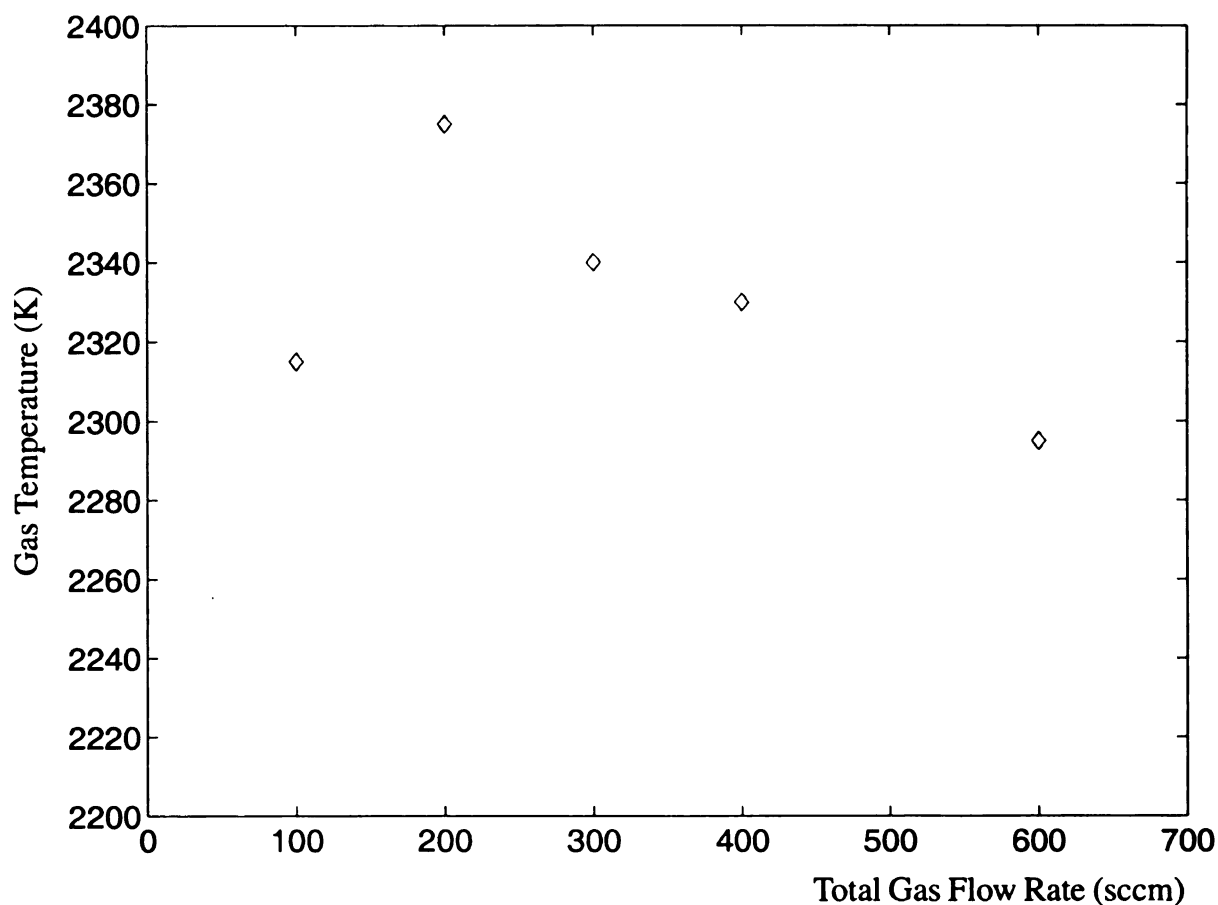


FIGURE 6.10 : GAS TEMPERATURE VS. TOTAL GAS FLOW RATE  
Pressure=120 Torr and  $\text{Ar:H}_2\text{:CH}_4=100:4:1$ ,  $f_t=105$  sccm by system II.

Figure 6.11 and 6.12 display the gas temperature plotted as a function of pressure,  $p$ , and absorbed microwave power,  $P_{\text{abs}}$ , respectively, with argon flow rate equal to 100 sccm and methane flow rate equal to 1 sccm. As shown in Figure 6.11, the gas temperature increases with the increases in pressure. At constant pressure, the higher hydrogen concentrations generally have higher gas temperature. This result is consistent with the data in Figure 6.8. Above 80 Torr, the uncertainty of the gas temperature is 100K. At 60 and 80 Torr, the uncertainty of the gas temperature is 150K.

In Figure 6.12, the gas temperature increases with increases in absorbed microwave power. The uncertainty of the gas temperature is 100K. The substrate temperature increases with increases in either pressure or absorbed microwave power is shown in Figure 3.12 and Figure 3.13. Above 800 W, the uncertainty of the gas temperature is 100K. Below 800 W, the uncertainty of the gas temperature is 150K.

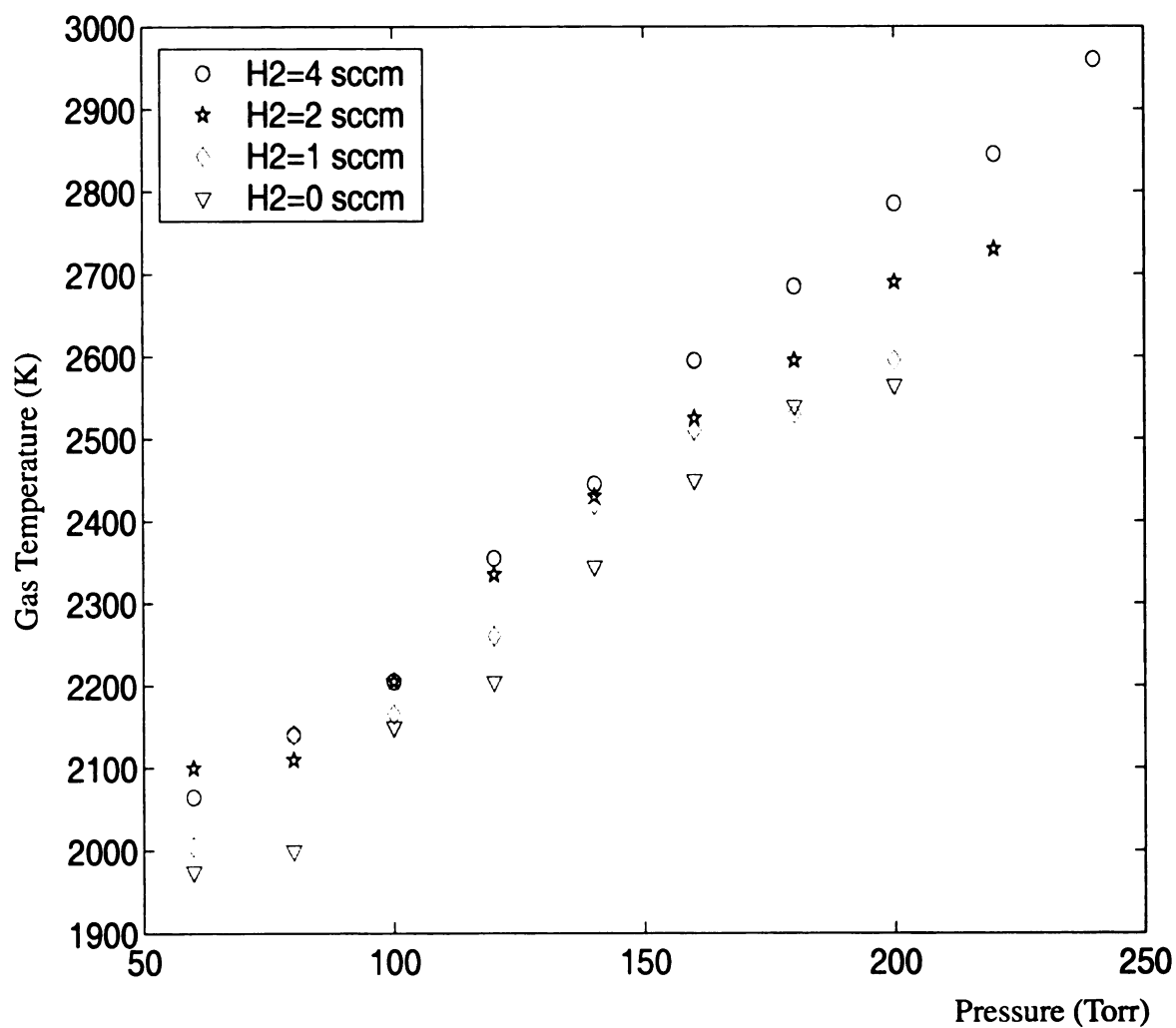


FIGURE 6.11 : GAS TEMPERATURE VS. PRESSURE  
Ar=100 sccm and CH<sub>4</sub>=1 sccm by system II.



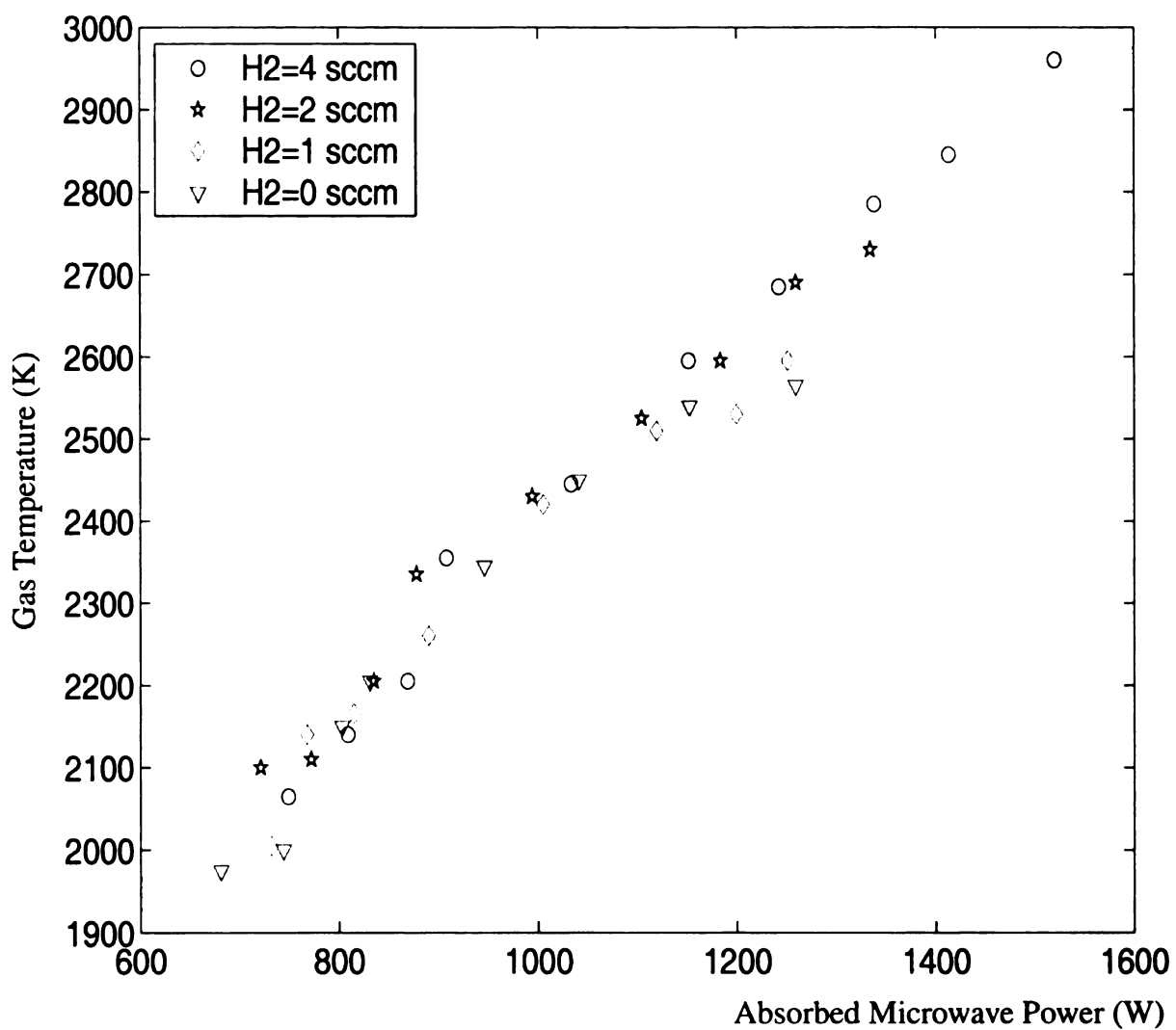


FIGURE 6.12 : GAS TEMPERATURE VS. MICROWAVE POWER  
Ar=100 sccm and CH<sub>4</sub>=1 sccm by system II.

Figure 6.13 displays the growth rate plotted as a function of gas temperature with an argon flow rate of 100 sccm, a methane flow rate of 1 sccm,  $t = 8$  hours. The same experimental data points that are shown in Figure 6.13 are also displayed in Figures 6.11 and 6.12. Thus, it is important to note that as gas temperature increases, the pressure and microwave power are also increasing. Figure 6.13 shows that growth rate increases as gas temperature increases.

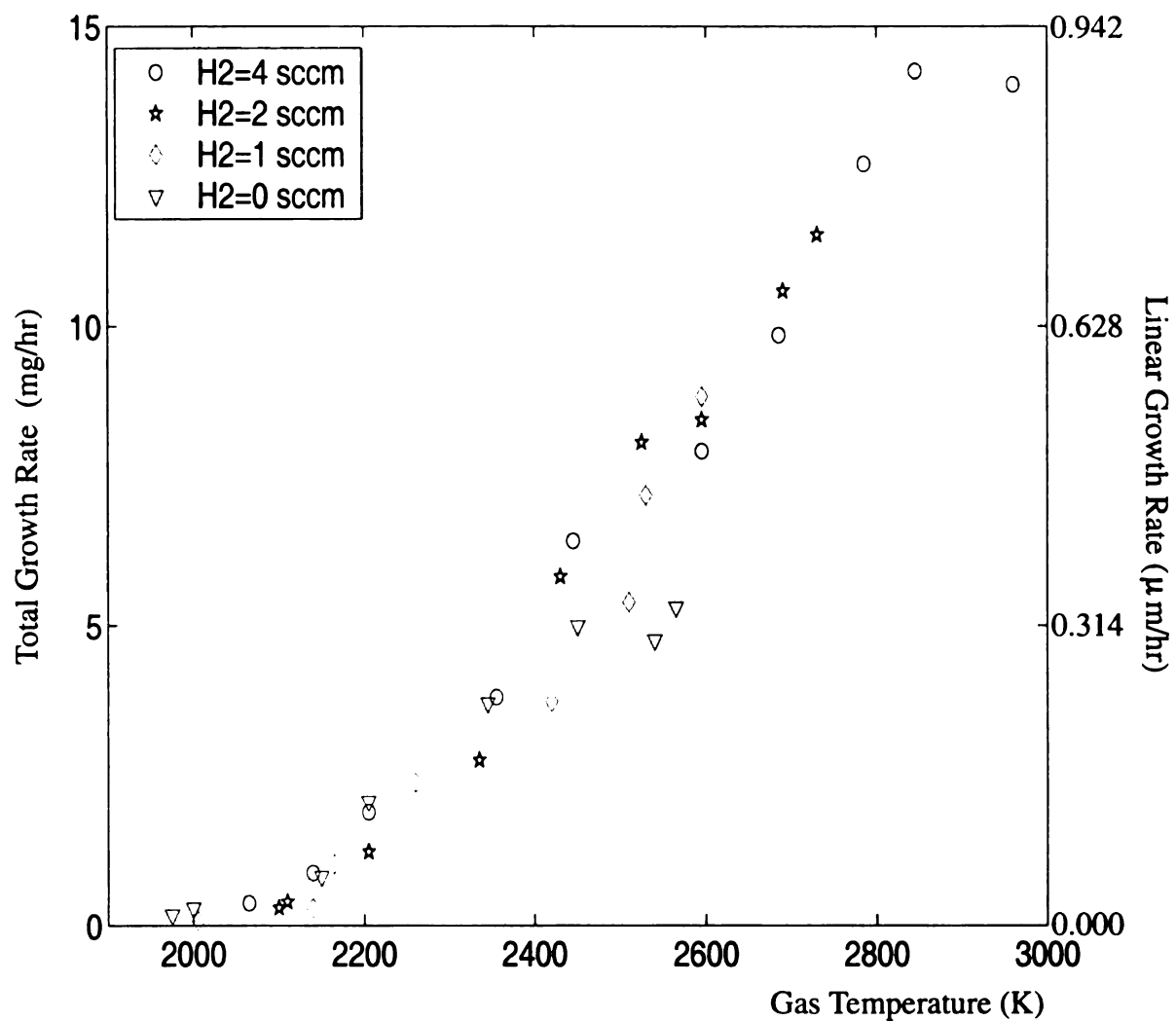


FIGURE 6.13 : GROWTH RATE VS. GAS TEMPERATURE  
 Ar=100 sccm, CH<sub>4</sub>=1 sccm, and t=8 hours by system II.

Figure 6.14 displays the growth rate plotted as a function of substrate temperature with an argon flow rate of 100 sccm, a methane flow rate of 1 sccm,  $t = 8$  hours. It is important to note that as substrate temperature increases, the pressure and microwave power are also increasing. Figure 6.14 shows that growth rate increases as substrate temperature increases. Between 60-100 Torr, the substrate temperatures were too low to be detected by the back-side temperature measurement using a pyrometer.

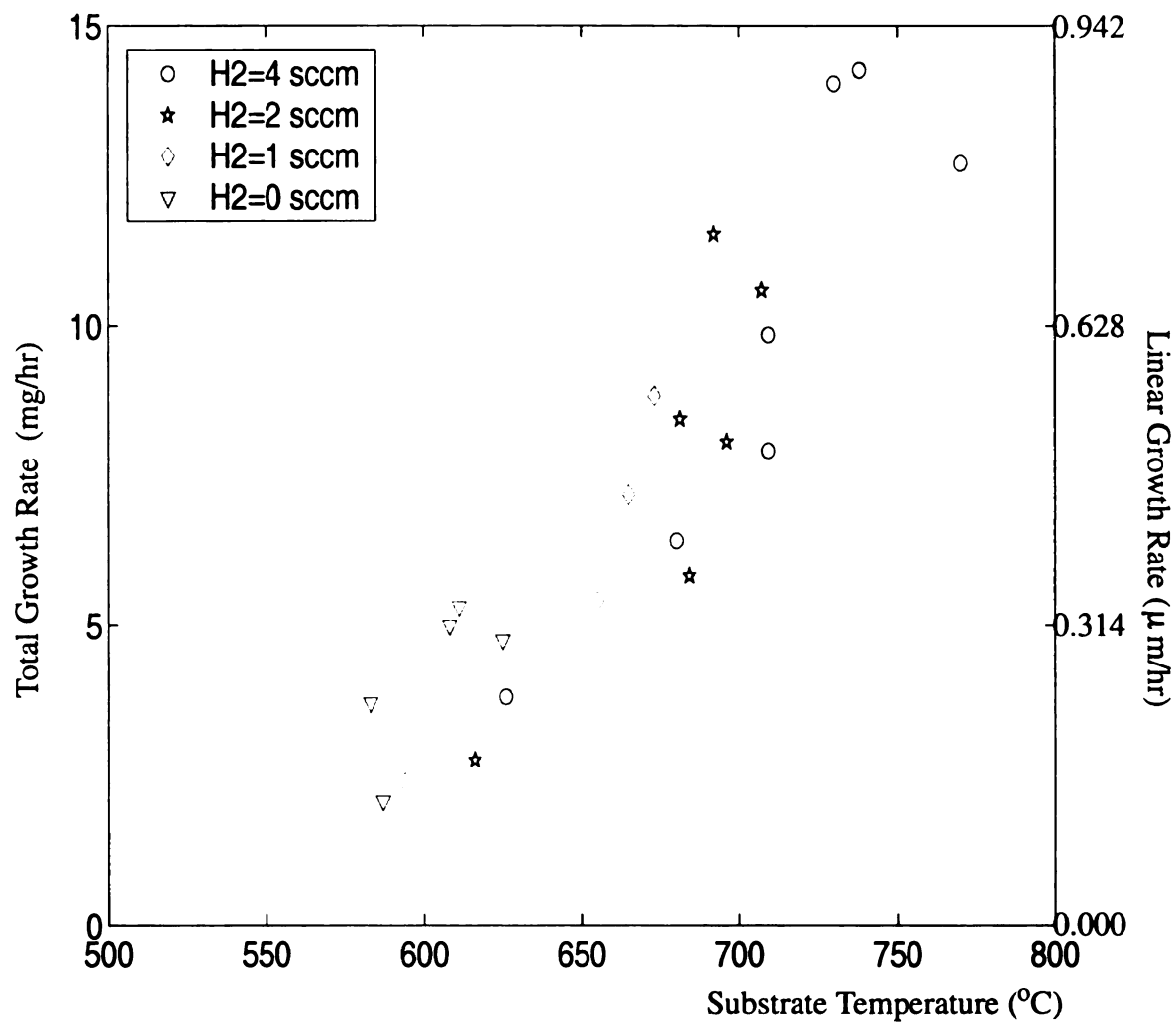


FIGURE 6.14 : GROWTH RATE VS. SUBSTRATE TEMPERATURE  
Ar=100 sccm, CH<sub>4</sub>=1 sccm, and t=8 hours by system II.

### 6.5.3 CN Emissions versus Controlled Nitrogen Impurity

Figure 6.15 displays the CN emission intensity plotted as a function of nitrogen impurities with pressure at 120 Torr and gas chemistry fixed at  $\text{Ar:H}_2\text{:CH}_4=100:4:1$ ,  $f_t=105$  sccm. As shown, the CN emission intensity strongly increases as the controlled nitrogen impurity increases from a few ppm to 1500 ppm.

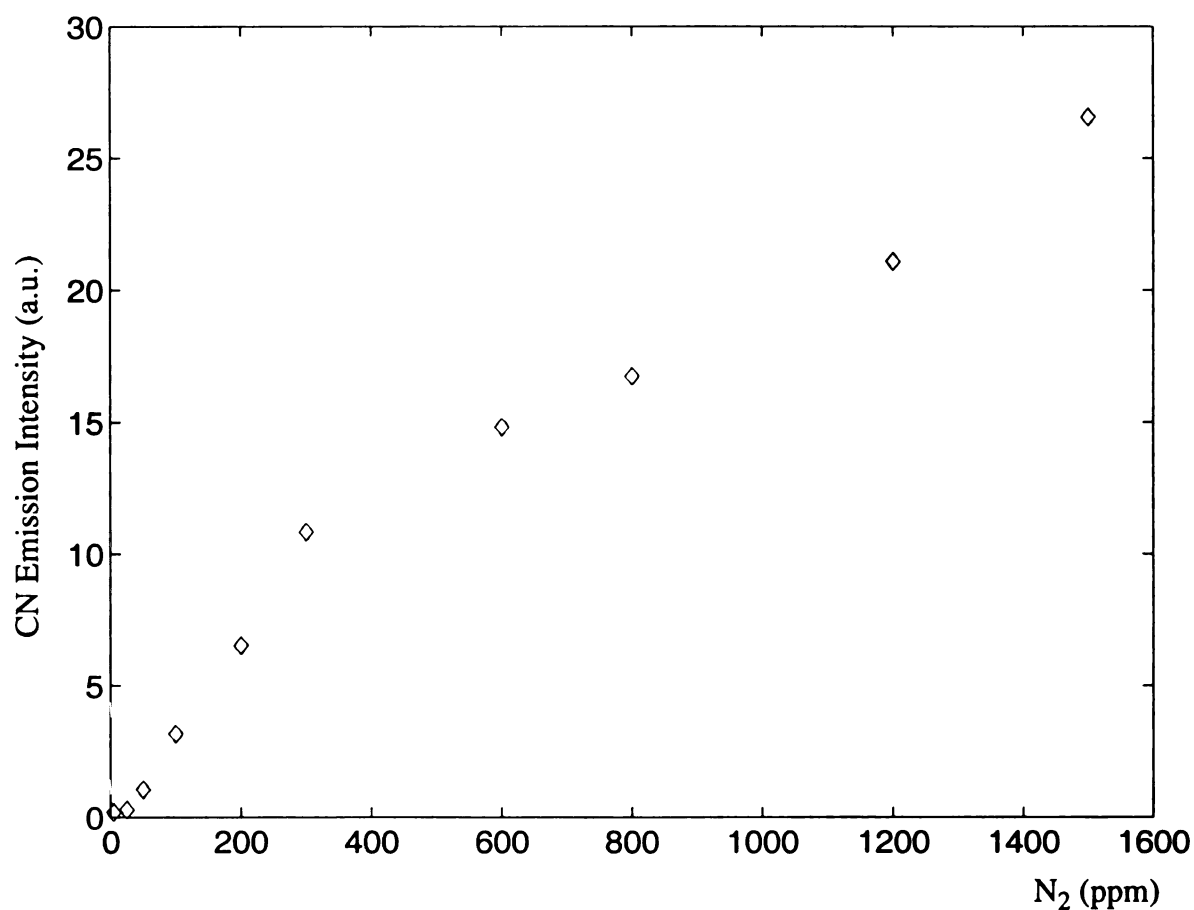


FIGURE 6.15 : CN EMISSION INTENSITY VS. NITROGEN IMPURITIES  
Pressure=120 Torr,  $\text{Ar:H}_2\text{:CH}_4=100:4:1$ ,  $f_t=105$  sccm by system II.

## 6.6 Summary

The results of optical emission spectroscopy show that the plasma properties are influenced by the input variables: Ar/H<sub>2</sub>/CH<sub>4</sub> gas chemistry, deposition pressure,  $p$ , and absorbed microwave power,  $P_{\text{abs}}$ . Figure 6.3 and Figure 6.4 show that the experimentally measured C<sub>2</sub> emission intensity generally decreases as hydrogen concentration increases, and is essentially constant as total gas flow rate increases. As shown in Figure 6.5 and Figure 6.6, the C<sub>2</sub> emission intensity increases as pressure and power increase.

Gruen et al. believe that there is a close relationship between total growth rate and the concentration of C<sub>2</sub> dimer in the plasma and confirm that C<sub>2</sub> dimer is the growth species of the ultra-nanocrystalline diamond [Zhou 1998]. Based upon the comparison of Figure 6.3 with Figure 4.17, and the results shown in Figure 6.7, total growth rate is usually higher when the C<sub>2</sub> emission intensity is higher except when the hydrogen concentration is increased. These measurements indirectly support that C<sub>2</sub> may be an important growth species. This is no longer valid at higher hydrogen concentration. The plasma deposition chemistry may change and maybe other radicals such as CH<sub>3</sub> are also present and influence the growth mechanism.

As shown in the results of Figure 6.8, Figure 6.11, and Figure 6.12, the gas temperature increases as hydrogen concentration increases, and increases as pressure and absorbed microwave power increases. The comparisons of Figure 6.8 with Figure 4.18, Figures 6.11 and 6.12 with Figures 3.12 and 3.13 show that substrate temperature varies with gas temperature in a manner similar to the measured gas temperature. Based upon the

results shown in Figures 6.9 and 6.13, total growth rate is higher when the gas temperature is higher. As shown in Figure 6.14, total growth rate is higher when the substrate temperature is higher. The gas temperature measured for the system II (1975K to 2960K between 60-240 Torr pressure regime) is higher than 1300 °C (1573 K, determined by Goyette et al.). The different gas temperature may be caused by: (1) the reactor geometry difference of these two systems (MSU-MPACVD system II versus ASTeX PDS-17 MPECVD system), and (2) the higher temperature observed in MSU-MPACVD system II should lead to higher chemically active species concentrations and this reactor can be more efficient than the commercial ASTeX PDS-17 MPECVD system. That is increases in gas temperature are expected to increase the dissociation of neutral species and produce higher chemically active species concentrations. The measured temperature (gas temperature and substrate temperature) at the higher pressure regime probably explains why the film growth rates are higher when the gas temperature is higher.

The idea that molecular nitrogen becomes chemically active in the plasma discharge is proven by the presence of the CN emission in Figure 6.15. It also indicates that the molecular nitrogen interacts with methane in the gas phase inside the plasma discharges. Therefore, nitrogen does change the bulk plasma properties.



## **7 Ultra-nanocrystalline Diamond Film Application**

### **7.1 Introduction**

Diamond's marvelous physical, chemical, and electronic properties have attracted researchers throughout the world. For instance, (1) its transparency over a wide wavelength range and capability of withstanding high electromagnetic radiation power fluxes from laser beams and x-ray sources make it a good candidate as a wear-resistant, transparent, and protective coating for optical components and x-ray lithography masks [Zhu 1991] that can be operated in hostile environments; (2) its extreme hardness, strength, chemical resistance, low coefficient of friction, high wear resistance, and excellent chemical and thermal stability make diamond an excellent coating material for abrasive and wear-resistant applications; (3) its high thermal conductivity, high hole mobility, and wide band gap have the potential to fabricate active semiconductor diamond elements for high power/high frequency and high frequency/high packaging density electronic devices that can be utilized in high temperature and chemically harsh environments; (4) its biocompatibility and high wear resistance indicates that diamond films have potential for use in the biomedical implantation and biosensors applications.

Nevertheless, diamond grown by the traditional  $\text{H}_2\text{-CH}_4$  CVD method usually has very rough as-deposited surfaces. The rough surface is problematic in several ways: too much light scattering for optical coating, increased coefficient of friction for diamond coated tools, and higher packaging costs for sensors. Moreover, post processing is time consuming, expensive, and not reliable.

Thus, smooth nanocrystalline diamond may be a very desirable material that enables many applications of CVD diamond. Recent years, an increasing amount of research has been devoted to the applications of nanocrystalline diamond: (1) RF MEMS and retinal implants by J.A. Carlisle et al.; (2) N-type conduction for nitrogen-doped nanocrystalline diamond films by O.A. Williams et al., by S. Bhattacharyya et al., and by Y. Dai et al.; (3) tool coatings by N. Salk et al. and by F.H. Sun et al.; (4) optical coatings by K. Yoshinori et al.; (5) SAW (Surface Acoustic Wave) devices by Y.K. Liu et al.; (6) biomedical applications by A.N. Jones et al., by M. Amaral et al., and by Y. Kousar et al.; and so on [Diam 2003].

In this chapter, three ultra-nanocrystalline diamond applications are briefly explored: (1) optical coatings for silicon substrates (Section 7.2), (2) tribological coatings for SiC chemical process pump seals (Section 7.3), and (3) SAW device applications (Section 7.4). The experimental fabrication, experimental measurements, results, and summaries for each application are presented in the sections below.

## **7.2 IR Optical Transmission Window**

### **7.2.1 Introduction**

Chemical resistance, wide optical transmission band, high resistance to abrasion and high index of refraction are some of diamond's unique properties. These properties make diamond of interest as an optical coating for semiconductors, both for the purpose of protection and for modifying the reflectivity of semiconductor materials. Silicon is used as a semiconductor substrate material for a variety of optical applications including infrared

(IR) windows. At an air/silicon interface, the reflective loss for photons ranges from approximately 30% at long (IR) wavelengths to 50% at short (blue-visible) wavelengths. The loss is compounded due to reflection at front and back surfaces [Rein 2000]. High-quality single-crystalline diamond is transparent from ultraviolet, through visible and infrared, and into the microwave portion of the electromagnetic spectrum. There's a slight absorption in the infrared, due to C-C bond vibrations, from 2.5  $\mu\text{m}$  to 6  $\mu\text{m}$  (with the largest peak at 5  $\mu\text{m}$  wavelength corresponding to an absorption coefficient of approximately  $12\text{ cm}^{-1}$  [Zait 1998] and [Thom 1993]), which is weak and maybe negligible if the film is thinner than 250  $\mu\text{m}$  [Ulc 1998]. Therefore, diamond film coatings are good candidates for optical applications that require the good chemical and mechanical surface properties of diamond and with the appropriate thickness of the coatings, it can even improve the optical performance.

The application of polycrystalline diamond films synthesized with good optical quality by regular  $\text{CH}_4/\text{H}_2$  CVD has proven difficult [Angu 1998], [Ong 1989], and [Wang 1990]. The difficulties arise due to scattering from the rough surface of the polycrystalline diamond films and the absorption from the defects and impurities inside the bulk of the crystals. However, the work of Ulczynski and Reinhard et al. [Ulc 1998], [Rein 2000], who make use of the traditional  $\text{CH}_4/\text{H}_2$  (sometimes with additional  $\text{O}_2$ ) polycrystalline diamond growth has achieved as-deposited, non-polished CVD polycrystalline thin diamond films with near ideal optical transmission throughout the visible and near- to mid-infrared. This thesis work investigates the use of UNCD for a similar optical application, i.e. it takes advantage of the smooth ultra-nanocrystalline diamond surfaces for making

optical coatings on silicon substrates with as grown ultra-nanocrystalline diamond thin films. The hydrogen free environment has also made it a clean and safe deposition procedure to produce diamond coated optical components.

The goal of this UNCD application investigation is to study the optical properties of these films. This portion of Chapter 7 addresses the results of the investigation of the optical properties of ultra-nanocrystalline diamond. The methods for producing the samples utilized in the research and the experimental conditions are briefly described in Section 7.2.2. The theoretical model and IR transmission measurements on the samples are described in Sections 7.2.3.1 and 7.2.3.2, respectively. Experimental results in the infrared, which are compared with theoretical calculations for the as grown single layer (diamond) and two layers (diamond/SiO<sub>2</sub>) and for one-side and both-side optical coatings on silicon substrates are presented in Section 7.2.4. Finally, Section 7.2.5 summarizes the results of the ultra-nanocrystalline diamond IR window application.

## **7.2.2 Experimental Method**

Infrared transmission through single-layer diamond coated and two-layer diamond/SiO<sub>2</sub> coated silicon substrates was experimentally investigated. A sketch of each of the different UNCD coated substrates is shown in Figure 7.1. Substrates are 3" diameter, 254-305  $\mu\text{m}$  thick, N/phos-type, (100) silicon wafers, both side polished, with a resistivity of approximately 10  $\Omega\text{-cm}$ . A SiO<sub>2</sub> layer was thermally grown in a furnace with high purity dry oxygen at 1100 °C. The oxide thickness was measured by ellipsometry. Prior to diamond deposition, either directly on silicon or on a silicon dioxide layer, substrates were prepared by scratch seeding (Procedure is described in Section 3.3.1.2.). Ultra-nanocrys-

talline diamond films for optical coatings were grown using system II with argon, hydrogen, and methane gas mixtures. The deposition details were described in Sections 3.2.2.2, 3.2.3.2, 3.2.4.1, and 3.3.2.2. Although the reactor is capable of operating in a wide experimental field map (see Section 3.2.5), in this study, the experimental deposition parameters were confined to the following regime: the deposition pressure was 120 Torr and 160 Torr, the microwave power was between 910-1314 W, the gas chemistry was  $\text{Ar}/\text{H}_2/\text{CH}_4=(99-95)/(0-4)/1$  (%). The resulting ultra-nanocrystalline diamond films have RMS roughness of 7-18 nm depending on the deposition conditions.

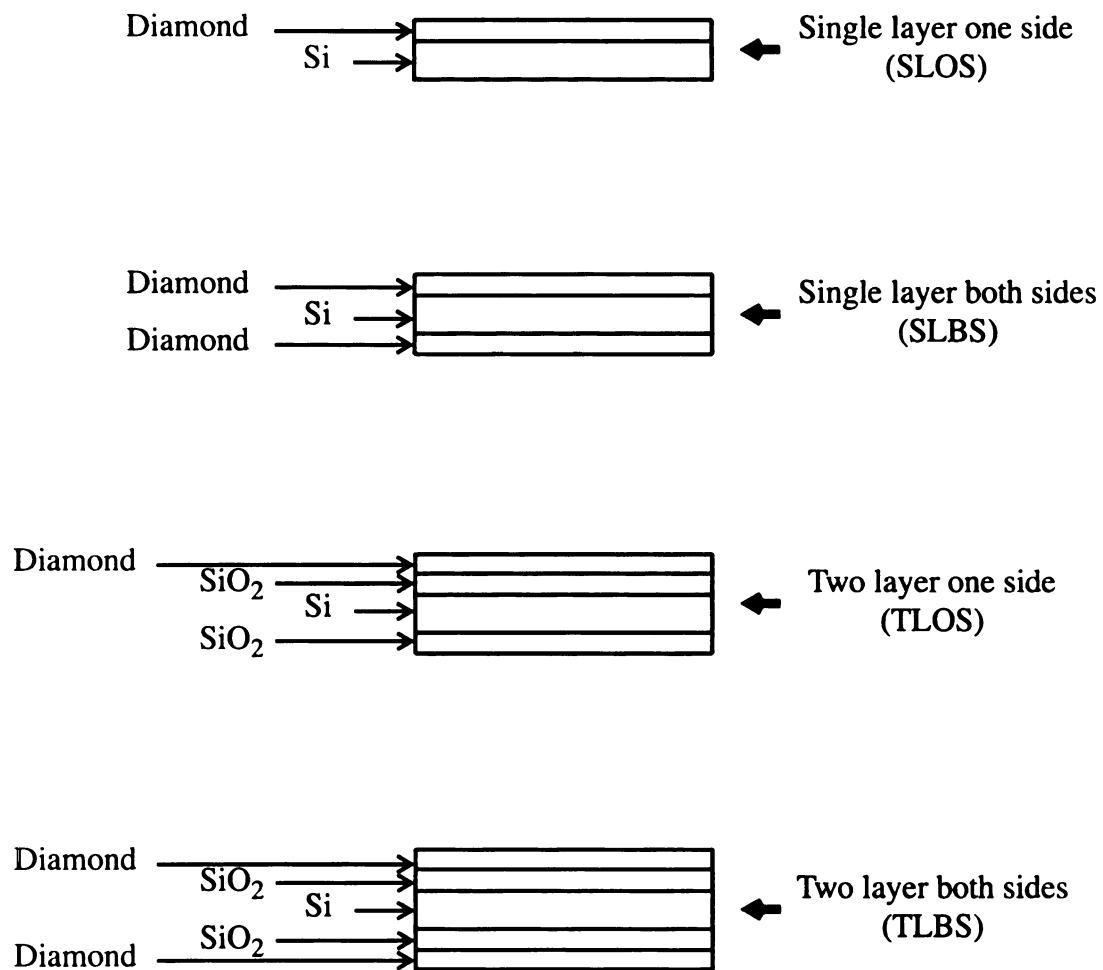


FIGURE 7.1 : A SKETCH OF CROSS-SECTION VIEW OF UNCD COATED SI SUBSTRATES

## 7.2.3 Theoretical Calculation and Transmission Measurement

### 7.2.3.1 Theoretical Calculations

The theoretical calculations were based on the following assumptions [Huan 2001].

- A planar, lossless diamond film of uniform thickness
- A normally incident EM wave
- Transmission is only limited by specular reflection
- Surfaces of the films are smooth.

The surface roughness (7 nm to 18 nm) of the films studied here is ignored in the theoretical calculations because the infrared wavelength (2.5  $\mu\text{m}$  to 14.3  $\mu\text{m}$ ) utilized in the measurements is much larger than the surface roughness. Therefore, the assumption of specular reflection is meaningful. When using the algebraic equations [Ulcz 1998], the N-layer problem is complicated and difficult to carry out, because it involves summing up N infinite series, each term of which is itself a series. Another simpler method of analysis, called Matrix Approach, was invented by Rouard in 1937 [Nuss 1976]. Rouard discovered that a multiple-layer film could be analyzed by representing each layer by a 2x2 matrix  $M_j$ . This is the preferred method and is used in this research.

The matrix,  $M$ , is the characteristic matrix of the coating layer and is only a function of the layer parameters: the refractive index,  $n$ , the phase shift,  $\delta$ , and the layer thickness,  $t$ . That is

$$M_j = \begin{bmatrix} \cos \delta_j & i \frac{\sin \delta_j}{n_j} \\ i n_j \sin \delta_j & \cos \delta_j \end{bmatrix} \quad (7.2)$$

The phase shift is defined as:

$$\delta_j = \frac{2\pi}{\lambda} n_j t_j \cos \theta_j \quad (7.3)$$

For normal incidence,  $\cos \theta_j = 1$ .

$$\delta_j = \frac{2\pi}{\lambda} n_j t_j \quad (7.4)$$

When there is more than one layer, the matrix has the following form:

$$M = \prod_i^j M_i \quad (7.5)$$

If we simply take the product of the matrices representing each layer, then the effect of a combination of layers is obtained. Special matrices used are

$$\begin{bmatrix} n_o & -1 \\ n_o & 1 \end{bmatrix} \text{ and } \begin{bmatrix} 1 \\ n_f \end{bmatrix} \text{ which represent top and bottom matrices;}$$

$$\begin{bmatrix} n_o & -1 \\ n_o & 1 \end{bmatrix} \text{ is the top media matrix, where } n_o \text{ is the index of refraction of air; and}$$

$$\begin{bmatrix} 1 \\ n_f \end{bmatrix} \text{ is the bottom media matrix, where } n_f \text{ is the index of refraction of the substrate.}$$



The reflectivity of a substrate with coating layers is given by [Nuss 1976]:

$$R = \left| \frac{a}{b} \right|^2 \quad (7.6)$$

a and b are determined by the matrix method.

$$\begin{bmatrix} a \\ b \end{bmatrix} = \begin{bmatrix} n_o & -1 \\ n_o & 1 \end{bmatrix} \cdot M \cdot \begin{bmatrix} 1 \\ n_f \end{bmatrix} \quad (7.7)$$

With all the assumptions described at the beginning of this session, the ideal smooth, no-loss film transmission calculation is then given by:

$$T = 1 - R \quad (7.8)$$

When the light is not sufficiently monochromatic to produce interference effects over the thickness of the semiconductor substrates, the through transmission,  $T_T$ , is given as:

$$T_T = \frac{(1 - R_F)(1 - R_B)}{(1 - R_F R_B)} \quad (8.10)$$

$R_F$  and  $R_B$  are the reflections corresponding to the front and back surfaces respectively.

Equation 8.10 was the equation that was used for the theoretical calculation in this thesis.

### 7.2.3.2 IR Transmission Measurements

A Beckman Spectrophotometer model IR4220 was used to perform the transmission measurements in this thesis research. The IR4220 Infrared Spectrophotometer has a range of  $4000\text{ cm}^{-1}$  to  $250\text{ cm}^{-1}$  and is equipped with a nichrome source and a thermocouple detector. The beam dimension is about  $10\text{ mm} \times 14\text{ mm}$ . The grating in the IR4220 changes at  $650\text{ cm}^{-1}$  and mostly, it has higher dispersion values between  $250\text{ cm}^{-1}$  and  $650\text{ cm}^{-1}$ . Therefore, the measurements performed here were from  $4000\text{ cm}^{-1}$  to  $700\text{ cm}^{-1}$ , ( $2.5\text{ }\mu\text{m}$  to  $14.3\text{ }\mu\text{m}$ ). The measurements were made with a double beam at a scanning speed of  $150\text{ cm}^{-1}/\text{min}$ . The instrument response time was set at 1 second. The measured transmission data of the films were normalized by the transmission value of air to obtain the percentage of the transmission. The spike around  $2333\text{ cm}^{-1}$  ( $\sim 4.29\text{ }\mu\text{m}$ ) in the measurements is random and has been confirmed with other users that it's caused by the instrument.

Equation 8.11, the Sellmeier equation is used to calculate the wavelength dependence of the refractive index for diamond [Klei 1999].

$$n_d^2 - 1 = \frac{4.3356 \cdot \lambda^2}{\lambda^2 - (0.1060)^2} + \frac{0.3306 \cdot \lambda^2}{\lambda^2 - (0.1750)^2} \quad (8.11)$$

Silicon dioxide refractive index is assumed to be a constant of 1.46. Silicon refractive index is 3.45. Air refractive index is 1. An uncoated, both-side-polished Si wafer has the transmission value around 53%.

## **7.2.4 Experimental Results**

### **7.2.4.1 Introduction**

The following experimental results are divided into four groups: (1) single layer one side (SLOS) (Section 7.2.4.2), (2) single layer both sides (SLBS) (Section 7.2.4.3), (3) two layer one side (TLOS) (Section 7.2.4.4), and (4) two layer both sides (TLBS) (Section 7.2.4.5). A sketch of each of these structures is shown in Figure 7.1. The transmission measurements were compared to the theoretical calculations. From Section 7.2.4.2 through Section 7.2.4.5, the dotted curves represent the experimental measurements and solid curves represent the theoretical calculations determined from the equation 8.10.

### **7.2.4.2 Single Layer One Side With Ultra-nanocrystalline Diamond Optical Coatings**

Figure 7.2 displays the optical transmission measurements compared to the theoretical calculations for two different deposition pressures. The deposition conditions were: (1) gas chemistry of  $\text{Ar}/\text{H}_2/\text{CH}_4 = 100/4/1$  sccm, (2) film thickness=850 nm, and (3) deposition pressure of 120 Torr shown in Figure 7.2(a) and 160 Torr shown in Figure 7.2(b).

As shown in Figure 7.2, there is no difference in the optical transmission between the sample deposited by 120 Torr and the other by 160 Torr. The wavenumbers to obtain maximum and minimum transmission are around the same places when film thickness is about the same. The theoretical calculations and experimental results are in good agreement.

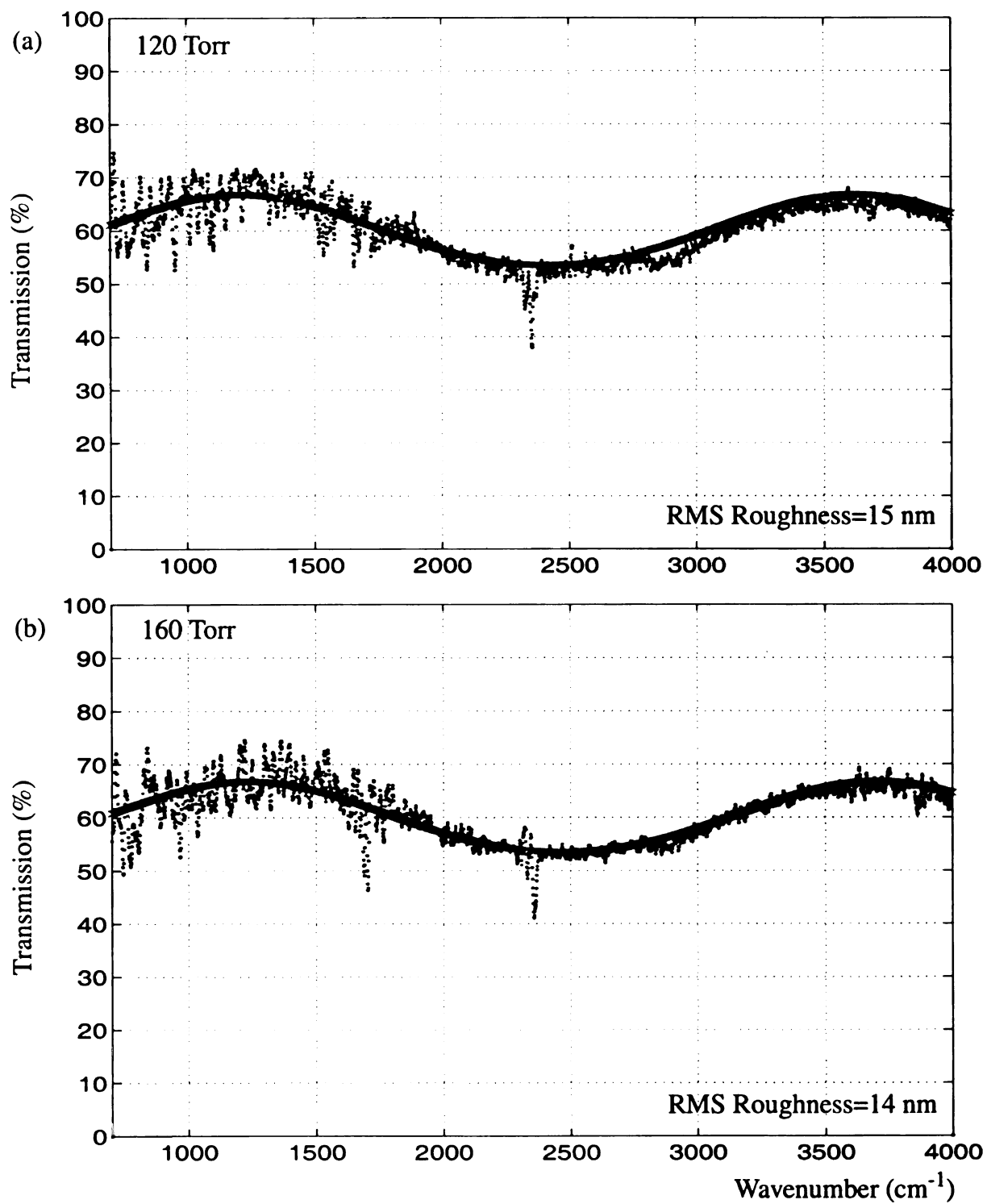


FIGURE 7.2 : OPTICAL TRANSMISSION OF SINGLE LAYER ONE SIDE  
 $\text{Ar}/\text{H}_2/\text{CH}_4=100/4/1$  sccm and Film=850 nm by system II.

Figure 7.3 displays the optical transmission measurements and associated theoretical calculations as the  $H_2$  vol% was varied from 0-4%. The deposition conditions were: (1) pressure at 120 Torr, (2)  $Ar/H_2/CH_4=100/4/1$  sccm,  $Ar/H_2/CH_4=100/1/1$  sccm,  $Ar/H_2/CH_4=100/0/1$  sccm, and (3) film thickness=657 nm.

Figure 7.4 displays the optical transmission measurements and associated model calculations as the  $H_2$  vol% was varied from 1-2%. The deposition conditions were: (1) pressure at 160 Torr, (2)  $Ar/H_2/CH_4=100/2/1$  sccm,  $Ar/H_2/CH_4=100/1/1$  sccm, and (3) film thickness=480 nm.

Figure 7.3 and 7.4 indicate that with  $Ar=100$  sccm and  $CH_4=1$  sccm, varying the hydrogen flow from 0-4 sccm, the films' optical properties do not vary. The wavenumbers to obtain maximum and minimum transmission are around the same places when the film thickness is about the same. Again, the experimental measurements are in excellent agreement with the theoretical calculations.

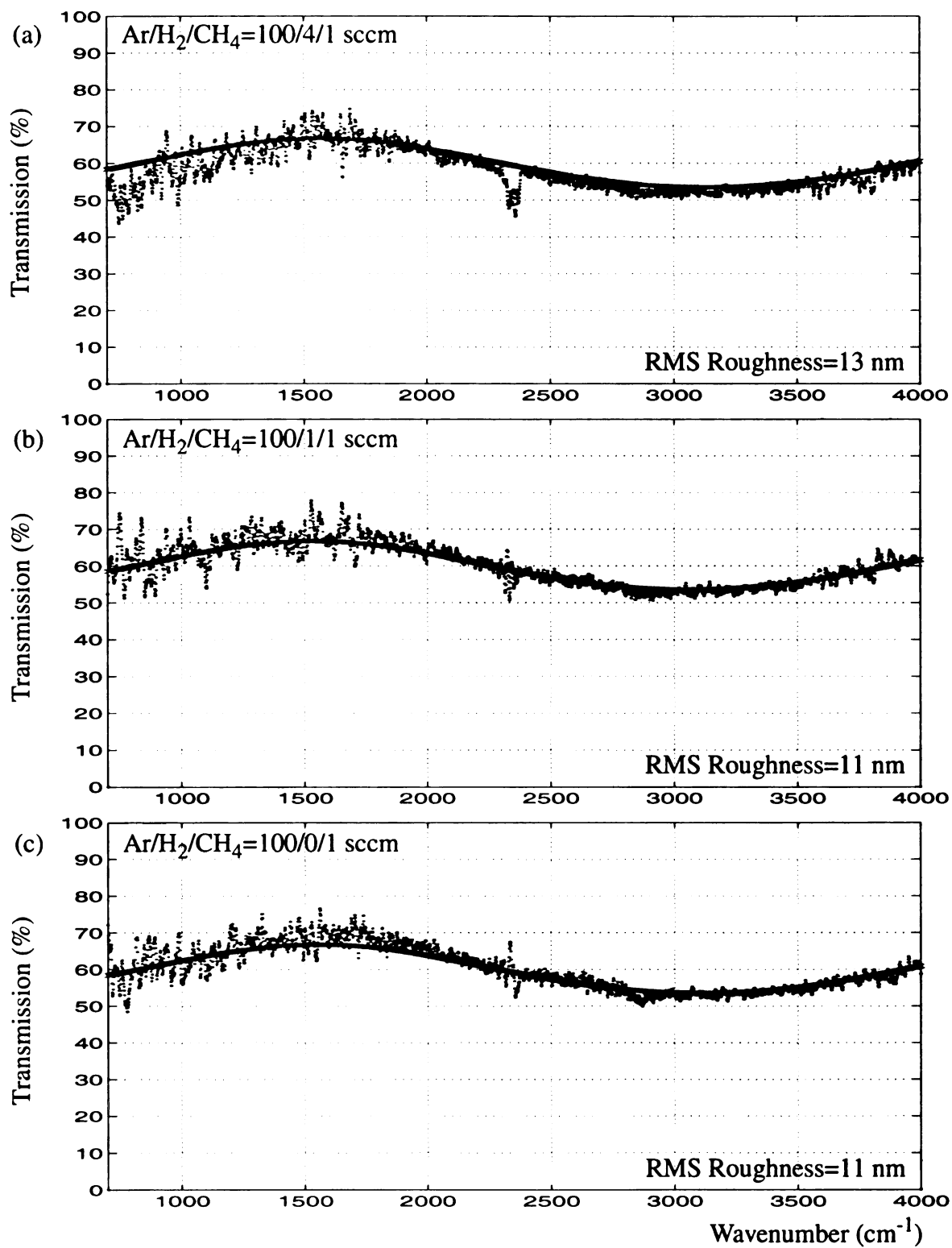


FIGURE 7.3 : OPTICAL TRANSMISSION OF SINGLE LAYER ONE SIDE  
Pressure=120 Torr and Film=675 nm by system II.

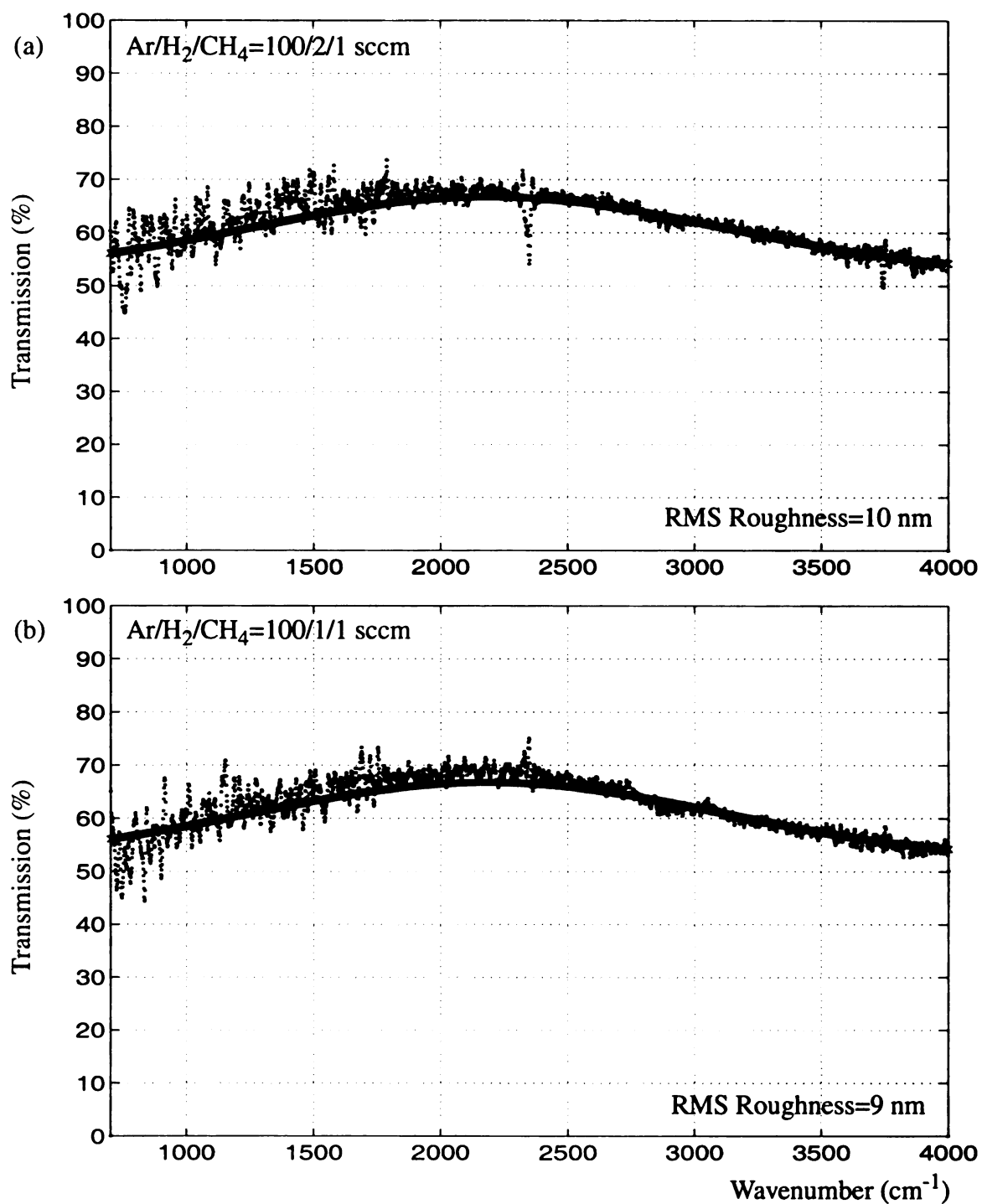


FIGURE 7.4 : OPTICAL TRANSMISSION OF SINGLE LAYER ONE SIDE  
 Pressure=160 Torr and Film=480 nm by system II.

Figure 7.5 displays the optical transmission measurements compared to theoretical calculations for two different film thickness. The deposition conditions were: (1) pressure at 120 Torr, (2)  $\text{Ar}/\text{H}_2/\text{CH}_4 = 100/2/1$  sccm, and (3) the film thickness=870 nm and 620 nm.

Figure 7.6 displays the optical transmission measurements compared to theoretical calculations for two different film thickness. The deposition conditions were: (1) pressure at 120 Torr, (2)  $\text{Ar}/\text{H}_2/\text{CH}_4 = 100/1/1$ , and (3) the film thickness=430 nm shown in Figure 7.6(a) and 675 nm.

As shown in Figure 7.5 and Figure 7.6, films produced with the same deposition pressure and gas chemistry have a similar optical transmission behavior. As expected from the theory, the optical transmission performance mainly depends on the ultra-nanocrystalline diamond film thickness.



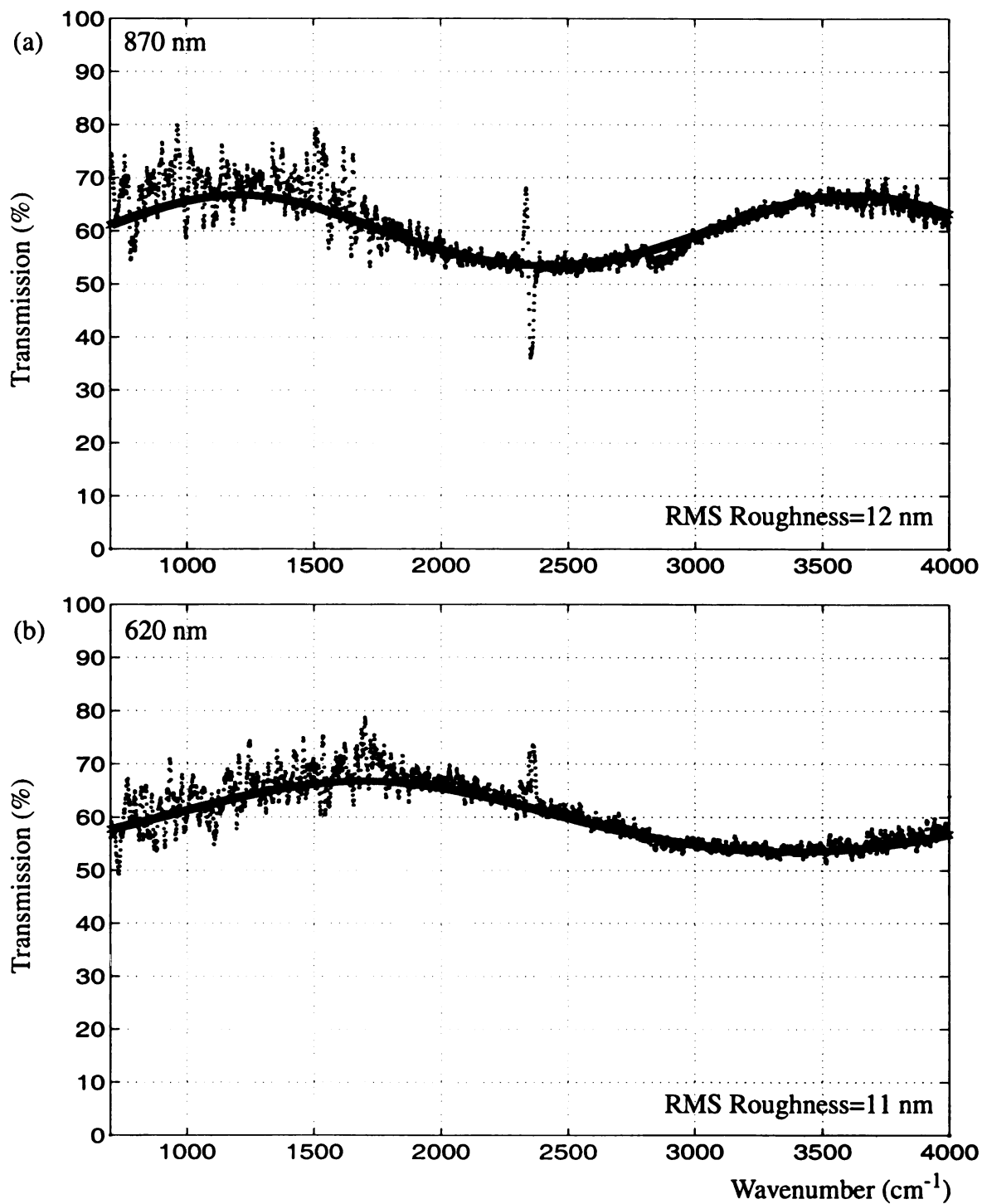


FIGURE 7.5 : OPTICAL TRANSMISSION OF SINGLE LAYER ONE SIDE  
Pressure=120 Torr and Ar/H<sub>2</sub>/CH<sub>4</sub>=100/2/1 sccm by system II.

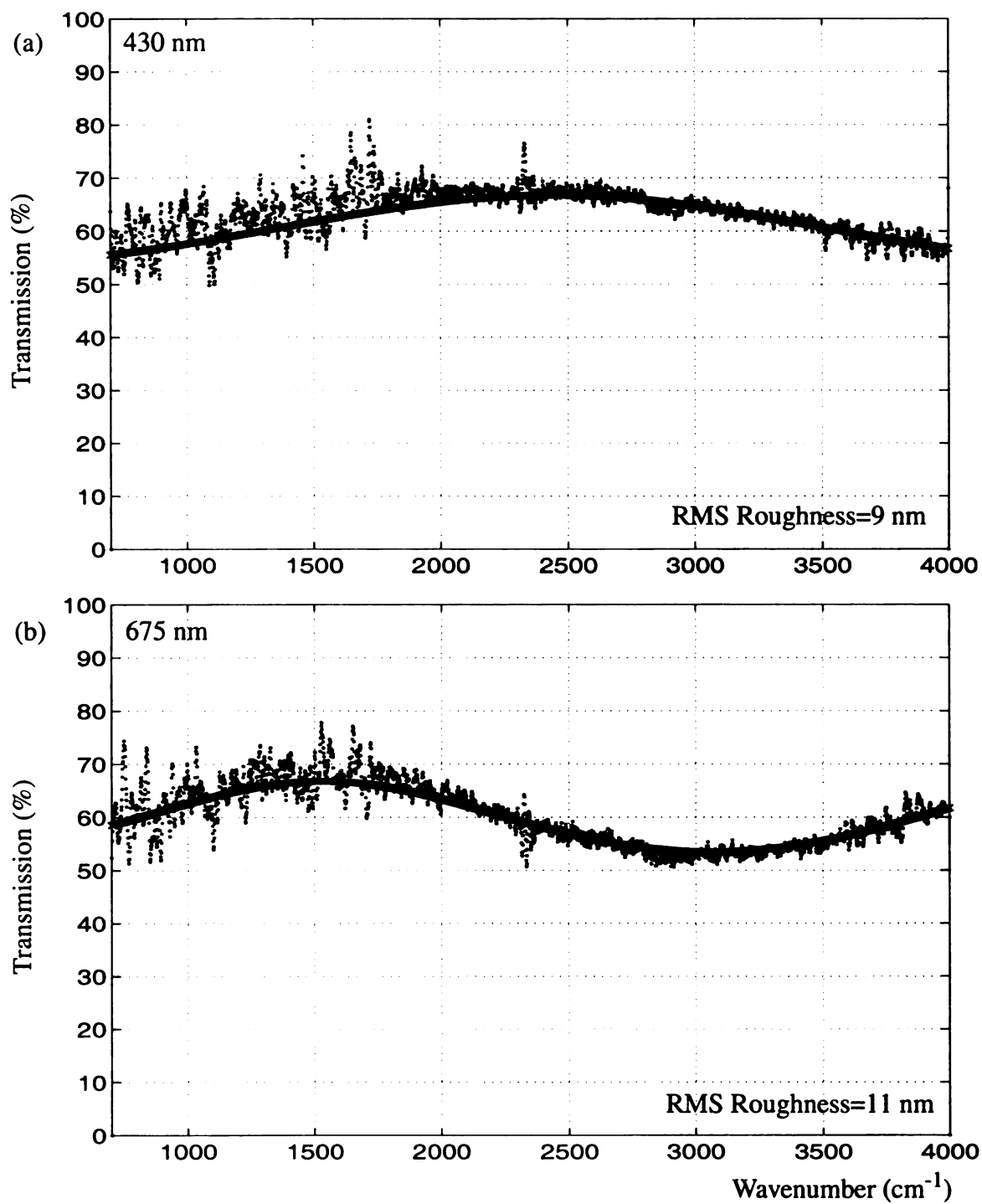


FIGURE 7.6 : OPTICAL TRANSMISSION OF SINGLE LAYER ONE SIDE  
Pressure=120 Torr and Ar/H<sub>2</sub>/CH<sub>4</sub>=100/1/1 sccm by system II.

#### **7.2.4.3 Single Layer Both Side With Ultra-nanocrystalline Diamond Optical Coatings**

Figure 7.7 displays the optical transmission measurements compared to theoretical calculations for SLBS and SLOS substrates. The deposition conditions were pressure= 120 Torr and  $\text{Ar}/\text{H}_2/\text{CH}_4 = 100/2/1$  sccm. As predicted from the theoretical calculations, the SLBS substrate improves the optical transmission by 33% over the SLOS substrate around  $6.15\ \mu\text{m}$  wavelength.

Figure 7.8 displays the optical transmission measurements compared to theoretical calculations for three different SLBS substrates. The deposition conditions were pressure at 120 Torr and  $\text{Ar}/\text{H}_2/\text{CH}_4 = 100/4/1$  sccm. Sample(a) film thickness=450 nm and 485 nm, sample(b) film thickness=675 nm & 590 nm, and sample(c) film thickness=895 nm & 405 nm. Theoretical calculations and experimental results again match well.

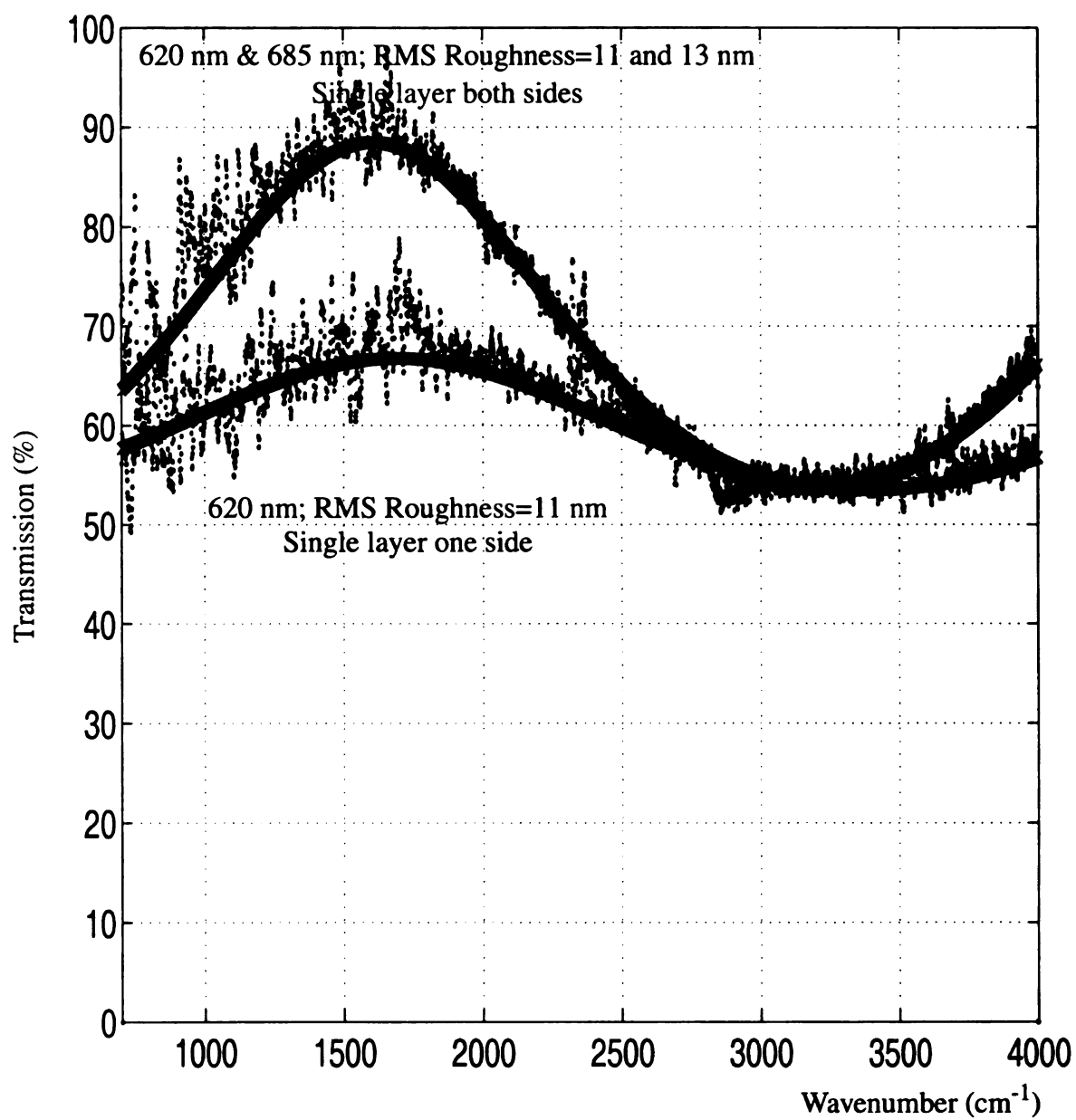


FIGURE 7.7 : OPTICAL TRANSMISSION OF SINGLE LAYER  
Pressure=120 Torr and Ar/H<sub>2</sub>/CH<sub>4</sub>=100/2/1 sccm by system II.

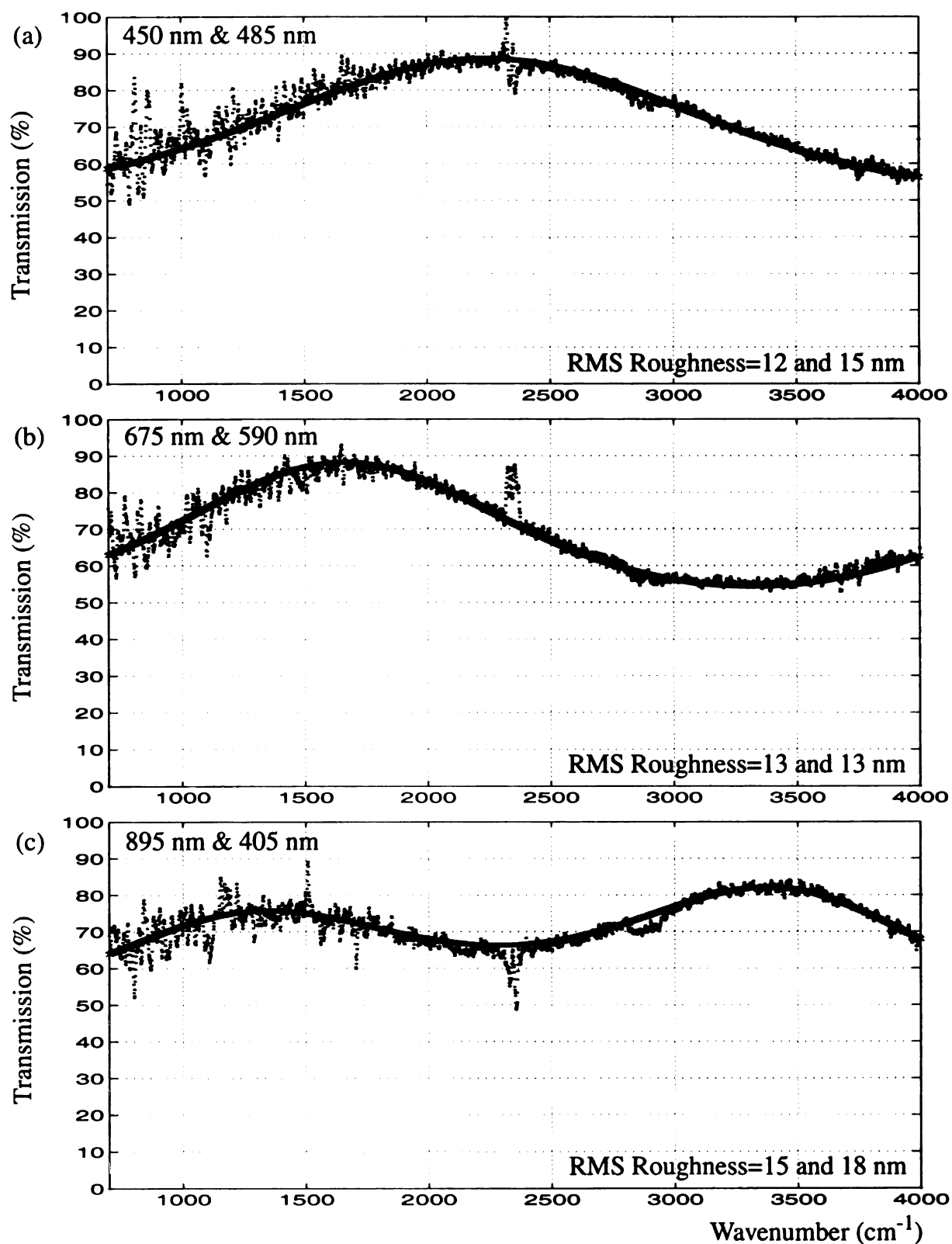


FIGURE 7.8 : OPTICAL TRANSMISSION OF SINGLE LAYER BOTH SIDES  
Pressure=120 Torr and Ar/H<sub>2</sub>/CH<sub>4</sub>=100/4/1 sccm by system II.

#### 7.2.4.4 Two Layer One Side Diamond/SiO<sub>2</sub>/Si/SiO<sub>2</sub> Optical Coatings

Figure 7.9 displays the optical transmission measurements compared to theoretical calculations for TLOS UNCD coated substrates and SiO<sub>2</sub>/Si substrate. The deposition conditions for the film transmission measurement shown in Figure 7.9(a) were: pressure=120 Torr and Ar/H<sub>2</sub>/CH<sub>4</sub>= 100/1/1 sccm on SiO<sub>2</sub>/Si substrate with SiO<sub>2</sub> layer thickness=74.4 nm. The diamond film thickness is 650 nm. The SiO<sub>2</sub> layered on Si wafer was thermally grown in a furnace with high purity dry oxygen at 1100 °C. The transmission measurement of SiO<sub>2</sub>/Si/SiO<sub>2</sub> substrate (before diamond deposition) was displayed in Figure 7.9(b).

The optical transmission measurements again agree with theoretical calculations. The transmission values are relatively low because neither the oxide or diamond thickness have been optimized for anti-reflection performance in this spectral range. The absorption around 1100 cm<sup>-1</sup> (9 μm) displays an oxide absorption, due to the stretching and bending mode excitations in the oxide.

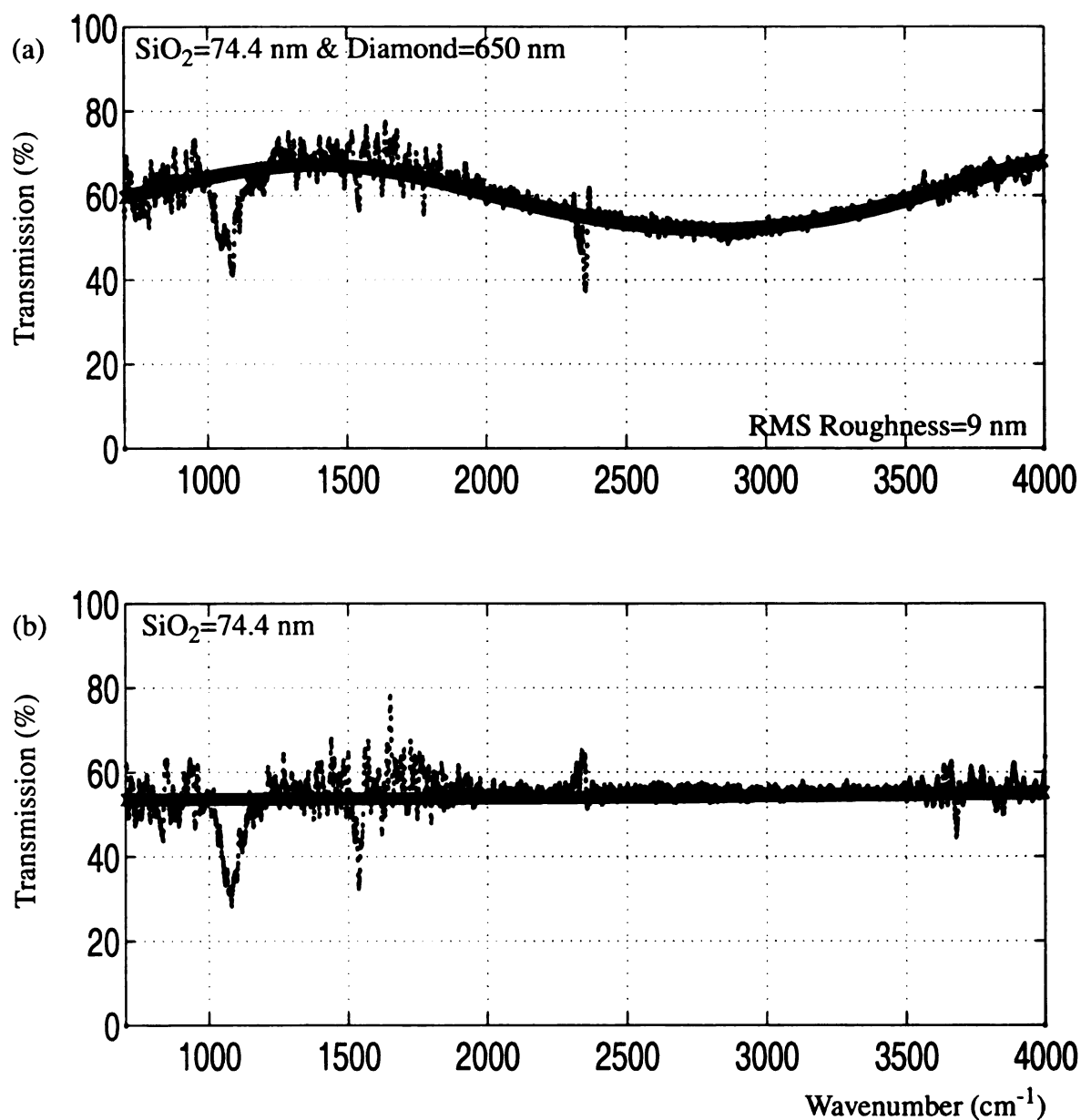


FIGURE 7.9 : OPTICAL TRANSMISSION OF TWO LAYERS ONE SIDE  
 Top: Pressure=120 Torr,  $\text{Ar}/\text{H}_2/\text{CH}_4=100/1/1$  sccm by system II.  
 Bottom: Thermally grown with high purity dry oxygen at  $1100^\circ\text{C}$  in a furnace.

#### 7.2.4.5 Two Layer Both Side Diamond/SiO<sub>2</sub>/Si/SiO<sub>2</sub>/Diamond Optical Coatings

Figure 7.10 displays optical transmission measurements compared to theoretical calculations for TLBS substrate and TLOS substrate. The deposition conditions were: pressure at 120 Torr and Ar/H<sub>2</sub>/CH<sub>4</sub>= 100/1/1 sccm on SiO<sub>2</sub>/Si/SiO<sub>2</sub> substrate with SiO<sub>2</sub> thickness=74.4 nm. The diamond film thickness is 650 nm and 340 nm. As expected, the transmission measurement of the TLBS, Diamond/SiO<sub>2</sub>/Si/SiO<sub>2</sub>/Diamond, sample displays much improved transmission when compared to the TLOS, Diamond/SiO<sub>2</sub>/Si/SiO<sub>2</sub>, substrate.

The optical transmission measurements agree well with theoretical calculations. The optical transmission is higher than that of the two-layer-one-side Diamond/SiO<sub>2</sub> optical coatings but generally lower than those of single-layer-both-side ultra-nanocrystalline diamond coated films (Compare Figure 7.10 with Figure 7.8(a) and Figure 7.8(b).). It is because neither the oxide or diamond thickness have been optimized for anti-reflection performance in this spectral range. The SiO<sub>2</sub> layer is not a good Fabry-Perot medium if the window is designed for a wide range of infrared wavelength because SiO<sub>2</sub> absorbs heavily in portions of IR wavelength.



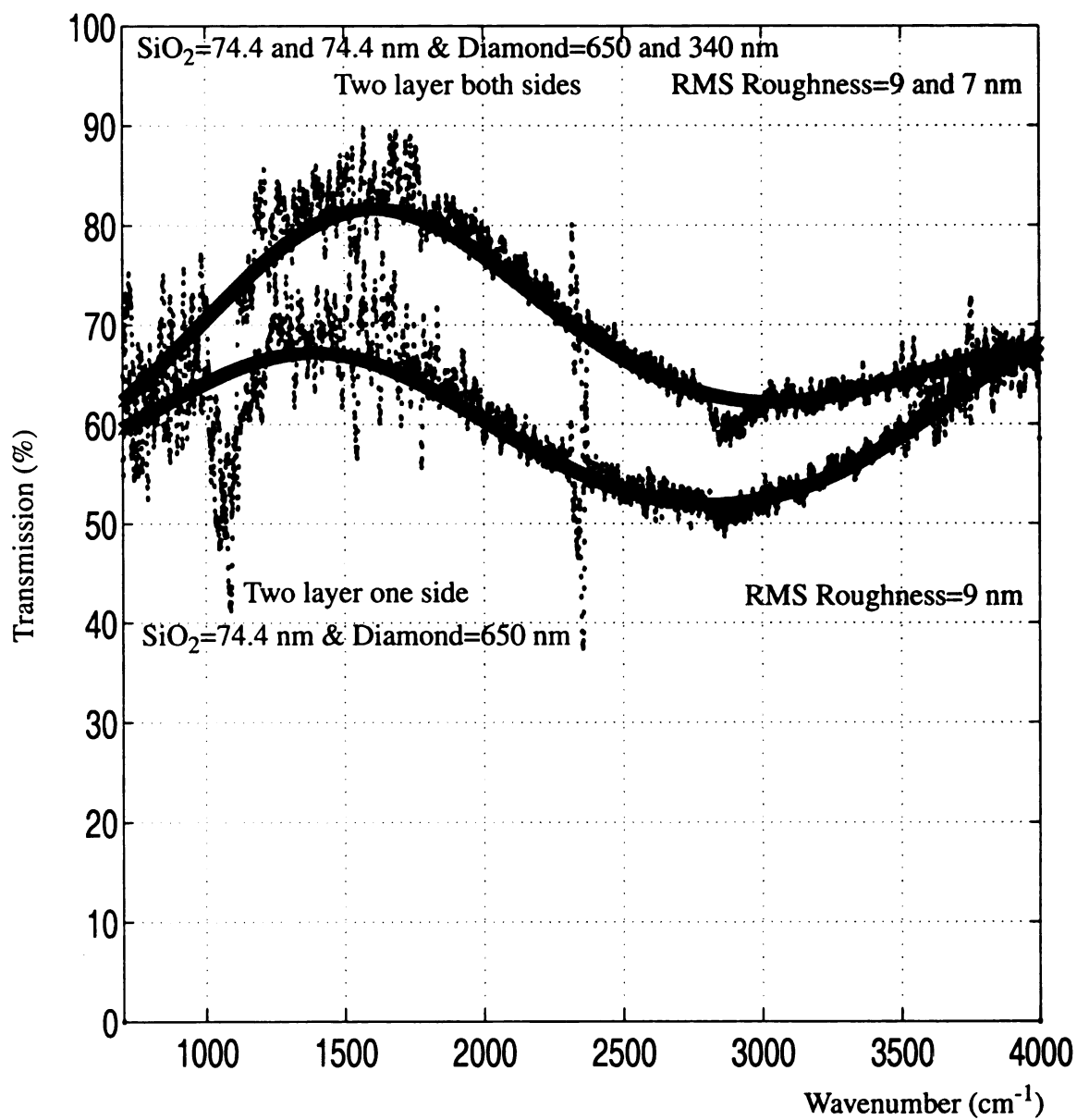


FIGURE 7.10 : OPTICAL TRANSMISSION OF TWO LAYERS  
Pressure=120 Torr and Ar/H<sub>2</sub>/CH<sub>4</sub>=100/1/1 sccm by system II.

### 7.2.5 Summary

Ultra-nanocrystalline diamond coatings applied as a IR optical transmission window have demonstrated that the ultra-nanocrystalline diamond has similar optical properties to high-quality diamond over 2.5-14.3  $\mu\text{m}$  wavelength. This is demonstrated by the fact that in all cases, the experimental measurements fit well with the theoretical calculations. In the theoretical model, a diamond slab (a planar, lossless diamond film of uniform thickness) was assumed. Thus, grain boundaries and other possible losses in the films were ignored. It's shown in the experimental results that the many ultra-nanocrystalline diamond grain boundaries have little effect on the experimental performance.

As expected, the IR optical transmission is sensitive to the thickness of the coatings and the differences in thickness of both sides. With the aid of theoretical calculations, the design and fabrication of ultra-nanocrystalline diamond IR optical windows can be achieved. Over a wide range of experimental deposition conditions, i.e. argon flow rate fixed at 100 sccm, methane flow rate fixed at 1 sccm, and varying the hydrogen flow from 0 to 4 sccm at 120 Torr or 160 Tor, there is no noticeable effect in the IR optical transmission. The upper limit for optical absorption is about  $494\text{ cm}^{-1}$ , which is determined with the film thickness of 405 nm and approximately 2% difference between the experimental measurements and the theoretical calculations.

It was demonstrated that the both-side coated ultra-nanocrystalline diamond IR windows have higher transmission than those of one-side coatings. In this research, two layered coatings do not have higher transmission than single layer because the thickness of diamond films and  $\text{SiO}_2$  layers were not optimally designed. For operating over a wide

span of infrared wavelength,  $\text{SiO}_2$  probably is not a good choice. The dip of the transmission in two-layered coatings around  $1100\text{cm}^{-1}$  ( $9\text{ }\mu\text{m}$ ) is an oxide absorption, due to the stretching and bending mode excitations in the oxide.

There is no visible IR-active single phonon absorption ( $1000\text{ cm}^{-1}$  to  $1500\text{ cm}^{-1}$ ) in the measurements, therefore the films are absent of significant defects or impurities. The intrinsic optical properties of diamond are associated with the arrangement of the carbon atoms on a diamond lattice. Since the thickness of the films is very thin, the multi-phonon absorption ( $2\text{ }\mu\text{m}$  to  $7\text{ }\mu\text{m}$ , about  $1428\text{ cm}^{-1}$  to  $5000\text{ cm}^{-1}$ ) is not seen in the measurements because the weakness of the absorption. However, the absorption around  $2830\text{ cm}^{-1}$  to  $2925\text{ cm}^{-1}$ , due to  $\text{CH}_x$  has been observed in several films. This indicates that there may be hydrogen exists in the films, which is usually predominantly bonded to  $\text{sp}^3$ -carbon in the grain boundaries or at the surface.

## **7.3 Tribological Application-Seal Coatings**

### **7.3.1 Introduction**

Diamond films grown by chemical vapor deposition have attracted considerable scientific interests due to their excellent properties, like high hardness, high wear resistance, and good tribological properties [Asma 1999], [Asma 2001], [Gabl 2000], [Lee 1999], and [Neer 1998]. A wide range of research on the engineering applications of diamond coating, including oilless bearings, seals, and cutting tools has been generated. Having a smooth coated surface in tribological applications is extremely important for diamond coatings in sliding contact with metals because the friction decreases as the surface

roughness decreases [Holl 1994], [Kohz 1994], and [Bogl 1995]. A reduction in wear rate was found when smoother diamond coating was sliding with mating AISI 52100 steel ball [Kohz 1994]. Casey M. and Wilks J. developed theories that explained the friction mechanism of diamond versus the surface roughness. They interpreted the friction in terms of the force required for the asperities on one surface to slide over those of the other [Case 1973]. Thus, very smooth films are desirable. During the last few years, developing diamond film coatings with a smooth surface for tribological applications has been attempted. The attention has been paid to the nanocrystalline diamond films [Holl 1998] and [Erde 1999].

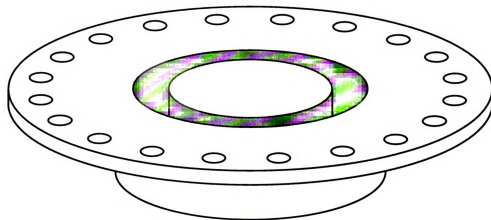
The aim of this research is to explore the applications to ultra-nanocrystalline diamond coatings on SiC chemical process pump seals. The experimental method and measurements utilized in this research are briefly described in Section 7.3.2. The primarily experimental results are presented in Section 7.3.3. Section 7.3.4 discusses and summarizes the work of ultra-nanocrystalline diamond coatings on SiC seals.

This application investigation was the results of the collaboration between Material Science Chemistry Division of Argonne National Laboratory (ANL), Flow Serve Company (FSC), and the author. ANL and FSC supplied the SiC seals and agreed to perform the experimental measurements and mechanical tests. The author deposited UNCD films on the SiC seals.

### 7.3.2 Experimental Deposition Method

The substrates used for ultra-nanocrystalline diamond coatings were 30  $\mu\text{m}$  lapped SiC seals with an outside diameter of 4.9 cm, inside diameter of 3.55 cm, and height of 1.55 cm. The thermally floating substrate holder set-up is shown in Figure 7.11. As shown in Figure 7.11(a), a moly substrate holder was designed and built by MSU researchers. It was designed to allow the pump seal, shown in Figure 7.12 to be placed inside the cut-out region, i.e. the grey area of Figure 7.11(a). Once placed in the moly holder, only the portion of the SiC seal that was to be coated was exposed to the deposition discharge. See Figure 7.11(b). After deposition, the seal was removed from the substrate holder and only the top surface of the seal shown in Figure 7.12 was coated with UNCD.

(a)



Top view of the seal substrate holder.  
A SiC seal was inserted into the grey area.

(b)

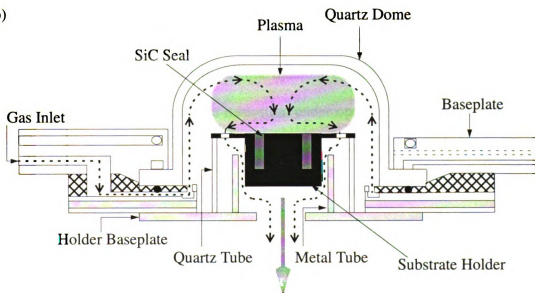


FIGURE 7.11 : SEAL COATING SUBSTRATE HOLDER SET UP  
SiC seal coating thermal floating substrate holder set-up.

Prior to diamond deposition, the top surface of the SiC substrate was prepared by scratch seeding (Procedure is described in Section 3.3.1.2.) Ultra-nanocrystalline diamond coatings for SiC seals were deposited by MSU-MPACVD reactor system II with Ar-H<sub>2</sub>-CH<sub>4</sub> plasma discharges. The details were previously described in Sections 3.2.2.2, 3.2.3.2, 3.2.4.1, and 3.3.2.2. These exploratory experiments were performed under the following deposition conditions: pressure of 160 Torr, microwave power between 1108-1226 W, gas chemistry confined within Ar/H<sub>2</sub>/CH<sub>4</sub>=(99-95)/(0-4)/1%, the total gas flow rate between 101-105 sccm, and the deposition time between 8-24 hours. Only three SiC seals were coated for this investigation.

### **7.3.3 Experimental Measurements and Results**

The Raman spectroscopy characterization indicated that the deposited films on the 30  $\mu\text{m}$  lapped SiC seals were ultra-nanocrystalline diamond. Before deposition and seeding, the typical surface roughness of each seal was on the order of a few to 10's of micrometers. A typical ultra-nanocrystalline diamond coated SiC seal is shown in Figure 7.12. The visual appearance and the inspection under optical microscopy suggest a very uniform coating.

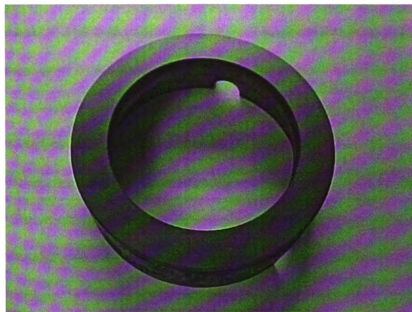


FIGURE 7.12 : A ULTRA-NANOCRYSTALLINE DIAMOND COATED SiC SEAL

A profilometer (interferometric imaging), at MSC Division of ANL was used to perform the surface roughness characterization. A typical surface profile of the diamond coated SiC seal is shown in Figure 7.13. The scanned area is  $5252 \times 3985 \mu\text{m}^2$  ( $\sim 20 \text{ mm}^2$ ). As shown in Figure 7.13, the surface roughness is within  $\pm 0.63 \mu\text{m}$ , even though the initial surface roughness of SiC substrate was on the order of a few to 10's of micrometers.



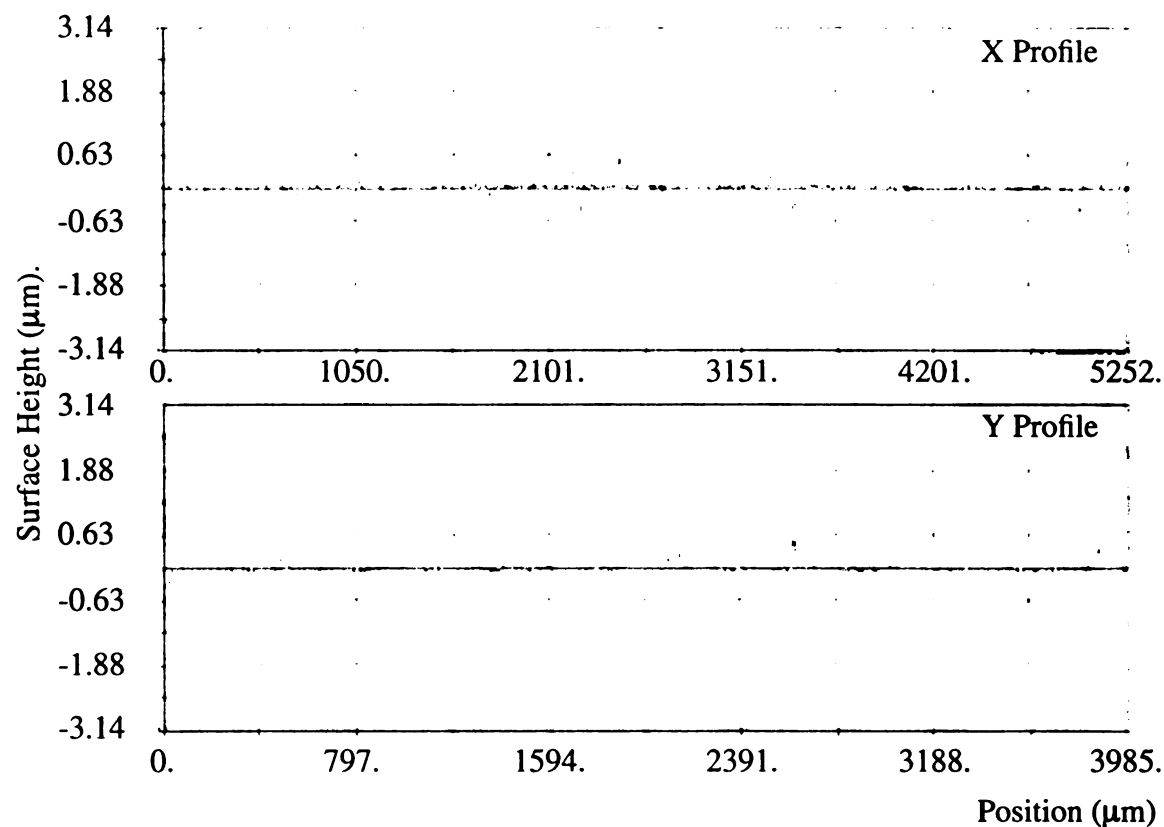


FIGURE 7.13 : SURFACE PROFILE INSPECTED BY INTERFEROMETRIC IMAGING [HUAN 2001]

Pressure=160 Torr, Ar/H<sub>2</sub>/CH<sub>4</sub>=100/2/1 sccm and deposition time=8 hours  
by system II.

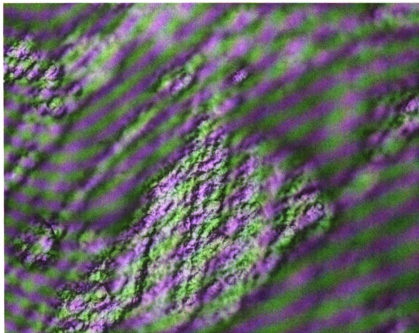
The ultra-nanocrystalline diamond films deposited by MSU-MPACVD reactor system II with deposition pressure of 160 Torr, Ar/H<sub>2</sub>/CH<sub>4</sub>=100/2/1 sccm, and deposition time of 8 hours passed the adhesion test but did not perform well in the wear durability test on the water pump at ANL (The wear resistance test was taken against SiC counterface.).

As we have learned from Figure 4.22 and Figure 5.20,  $\text{Ar}/\text{H}_2/\text{CH}_4=100/4/1$  sccm gas chemistry yields 1.59 times higher growth rate than  $\text{Ar}/\text{H}_2/\text{CH}_4=100/0/1$  sccm gas chemistry but the RMS surface roughness is 2.36 times worse. As supplied by ANL, the SiC seals were 30  $\mu\text{m}$  lapped and thus had rough deposition surfaces. From the viewpoint of ultra-nanocrystalline diamond, there are lots of big potholes and deep ditches on the surface of the seal. In order to achieve a smooth surface, one must fill the “holes” and “ditches” on the substrates. To fill them up quickly and still have a smooth surface, a different deposition process chemistry was developed. The ultra-nanocrystalline diamond deposition process started with a high-growth-rate gas chemistry ratio and ended with a low-surface-roughness gas chemistry ratio. It was hoped that the process would substantially reduce the deposition time and the surface roughness and also achieve a continuous film.

Two more seals were coated with UNCD. One was deposited with  $\text{Ar}:\text{H}_2:\text{CH}_4=100:2:1$  gas chemistry ratio,  $f_t=103$  sccm for 24 hours. The other was first deposited with  $\text{Ar}:\text{H}_2:\text{CH}_4=100:4:1$  gas chemistry ratio,  $f_t=105$  sccm for 8 hours and followed by  $\text{Ar}:\text{CH}_4=100:1$  gas chemistry ratio,  $f_t=101$  sccm for 16 hours [Suma 2002]. Although the surface profile of the seals could not be carried out at MSU because the lack of the appropriate equipment, one was able to compare the optical microscopy images of the coated seals (See Figure 7.14.). The seal deposited with the two different gas chemistry ratio method is much smoother (See Figure 7.14(b).). The collaboration with ANL and FSC was ended before these seals could be tested. Thus, the author was not able to determine the mechanical properties of these coated seals. Even though the final test results

were not available to MSU researchers, from the work reported above, one may draw the conclusion that the ultra-nanocrystalline diamond coating for the SiC seal had lower surface roughness when lower hydrogen concentrations are present in the deposition process. As a result, the process may lead to lower friction coefficient and smaller wear coefficient. Therefore, it may have potential to pass the long term durability test in the water pump.

(a)



(b)

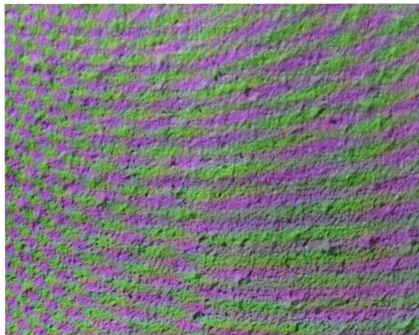


FIGURE 7.14 : SURFACE PROFILE INSPECTED BY OPTICAL MICROSCOPY

(a): Pressure=160 Torr,  $\text{Ar}/\text{H}_2/\text{CH}_4=100/2/1$  sccm, and  $t=24$  hours ( $26\text{ }\mu\text{m} \times 20\text{ }\mu\text{m}$ ).

(b): Pressure=160 Torr,  $\text{Ar}/\text{H}_2/\text{CH}_4=100/4/1$  sccm, and  $t=8$  hours then followed by  $\text{Ar}/\text{CH}_4=100/1$  sccm, and  $t=16$  hours ( $13\text{ }\mu\text{m} \times 10\text{ }\mu\text{m}$ ) by system II.

### 7.3.4 Summary

Ultra-nanocrystalline diamond coatings for SiC seals was experimentally explored. The SiC seals were successfully coated with UNCD. The films were uniformly coated and adhered well on the SiC substrates. The reason why the first UNCD coated SiC seal did not perform well in the wear-resistant test probably was caused by the initially very rough SiC substrate surface (30  $\mu\text{m}$ ). If the SiC seals were initially mechanically polished to achieve excellent smoothness and then the deposition methodologies developed and described in Chapters 3 and 4 of this thesis were employed for the coatings. It appears possible to uniformly coat UNCD on SiC chemical process pump seals.

An additional improvement may also be carried out for the ultra-nanocrystalline diamond coatings on the SiC chemical process pump seals. That is, if the SiC seal surface must be rough, then one can use a combined gas chemistry growth step process described in Section 7.3.3 to (1) quickly fill up the big and deep tracks left on the 30  $\mu\text{m}$  lapped surface, (2) deposit the coatings in a clean environment, and (3) synthesize smooth films which deduce low friction coefficient, low wear rate, and low counterface coefficient. Therefore, prolong the mean life time of the pumps, reduce leakage of hazardous gases, and lower the friction energy loss.

## 7.4 SAW Devices Based on Ultra-nanocrystalline Diamond

### 7.4.1 Introduction

Filters operating at high frequencies up to many gigahertz are required in telecommunications to speed up data transmission. Since diamond films have a large SAW (surface acoustic wave) velocity  $\sim 1 \times 10^4$  m/sec, their use as a SAW substrate can provide great advantages in the fabrication of high frequency SAW devices. However, diamond is not piezoelectric. It must be combined with a piezoelectric thin film, such as ZnO and AlN.

Diamond films used as surface acoustic wave substrate materials have attracted researchers' attention for relaxing the lithographic criteria [Yama 1989] and [Naka 1998]. The need for a piezoelectric overlayer, often ZnO, has introduced additional complexities: (1) velocity dispersion of the layered structure and (2) allowance of multiple modes. Nevertheless, there are successful devices composed of ZnO, polycrystalline diamond, and Si layered structures and they have been fabricated through different diamond synthesis methodologies [Naka 1994], [Naka 1995], [Higa 1997], and [Asso 2001]. However, quite often, the micron sized polycrystalline diamond films on Si Substrates are rough and require post processing, like mechanical polishing or etching during the device fabrication processing. Moreover, the intergrain phonon scattering in polycrystalline diamond can affect the device performance if the lateral grain dimensions are on the length scales between acoustic wavelengths and SAW device aperture and transducer separations [Bi 2002]. One of the properties of ultra-nanocrystalline diamond that has received much attention is its smooth surfaces that are the result of by the films' small crystal size. The

utility of ultra-nanocrystalline diamond may solve the above fabrication problems if the elastic properties of ultra-nanocrystalline diamond do not differ from those of their high-quality, larger grained counterparts.

The motivation of this application investigation were: (1) to study the elastic response of ultra-nanocrystalline diamond in the 1 GHz regime, and (2) to investigate the possibility of ultra-nanocrystalline diamond as a SAW substrate material. The UNCD samples produced for this research and deposition conditions are briefly described in Section 7.4.2. The theoretical calculations and measurements on the samples are described in Section 7.4.3. Experimental results compared with theoretical calculations for high-quality polycrystalline diamond are presented in Section 7.4.4. Finally, Section 7.4.5 summarizes the research of ultra-nanocrystalline diamond SAW devices.

This application investigation was the result of a collaborative effort between the Physics Department at Michigan State University and the author. The UNCD film used in the SAW-device fabrication was synthesized by the author. The SAW device design, fabrication, and testing were carried out by Dr. Bi and Dr. Golding.

## **7.4.2 Experimental Method**

Ultra-nanocrystalline diamond film for a SAW-device substrate was grown on a 3"(100) silicon wafer by MSU-MPACVD reactor system II with a mixture of argon, hydrogen, and methane gases. The deposition details have been previously described in Sections 3.2.2.2, 3.2.3.2, 3.2.4.1, and 3.3.2.2. Prior to the deposition, the Si wafer was prepared by scratch seeding (Procedure is described in Section 3.3.1.2.) The deposition

conditions were: the pressure was 160 Torr, the microwave power was 1.1 kW, and the gas chemistry was  $\text{Ar}/\text{H}_2/\text{CH}_4=100/4/1$  sccm. The resulting ultra-nanocrystalline film, shown in Figure 7.15, had a RMS surface roughness of 50 nm. The upper limit on the average grain size was estimated to be approximately 30 nm, shown in Figure 7.15(a) [Bi 2002]. As shown in Figure 7.15(b), the SAW device was fabricated on a 23- $\mu\text{m}$ -thick ultra-nanocrystalline diamond film which was deposited uniformly over three inch Si substrate. The photolithographic IDTs (interdigital transducers) consisted of 100-nm-thick Al electrodes. The Al electrodes were prepared on the UNCD as-grown surfaces by thermal evaporation which were then followed by lift-off processing. A ZnO layer with thickness between 1.0 and 2.5  $\mu\text{m}$ , served as the piezoelectric layer, and was sputtered on the ultra-nanocrystalline diamond growth surface (DC triode sputtering in 85% of argon and 15% of oxygen at 5 mTorr) after IDT preparation [Bi 2002].



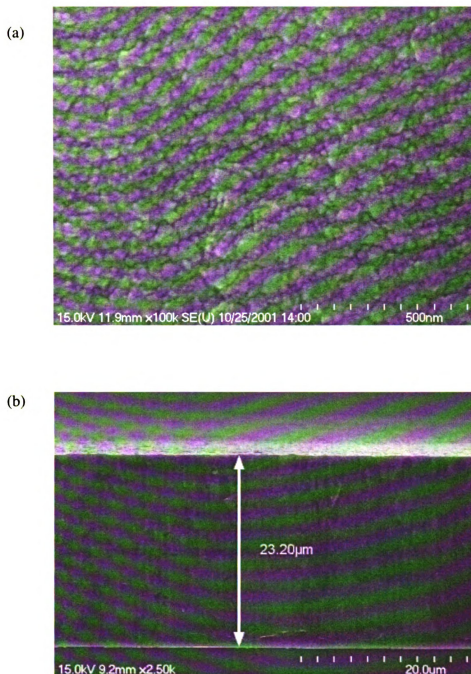


FIGURE 7.15 : SEM IMAGES OF UNCD ON A SI SUBSTRATE [BI 2002]

(a) Plan view image of as grown UNCD film.

(b) Cross-section image of UNCD grown on a Si substrate.  
Pressure= 160 Torr,  $\text{Ar}/\text{H}_2/\text{CH}_4=100/4/1$  sccm by systemII

### 7.4.3 Theoretical Calculations and Measurements

The theoretical calculations and measurements were carried out by Dr. Bi and Dr. Golding at Physics Department of Michigan State University. As described in [Bi 2002]: “The modal velocities of ZnO/Diamond/Si multilayers were calculated with a matrix-based approach and the Si(100) wafer was treated as an infinite half-space. The surface wave phase velocity is a function of  $kh_{\text{diamond}}$  and  $kh_{\text{ZnO}}$ . Here  $k = \frac{2\pi}{\lambda}$ ,  $\lambda$  is the acoustic wavelength. If  $kh_{\text{diamond}} > 4$ , then Si substrate is insignificant. That satisfied the experimental conditions. Therefore,  $kh_{\text{diamond}}$  equal to 4 was set for all numerical calculations. The nanocrystalline diamond layer was treated either as an isotropic medium or a (100) oriented crystalline diamond layer. For these two cases in the measurement range studies, the dispersion curves for the two lowest modes were indistinguishable. The density of nanocrystalline diamond was taken as  $3.5 \text{ g/cm}^{-3}$ . The calculations agree well with the published results by H. Nakahata et al. [Naka 1995].

Saw-device experimental response was studied with frequency and time domain methods. Phase velocities were measured with a network analyzer and the group velocities were measured by time-of-flight techniques. The measurements were done at room temperature without employing any impedance matching structures.”

### 7.4.4 Experimental Results

As described in [Bi 2002]: “For a given value of  $kh_{\text{ZnO}}$ , the phase velocities of several modes are found and the modes are highly dispersive at small values of  $kh_{\text{ZnO}}$ . At large  $kh_{\text{ZnO}}$ , the lowest order mode tends toward the phase velocity of the Rayleigh wave on ZnO but as  $kh_{\text{ZnO}} \rightarrow 0$ , it approaches the diamond Rayleigh wave velocity. The

experimental data agree well with the control device (SAW devices built on a 300- $\mu\text{m}$ -thick polycrystalline diamond substrates supplied by Diamonex Corp.) and the theoretical calculations.”

#### **7.4.5 Summary**

As described in [Bi 2002]: “The utility of as grown ultra-nanocrystalline diamond as a high frequency SAW device substrate material is demonstrated. The elastic properties of ultra-nanocrystalline diamond and polycrystalline diamond are indistinguishable in this study. SAW devices based on ultra-nanocrystalline diamond and on polycrystalline diamond substrates are indistinguishable (within combined uncertainties) and both agree well with the theoretical calculated dispersion curves which are based on elastically isotropic or single crystal diamond. (In this study, the uncertainty of the measurements of  $kh_{\text{ZnO}}$  is about  $\pm 10\%$ .) The merits of smooth surface, absence of intergrain scattering, and elastic isotropy have put ultra-nanocrystalline diamond in the advantages over the polycrystalline diamond. Another achievement is that the surface acoustic wave velocities over  $1 \times 10^4$  m/s have been realized on the as grown ultra-nanocrystalline diamond surface.”

## 8 Summary

### 8.1 Introduction

Research activities for the thesis research reported here were initiated in 1997. At that time, microwave plasma assisted ultra-nanocrystalline diamond CVD was a recent development. Using Ar/H<sub>2</sub>/CH<sub>4</sub> or Ar/H<sub>2</sub>/C<sub>60</sub> chemistries, ultra-nanocrystalline diamond film synthesis had already been proposed and had been demonstrated over a limited experimental regime, i.e. pressure, substrate size, etc. For example, Gruen et al [Zuik 1995], [Erde 1996] reported on the growth of ultra-nanocrystalline diamond films with gas mixtures of argon ( $\geq 97\%$ ), methane (1%) or C<sub>60</sub> ( $\sim 600^\circ\text{C}$ ), and hydrogen (1-2%). Microwave discharges were created over limited substrate areas,  $< 20\text{ cm}^2$ , and from 80-100 Torr. The best films were produced when the input hydrogen gas content was reduced to 1% or less, and the deposition rate increased as the pressure increased. However, these mostly argon microwave discharges were difficult to control as pressure increased or as hydrogen content decreased and the initial experiments suffered from the lack of reactor and process versatility. Thus in 1997 ultra-nanocrystalline diamond film deposition technologies and associated deposition experience were very limited.

In order to apply and utilize the many beneficial properties of ultra-nanocrystalline diamond material in 1997, there was the need to develop process technologies and methodologies that enabled the routine and repeatable synthesis of smooth and uniform ultra-nanocrystalline diamond films over large substrate surfaces and with improved deposition rates.

Thus an important initial objective of this thesis research was to utilize previously developed MSU microwave plasma reactor technology and to explore new process technologies and methodologies that enabled smooth and uniform ultra-nanocrystalline diamond synthesis over a large experimental parameter space. Initial objectives were to develop techniques to deposit ultra-nanocrystalline diamond films uniformly over three inch silicon substrates, over a 80-150 Torr pressure regime, and in an almost “hydrogen free” (1% or less) gaseous environment. The research activities summarized in this thesis have achieved these objectives. The methodologies and procedures that were developed utilize technologies that can be readily extended to larger diameter substrates by employing a similar, scaled up 915MHz reactor design. Thus it is expected that the results of this thesis can be easily scaled up to 6-8 inch substrates.

In particular, the research activities of this thesis have been demonstrated that in order to routinely synthesize high quality ultra-nanocrystalline diamond films the reactor deposition process must be performed in a high purity, i.e., base pressure:  $10^{-7}$ ~ $10^{-6}$  Torr, deposition environment. This was observed by comparing the experimental performance between System I and System II (See Chapter 4 and Chapter 5). Under the high vacuum conditions of System II, the film deposition is more repeatable, smoother, and more uniform and can be performed over a much larger experimental parameter space (60-240 Torr), and deposition can take place without any input hydrogen gas. Using (0-1%)  $H_2$ , large, uniform, intense, greenish-white, hydrogen deficient, argon discharges were sustained in contact with three inch silicon substrates over a 60-200 Torr pressure regime. Using (2-4%)  $H_2$  high quality film deposition was extended to 240 Torr. At a given pres-

sure, uniform film deposition was achieved by optimizing substrate holder geometry, substrate position, microwave power, gas chemistry and total gas flow rate. Film crystal sizes ranged from 3-30 nm and film roughness from 11-50 nm. Film uniformities of almost 100% were achieved over three inch silicon wafers. At a pressure of 220 Torr with  $\text{CH}_4$  ~1% and  $\text{H}_2$  ~4%, linear growth rates as high as ~ 0.9  $\mu\text{m}$  (total growth rate 14.25 mg/hr) were achieved. It is not possible to directly compare these growth rates with those of other research groups [Zuik 1995], [McCa 1998], [Zhou 1998], because of major differences in reactor geometry, substrate heating, deposition area, and growth rate measurement techniques. However, it is clear that the maximum total growth rate reported is the highest reported for ultra-nanocrystalline diamond film synthesis.

## **8.2 The Performance Comparison Between Systems I and II**

The initial film synthesis experiments were performed using system I. This system did not have high vacuum capability, i.e. it was only pumped down to  $\sim 2 \times 10^{-2}$  Torr before each experimental run and the leak rate was ~12.6 mTorr/hr. However, it was still useful for the initial exploratory experiments presented in this thesis. The initial experimental process methodology, such as discharge start-up, discharge positioning over the substrate, discharge stabilization, etc. were developed with the system I reactor. Once the construction of system II was completed, system II was used. The initial experiments with system II indicated that the film quality improved considerably. Thus, the remaining experimental results were performed with reactor system II.

Since this thesis utilized both reactor systems, it is useful to compare their performance here. Table 8.1 summarizes the performance of these reactors. Besides the high vacuum capability (base pressure  $10^{-7}$  Torr, leak rate 4 mTorr/hr), a minor difference between systems I and II is that system II was less energy efficient than system I (see Table 4.3). This may have been caused by the differences in reactor cooling. To improve the energy efficiency of system II, the reactor operator can increase the temperature set point of the Neslab chiller from 15 °C to a higher degree, i.e. lowering the cooling efficiency.

**TABLE 8.1: EXPERIMENTAL PERFORMANCE OF SYSTEMS I & II**

System	Reactor Performance	Film Characteristics
<b>I</b>	$G_T$ : 0.163-12.963mg/hr $G_{ave}$ : 0.010-0.809 $\mu\text{m/hr}$ $S_y$ : 4411-69 kW*hr/g C: 0.504-33.382%	Film texture: (111)or(220) or No preferred $I(220)/I(111)=0.06-4.04$ Film roughness: 14-149 nm Morphology: mostly (111) triangular Crystal size: 30-2700 nm
<b>II</b>	$G_T$ : 0.175-14.25 mg/hr $G_{ave}$ : 0.011-0.889 $\mu\text{m/hr}$ $S_y$ : 4229-99 kW*hr/g C: 0.542-44.094%	Film texture: mostly (220) $I(220)/I(111)=0.13-9.31$ Film roughness: 11-50 nm Morphology: featureless Crystal size: 3-30 nm

As shown in Table 8.1, the growth rate, specific yield, and carbon conversion efficiency for the two systems are similar. However, system II allows a stabilized and flame free discharge operation over a larger range of pressures, total gas flow rates, and  $\text{H}_2/\text{CH}_4$  ratios, i.e. system II allowed deposition to occur over a larger input experimental param-

ter space. For system I, the plasma could not be stabilized and/or flame free if the hydrogen to methane ratio was under three. On the other hand, experiments that utilized system II were performed with hydrogen to methane ratios as low as zero.

A very important difference between the two reactors was the film quality. When comparing the results under the same input experimental conditions, it was observed that system II has lower film roughness, smaller crystal size, much better film uniformity. Experiments were repeatable. Thus the best over all deposition performance was achieved with the high-purity system II.

### **8.3 Summary of Experimental Performance**

Since system II had the best overall operational performance, this section only summarizes system II experimental data. With system II, the input parameters were performed in the following regime: the deposition pressure was between 60-240 Torr, the microwave power was between 732-1518 W, the gas chemistry was:  $\text{Ar}/\text{H}_2/\text{CH}_4=(99-90)/(0-9)/1$  (%), total gas flow rate was between 101-630 sccm. The films were deposited on 3" diameter Si substrates. 100% uniformity was achieved at pressures of 60-80 Torr.



- Growth Rate (See Figures 4.22 and 4.23)
  - a) Growth rate increased as pressure and microwave power increased. The highest growth rate of 14.25 mg/hr ( $\sim 0.9 \mu\text{m/hr}$ ) was achieved at 220 Torr, with  $\text{Ar:H}_2\text{:CH}_4=100:4:1$ ,  $f_t=105$  sccm, and 1.4 kW of input power.
  - b) Growth rate was independent of total gas flow rate.
  - c) Growth rate was constant as the deposition time was varied from 8 to 25 hours.
  - d) Growth rate increased dramatically as  $\text{H}_2$  concentration increased from 0-9%.
- Carbon Conversion Efficiency (See Figures 4.32, and 4.33)
  - a) Carbon conversion efficiency increased as total gas flow rate decreased.
  - b) Carbon conversion efficiency as high as 44% was achieved under the conditions: 220 Torr, 1.4kW,  $\text{Ar:H}_2\text{:CH}_4=100:4:1$ ,  $f_t=105$  sccm.
- Film Roughness (See Figure 5.20)
  - a) Film roughness increases as pressure increases; for example, surface roughness of 12 nm (with average film thickness  $0.611 \mu\text{m}$ ) at 100 Torr versus surface roughness of 26 nm (with average film thickness of  $5.284 \mu\text{m}$ ) at 200 Torr. Film roughness of 11 nm was achieved under the conditions: 120 Torr, 898W,  $\text{Ar:CH}_4=100:1$ ,  $f_t=101$  sccm, and average film thickness= $1.029 \mu\text{m}$ .
  - b) Film roughness increases dramatically as  $\text{H}_2$  concentration is increased (11 nm at 0 vol% versus 44 nm at 9%).
  - c) Film roughness increases as flow rate is increased.
- Film characterization by XRD, Raman (Figure 5.22), and TEM (Figure 5.36), show deposited films are diamond for all the films.
- Film Morphology is featureless (See Figures 2.6, 5.28, and 7.15(a)).

- The crystal sizes range from 3-30 nm with an upper bound of 30 nm for the films produced in lower leak rate system, systemII (See Figure 5.34 for representative film crystal size distribution).
- Cross-section TEM images show an interlayer between UNCD films and Si substrates in most cases.

As shown in Figures 5.17 through 5.20, films with roughness of less than 50 nm and with crystal size of less than 30 nm can be achieved under the following experimental conditions: deposition pressure between 60-240 Torr, microwave power between 732-1518 W, gas chemistry confined within  $\text{Ar}/\text{H}_2/\text{CH}_4=(99-90)/(0-9)/1$  (%), total gas flow rate between 101-111 sccm, and deposition time up to 25 hours. If film roughness < 30 nm is required, then the deposition conditions are limited to: pressure between 60-200 Torr, microwave power between 732-1310 W, gas chemistry confined within:  $\text{Ar}/\text{H}_2/\text{CH}_4=(99-95)/(0-4)/1$  (%), total gas flow rate between 101-105 sccm, and deposition time up to 8 hours.

It was observed that the deposition operational field map that developed the relationship between substrate temperature,  $T_s$ , pressure,  $p$ , and input power,  $P_{\text{abs}}$ , for ultra-nanocrystalline diamond synthesis behaved differently from that of more common  $\text{H}_2/\text{CH}_4$  deposition process. If the gas chemistry was held constant, then a unique MCPR operational field map of UNCD growth was established experimentally (See Figure 3.12). However, when input gas mixtures are varied, the curves change. This is particularly true for changes in input hydrogen concentrations. Thus, this feature of the field map versus

input gas concentrations is an important difference from the conventional  $H_2/CH_4$  deposition process.

Table 8.2 shows a comparison of crystal sizes of ultra-nanocrystalline diamond. The experiments performed by Csencsits et al. [Csen 1996], Erdemir et al. [Erde 1996], Gruen et al. [Grue 1996], Luo et al. [Luo], and Qin et al. [Qin 1998] were using a microwave plasma chemical vapor deposition reactor (ASTeX PDS-17) and heated substrate holder.

**TABLE 8.2: CRYSTAL SIZE COMPARISON OF ULTRA-NANOCRYSTALLINE DIAMOND FILMS**

Reference	Gas Chemistry	Flow Rate (sccm)	P (Torr)	M.P. (W)	T <sub>s</sub> (°C)	t <sub>Film</sub> (μm)	Crystal Size (nm)	S.R. (nm)
[Csen 1996]	NA	~100	100	1500	850	NA	ave.=7.7 (equiaxed) 110 (dendritic)	30-50
[Csen 1996]	Ar:H <sub>2</sub> :C <sub>60</sub> =98:2	~100	100	1500	850	NA	ave.=14.9 (equiaxed)	NA
[Erde 1996]	Ar:H <sub>2</sub> :CH <sub>4</sub> =98:2:1	101	100	1500	800-850	NA	10-30	20-40
[Erde 1996]	Ar:H <sub>2</sub> :C <sub>60</sub> =97:2:1	100	100	1500	800-850	≤ 6	ave.=15 range: 3-110	20-50
[Grue 1998]	Ar:H <sub>2</sub> :CH <sub>4</sub> =90:9:1	100	100	1200	800	5	30-50	54.19
[Grue 1998]	Ar:H <sub>2</sub> :CH <sub>4</sub> =97:2:1	100	100	1200	800	5	10-30	18.84
[Grue 1998]	Ar:H <sub>2</sub> :CH <sub>4</sub> =99:0:1	100	100	1200	800	5	3-20	NA
Luo	Ar,H <sub>2</sub> , C <sub>60</sub>	NA	NA	1500	850	NA	20 nm within an array of larger crystals (~300 nm)	NA

TABLE 8.2 (cont'd)

Reference	Gas Chemistry	Flow Rate (sccm)	P (Torr)	M.P. (W)	T <sub>s</sub> (°C)	t <sub>Film</sub> (μm)	Crystal Size (nm)	S.R. (nm)
[Qin 1998]	Ar,H <sub>2</sub> , C <sub>60</sub>	NA	100	800	800	NA	ave.=3-5 occasionally see size of 15 nm	NA
Author	Ar/H <sub>2</sub> /CH <sub>4</sub> =100/4/1	105	120	945	626	ave. =1.9	predominant ≤ 7 20 nm has been seen	24

M.P.: Microwave power

## 8.4 Plasma Diagnostics Using System II

Goyette et al. [Goye 1998] observed a strong linear correlation between the experimentally measured C<sub>2</sub> emission intensity and the experimentally measured C<sub>2</sub> concentrations. They observed the C<sub>2</sub> densities were linearly related to C<sub>2</sub> emission intensity. Based on the work of Goyette et al., in this thesis, it is assumed that C<sub>2</sub> emission intensity measurements are linearly related to C<sub>2</sub> concentrations in the discharge.

Experimentally measured C<sub>2</sub> emission intensities increased as pressure or microwave power increased. C<sub>2</sub> emission intensity generally decreased as hydrogen concentration increases. Therefore, if the observed behavior by Goyette et al. also holds for the MSU reactors, C<sub>2</sub> concentration increased as pressure or microwave power increased. C<sub>2</sub> concentration generally decreased as hydrogen concentration increased. It was observed that total growth rate is usually higher when the C<sub>2</sub> emission intensity is higher except when the hydrogen concentration is increased. Thus these measurements indirectly support the hypothesis that C<sub>2</sub> is an important growth species. This is no longer valid at higher hydrogen concentrations. The plasma deposition chemistry may change

and maybe other radicals such as  $\text{CH}_3$  are also present and influence the growth mechanism. It was also observed that the film roughness increased as hydrogen percentage increased. This suggests the discharge and deposition chemistry may change their behavior towards  $\text{H}_2/\text{CH}_4$  discharges.

The gas temperature ranges from 1975K to 2960K between 60-240 Torr pressure regime and increases as pressure or microwave power increases. The gas temperature also increases as hydrogen concentration increases. The gas temperature measured for the reactor of system II is higher than the 1300 °C (1573 K) reported by Goyette et al. The different temperature may be caused by: (1) the reactor geometry difference of these two systems (MSU-MPACVD system II versus ASTeX PDS-17 MPECVD system), and (2) the higher temperature observed in MSU-MPACVD system II should lead to higher chemically active species concentrations and the MSU system II reactor may be more efficient. That is increases in gas temperature are expected to increase the dissociation of neutral gas species and produce higher chemically active species concentrations in the discharge. The measured temperature at the higher pressure regime probably explains why the film growth rates are higher when the gas temperature is higher.

## **8.5 Controlled Nitrogen Impurity Study By System II**

The addition of nitrogen impurities decrease the growth rate and the carbon conversion efficiency approximately 38%, and increases the specific yield approximately 68% as nitrogen impurity increases from a few ppm to 2500 ppm. Adding nitrogen impurity into the deposition process has no significant effect on film roughness. The films all have

featureless morphology and the films begin to look opaque. Therefore, the optical properties of the films have been changed. The molecular nitrogen becomes chemically active in the plasma discharge and it interacts with methane in the gas phase inside the plasma discharges.

## **8.6 Ultra-nanocrystalline Diamond Film Applications**

The study results of ultra-nanocrystalline diamond coatings as the IR optical transmission window have demonstrated that the ultra-nanocrystalline diamond has similar optical properties as high-quality diamond in this region of infrared wavelength. There is no visible IR-active single phonon absorption ( $1000\text{ cm}^{-1}$  to  $1500\text{ cm}^{-1}$ ) in measurements, therefore the films are absent of significant defects or impurities (The intrinsic optical properties of diamond are associated with the arrangement of the carbon atoms on a diamond lattice.).

A maximum of 89% is achieved by one layer both-side ultra-nanocrystalline diamond coated silicon substrates. In this research, two layered coatings do not show higher transmission than single layer because of the thickness of diamond films and  $\text{SiO}_2$  layers. The IR optical transmission is sensitive to the thickness of the coatings and the differences in thickness of both sides. With the aid of simulation by the theory, the design and fabrication of ultra-nanocrystalline diamond IR optical window at desired increment can be achieved.

The utility of as grown ultra-nanocrystalline diamond as a high frequency SAW device substrate material is demonstrated. The elastic properties of ultra-nanocrystalline

diamond and polycrystalline diamond are indistinguishable. The merits of a smooth surface, the absence of intergrain scattering, and the elastic isotropy give ultra-nanocrystalline diamond in the advantages over the polycrystalline diamond.

## **8.7 Recommendations for Future Research**

(1) The experimental work in this thesis indicates that a maximum deposition rate of 14.25 mg/hr ( $\sim 0.9 \mu\text{m/hr}$ ) was achieved at 220 torr. These experiments were limited to three inch diameter substrates. Thus, the process costs are still high for commercial applications of UNCD. It is useful to extend the process to larger substrate areas and higher deposition rates. Thus, future work should investigate the potential scale up of this methodology and process to six-eight inch diameter substrates and modify this process to increase the deposition rates. One potential method of increasing deposition rates is to try to deposit UNCD films at higher pressures.

(2) From the results of this thesis research, growth rate is essentially independent of total gas flow rate. However, the low-total-gas-flow-rate has higher carbon conversion efficiency and lower film roughness. More research in low or even lower total gas flow rate is recommended.

(3) In order to have a better understanding of the ultra-nanocrystalline diamond synthesis. More study of the relationship between internal variables, such as electron temperature, and input and output variables must be carried out.

(4) Using a heater substrate holder set-up to (i) allow the independent control of the substrate temperature, (ii) improve the growth rate, and (iii) improve the film quality at deposition pressure of 60-80 Torr. (At deposition pressure of 80 Torr, the testing results of heater showed 77% increases in growth rate and film roughness decreased from 26 nm to 12 nm.)

(5) A transitional interlayer exists between silicon substrate and ultra-nanocrystalline diamond film. Further probing using EELS (Electron Energy Loss Spectroscopy) is recommended to identify the nature of this interlayer.

(6) As the grain sizes decrease, there is an increasing fraction of the carbon atoms with complex bonding configuration resides in or near grain boundaries. It makes film structure quality determined by Raman ambiguous and undetermined most of the time. Therefore, determine the film quality of ultra-nanocrystalline diamond films with x-ray absorption spectroscopy is recommended.

(7) In addition to [Bi 2002], it is of interest to compare the propagation loss of SAW devices of ultra-nanocrystalline diamond with that of polycrystalline diamond.

(8) Develop a combined (i) gas chemistry growth steps or (ii) deposition pressure to synthesize smooth ultra-nanocrystalline diamond films efficiently.

(9) The SAD patterns indicate that ultra-nanocrystalline diamond has random orientation. However, the XRD results show mostly preferred (220) orientation. Neither SAD



pattern nor the X-ray two-theta scan is able to quantitatively determine the texture of the films. Therefore, to verify the texture of ultra-nanocrystalline diamond films quantitatively, a more detail study by X-ray pole figures and inverse pole figures is recommended.

## 9 Appendix

### 9.1 System I

$f_t$ : total gas flow rate

$p$ : pressure

$t$ : time

$T_s$ : substrate temperature

$P_{abs}$ : microwave power

$G_t$ : total growth rate

$G_{ave}$ : linear growth rate

$S$ : specific yield

$C$ : carbon conversion efficiency

RMS: root mean square surface roughness

$\frac{I(220)}{I(111)}$ : XRD ratio of integrated intensities of diamond <220> and <111> peaks

Experimental data for the experiments performed in systems I.

**TABLE 9.1: EXPERIMENT DATA FOR SYSTEM I**

Ar %	H <sub>2</sub> %	CH <sub>4</sub> %	$f_t$ sccm	$p$ Torr	$t$ hr	$T_s$ °C	$P_{abs}$ W	$G_t$ mg/hr	$G_{ave}$ μm/hr	$S$ kWh/g	$C$ %	RMS nm	$\frac{I(220)}{I(111)}$
98.68	0.99	0.33	304	120	8	794	717	0.238	0.015	3013	0.736	NA	0.06
98.52	0.99	0.49	203	120	8	815	719	0.163	0.010	4411	0.504	NA	0
98.04	1.47	0.49	204	120	8	810	756	0.463	0.029	1633	1.433	NA	0.12
98.04	1.47	0.49	408	120	8	870	867	0.325	0.020	2668	0.503	NA	0.25
97.56	1.95	0.49	102.5	120	8	788	832	0.588	0.037	1415	3.639	80	0.10
97.56	1.95	0.49	205	120	8	813	765	0.838	0.052	913	2.593	NA	0.16
97.56	1.95	0.49	205	120	8	806	741	0.725	0.045	1022	2.243	NA	0.12
97.56	1.95	0.49	307.5	120	8	790	702	0.750	0.047	936	1.547	NA	0.14
97.56	1.95	0.49	410	120	8	820	836	0.738	0.046	1133	1.142	NA	NA

**TABLE 9.1 (cont'd)**

Ar %	H <sub>2</sub> %	CH <sub>4</sub> %	f <sub>t</sub> sccm	p Torr	t hr	T <sub>s</sub> °C	P <sub>abs</sub> W	G <sub>t</sub> mg/hr	G <sub>ave</sub> μm/hr	S kWh/g	C %	RMS nm	I(220) I(111)
97.56	1.95	0.49	615	120	8	830	821	0.750	0.047	1095	0.774	NA	NA
97.56	1.95	0.49	615	120	8	807	839	0.763	0.048	1100	0.787	30	0.18
97.56	1.95	0.49	615	120	48	815	839	1.004	0.063	836	1.036	149	0.12
97.56	1.95	0.49	615	120	24	850	821	0.950	0.059	864	0.980	71	0.15
97.56	1.95	0.49	615	120	4	810	821	0.700	0.044	1173	0.722	NA	NA
97.56	1.95	0.49	615	120	4	840	858	0.675	0.042	1271	0.696	NA	NA
97.56	1.95	0.49	615	120	4	850	728	0.550	0.034	1324	0.567	NA	NA
97.56	1.95	0.49	615	120	4	830	802	0.675	0.042	1188	0.696	15	0.17
97.56	1.95	0.49	615	120	2	850	847	0.700	0.044	1210	0.722	14	0
97.56	1.95	0.49	615	120	1	815	847	0.500	0.031	1694	0.516	NA	NA
97.40	1.95	0.65	308	120	8	830	784	1.125	0.070	697	1.741	NA	0.23
97.32	1.95	0.73	616.5	120	8	830	865	1.038	0.065	833	0.714	NA	NA
97.09	1.94	0.97	206	120	8	900	821	2.025	0.126	405	3.134	NA	0.38
96.39	2.89	0.72	622.5	120	8	850	895	2.163	0.135	414	1.487	NA	0.20
96.39	2.89	0.72	622.5	120	8	850	899	2.313	0.144	389	1.590	NA	0.17
96.15	2.88	0.96	104	120	8	830	839	3.450	0.216	243	10.675	93	0.40
96.15	2.88	0.96	416	120	8	900	832	2.188	0.136	380	1.693	NA	0.26
96.15	2.88	0.96	624	120	8	823	821	2.838	0.177	289	1.464	90	0.24
95.24	3.81	0.95	105	120	8	844	858	4.625	0.289	186	14.311	NA	0.20
95.24	3.81	0.95	105	120	8	855	854	4.263	0.266	200	13.191	NA	0.10
95.24	3.81	0.95	105	120	8	850	858	4.625	0.289	186	14.311	96	0.47
95.24	3.81	0.95	105	120	8	850	873	4.438	0.277	197	13.733	NA	0.08
95.24	3.81	0.95	315	120	8	880	795	3.588	0.224	222	3.701	NA	0.16
95.24	3.81	0.95	630	120	8	875	795	3.525	0.220	226	1.818	119	0.20
93.46	5.61	0.93	642	120	8	845	876	7.238	0.452	121	3.733	NA	1.04
92.59	5.56	1.85	108	120	8	900	876	10.950	0.683	80	16.941	NA	2.74
92.59	5.56	1.85	108	120	8	890	925	11.325	0.707	82	17.522	NA	4.04
92.59	5.56	1.85	216	120	8	897	906	11.513	0.718	79	8.906	NA	3.93
90.91	7.27	1.82	110	120	8	850	888	12.963	0.809	69	20.056	NA	2.59

**TABLE 9.1 (cont'd)**

Ar %	H <sub>2</sub> %	CH <sub>4</sub> %	f <sub>t</sub> sccm	p Torr	t hr	T <sub>s</sub> °C	P <sub>abs</sub> W	G <sub>t</sub> mg/hr	G <sub>ave</sub> μm/hr	S kWh/g	C %	RMS nm	$\frac{I(220)}{I(111)}$
99.17	0.66	0.17	605	140	8	755	705	0.188	0.012	3750	0.582	NA	NA
97.56	1.95	0.49	102.5	140	8	840	828	1.100	0.069	753	6.808	NA	0.22
97.56	1.95	0.49	205	140	8	840	820	1.100	0.069	745	3.404	NA	0.17
97.56	1.95	0.49	307.5	140	8	845	816	1.025	0.064	796	2.114	NA	0.16
97.56	1.95	0.49	410	140	8	850	809	1.188	0.074	681	1.838	NA	0.17
97.56	1.95	0.49	615	140	8	830	784	1.238	0.077	633	1.277	43	0.19
97.56	1.95	0.49	615	140	24	825	705	1.625	0.101	434	1.676	94	NA
96.15	2.88	0.96	104	140	8	850	947	5.088	0.317	186	15.744	NA	1.16
96.15	2.88	0.96	208	140	8	904	956	4.888	0.305	196	7.563	NA	0.60
96.15	2.88	0.96	312	140	8	900	954	4.988	0.311	191	5.145	NA	0.46
96.15	2.88	0.96	416	140	8	950	932	4.888	0.305	191	3.781	NA	0.49
96.15	2.88	0.96	624	140	8	860	932	5.413	0.338	172	2.792	NA	0.34
95.24	3.81	0.95	105	140	8	867	956	7.163	0.447	133	22.165	NA	1.83
95.24	3.81	0.95	210	140	8	890	987	7.350	0.459	134	11.372	NA	1.99
95.24	3.81	0.95	315	140	8	888	965	6.950	0.434	139	7.169	NA	0.71
95.24	3.81	0.95	420	140	8	880	972	6.863	0.428	142	5.309	NA	0.63
95.24	3.81	0.95	630	140	8	885	965	7.100	0.443	136	3.662	NA	0.40
98.36	1.31	0.33	305	160	8	800	838	1.05	0.066	798	3.249	NA	NA
97.56	1.95	0.49	615	160	8	850	903	1.825	0.114	495	1.882	58	0.18
97.56	1.95	0.49	615	160	20	860	898	2.21	0.138	406	2.279	95	NA
96.15	2.88	0.96	208	160	8	910	1017	8.675	0.541	117	13.422	NA	3.62
95.24	3.81	0.95	105	160	8	900	959	10.788	0.673	89	33.382	NA	3.02

## 9.2 System II

Experimental data for the experiments reported in Section 4.3.

**TABLE 9.2: EXPERIMENT DATA FOR SYSTEM II**

Ar/H <sub>2</sub> /CH <sub>4</sub> sccm	p Torr	t hr	T <sub>s</sub> °C	P <sub>abs</sub> W	G <sub>t</sub> mg/hr	G <sub>ave</sub> μm/hr	S kWh/g	C %	RMS nm	$\frac{I(220)}{I(111)}$
100/10/1	120	8	619	902	5.400	0.337	167	16.709	44	1.81
100/8/1	120	8	659	977	5.263	0.328	186	16.285	41	2.62
100/6/1	120	8	637	977	4.538	0.283	215	14.042	37	2.66
600/24/6	120	8	637	942	3.925	0.245	240	2.024	82	0.13
400/16/4	120	8	630	898	4.038	0.252	222	3.124	81	0.14
300/12/3	120	8	621	898	3.875	0.242	232	3.997	75	0.33
200/8/2	120	8	629	907	3.538	0.221	256	5.474	54	1.23
600/12/6	120	8	605	926	3.025	0.189	306	1.560	34	0.64
400/8/4	120	8	607	871	3.038	0.189	287	2.350	34	1.05
300/6/3	120	8	596	871	3.025	0.189	288	3.120	33	1.00
200/4/2	120	8	600	878	2.738	0.171	321	4.236	17	4.17
100/4/1	60	8	UFL	768	0.375	0.023	2048	1.160	13	0
100/4/1	80	8	UFL	800	0.875	0.055	914	2.708	26	0.24
100/4/1	80	8	726*	851	1.55	0.097	549	4.796	12	0.50
100/4/1	100	8	UFL	847	1.888	0.118	449	5.842	19	0.71
100/4/1	120	8	626	945	3.800	0.237	249	11.758	24	1.19
100/4/1	120	8	650	973	3.663	0.228	266	11.335	25	NA
100/4/1	120	16	629	965	3.881	0.242	249	12.009	23	3.51
100/4/1	120	16	642	965	3.825	0.239	252	11.836	23	3.08
100/4/1	140	8	680	1053	6.413	0.400	164	19.844	25	5.01
100/4/1	160	8	709	1214	7.913	0.494	153	24.485	32	1.96

**TABLE 9.2 (cont'd)**

Ar/H <sub>2</sub> /CH <sub>4</sub> sccm	p Torr	t hr	T <sub>s</sub> °C	P <sub>abs</sub> W	G <sub>t</sub> mg/hr	G <sub>ave</sub> μm/hr	S kWh/g	C %	RMS nm	I(220) I(111)
100/4/1	160	8	697	1223	8.238	0.514	148	25.491	NA	NA
100/4/1	160	11	678	1246	7.873	0.491	158	24.362	36	NA
100/4/1	160	24	672	1139	8.658	0.540	132	26.791	50	NA
100/4/1	160	25	675	1181	7.936	0.495	149	24.557	47	NA
100/4/1	180	8	709	1361	9.850	0.614	138	30.479	33	2.69
100/4/1	200	8	770	1429	12.700	0.792	113	39.298	32	4.31
100/4/1	220	8	738	1405	14.250	0.889	99	44.094	47	3.85
100/4/1	240	8	730	1518	14.025	0.875	108	43.398	34	3.18
100/2/1	60	8	UFL	752	0.297	0.019	2532	0.919	24	0
100/2/1	80	8	UFL	772	0.395	0.025	1954	1.222	22	0.15
100/2/1	100	8	UFL	851	1.225	0.076	695	3.791	12	0.70
100/2/1	120	8	616	906	2.750	0.172	329	8.509	16	1.90
100/2/1	140	8	684	1017	5.813	0.363	175	17.987	21	6.42
100/2/1	160	8	696	1147	8.063	0.503	142	24.950	25	6.26
100/2/1	160	8	706	1160	7.575	0.473	153	23.440	NA	NA
100/2/1	180	8	681	1211	8.438	0.526	144	26.110	25	5.01
100/2/1	200	8	707	1310	10.588	0.660	124	32.763	26	3.71
100/2/1	220	8	692	1322	11.525	0.719	115	35.662	35	4.62
100/1/1	60	8	UFL	732	0.075	0.005	9760	0.232	17	0
100/1/1	80	8	UFL	768	0.289	0.018	2657	0.894	25	0
100/1/1	100	8	UFL	815	1.025	0.064	795	3.172	13	0.25
100/1/1	120	8	594	890	2.375	0.148	375	7.349	13	1.55
100/1/1	120	8	601	894	2.238	0.140	399	6.925	13	NA
100/1/1	140	8	621	1005	3.725	0.232	270	11.526	17	4.27
100/1/1	160	8	655	1119	5.388	0.336	208	16.672	19	3.48
100/1/1	180	8	665	1199	7.175	0.448	167	22.202	22	5.21

**TABLE 9.2 (cont'd)**

Ar/H <sub>2</sub> /CH <sub>4</sub> sccm	p Torr	t hr	T <sub>s</sub> °C	P <sub>abs</sub> W	G <sub>t</sub> mg/hr	G <sub>ave</sub> μm/hr	S kWh/g	C %	RMS nm	$\frac{I(220)}{I(111)}$
100/1/1	200	8	673	1251	8.825	0.551	142	27.307	22	5.58
100/1/1	200	8	677	1314	8.838	0.551	149	27.348	27	5.99
100/0/1	60	8	UFL	740	0.175	0.011	4229	0.542	27	0
100/0/1	80	8	UFL	772	0.288	0.018	2681	0.891	23	0
100/0/1	100	8	UFL	803	0.813	0.051	988	2.516	16	0.19
100/0/1	120	8	587	898	2.063	0.129	435	6.384	11	1.40
100/0/1	140	8	583	946	3.700	0.231	256	11.449	14	8.31
100/0/1	160	8	608	1037	4.988	0.311	208	15.435	13	9.31
100/0/1	180	8	625	1144	4.750	0.296	241	14.698	17	3.92
100/0/1	200	8	611	1227	5.300	0.331	232	16.400	18	3.94
100/0/1	200	8	604	1220	6.038	0.377	202	18.684	18	4.46

\*: Temperature was measured by thermal couple and the experiment was performed with heated stage.

**TABLE 9.3: CONTROLLED N<sub>2</sub> IMPURITY STUDY BY SYSTEM II**

Ar/H <sub>2</sub> /CH <sub>4</sub> sccm	f <sub>t</sub> sccm	N <sub>2</sub> ppm	t hr	T <sub>s</sub> °C	P <sub>abs</sub> W	G <sub>t</sub> mg/hr	G <sub>ave</sub> μm/hr	S kWh/g	C %	RMS nm	$\frac{I(220)}{I(111)}$
100/4/1	105	5	8	626	945	3.800	0.237	249	11.758	24	1.19
100/4/1	105	100	8	646	957	3.813	0.238	251	11.799	21	1.27
100/4/1	105	200	8	640	969	2.925	0.182	331	9.051	20	0.63
100/4/1	105	300	8	645	969	3.388	0.211	286	10.484	20	1.21
100/4/1	105	600	8	645	969	3.225	0.201	300	9.979	21	0.86
100/4/1	105	800	8	642	969	3.000	0.187	323	9.283	21	0.65
100/4/1	105	1200	8	645	957	2.775	0.173	345	8.587	24	0.36
100/4/1	105	1500	8	646	973	2.625	0.164	371	8.123	23	0.51
100/4/1	105	2000	8	636	981	2.563	0.160	383	7.931	21	0.73
100/4/1	105	2500	8	625	985	2.350	0.147	419	7.272	18	0.81



## 9.3 OES

Experimental data for the OES measurements reported in Chapter 6.

**TABLE 9.4: OES DATA**

Ar/H <sub>2</sub> /CH <sub>4</sub> (sccm)	Pressure (Torr)	P <sub>abs</sub> (W)	C <sub>2</sub> (a.u.)	T <sub>g</sub> (K)
100/0/1	60	681	1.36	1975
100/0/1	80	744	2.54	2000
100/0/1	100	803	2.28	2150
100/0/1	120	831	3.69	2205
100/0//1	140	946	9.61	2345
100/0/1	160	1041	24.17	2450
100/0/1	180	1152	20.05	2540
100/0/1	200	1259	13.96	2565
100/1/1	60	721	1.92	2005
100/1/1	80	768	2.47	2140
100/1/1	100	831	4.26	2165
100/1/1	120	871	6.4	2260
100/1//1	140	986	21.63	2420
100/1/1	160	1080	46.58	2510
100/1/1	180	1164	78.14	2530
100/1/1	200	1259	88.44	2595
100/2/1	60	721	1.29	2100
100/2/1	80	772	1.99	2110
100/2/1	100	835	4.25	2205
100/2/1	120	878	8.86	2335
100/2//1	140	994	19.87	2430
100/2/1	160	1104	47.26	2525
100/2/1	180	1183	83.41	2595
100/2/1	200	1259	125.66	2690
100/2/1	220	1334	157.59	2730

**TABLE 9.4 (cont'd)**

Ar/H <sub>2</sub> /CH <sub>4</sub> (sccm)	Pressure (Torr)	P <sub>abs</sub> (W)	C <sub>2</sub> (a.u.)	T <sub>g</sub> (K)
100/4/1	80	809	0.83	2140
100/4/1	100	869	2.86	2205
100/4/1	120	908	7.88	2355
100/4//1	140	1033	18.09	2445
100/4/1	160	1151	40.59	2595
100/4/1	180	1242	79.2	2685
100/4/1	200	1338	81.54	2785
100/4/1	220	1413	82.63	2845
100/4/1	240	1520	64.57	2960
100/0/1	120	851	2.75	2215
100/1/1	120	863	4.23	2220
100/2/1	120	871	5.74	2270
100/4/1	120	894	5.6	2340
100/6/1	120	908	5.22	2585
100/8/1	120	922	4.46	2680
100/10/1	120	934	3.31	2745
100/4/1	120	908	3.87	2315
200/8/2	120	908	4.33	2375
300/12/3	120	908	4.5	2340
400/16/4	120	908	4.28	2330
600/24/6	120	908	4.64	2295

**TABLE 9.5: CN STUDY**

Ar/H <sub>2</sub> /CH <sub>4</sub> (Sccm)	N <sub>2</sub> (ppm)	Pressure (Torr)	P <sub>abs</sub> (W)	CN
100/4/1	0	120	908	0.18
100/4/1	25	120	908	0.28
100/4/1	50	120	908	1.05
100/4/1	100	120	908	3.16
100/4/1	200	120	908	6.52
100/4/1	300	120	908	10.84
100/4/1	600	120	908	14.82
100/4/1	800	120	908	16.74
100/4/1	1200	120	908	21.08
100/4/1	1500	120	908	26.55

## 9.4 Gas Temperature Measurements

Matlab program used for fitting the R25 to R45 emission lines to the experimental data in determining the rotational temperature.

```
%Calculation of the intensity of the optical emission spectrum
```

```
%Rotational quantum number J
```

```
%Bvu and Bvg molecular constant ( $\text{cm}^{-1}$ )
```

```
%
```

```
a=zeros(90);
```

```
lam=zeros(90);
```

```
for J=1:90
```

```
    Jp=J;
```

```
    Jpp=Jp-1;
```

```
    Bvu=1.7456;
```

```
    Bvg=1.62405;
```

```
    nu=Bvu*Jp*(Jp+1)-Bvg*Jpp*(Jpp+1); %( $\text{cm}^{-1}$ )
```

```
    h=6.63*10(-34); % (Joule*sec)
```

```
    center=5165.2*10(-10); %wavelength (m)
```

```
    cencm=5165.2*10(-8); %wavelength (cm)
```

```
    nucen=1/cencm; %wavenumber ( $\text{cm}^{-1}$ )
```

```
    em=nucen+nu; %( $\text{cm}^{-1}$ )+( $\text{cm}^{-1}$ )
```

```
    lambda=1/em; % (cm)
```

```
    ang=lambda*1.0*10(8);
```

```

S=(J+1)*(J-1)/J;

c=3.0*10^(8);      %(m/sec)

nu1=Bvu*Jp*(Jp+1);

En=100.0*h*c*nu1;

k=1.38*10^(-23);    %[Joule*(K)^(-1)]

T=2500.0;

arg=exp(-En/(k*T));

amp=S*arg;          %Intensity

a(J)=amp;

lam(J)=ang;

end

plot(lam,a,'k.', lam,a,'g-')

```

## 9.5 X-ray Diffraction Crystallography

The most outstanding fact which x-ray diffraction technique has revealed about crystals is that they are composed of atoms arranged in a pattern periodic in three dimensions. Unlike amorphous materials, a crystal has constant interplanar spacing  $d_{hkl}$  which is a function both of the plane indices (hkl) and the lattice constants of the crystal. From the Bragg's law (The diffraction directions are solely determined by the size and shape of the unit cell of the crystal.):

$$n\lambda = 2d\sin\theta \quad (9.1)$$

$n$ : order of reflection,  $n=1,2,3,\dots$  ( $n=0$ , the diffracted beam is in the same direction as the transmitted beam. It can not be observed.)

$\lambda$  : wavelength of the light source

$d$ : interplanar spacing

$\theta$  : incident and reflected angles

With x-ray of known wavelength  $\lambda$ , varying incident angle  $\theta$ , and measuring peaks, then we can determine the unknown spacing of crystal planes. The intensities of the diffracted beams which are corresponding to the structure factor of the crystal are the resultant wave scattered by all the atoms of the unit cell of that crystal. Comparing the peak-position information of our samples in the intensity versus  $2\theta$  plot ( $2\theta$ : the angle between diffracted beam and transmitted) which were obtained by the diffraction analysis with a x-ray diffractometer to ASTM (American Society for Testing Materials) Inorganic

Powder Diffraction File, we can identify the diamond peaks to prove the presence of the diamond in the films. The different intensity ratio of the peaks to the powder diffraction file can be an indicate of crystal orientation/texture of the films.

The x-ray diffractometer at Chemistry department of MSU is a Rigaku 200 rotating anode powder diffractometer with maximum power: 60 kV and maximum current: 200 mA.

## **9.6 Atomic Force Microscopy**

TappingMode AFM operates by scanning a tip attached to the end of an oscillating cantilever across the sample surface. The cantilever is oscillated at or near its resonance frequency and it can be on either side of the resonant frequency. During scanning, the tip lightly taps on the sample surface, contacting the surface at the bottom of its swing. The tip undergoes deflections as it is scanning along the sample surface. The deflection is detected by a laser light from a solid state diode which is reflected off the back of the cantilever and collected by a position sensitive detector consisting of two closely spaced photodiodes whose output signal is collected by a differential amplifier. Angular displacement of cantilever results in one photodiode collecting more light than the other photodiode, producing an output signal (the difference between the photodiode signals normalized by their sum) which is proportional to the deflection of the cantilever. By maintaining a constant RMS of the oscillation signal acquired by the split photodiode detector, the feedback loop maintains a constant oscillation amplitude. The topographic image of the sample is formed by the vertical position of the scanner at each (x,y) data

point in order to maintain a constant setpoint amplitude. A constant tip-sample interaction is maintained during imaging by maintaining a constant oscillation amplitude.

The probes used in this research were TESP (TappingMode Etched Silicon Probe) which had nominal tip radius of curvature of 5 -10 nm. For this thesis research, 5  $\mu\text{m}$  x 5  $\mu\text{m}$  images were acquired with the number of samples parameter set to 512, then the pixel size is 9.8 nm ( $5 \mu\text{m}/512 = 0.0098 \mu\text{m} = 9.8 \text{ nm}$ ). Thus, the features smaller than 9.8 nm will not be resolved. The vertical resolution is affected by the conversion of 16 bits over the vertical range of the scanner. For example, a scanner may have a full vertical movement of 6  $\mu\text{m}$  over 440 V. By reducing the Z-limit to 110V, the full vertical movement of the scanner reduced to 1.5  $\mu\text{m}$  over the same 16 bits. There, the Z resolution is increased by the smaller vertical sample size.

The AFM system at KMF (W. M. Keck Microfabrication Facility at Michigan State University, a NSF MRSEC facility) at PHY department of MSU is a SPM (Scanning Probe Microscopy) model DI D3100.



## 10 References:

- [Angu] J.C.Angus, H.A.Will, and W.S.Stanko, J. Appl. Phys. 39, 2915 (1968).
- [Angu] J.C.Angus, F.A.Buck, M.Sunkara, T.F. Groth, C.C. Hayman, and R. Gat, "Diamond Growth at Low Pressures," MRS Bulletin, pp38-47, Oct.1989.
- [Angu] J.C.Angus, C.C.Hayman, and R.W.Hoffman, in Diamond Optics, SPIE Proceedings, 969, Intl. Soc. For Optical Engineering, Bellingham, Washington, 2, 1988.
- [Asma] M.Asmann, J.Heberlein, and E.Pfender, Diamond Relat. Mater. 5,1, 1999.
- [Asma] M.Asmann, R.F.Cook, J.V.Heberlein, and E.Pfender, J. Mater. Res. 16, 469, 2001.
- [Asmu] J.Asmussen, J.Mossbrucker, S.Khatami, W.S.Huang, B.Wright, and V.Ayres, "The effect of nitrogen on the growth, morphology, and crystalline quality of MPACVD diamond films," diamond and Related Materials 8: 220-225, 1999.
- [Asmu] J.Asmussen and W.S.Huang,"Process For Synthesizing Uniform Nanocrystalline Diamond," Practitioner's Docket Nd. MSU 4.1-572 (ID01-060).
- [Asso] M.B.Assouar, F.Benedic, O.Elmazria, M.Belmahi, R.J.Rioboo, and P.Alnot, "MPACVD Diamond Films for Surface Acoustic Wave filters," Diamond and Related Materials 10(3-7): 681-685, 2001.
- [Bach] P.K.Bachmann, D.Leers, and H.Lydtin, "Towards a general concept of diamond chemical vapor deposition", Diamond and Related Materials, Vol. 1, pp.1-12, (1991).
- [Batt] C.C.Battaile, D.J.Srolovitz, and J.E.Butler, "Morphologies of Diamond Films From Atomic-Scale Simulations of Chemical Vapor Deposition," Diamond and Related Materials, Vol. 6(9): 1198-1206,1997.
- [Begh] M.G.Beghi, A.C.Ferrari, C.E.Bottani, A.Libassi, B.K.Tanner, K.B.K.Teo, J.Robertson, "Elastic constants and structural properties of nanometer-thick diamond-like carbon films," Diamond and Related Materials 11(3-6): 1062-1067, 2002
- [Begh] M.G.Beghi, C.S.Casari, A.L.Bassi, C.E.Bottani, A.C.Ferrari, J.Robertson, and P.Milani, "Acoustic phonon propagation and elastic properties of nano-sized carbon films investigated by Brillouin light scattering," Thin Solid Films, 420-421, pp.300-305, 2002.

- [Bhus] D.M.Bhusari, J.R.Yang, T.Y.Wang, K.H.Chen, S.T.Lin, and L.C.Chen, "Effects of substrate pretreatment and methane fraction on the optical transparency of nanocrystalline diamond thin films," *Journal of Materials Research*, 13(7): 1769-1773, 1998.
- [Bi] B.K.Bi, B.Golding, W.S.Huang, and J.Asmussen, "Surface Acoustic Wave Devices Based on Unpolished Nanocrystalline Diamond," *Practitioner's Docket* Nd. MSU 4.1-571 (ID01-061).
- [Bi] B.K.Bi, W.S.huang, J.Asmussen, and B.Golding, "Surface Acoustic Wave on Nanocrystalline Diamond," *Diamond and Related Materials* 11(3-6), 677-680, 2002.
- [Bogl] U.Bogli, A.Blatter, S.M.Pimenov, E.D.Obratzsova, A.A.Smolín, M.Maillat, A.Leijala, J.Burger, H.E.Hintermann, E.N.Loubnin, "Tribological Properties of Smooth Polycrystalline Diamond Films," *Diamond and related Materials* 4(7): 1009-1019, 1995.
- [Butl] J.E.Butler, R.L.Woodin, *Philos. Trans. R. Soc. London Ser. A* 342, (1993), pp.209-224.
- [Case] M.Casey and J.Wilks, "Friction of Diamond Sliding on Polishing Cube Faces of Diamond," *J. Phys. D: Appl. Phys.* 6(15): 1772-1781, 1973.
- [Chen] L.C.Chen, P.D.Kichambare, K.H.Chen, J.J.Wu, J.R.Yang, and S.T.Lin, "Growth of highly transparent nanocrystalline diamond films and a spectroscopic study of the growth," *Journal of Applied Physics*, 89(1): 753-759, 2001.
- [Chen] Y.Y.Chen, T.T.Wu, and T.T.Chou, "Analysis of the frequency response of a dispersive IDT/ZnO/sapphire SAW filter using effective permittivity and the coupling of modes model," *J. Phys. D: Appl. Phys.* 37, pp.120-127, 2004.
- [Clay] K.J.Clay, S.P.Speakman, G.A.J.Amaratunga, and S.R.P.Silva, "Characterization of a-C:H:N Deposition from CH<sub>4</sub>/N<sub>2</sub> RF Plasmas Using Optical Emission Spectroscopy," *J. Appl. Phys.* 79(9), 7227, 1996.
- [Coll] C.B.Collins, F.Davanloo, T.J.Lee, J.H.You, and H.Park, in *Laser Ablation in Materials Processing: Fundamentals and Applications*, edited by B.Braren, J.J.Dubowski, and D.Norton (Mater. Res. Soc. Symp. Proc. 285, pp. 547, Pittsburgh, PA, 1993).
- [Coll] C.B.Collins, F.Davanloo, J.H.You, and H.Park, in *Laser Applications*, edited by A.A.Mak, SPIE Proc. 2097, pp.129, 1994.

- [Csen] R.Csencsits, D.M.Gruen, A.R.Krauss, and C.Zuiker, "TEM Study of Diamond Films Grown From Fullerene Precursors," *Mat. Res. Soc. Symp. Proc.* Vol. 403, pp.291-296, 1996.
- [Dava] F.Davanloo, H.Park, and C.B.Collins, "Protective coatings of nanophase diamond deposited directly on stainless steel substrates," *Journal of Materials Research*, 11(8): 2042-2050, 1996.
- [Derj] B.V.Derjaguin, D.V.Fedosseev, V.M.Lukyanovich, B.V.Spitsyn, V.A.Ryabov, and A.V.Lavrentyev, *J. Cryst. Growth* 2, 380 (1968).
- [Diam] Abstracts, 14<sup>th</sup> European Conference on Diamond, Diamond-Like Materials, Carbon Nanotubes, Nitrides & Silicon Carbide, 2003.
- [Endl] I.Endler, K.Bartsch, A.Leonhardt, H.J.Scheibe, H.Ziegele, I.Fuchs, C.Raatz, "Preparation and wear behavior of woodworking tools coated with superhard layers," *Diamond and Related Materials*, 8(2-5): 834-839, 1999
- [Erde] A.Erdemir, C.Bindal, G.R.Fenske, C.Zuiker, R.Csencsits, A.R.Krauss, D.M.Gruen, "Tribological characterization of smooth diamond films grown in Ar-C-60 and Ar-CH<sub>4</sub> plasmas," *Diamond films and Technology*, 6(1): 31-47 1996
- [Erde] A.Erdemir, G.R.Fenske, A.R.Krauss, D.M.Gruen, T.McCauley, and R.T.Csencsits, "Tribological properties of nanocrystalline diamond films," *Surf. Coat. Technol.* 121: 565-572, 1999.
- [Erz] R.Erz, W.Dotter, K.Jung, and H.Ehrhardt, "Preparation of smooth and nanocrystalline diamond films," *Diamond and Related Materials*, 2, pp.449-453, 1993.
- [Ever] W.G.Eversole, U.S. Patent No. 3030188, 23.07.1958.
- [Ferr] A.C.Ferrari, J.Robertson, "Elastic constants of tetrahedral amorphous carbon films by surface Brillouin scattering," *Applied Physics Letters* 75(13): 1893-1895, 1999.
- [Gabl] J.Gabler, L.Schafer, and H.Westermann, *Diamond Relat. Mater.* 9, 921, 2000.
- [Gayd] A.G.Gaydon, "Dissociation Energies and Spectra of Diatomic Molecules," London, Chapman and Hall LTD, 1968.
- [Gicq] A.Gicquel, K.Hassouni, Y.Breton, M.Chenevier, and J.C.Cubertafo, "Gas Temperature Measurements by Laser Spectroscopic Techniques and by Optical Emission Spectroscopy," *Diamond and Related Materials* 5, 366, 1996.

- [Good] D.G.Goodwin, J.E.Butler, in: M.A. Prelas, G.Popovia, L.K.Bigelow (Eds.), Handbook of Industrial Diamonds and Diamond Films, Marcel Dekker. New York, 1996, pp.1-70.
- [Goy1] A.N.Goyette, J.E.Lawler, L.W.Anderson, D.M.Gruen, T.G.McCauley, D.Zhou, and A.R.Krauss, "C<sub>2</sub> Swan Band Emission Intensity as A Function of C<sub>2</sub> Density", Plasma Sources Sci. Technol. 7, pp.149-153, 1998.
- [Goy2] A.N.Goyette, J.E.Lawler, L.W.Anderson, D.M.Gruen, T.G.McCauley, D.Zhou, and A.R.Krauss, "Spectroscopic Determination of Carbon Dimer Density in Ar-H<sub>2</sub>-CH<sub>4</sub> and Ar-H<sub>2</sub>-C<sub>60</sub> plasmas", J. Phys. D: Appl. Phys. vol. 31, pp.1975-1986, 1998.
- [Grim] M.H.Grimsditch, Anastassakis, E. and Cardona, M.; Phys. Rev. B 5 p 580 (1978)
- [Grae] J.E.Graebner, S.Jin, G.W.Kammlott, B.Bacon, L.Seibles, and W. Banholzer, Anisotropic, "Thermal Conductivity in Chemical Vapor Deposition Diamond," J. Appl. Phys., 71(11): 5353-5356, 1992.
- [Grot] T. Grotjohn, "A Review of CVD Diamond Research," 1994.
- [Grot] T.A.Grotjohn, W.S.Huang, J.Sivagnaname, J.Asmussen, D.Story, 'Plasma Diagnostic Measurements and Numerical Modeling of Argon-Hydrogen-Methane Discharges used for Nanocrystalline Diamond Deposition in a Microwave CVD System,' 10<sup>th</sup> European Conference on Diamond, Diamond-Like Materials, Carbon Nanotubes, Nitrides & Silicon Carbide, 1999.
- [Grue] Deter M.Gruen, Xianzheng Pan, Alan R.Krauss, Shengzhong Liu, Jianshu Luo, and Christopher M.Foster, J. Vac. Sci. Technol. A 12(4), Jul/Aug 1994.
- [Grue] D.M.Gruen, C.D.Zuiker, A.R.Krauss, and X.Pan, "Carbon dimer, C<sub>2</sub>, as a growth species for diamond films from methane/hydrogen/argon microwave plasmas," J. Vac. Sci. Technol. A 13(3), pp.1628-1632, 1995.
- [Grue] D.M.Gruen, P.C.Redfern, D.A.Horner, P.Zapol, and L.A.Curtiss, "Theoretical studies on nanocrystalline diamond: Nucleation by dicarbon and electronic structure of planar defects," J. Phys. Chem., B, 103(26): 5459-5467, 1999.
- [Hami] D.R.Hamilton and R.G.Seidensticker, J. Appl. Phys. 34, 1450 (1960).
- [Hayw] I.P.Hayward, I.L.Singer, L.E.Seitzman, "Effect of Roughness on The Friction of Diamond on CVD Diamond Coatings," Wear, 157(2): 215-227, 1992
- [Herz] G.Herzberg, "Spectra of Diatomic Molecules," New York: Van Nostrand Reinhold, 1950.

- [Higa] K.Higaki, H.Nakahata, H.Kitabayashi, S.Fujii, K.Tanabe, Y.Seki, and S.Shikata, "High Power Durability of Diamond Surface Acoustic Wave Filter," IEEE TRansactions on Ultrasonics Ferroelectrics and Frequency Control 44(6): 1395-1400, 1997.
- [Holl] P.Hollman, A.Alahelisten, T.Bjork, S.Hogmark, "CVD-Diamond Coatings in Sliding Contact With AL, AL-17SI and Steel," Wear 179(1-2): 11-16, 1994.
- [Holl] P.Hollman, O.Wanstrand, S.Hogmark, "Friction Properties of smooth nanocrystalline diamond coatings," Diamond and Related Materials, 7: 1471-1477, 1998.
- [Hong] T.M.Hong, S.H.Chen, Y.S.Chiou, and C.F.Chen, "Optical Emission Spectroscopy Studies of the Effect of Nitrogen Addition on Diamond Synthesis in a CH<sub>4</sub>-CO<sub>2</sub> Gas Mixture," Appl. Phys. Lett. 67(15), 2149, 1995.
- [Hong] S.P.Hong, H.Yoshikawa, K.Wazumi, Y.Koga, "Synthesis and tribological characteristics of nanocrystalline diamond film using CH<sub>4</sub>/H-2 microwave plasmas," Diamond and Related Materials, 11(3-6): 877-881, 2002.
- [Huan] W.S.Huang, J.Asmussen, B.Wright, D.M.Gruen, S.L.Jiao, A.R.Krauss, A.Sumant, M.A.Crimp, and L.Zeng, "Microwave-Plasma Assisted Chemical Vapor Deposition of Ultra-Nanocrystalline Diamond Films", CFMR 2000 Conference.
- [Huan] W.S.Huang, J.Asmussen, B.Wright, A.R.Krauss, D.M.Gruen, and A.Sumant, "The Deposition of Ultra-Nanocrystalline Diamond Films Using a Ar/H<sub>2</sub>/CH<sub>4</sub> Microwave Discharge", ICOP 2000 Conference.
- [Huan] W.S.Huang, J.Asmussen, T.A. Grotjohn, D.M.Gruen, S.L.Jiao, A.R.Krauss, and A.Sumant, "Microwave-Plasma Assisted Chemical Vapor Deposition of Nanocrystalline Diamond Films", NSF-MRSEC 2001.
- [Jian] X.Jiang, "Rayleigh mode in amorphous hydrogenated carbon films," Physical Review B 43(3), 2372-2377, 1991.
- [Jiao] S.L.Jiao, "JiaoWorkSummary-DEC99", Two cross-section TEM dark field images of the MSU-nanocrystalline diamond film with SAED (Selected Area Electron Diffraction) patterns were taken. The SAED pattern in diamond was obtained from a selected area including the cone-shaped feature. The arcs on the rings strongly indicate the material is textured. By forming a dark field image with the arc (by selecting the marked spot on the (111) ring), these oriented grains are located and shown uniformly distributed inside the cone-shaped object. It's intrigue to observe that nanocrystalline diamond crystals have the tendency to agglomerate to form the oriented texture. Unpublished.

- [Kani] D.R.Kania, M.I.Landstrass and M.A.Plano, "Diamond Radiation Detectors," *Diamond and Related Materials*, 2 (1993), pp1012-1019.
- [Khat] Saeid Khatami: *Controlled synthesis of diamond films using a microwave discharge (Non-equilibrium plasma)*, Ph. D. thesis at the Michigan State University, Department of Electrical Engineering (1997).
- [Klei] I. R.Kleindienst: Master Thesis at the Michigan State University, Department of Electrical Computer Engineering 1999.
- [Knig] D.S.Knight, W.B.White, "Characterization of diamond films by Raman spectroscopy," *J. Materials Research*, Vol. 4, No. 2, 1989, pp.385-393.
- [Kohz] M.Kohzaki, S.Noda, *Diamond Films Technol.* 3(3) 135, 1994.
- [Kond] K.Kondo, S.Sawai, "Fabricating Nanocrystalline Diamond Ceramics by A Shock Compaction Method," *Journal of The American Ceramic Society*, 73 (7): 1983-1991, 1990.
- [Kono] V.I.Konov, A.A.Smolín, V.G.Ralchenko, S.M.Pimenov, E.D.Obratsova, E.N.Loubnin, S.M.Metev, and G.Sepold, "D.C. arc plasma deposition of smooth nanocrystalline diamond films," *Diamond and Related Materials*, 4, pp.1073-1078, 1995.
- [Kuo] K.P.Kuo and J.Asmussen, *Diamond Relat. Mater.* 6, 1907 (1992).
- [Kuo] Kuo-Ping Kuo: *High pressure synthesis of diamond films using microwave cavity plasma reactor*, Ph. D thesis at the Michigan State University, Department of Electrical Engineering (1997).
- [Lee] S.T.Lee, Z.Lin, and X.Jiang, *Mater. Sci. Eng. R* 25, 123, 1999.
- [Li] J.Q.Li, D.Y.He, W.T.Guo, J.H.Zhang, Y.I.Sun, Q.S.Lei, and X.Gao, "Nanocrystalline Diamond Thin films As Infrared Optical Protective Coatings," *International Journal of Modern Physics B*, 16(6-7): 1013-1017, 2002.
- [Lin] T.Lin, G.Y.Yu, A.T.S.We, Z.X.Shen, and K.P.Loh, "Compositional mapping of the argon-methane-hydrogen system for polycrystalline to nanocrystalline diamond film growth in a hot-filament chemical vapor deposition system," *Applied Physics Letters*, 77(17): 2692-2694, 2000.
- [Liu] Huimin Liu and David S. Dandy, *Diamond Chemical Vapor Deposition*, Noyes Publications, 1995.
- [Luo] J.S.Luo, D.m.Gruen, and A.R.Krauss, X.Z.Pan, S.Z.Liu, *Electrochemical Society Proceedings Volume* 95-10.

- [Mats] S.Matsumoto, Y.Sato, M.Kamo, N.Setaka, "Vapor deposition of diamond particles from methane", Jpn. J. Appl. Phys. 21, part2, 1982, pp. L183-185.
- [May] Paul W. May "CVD Diamond - a new Technology for the future", Endeavour Magazine 19 (3), 1995 pp. 101-106.
- [McCa] T.G.McCauley, D.M.Gruen, and A.R.Krauss, "Temperature dependence of the growth rate for nanocrystalline diamond films deposited from Ar/CH<sub>4</sub> microwave plasma," Appl. Phys. Lett. Vol. 73, No. 12, 1998, pp.1646-1648.
- [Mirt] M.Mirtich, J. C.Angus, "Dual ion beam deposition of carbon films with diamondlike properties," National Aeronautics and Space Administration, Washington D. C. (1984).
- [Miyoi] K.Miyoshi, R.L.C.WU, A.Garscadden, P.N.Barnes, H.E.Jackson, "Friction and Wear of Plasma-Deposited Diamond Films," Journal of Applied Physics, 74 (7): 4446-4454, 1993
- [Mori] Y.Mori, H.Yagi, M.Deguchi, M.Kitabatake, K.Nishimura, A.Hatta, T.Ito, T. Hirao, T.Sasaki, and A.Hiraki, "Crystallinities and electrical properties of homoepitaxial diamond films grown from carbon monoxide", 2nd Int. Conf. on the appli. of Diamond Films and Related Materials. Yoshikawa, Vol. 2, Tokyo, Japan, 1993, pp393-398.
- [Mori] T.Morita, K.Banshoya, T.Tsutsumoto, and Y.Murase, "Effects of Work Materials on cutting performance of diamond0coated cemented carbide tools," Forest Products Journal, 48(5): 43-50, 1998.
- [Moss] J.Mossbrucker: Polarized Raman Spectra of diamond films, Dissertation at the Kaiserslautern University (1997).
- [Moss] EMISSION.BAS, 03-04-1998.
- [Moss] J.Mossbrucker, S.Khatami, W.S.Huang, B.Wright, V.Ayres, and J.Asmussen,"The Effect of Nitrogen on the Growth, Morphology, and Crystalline Quality of MPACVD Diamond Films," Diamond and Related Materials 8 (2-5): 220-225, 1999.
- [Naka] H.Nakahata, K.Higaki, A.Hachigo, S.Shikata, N.Fujimori, Y.Takahashi, T.Kajihara, and Y.Yamamoto, "High-Frequency Surface-Acoustic-Wave Filter Using ZnO/Diamond/Si Structure," Japanese Journal of Applied Physics Part1-Regular Papers Short notes & Review Papers, 33(1A): 322-328, 1994.
- [Naka] H.Nakahata, A.Hachigo, K.Higaki, S.Fujii, S.I.Shikata, and N.Fujimori, "Theoretical Study on SAW Characteristics of Layered Structures Including a Dia-

mond Layer," IEEE Transactions on Ultrasonics Ferroelectrics and Frequency Control 42(2): 362-375, 1995.

- [Naka] H.Nakahata, H.Kitabayashi, T.Uemura, A.Higaki, S.Fujii, Y.Seki, K.Yoshida, and S.Shikata, "Study on Surface Acoustic Wave Characterization of SiO<sub>2</sub>/interdigital-transducer/ZnO/Diamond Structure and Fabrication of 2.5 GHz Narrow Band Filter," Japanese Journal of Applied Physics Part1-Regular Papers Short notes & Review Papers, 37(5B): 2918-2922 Sp. Iss. SI 1998.
- [Naka] H.Nakahata, S.Fujii, K.Higaki, A.Hachigo, H.Kitabayashi, S.Shikata, and N.Fujimori, "Diamond-based surface acoustic wave devices," Semiconductor Science and Technology, 18, S96-S104, 2003.
- [Neer] D.Neerinck, P.Persoone, M.Sercu, and A.Goel, Thin Solid Film 317, 402, 1998.
- [Nied] P.Niedzielski, S.Miklaszewski, P.Beer, and A.Sokolowska, "Tribological properties of NCD coated cemented carbides in contact with wood," Diamond and Related Materials, 10(1): 1-6, 2001.
- [Nist] L.C.Nistor, J.Van Landuyt, V.G.Ralchenko, E.D.Obraztsova, and A.A.Smolín, "Nanocrystalline diamond films: transmission electron microscopy and Raman spectroscopy characterization," Diamond and related Materials, 6, pp.159-168, 1997.
- [Nuss] A.Nussbaum and R.A.Phillips, "Contemporary Optics for Scientists and Engineers", Prentice Hall Inc, Englewood Cliff, NJ 1976, pp.191.
- [Ong] T.P.Ong and R.P.H.Chang, "Low-temperature deposition of diamond films for optical coating," Appl. Phys. Lett., 55(20): 2063-2065, 1989.
- [Orr] R.Orr, "The impact of thin film diamond on advanced engineering systems," presented at the global business and technical outlook for high performance inorganic thin film coatings, Gorham advanced materials institute, Monterey, California, Oct.30-Nov.1,1988.
- [Pan] L.S.Pan, S.Han, D.R.Kania, M.A.Plano, and M.I.Landstrass, "Electrical Properties of High Quality Diamond Films", Diamond and Related Materials, Vol. 2, 1993, pp820-824.
- [Pier] H.O.Pierson, Handbook of Carbon, Graphite, Diamond and Fullerenes, Noyes Publications, Park Ridge, New Jersey 1993.
- [Pras] C.V.V.Prasad and P.F.Bernath, "Fourier Transform Spectroscopy of The Swan ( $d^3\Pi_g-a^3\Pi_u$ ) System of The Jet-Cooled C<sub>2</sub> Molecule", Astrophys. J., Vol. 426, pp.812-821, 1994.



- [Qadr] S.B.Qadri, C.Kim, E.F.Skelton, T.Hahn, and J.E.Bulter, "Thermal Expansion of Chemical Vapor Deposition Grown Diamond Film, Thin Solid Films, 236(1-2): 103-105, 1993.
- [Qin] L.C.Qin, D.Zhou, A.R.Krauss, and D.M.Gruen, NanoStructure Materials, Vol.10, No.4, pp.649-660, 1998.
- [Rang] S.Ranganathan, Acta. Crystallogr. 21, 197, 1966.
- [Redf] P.C.Redfern, D.A.Horner, L.A.Curtiss, and D.M.Gruen, "Theoretical Studies of Growth of Diamond (110) from Dicarbon," J. Phys. Chem. 100(28): pp.11654-11663, 1996.
- [Rein] D.K.Reinhard and I.R.Kleindienst, "Diamond films as optical coatings for silicon," New Diamond and Frontier Carbon Technology 10(1): 13-23, 2000.
- [Shar] T.Sharda, M.M.Rahaman, Y.Nukaya, T.Soga, T.Jimbo, and M.Umeno, "Structural and optical properties of diamond and nano-diamond films grown by microwave plasma chemical vapor deposition," Diamond and Related Materials, 10, pp.561-567, 2001.
- [Shar] T.Sharda, T.Soga, and T.Jimbo, "Optical properties of nanocrystalline diamond films by prism coupling technique," J. Appl. Phys., 93(1): 101-105, 2003.
- [Shio] Hiromu Shiomi, Keiichirou Tanabe, Yoshiki Nishibayashi and Naoji Fujimori, "Epitaxial Growth of High Quality Diamond Film by the Microwave Plasma-Assisted Chemical-Vapor-Deposition Method", Japanese Journal of Applied Physics, Vol. 29, No. 1, January, 1990, pp34-40.
- [Silv] M.Silveira, M.Becucci, E.Castelucci, F.Polla Mattiot, V.Barbarossa, R.Tomacielo, F.Galluzi, "Non-diamond carbon phases in plasma-assisted deposition of crystalline diamond films: a Raman study," Diamond and Related Materials 2 (1993), p. 1257-1262.
- [Silv] F.J.G.Silva, A.J.S.Fernandes, F.M.Costa, V.Teixeira, A.P.M.Baptista, E.Pereira, "Tribological behavior of CVD diamond films on steel substrates," Wear, 255: 846-853 Part 2, 2003
- [Spit] B.V.Spitsyn, L.L.Bouilovand and B.V.Derjaguin,"Vapor Growth of Diamond on Diamond and Other Surfaces," J. Cryst. Growth 52, 2 (1981), pp219-226.
- [Suma] A.Sumant: This film looks smoother than the previous one. I am thinking of sending that seal to Tony at flowserve to have look at its waviness then I can test that seal here at ANL. Conversations on August 29th 2000.

- [Sun] Y.N.Sun, H.Z.Yun, W.T.Guo, and J.Q.Li, "Diamond IR optical coatings by hot filament chemical vapor deposition," *Thin Solid films*, 212, pp.137-139, 1992.
- [Tamh] Amit Arvind Tamhane: *Growth ledges and morphological development in diamond films*, (1992) Ph.D. thesis, Ohio State University.
- [Tang] C.J.Tang, A.J.Neves, A.J.S.Fernandes, J.Gracio, and N.Ali, "A new elegant technique for polishing CVD diamond films," *Diamond and Related Materials*, 12, pp.1411-1416, 2003.
- [Tenn] S.Tennant, "On the Natural of the Diamond," *Phil. Trans. Roy. Soc. London*, 87, 123 (1797).
- [Thom] M.Thomas and W.J.Tropt, *Johns Hopkins APL Technical Digest*, 14, pp.16-23, 1993.
- [Thor] A.P.Thorne, "Spectrophysics," London, Chapman and Hall, 1988.
- [Ulcz] M.J.Ulczynski, "*Low-Temperature Deposition of Transparent Diamond Films with a Microwave Cavity Plasma Reactor*," Ph. D thesis at the Michigan State University, Department of Electrical Engineering (1998).
- [Ulcz] M.J.Ulczynski, B.Wright, and D.K.Reinhard,"Diamond-coated glass substrates," *Diamond and Related Materials*, 7(11-12):1639-1646, 1998.
- [Vavi] V.S. Vavilov, "Diamond as a Material in Solid State Electronics," *Mat. Res. Soc. Symp. Proc. Vol.242*, 1992, pp87-95.
- [Wang] T.Wang, H.W.Xin, Z.M.Zhang, Y.B.Dai, and H.S.Shen, "The fabrication of nanocrystalline diamond films using hot filament CVD," *Diamond and Related Materials*, 13, pp.6-13, 2004.
- [Wang] X.H.Wang, L.Pilione, W.Zhu, W.Yarbrough, W.Drawl, and R.Messier, "Infrared Optical Properties of CVD Diamond Films," *J. Mater. Res.*, 5, 2345, 1990.
- [Wild] C.Wild, W.Muler-Sebert, T.Eckermann and P.Koidl,"Applications of Diamond Films and Related Materials," Editor: Y.Tzeng, M.Yoshikawa, M.Murakawa, and A.Feldman, Elsevier Science Publishers. B.V. 1991.
- [Xu] T.Xu, S.R.Yang, M.Chen, J.Tian, Q.Xue, J.Li, and W.T.Guo, "Influence of Nitrogen Ion Implantation on Tribological Properties of Nanocrystalline Diamond Films," *J. Phys. D: Appl. Phys.* 35(8), 788-793, 2002.
- [Yama] K.Yamanouchi, N.Sakumi, T.Satoh, *Proceedings IEEE Ultrasonics Symposium*, p351, 1989.

- [Yang] W.B.Yang, F.X.Lu, and Z.X.Cao, "Growth of nanocrystalline diamond protective coatings on quartz glass," J. Appl. Phys., 91(12): 10068-10073, 2002.
- [Yosh] H.Yoshikawa, C.Morel, and Y.Koga, "Synthesis of nanocrystalline diamond films using microwave plasma CVD," Diamond and Related Materials, 10, pp.1588-1591, 2001.
- [Yosh] M.Yoshikawa, G.Katagiri, H.Ishitani, A.Ishitani, M.Ono, K.Matsumura, "Characterization of crystalline quality of diamond films by Raman spectroscopy," Applied Physics Letters 55 (1989), pp.2608-2610.
- [Yosh] M.Yoshikawa, G.Katagiri, H.Ishida, A.Ishitani, T.Akamatsu, "Raman spectra of diamondlike amorphous carbon films," Journal of Applied Physics 64 (1988), p. 6464-6468.
- [Zait] A.M.Zaitsev, "Optical Properties", Chapter 7, M.A.Prelas, G.Popovich, and L.K.Bigelow, Hand book of Industrial Diamonds and Diamond Films, Marcell Dekker, Inc., New York, 232, 1998.
- [Zarr] M.Zarrabian, C.N.Fourches, G.Turban, C.Marhic, and M.Lancin, "Observation of nanocrystalline diamond in diamondlike carbon films deposited at room temperature in electron cyclotron resonance plasma," Applied Physics Letters, 70(19):2535-2537, 1997.
- [Zhan] Jie Zhang: *Experimental development of microwave cavity plasma reactors for large area and high rate diamond film deposition*, Ph. D. thesis at the Michigan State University, Department of Electrical Engineering (1993).
- [Zhan] J.Asmussen and J.Zhang,"Apparatus for the coating of Material on a Substrate Using a Microwave or UHF Plasma,"U.S.Patent N.5,311,103,May 10,1994.
- [Zhou] D.Zhou, D.M.Gruen, L.C.Qin, T.G.McCauley and A.R.Krauss, J. Appl. Phys. 84, 1981 (1998).
- [Zhu] W.Zhu, A.R.Badzian, and R.Messier, J. Mater. Sci. Lett. 2, 785, 1983.
- [Zhu] W.Zhu, A.Inspector, A.R.Badzian, T.Mckenna and R.Messier, 'Effect of Noble-Gases on Diamond Deposition from Methane-Hydrogen Microwave Plasmas,' J. Appl. Phys. 68, 1489, 1990.
- [Zhu] W.Zhu, B.R.Stoner, B.E.Williams, and J.T.Glass, "Growth and Characterization of Diamond Films on Nondiamond Substrates for Electronic Applications," Proceedings of IEEE 79, 5, p621-646, 1991.

- [Zuik] C.Zuiker, A.R.Krauss, D.M.Gruen, X.Pan, J.C.Li, R.Csencsits, A.Erdemir, C.Bindal, and G.Fenske, "Physical and tribological properties of diamond films grown in argon-carbon plasmas," *Thin Solid Films*, 270, pp.154-159, 1995.

